Fungal Cell-based Microcarriers and Their 3D Assembly as Encapsulation and Oral Delivery Systems for Bioactive Compounds

By

YIXING LU

DISSERTATION

Submitted in partial satisfaction of the requirements for the degree of

DOCTOR OF PHILOSOPHY

in

Food Science

in the

OFFICE OF GRADUATE STUDIES

of the

UNIVERSITY OF CALIFORNIA

DAVIS

Approved:

Nitin Nitin, Chair

Gail M. Bornhorst

Andrew J. Gravelle

Committee in Charge

2023

# Dedication

I dedicate this dissertation to my parents, Limin Lu and Qun Xu. Your unwavering love, support, and encouragement have made me who I am. Your belief in my abilities and your sacrifices have fueled my determination to pursue knowledge and reach new heights.

## Acknowledgements

I would like to express my deepest gratitude and appreciation to my advisor Dr. Nitin Nitin for his invaluable guidance, endless inspiration, and continuous encouragement throughout the entire journey of my Ph.D. study. His expertise and interdisciplinary mindset have been instrumental in shaping the direction and success of this work.

I would like to extend my gratitude to Dr. Gail Bornhorst for serving on my qualifying exam committee and dissertation committee and providing support and help for my research. I would also like to thank Dr. Andrew Gravelle for his critical feedback on this dissertation work. I gratefully acknowledge Dr. Stephanie Dungan, Dr. Maria Marco, Dr. Selina Wang, and Dr. Karen McDonald for their service on my qualifying exam committee and their constructive feedback on my research proposal.

I would also like to express my heartfelt appreciation to Dr. Rewa Rai for her mentorship and support from my first day in the lab, as well as her invaluable contribution to this work. I would like to thank Dr. Stephen Young for his help and advice at the beginning of my Ph.D. I am also grateful to Dr. Ingrid Brust-Mascher and Dr. Clay Swackhamer for providing their technical expertise and insights to this work. Thank you to Dr. Wally Yokoyama for his encouraging words and kind support. I would like to extend my gratitude to all the collaborators who have contributed their expertise, time, and effort to this research. Their input and collaboration have enriched the scope and quality of the work.

I would like to express my sincere appreciation to the Department of Food Science, University of California – Davis for the learning and research opportunities, fellowships, scholarships, and all forms of assistance during my Ph.D. study. I also would like to convey my

gratitude to the Designated Emphasis in Biotechnology program and Dr. Jamison-McClung for building a bridge between academia and the biotech industry and helping me explore and develop my career interest.

Furthermore, I am appreciative to my lab mates and colleagues for creating a stimulating and collaborative environment. Their knowledge sharing and discussions have been crucial in my academic growth. Their support and friendship have made the Ph.D. journey more enjoyable and memorable. I am also truly grateful to my friends around the globe for their love, trust, and accompany from close and afar. Without their support, I could have never preserved in this long journey.

Lastly, I would like to extend the deepest appreciation to my family: my parents, Qun Xu and Limin Lu, and my grandparents, Huifen Zhu and Minxin Xu. This accomplishment would not be possible without your unconditional love and support. Thank you for always believing in me and respecting my decisions. I hope I made you proud.

# Abstract

Plant-derived bioactive compounds are minor constituents of natural plant foods that exist in trace amounts but have validated benefits to human health. Despite the promising evidence on their therapeutic or health-maintaining effects, it cannot be directly translated into dietary recommendations. One of the many challenges is that the fraction of bioactive compounds that can be released from food matrices, defined as bioaccessibility, will be different depending on the compositions and structures of the food matrices and their physical and chemical interactions with the bioactive compound. Majority of the current studies investigated such a food matrix effect on bioaccessibility of plant-derived bioactive compounds by evaluating the effects of different processing techniques and conditions on the bioaccessibility. Considered as a top-down approach, this method often fails to decouple the effects from various contributing mechanisms, such as the chemical and structural factors, since the observed effects are lumped and collective.

This research adopted a bottom-up approach to investigate the multi-scale food matrix effect on bioaccessibility of plant-derived bioactive compounds during *in vitro* digestion. Inspired by natural foods, tissue-like encapsulation systems for bioactive compounds were constructed with different levels of compositional and structural complexities, using yeast-based microcarriers as the building blocks, and techniques such as 3D printing for guided cell assembly. A combined experimental and modeling approach was taken to investigate the bioactive compound – food matrix interactions in the encapsulation systems. The central hypothesis tested in the current research was that the encapsulation and release of bioactive compounds could be affected by the chemical and physical interactions among the bioactive compounds, the encapsulation matrices, and the digestion fluids' components at different scale levels, i.e., the sub-cellular, cellular, and tissue levels.

The encapsulation of bioactive compounds and their release profiles during *in vitro* digestion were evaluated for all the cell-based and tissue-like matrices. This research found that at a cellular level, it was mainly the interactions among the bioactive compounds, the cellular components, and the digestion fluids components that controlled the release kinetics. Such interactions included complex formation and dissociation between compounds and cellular proteins, partition among the extracellular environment and intracellular lipid-rich phase and protein-rich aqueous phase, as well as the changes in cellular composition and intracellular structures during digestion. At a tissue level, besides the abovementioned interactions, physical barriers to compounds' release become more significant, such as diffusion impediment and physical entrapment due to the presence of extracellular matrix or the assembly of single cells. Moreover, this research incorporated the element of *in silico* evaluation by constructing predictive models for the encapsulation efficiency and release patterns of compounds in cell-based carriers, and printability of food inks. In the effort to construct the *in silico* evaluation pipelines, we exploited multimodal data to characterize the encapsulation systems and utilized statistical tools and machine learning/ deep learning algorithms for proper feature selection and model training.

Overall, the findings of this research resulted in a better understanding of the bioactive compound – food matrix interaction both during encapsulation and *in vitro* digestion, demonstrating the possibility to modulate the *in vitro* release kinetics of bioactive compounds by modifying the chemical or structural features of encapsulation matrices at the cell level or tissue level. Further development of the *in silico* pipelines for formulation evaluation and optimization could facilitate the design and development of novel nutraceuticals and functional foods.

# Table of Contents

## List of Tables

## List of Figures

# CHAPTER 1

# Introduction

## 1. Bioaccessibility of plant bioactive compounds: matrix effect

Foods are comprised of essential macronutrients such as carbohydrates, proteins, and fats, as well as nutritional or non-nutritional compounds that exist in trace amounts but are crucial for human health. Bioactive compounds are such minor constituents of foods or dietary supplements with potential health benefits that have been demonstrated by *in vitro* and *in vivo* experiments [1]. Among various food sources, plants have a large diversity of bioactive compounds, which are mainly secondary metabolites [2] that plants produce to increase their competitivity in their living environments [3]. There exists extensive evidence for the health benefits of plant-derived bioactive compounds. For example, since 2000, there has been a rapid increase in the number of publications on flavonoids, carotenoids, and other phytonutrients and health outcomes [4]. Several of these compounds have been evaluated in clinical trials to investigate their antioxidant [5,6], anti-inflammatory [7], and anti-cancer activities [8,9].

Despite the extensive and promising evidence on the therapeutic or health-maintaining effect of bioactive compounds, it cannot be directly translated into dietary recommendations. One of the many challenges is that the bioactivity of a compound could be different when ingested as part of a food structure, as opposed to being ingested as supplements (capsules, tablets, etc.) or injected intravenously [2,10]. There are many barriers that the bioactive compounds need to overcome as they move from ingestion to the sites of their metabolic activities in the body [11–13]. The first barrier is for the ingested compound to be released or liberated from the food matrix in the GI tract. The fraction of released compound from the food matrix is defined as

bioaccessibility [14]. The term "food matrix effect" appears in the food and nutrition literature mostly to denote that a chemical compound could behave differently in a free form than as part of a food material [15]. The food matrix has a direct impact on the bioaccessibility of bioactive compounds by affecting their chemical stability, enzymatic accessibility, and release from the food structure [16].

The food matrix has been described as an assembly of food molecules that interact with each other physically or chemically. The way those food components are structurally organized at micro-, meso-, and macroscopic scales and their molecular relationships could influence the physical, sensorial, and nutritional properties of foods [15,16]. Food matrix effect in the context of bioaccessibility is compound-specific and length scale-dependent [16]. Depending on the chemical nature of the bioactive compound, the food matrix components it can interact with are different even in the same food structure. For example, different polyphenols exhibited binding selectivity to different cell wall polysaccharides. Cellulose is the major binding component to catechin, but the negatively charged pectin can bind the positively charged cyanidin-3-glucoside much more effectively [17]. Moreover, the mechanism of food matrix effect might be different when the food is examined at different length scales, e.g., at the sub-cellular, cellular, tissue level or beyond. Oftentimes more than one mechanism and scale need to be considered for the release and absorption of a certain bioactive compound given the complexity of food structures and compositions.

### 1.1. Presence of physical barriers and/or impediment to digestion

#### *1.1.1. Cellular matrix*

In natural plant foods, like fruits, vegetables, nuts, etc., the nutrients and bioactive compounds often reside inside plant cells enclosed by cell walls. The plant cell wall

mainly consists of a network of cellulose microfibrils tied into a highly cross-linked matrix of pectin by cross-linking glycans [18]. Entrapment within an intact cell wall is proposed to be the mechanism responsible for the limited extent of digestion of lipids [19,20] and the limited bioaccessibility of lipophilic bioactive compounds, e.g. carotenoids [21], from plant foods. Various studies have shown that the lipolysis of lipid in almonds [22] and the bioaccessibility of carotenoids from tomatoes and carrots [23] were significantly enhanced after mechanical breakdown of the plant tissue matrices into smaller particles, which could be achieved during processing (i.e., cutting, grinding, pureeing), and oral mastication. Evidence from different studies supported that cell wall disruption is a prerequisite for the release of lipid and carotenoids from plant tissues [20,24], which only occurs in cells at the surface of the tissue fragments. Besides acting as a physical barrier, the cell wall also serves as the glue that binds cells together to form a hierarchical plant tissue structure [25]. Other than mechanical rupture of the cell wall, food processing such as heating or freezing can also disturb the cell tissue structure. Thermal treatment could solubilize the cell wall pectin that binds the cells together, leading to softening of the tissue, cell separation, and increase in the porosity of cell walls, so that the digestive enzymes may work more efficiently [26,27] and results in higher bioaccessibility of compounds such as $\beta$-carotene [26,28,29]. Freezing has been shown to damage the plant food matrix [30] due to formation of ice crystals, leading to better extractability and higher bioaccessibility of polyphenols [31].

### *1.1.2. Viscous matrix*

Physical impediments to digestion can also exist after the bioactive compounds are released from the cellular matrix. Increasing viscosity or the presence of hydrogels in the

food matrix largely impedes the diffusion of digestive enzymes to the bioactive compounds and the release of compounds out of the matrices [32,33], thus affecting the compound bioaccessibility. A hydrogel is defined as a biopolymer network that can hold a large amount of water and that is an intermediate between solid and liquid, possessing viscoelastic properties [34]. Gel formation and increased viscosity in food products could result from addition of polysaccharides-based (e.g., pectin) or protein-based (e.g., gelatin) gelling agents, during dairy fermentation through acid-induced coagulation of casein micelles [35], or the production of exopolysaccharide (EPS) by some bacteria in the formation starter culture [36], as well as the leaking of solubilized dietary fibers from plant cell walls into a fluid food matrix due to extensive heating and homogenizing [37].

1.2. Complex formation with food matrix components

In cellular matrices, the cell wall is not the only barrier to compound release. At the sub-cellular level, different compounds could be associated with different microstructural elements and organelles. For example, carotenoids are stored in an organelle called chromoplasts in plant cells. $\beta$-carotene could exist in the form of free crystals, or as membrane-bound carotene structures in chromoplasts [29]. The crystalline $\beta$-carotene could also complex with proteins [37]. Both the location and the physical states of carotenoids could affect their bioaccessibility [38,39]. It has been shown that in tomatoes, the chromoplast substructures represented an even more important barrier to the bioaccessibility of lycopene compared to the cell wall [24]. Thermal treatment increases the bioaccessibility of carotenoids not only by increasing the cell wall porosity, but also by weakening the complexation between carotenoids and the chromoplast substructure [27,40], facilitating their release from the cellular matrices. Not only the bioactive compounds, components in the digestion fluid can

also complex with food matrix molecules, reducing the compound bioaccessibility. In the carotenoids example, besides break down of the cell wall, another critical step determining its bioaccessibility is the micellization of carotenoids together with lipids facilitated by bile salts and lipases after being released from the food matrix [41,42]. The presence of cell wall polysaccharides could interfere with the micellization step by binding with bile salts, inhibiting lipase activity, and modifying the surface of lipid droplets [43–45]. It has been shown that degrading cell wall polysaccharides by enzymes [46,47] or high pressure homogenization [48] increased the bioaccessibility of carotenoids.

Select polyphenols exhibit binding affinity to various cell wall polysaccharides [17], mostly through non-covalent interactions, i.e., hydrogen bonding, electrostatic forces, and hydrophobic interactions [49]. The complexation between plant cell wall polysaccharides and various polyphenols has been shown to greatly limit the bioaccessibility of polyphenols in the upper gastrointestinal tract [50–54]. On the other hand, the cell wall polysaccharides have been shown to improve the stability of polyphenols during gastric and intestinal digestion [55], and protect the polyphenols until they reach the colon, where they can be fermented by the microbiota [56]. The interaction between polyphenols and gut microbiota has been reviewed elsewhere [57]. Besides complexation with polysaccharides, polyphenols are also known for their interaction with proteins, through either covalent or non-covalent bonds [49], among which hydrophobic interactions and hydrogen bonding are the most important driving forces for the formation of protein-polyphenol complexes [58]. The interaction with proteins also significantly alters the bioaccessibility of polyphenols. For example, it has been reported that addition of skimmed milk significantly increases the bioaccessibility of polyphenols in coffee beverage [59], and apple, grape, and orange juices [60], due to the binding of polyphenols to milk

proteins. The presence of proteins also improves the thermal stability of some polyphenols in these beverages [59].

1.3. Current approaches to study the food matrix effect and limitations

A majority of the current studies investigating the food matrix effect on bioaccessibility of bioactive compounds take a top-down approach. Given that the food matrix effect can be compound-specific, many studies compared the bioaccessibility of different bioactive compounds belonging to the same class, e.g., lutein and $\beta$-carotene as carotenoids, from the same or different food sources to elucidate the effect of chemical nature of the compound on its bioacessibility [39,61,62]. Another major body of studies focused on evaluating the effect of different processing techniques and conditions on the bioaccessibility of bioactive compounds. The effect of different heating methods (boiling, steaming, microwave, etc.), heating temperatures, drying, high pressure treatment, as well as different extent of breakdown (cutting, grinding, homogenizing, etc.) has been evaluated for a variety of compounds belonging to the carotenoid and polyphenol groups [63] and some examples were provided in previous sections [26–29].

Thinking of a plant food as a hierarchical structure, the abovementioned approaches, either by identifying different food sources or by processing the food with different conditions, are exerting influence on the plant food at the highest structural level. Then the collective or lumped effect on bioaccessibility was attributed to different hypothesized mechanisms at different length-scale levels. The major limitation of using such a top-down approach to study the relationship between food matrices and micronutrient bioaccessibility is that oftentimes more than one chemical or structural feature of the food matrix would be modified with a single processing treatment. For example, many studies showed that thermal

treatment would increase the bioaccessibility of carotenoids, which had been attributed to different mechanisms, such as weakening the complexation between carotenoids and proteins [40], increasing the cell wall porosity [20], solubilizing pectin that leaded to tissue softening and cell separation [27], etc. These include mechanisms of the cellular matrix effect at all length scales, from sub-cellular, to cellular, then to the tissue level. Potentially, the solubilized pectin could increase the viscosity of the liquid food matrix and impede the micellization of carotenoids [43], thus decreasing the bioaccessibility. Since more than one feature of the food matrix could be impacted simultaneously by a selected processing method, the changes in the compound bioaccessibility cannot be attributed to a specific structural or compositional feature. The same constraint also applies to the studies analyzing the bioaccessibility of different compounds from various food sources. For instance, many studies compared the bioavailability of polyphenols from different plant origins to investigate the effect of different molecular structures and conjugation forms of the polyphenol compounds on their bioaccessibility and bioavailability [64]. However, such studies often ignore the contribution from other food matrix components, such as the differences in cell wall composition, localization of compounds etc. [64,65] Even when comparing the bioaccessibility of the same compound from different sources, e.g., $\beta$-carotene from bell peppers of different colors [66], it is hard to decouple the effect of various matrix effect mechanisms on the observed differences in bioaccessibility.

One way to address such limitations is to use a bottom-up approach to study the food matrix effect in relation to the bioaccessibility of micronutrients. Instead of de-structuring the food with various processing techniques, the bottom-up approach constructs a model food matrix additively by starting with a basic building block, and then gradually increasing the

compositional and structural complexity of the matrix (***Figure 1. 1***). Using this approach, we can have better control over the specific features that are changed among different constructed matrices. The first step in this approach is to select an appropriate primary building block, which is the basic unit that houses the bioactive compounds. The following section discusses how the building blocks can be fabricated through encapsulation, and different types of encapsulation systems for bioactive compounds.

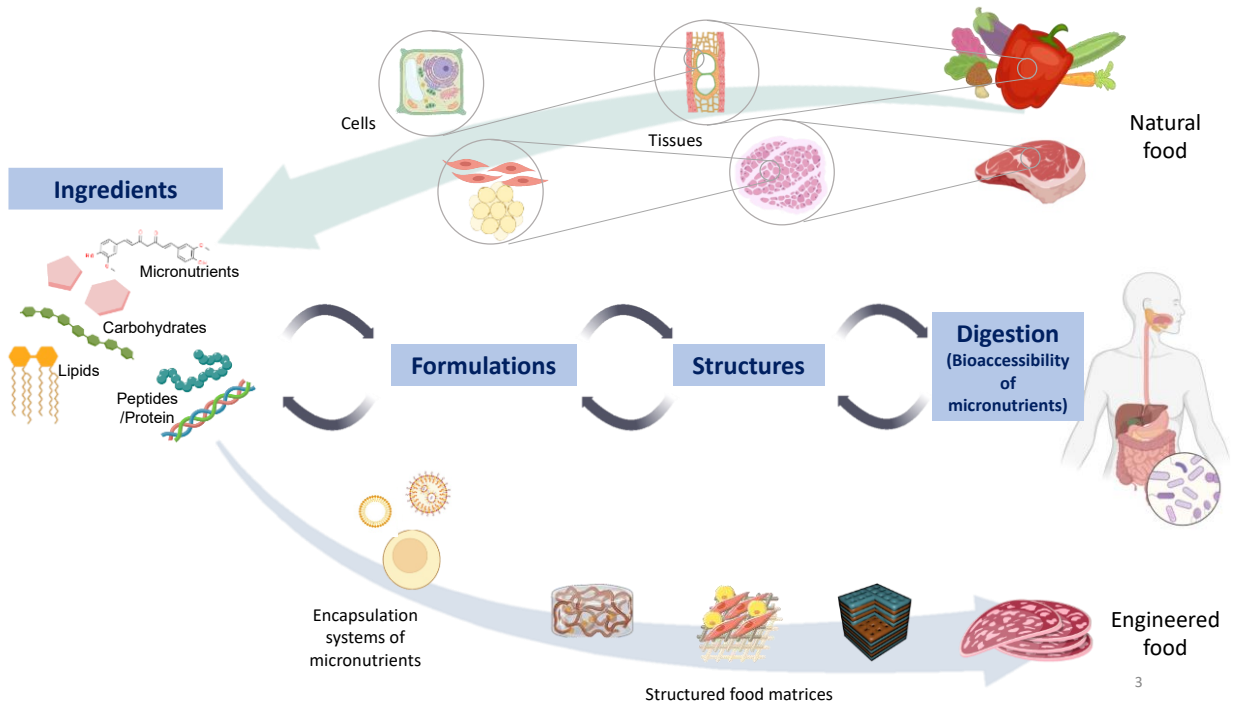


***Figure 1. 1: Illustration of the hierarchical structure of natural plant foods and their correspondence in model food at different length scales.***

## 2. Engineered and natural encapsulation systems for plant bioactive compounds

### 2.1. Definition and objectives of encapsulation

The encapsulation process involves enclosing target compounds into a matrix which serves as a protective barrier between the compounds and the external environment. Many

nutraceutical and functional food components would benefit from being encapsulated in edible delivery systems, including antioxidants, vitamins, bioactive peptides, flavors, and aromas etc [67–69]. Different encapsulation matrices are utilized to address different physiochemical concerns associated with specific functional component, such as instability during processing and storage, limited solubility in food formulations, low content in natural foods, etc. To serve as an ideal oral delivery system for bioactive compounds, the encapsulation matrices should also be able to release the compound in a controlled manner in the gastrointestinal tract: at a specific action site, with a controlled rate, or in response to an environmental trigger (e.g., pH, temperature, ionic strength, etc.). Similar to how the interaction between bioactive compounds and the food matrix would impact their bioaccessibility, the release of encapsulated compounds from encapsulation matrix also depends on the composition, structure, and the molecular interaction of the encapsulation matrix components with the bioactive compounds and the external environment. A wide variety of different types of encapsulation systems have been developed for bioactive compounds and other functional food components, which can be classified into two broad categories: engineered and natural encapsulation systems, which are differentiated by the way they are formed. Engineered encapsulation systems are formulations fabricated using various ingredients and techniques to achieve certain functionality of the compound of interest. Natural encapsulation systems often utilize a natural structure, e.g., a cell, or part of it, e.g., an organelle, to serve similar purposes.

## 2.2. Engineered encapsulation systems

For nutraceutical and functional food applications, engineered encapsulation systems are mostly colloidal delivery systems that are fabricated with edible materials to encapsulate,

retain, protect, and deliver bioactive compounds. Based on particle size, the colloidal delivery systems include nanoparticles (≤100 nm) and microparticles (>100 nm) [70]. Based on the materials and technologies used to structure the colloidal systems, they can be classified into lipid-based, surfactant-based, and biopolymer-based systems [71]. Lipid-based are created using emulsion technology. An emulsion consists of at least two immiscible liquid phases, mostly oil and water, with one of the phases dispersed as small droplets in the other [72]. An emulsion is a thermodynamically unstable system which requires intensive energy input, i.e., homogenization, to create such dispersion. Oftentimes, emulsifiers or texture modifiers are added to the system to maintain the stability of the emulsion for a longer period by adsorbing to the surface of the dispersed droplets or by increasing the viscosity of the continuous phase to retard droplet movement respectively [73]. Depending on how the emulsions are structured, examples of lipid-based encapsulation systems include conventional emulsion (e.g., oil-in-water O/W), multiple emulsion (e.g., W/O/W), multilayer emulsion, and solid lipid particle emulsions [71]. Another class of engineered encapsulation systems that is commonly used for lipophilic compounds is surfactant-based systems, such as simple micelles, mixed micelles, vesicles, liposomes, etc. [74,75] Most surfactant-based systems are based on the spontaneous self-assembly of the surfactant molecules in aqueous solutions [76]. Such self-assembly is driven by hydrophobic effects that result in reduction of free energy when the interaction between the lipophilic tails of surfactants and water molecules is avoided [77]. Lipophilic compounds can be incorporated into such colloidal structures as part of the surfactant layer or encapsulated in the core of micelles [71]. Biopolymers like proteins and polysaccharides can be used to create matrices to entrap bioactive compounds. Normally the process starts with a biopolymer solution and one or more environmental conditions are changed to induce the

formation of polymer aggregates, such as temperature, pH [78], ionic strength [79], or covalent crosslinking [80]. Two or more biopolymers can be combined to create encapsulation systems, either as a single-phase or two-phase systems [81]. When the two biopolymers can co-solubilize or form soluble complexes, they do not become segregated in the aqueous phase. The two-phase systems can occur through two mechanisms: associative separation (coacervation or co-precipitation of two biopolymers with attractive interactions) and segregative separation (e.g., W/W emulsion from two phase-separated aqueous phases) [82].

Some of the abovementioned engineered encapsulation systems have been used in the food industry, while others are mostly applied in pharmaceutical and cosmetic industries but have the potential to be adopted in the food industry. Overall, the engineered encapsulation systems are favored due to their versatility and flexibility, wide range of physiochemical properties, and the ease of modification. However, there are limitations especially when utilized for food applications, such as the cost of raw materials and fabrication technologies, intensive energy input, regulatory restrictions, environmental and sustainability considerations, etc.

## 2.3. Natural encapsulation systems

### *2.3.1. Non-cell carriers*

Besides the engineered colloidal delivery systems, there are naturally existing colloidal systems that can be used as encapsulation systems for bioactive compounds [83]. One such example is the oleosome, the organelle that stores lipid in plant cells. Oleosomes consist of a triacylglycerol core stabilized by an interfacial layer of phospholipids and proteins (oleosins) [84]. The high permeability of the interfacial membrane and the hydrophobic core make the oleosome a good delivery system for lipid-

soluble compounds, such as carotenoids [85] and aroma compounds [86]. Another natural delivery system that has similar structure to the oleosome is the milk fat globule. It also has a hydrophobic core that mainly consists of triacylglycerol, surrounded by an interfacial layer called milk fat globule membrane (MFGM) [87]. MFGMs have a more complex structure than the interfacial membrane of the oleosome. They contain a single layer of polar lipids and proteins derived from the endoplasmic reticulum, and a bilayer from the plasma membrane of the mammary gland secretory cells [88]. Milk fat globules are designed by nature to transport fatty acids, lipid-soluble micronutrients, and polar lipids that are essential for neonatal development. As a delivery system for exogeneous bioactive compounds, milk fat globules have been successfully isolated from cream and used to encapsulate bioactive compounds like Vitamin D3 [89] and curcumin [90]. Casein micelles are another natural delivery system from milk, delivering phosphate and calcium to neonates [91]. A few studies have explored the possibility of using native casein micelles as carriers for hydrophobic compounds such as curcumin [92], Vitamin A [93], sphingomyelins, phosphatidylcholines, and phosphatidylethanolamines [94]. Casein micelles are also good binders to metals and charged molecules. Incorporating iron into casein micelles is a breakthrough in this field since iron is considered one of the most difficult micronutrients for fortification in foods [95]. This technology has been patented and commercialized [96].

Utilizing intact nature-assembled colloidal structures as encapsulation systems has advantages including wide availability from common food materials with no need for fabrication, a well-defined regulatory status, the compositional and structural complexity of the natural systems enabling encapsulation of compounds with diverse properties.

Compared to engineered encapsulation systems, a major drawback that limits the application of natural encapsulation systems is the limited flexibility and control on their compositions and structures given they are complex biological systems. One solution to this challenge is to use the materials from these natural structures to construct artificial systems, for example: "reassembled casein micelles" fabricated from sodium caseinate, potassium citrate, dipotassium phosphate, and calcium chloride [97,98]; O/W emulsion and liposomes fabricated using MFGM [99,100] and oleosome membrane materials [101]. However, formulations developed using this approach can be classified as engineered encapsulation systems, losing one major advantage of using natural encapsulation systems – no need for fabrication and minimal processing. Moreover, because of their complex composition and structures, natural encapsulation systems are more difficult to characterize and study.

### *2.3.2. Yeast cell-based carriers*

#### *2.3.2.1. Encapsulation*

Another category of natural encapsulation system is cell-based carriers, among which yeast-based microencapsulation is the most extensively studied sub-field [102]. In the food sector, using yeast cells as micro-carriers has emerged as a practical encapsulation approach for the delivery of various types of compounds, such as antioxidants [103], aromas [104], and many bioactive compounds [105–107]. Undoubtedly, *Saccharomyces cerevisiae* is the most studied yeast strain for encapsulation applications due to its large-scale commercial production, high nutritional value, and availability as by-products of fermentation processes [108]. One of the biggest advantages of using yeast cells as encapsulation agents is that the cells with a micro-scale size (5-10 $\mu m$) can be used as is, eliminating the need to fabricate colloidal

structures as in engineered encapsulation systems, or to extract the materials as for the non-cell natural encapsulation agents. Dated back to the 1970s [109], the potential application of yeast cells as encapsulants has been explored in numerous studies, which reported that the yeast cells could enhance the oxidative and thermal stability of the encapsulated molecules during storage compared to colloidal carriers such as emulsions [103,110,111]. The yeast cell wall is rich in $\beta$-glucans and chitin, responsible for the cell rigidity [112]. Together with the plasma membrane, it formed a sturdy structure that is capable of housing both hydrophobic and hydrophilic compounds. The yeast cell wall has been shown to prevent lipid peroxidation and inhibit the oxidative damages to DNA associated with its radical scavenging properties [113].

Unlike engineered encapsulation systems where the loading yield of bioactive compounds can be controlled in the fabrication process, the loading yield and encapsulation efficiency into yeast cells are influenced by both intrinsic factors, like the chemical nature of the compounds and the biochemical properties of the cells, as well as extrinsic factors, i.e., the pre-treatments applied to yeast cells before encapsulation, compound-to-cell ratio, etc. The cell permeability to the compounds depends on their molecular size, shape, and the presence of hydroxyl groups [114]. Data reported on the maximum molecular sizes permitting passage through yeast cell walls varied from 700 Da [115] to 60 kDa [116]. Conservatively speaking, molecules smaller than 700 Da should diffuse freely through yeast cell walls. However, the plasma membrane might be the restrictive barrier for large or polar or charged molecules [117]. An early study by Bishop [114] showed that the presence of hydroxyl groups on the molecules increased the fluidity of the plasma membrane and the permeation rate

because the hydroxyl groups provided affinity to the polar head of phospholipid in the membrane and allowed emulsification of these molecules within the tightly packed phospholipid bilayer.

According to previous research, different pre-treatment methods have been utilized to increase the cell permeability to the compounds and/ or to deplete intracellular components to make space for the compounds. Examples of the pre-treatments include autolysis [118], plasmolysis [103], increasing temperature, pressure [103,107], freeze-drying [119], pulsed electric field (PEF) treatment, osmoporation [120], etc. The kinetics and thermodynamics of compound loading are the two aspects that describe the effects of these pre-treatment methods on the encapsulation process. It is agreed among all the studies that the pre-treatments could increase the permeation rate or kinetics of compounds into the cells. For example, Dimopoulos et al. [121] reported that autolysis and PEF treatment increased the encapsulation rate of oregano essential oils in yeast cells. Permeation rate of essential oils into yeast cells was also shown to increase abruptly when temperature was raised above 40 °C, due to the phase transition of phospholipid bilayers from gel phase to liquid crystalline phase [114]. Young and Nitin [105] used vacuum-facilitated infusion to encapsulate curcumin and fisetin (dissolved in ethanolic solution) into yeast cells and showed an expedited infusion and higher loading yield compared to passive diffusion under atmospheric pressure. Such phenomenon was hypothetically attributed to a synergistic effect of increased cell permeability due to ethanol [122] and vacuum [123], larger concentration gradient due to ethanol evaporation under vacuum, and an intensified capillary flow of liquid into pores on the cell surface due to the vacuum treatment [124]. However, not

all studies agreed upon whether increasing cell permeability and depletion of intracellular components would increase the final loading yield and efficiency. Czerniak et al. [125] reported that the encapsulation efficiency of fish oil increased from 32.6% to 45.3% after treating yeast cells with autolysis and addition of ethyl acetate, which hydrolyzed the cell wall and increased cell membrane permeability respectively. Shi et al. [103] showed that pre-treating yeast cells with plasmolysis and incubating compounds with cells at elevated temperature and pressure could increase the encapsulation efficiency of chlorogenic acid from 6.2% to 12.6%. On the contrary, Young and Nitin [105] reported that the encapsulation yields of curcumin and fisetin in yeast cell wall particles (YCWPs), created by removing most of the cell organelles through harsh thermal and chemical treatment, were lower than those in native yeast cells. Similarly, Paramera et al. [106] revealed that plasmolysis with NaCl did not change the final loading yield of curcumin in yeast. Autolysis and PEF treatment also only increased the permeation rate of oregano essential oils into yeast cells, but not final loading [121]. These results imply that the thermodynamics aspects of encapsulation are not only affected by the cell permeability to the compounds, but also by the capacity of retaining the compounds inside cells, through physical entrapment and/ or complexation between intracellular components and the encapsulated compounds. To the best of the author's knowledge, the effect of cellular biochemical compositions on encapsulation efficiency of yeast-based microcarriers has not been fully elucidated.

*2.3.2.2. In vitro digestion*

Besides encapsulation efficiency, another important feature to evaluate for an oral delivery system of bioactive compounds is the release profile of encapsulated compounds during digestion. *In vitro* digestion using a shaking-beaker method has been commonly applied on yeast cell-based encapsulation systems. Usually, the content of a microcapsule could be released in two routes once submerged in a solution: disintegration [126] and dissolution [127]. Due to the micro-scale size and rigid cell wall, the physical structure of yeast cells could stay intact after digestion [128], although changes in chemical compositions are expected due to the exposure to pH switch, enzymes, and bile salt during digestion. Therefore, dissolution is believed to be the major process through which the encapsulated compounds get released from the yeast-based microcarriers. Paramera et al. [106] have reported that sustained release in simulated gastric fluid and slower degradation in simulated intestinal fluid were observed for curcumin in yeast microcarriers compared to those encapsulated in modified starch and $\beta$-cyclodextrin. Young et al. [128] compared the release profile of curcumin from native yeast and YCWPs in a sequential *in vitro* gastric and intestinal digestion. The results highlighted the important role of gastric phase and the presence of bile salt in the simulated intestinal fluid on the release of curcumin. Moreover, the release rate of curcumin from YCWPs was much faster than that from native yeast cells, indicating the impact of cellular components and their interaction with the encapsulated compounds on the bioaccessibility, which echoes the mechanisms of food matrix effect on bioactive compounds' bioaccessibility, as discussed in the first section.

## 2.4. Beyond the colloidal delivery systems

Both the engineered and natural encapsulation systems discussed so far could be considered as colloidal delivery systems given their sub-micron or micro-scale sizes. Colloidal delivery systems have the advantage of being easily incorporated into food formulations as ingredients. However, if considering these colloidal encapsulation systems as model food matrices to evaluate the bioaccessibility of encapsulated compounds, important features of natural food matrices are still missing, such as the compositional and structural complexity of the cellular matrix, different length scales of looking at the matrix, and the importance of diffusion in the release of compounds, etc. In order to investigate the food matrix effect at different scales, it is necessary to go beyond the current colloidal encapsulation systems by incorporating higher-level structural features into the systems. The following section discusses the methods that can be used to extend the cell-based encapsulation systems to tissue-like materials, which allow us to study higher-scale matrix effect on bioaccessibility of bioactive compounds.

## 3. From cell-based to tissue-like encapsulation systems for plant bioactive compounds

### 3.1. Definition and scope of "tissue-like structures"

In general, "tissue" is defined as a group of cells organized together to perform a specific function. In plant tissues, cell walls are responsible both for maintaining the cell shape as well as for holding the cells together; whereas for animal tissues, there exists extracellular matrix such as collagen where the cells are embedded [129]. The term "tissue-like structure" defined here emphasizes the structural components of a tissue rather than any biological functions it performs. Specifically, a tissue-like structure is defined as a collection of self-assembled or guided-assembled cells with or without the presence of extracellular matrix. In

line with the focus of this dissertation on plant-derived bioactive compounds, the natural or engineered tissue-like structures discussed here are only limited to non-animal sources.

### 3.2. Natural tissue-like structures

Plant tissues from fruits and vegetables are natural reservoir of various bioactive compounds. However, the inherent amount of these bioactive compounds is normally very low. To be considered as functional, a food must be "satisfactorily demonstrated to affect beneficially one or more target functions in the body, beyond adequate nutritional effects and it must demonstrate its effect in amounts that can normally be expected to be consumed in the diet" [130]. Therefore, although many fruits and vegetables contain bioactive compounds with demonstrated health benefits, they cannot be regarded as functional foods due to the low inherent quantity of bioactive compounds per serving. To enhance the nutritional value of plant foods or plant-based by-products from food manufacturing, efforts have been dedicated to explore the feasibility of incorporating bioactive compounds into plant tissues without destroying the initial food matrix [131]. Impregnation processes with osmotic treatment under either atmospheric or vacuum pressures have been shown to infuse grape phenolics [132], minerals, probiotics, [131] etc. into fruits and vegetables. During osmotic treatment, there are two counter-current flows happening: loss of water from the plant tissue and transfer of solutes from the solution into the tissue. The extent of impregnation depends on the concentration and viscosity of the osmotic solution, the pressure, and the cell types as well as the volume occupied by intercellular space [132,133]. The vacuum infusion method originally developed for yeast cell encapsulation systems has also been applied to efficiently infuse resveratrol into grape skin powders, where improved stability and bioaccessibility of resveratrol was observed [134].

Other than plant tissues, edible filamentous fungus (FF) can form another non-animal, natural tissue-like structure. During submerged fermentation of FF, distinct fungal morphologies could be observed due to different microorganisms and culturing conditions used [135]. Fungal pellet (FP) is a dense, spherical aggregate of intertwining fungal hyphae that are spontaneously formed by several FF species [136], such as *Aspergillus spp.*, *Penicillium spp.* etc. [137,138], under submerged, shaking culture conditions. FF has been identified as a sustainable source of alternative protein, since they can grow on a variety of substrates [139–141], including food processing by-products and wastes, making the fungal biomass an affordable substitute to meat products which has a lower water and carbon footprint [142]. To the author's knowledge, there has been no prior studies on infusing exogeneous bioactive compounds into filamentous fungal cells and evaluating their bioaccessibility.

### 3.3. Engineered tissue-like structures

Unlike directly using natural multicellular matrices, engineering tissue-like structures is a bottom-up approach where individual cells are used as building blocks to construct hierarchical structures, through self-assembly and guided patterning. This was inspired by the methods used in tissue engineering to generate 3D tissue structures from cells and biomaterials with an ultimate goal of restoring the physiological functions lost in diseased organs [143]. Both cell-cell and cell-extracellular matrix interaction are crucial for the formation of higher-order 3D structures required for the anatomical and functional mimicry of tissues [144]. Cell self-assembly enables cell-cell contact and interaction, while additive manufacturing with cell-laden bioinks allows spatial arrangement of cells. The following sub-sections provide an overview of current methods in cell self-assembly and additive manufacturing, as well as their relevance to engineering tissue-like structures for food-related applications.

### *3.3.1. Self-assembly approaches*

Different methods of cell surface modification have been developed to reconstitute functional cell-cell contact *ex vivo* and in 3D [145], as summarized in **Table 1. 1**. Cell self-assembly could be induced by decorating the cell surfaces with ligands that have complementary functional groups that could recognize and conjugate with each other. Such conjugation could be mediated through covalent bonds, i.e., chemoselective ligation [144], or non-covalent interactions, such as the avidin-biotin binding system (protein-ligand interaction) [146–148], hybridization of complementary oligonucleotides [145,149], and electrostatic attraction between oppositely charged polyelectrolytes [150–152]. These functional groups or polymers responsible for conjugation could be introduced to the cell surface through various mechanisms as well [153]. Examples are metabolic labeling of cell surface oligosaccharides in glycoproteins and glycolipids [145,149,154], amide bond formation between protein amino groups and N-hydroxysuccinimide (NHS)-esters [148,155], incorporation of a biocompatible anchoring molecule into the plasma membrane bilayer through hydrophobic interaction [146], layer-by-layer coating of polyelectrolytes on cell surface [151,156,157], and liposome delivery and fusion of functional groups to cell membranes [144].

Considering the objective of constructing tissue-like encapsulation systems for food-related applications, appropriate cell self-assembly methods should have the following features: (1) feasible using food-grade materials; (2) low in cost; (3) simple in preparation procedures. Some of the abovementioned methods such as functional group ligation and DNA hybridization are highly selective and capable of programmable assembly [149], which are desirable features for tissue engineering. However, such features are not

prioritized for the current application of constructing tissue-like encapsulation systems. Moreover, these methods either require introduction of synthesized molecules that are not necessarily food-grade and/ or are too costly and complicated to perform. Among all the available methods, electrostatic cell assembly facilitated by polyelectrolyte coating seems to be the most suitable and feasible method. Polyelectrolyte cell surface modification has been applied to different cell types, including yeast cells [156,157]. Subsequently, electrostatic aggregation of colloidal particles and cells has been used to create micro scale assemblies with unique properties [151,152,158].

**Table 1. 1: Methods for cell surface modification and cell self-assembly.**

| | **Conjugation mechanisms** | **Cell surface modification methods** | **Site of modification** | **Reference** |
|---|---|---|---|---|
| Covalent bond | Chemoselective ligation | Liposome fusion | Negatively charged cell surface | 144 |
| Non-covalent bond | Biotin-avidin binding system | Chemical reaction with NHS-biotin | Amino groups of membrane proteins | 148 |
| | | Hydrophobic interaction | Lipid bilayer of cell membrane | 146 |
| | DNA hybridization | Metabolic reaction + Staudinger ligation | Cell surface glycan | 145,149 |
| | | Chemical reaction with NHS-DNA | Amino groups of membrane proteins | 155 |
| | Electrostatic interaction | Electrostatic interaction | Negatively charged cell surface | 150,151 |

### *3.3.2. Additive manufacturing*

Additive manufacturing, as its name suggests, is the process of constructing a 3D object by adding materials together, as opposed to subtractive manufacturing, which represents the traditional machining processes with removal of materials [159]. It enables constructing complex structures with high precision guided by a digital 3D model. In

almost 30 years since its introduction, 3D printing has revolutionized processing in many industries, from aerospace to medicine [160]. In the food sector, 3D printing is also an emerging concept for precision and modular food manufacturing to address the need for customizing food based on personal preferences and nutritional requirements [161]. Among the various 3D printing techniques that have been explored for food applications, such as selective laser sintering, extrusion-based printing, inkjet printing, and binder jetting [162], extrusion-based 3D printing is the most widely used technique [163,164]. This technique has the versatility to print different types of food materials, such as hot-melt extrusion of chocolate [165], room-temperature extrusion of dough, frosting, and Nutella etc. [166,167], as well as extrusion of food hydrocolloids [168,169]. Food-grade hydrocolloid agents, such as various polysaccharides, can either be crosslinked to form gels via chemical modification [170] or ionic complexation [171], or added as thickening agents to modify food properties [172]. Previous studies have demonstrated the potential of developing 3D printed structures using hydrogels composed of starch [170], agar [168], alginate [173], pectin [174] or other polysaccharide-based food inks [175]. However, achieving optimal compositions for a reproducible and high-resolution printing using food-grade materials remains a significant challenge. The challenges result from the lack of comprehensive understanding of a relationship between formulation parameters, rheological properties, and printability features, i.e., extrudability and post-printing stackability [176].

Recently, inspired by the 3D printing of cell-laden bioinks into different structures mimicking the microarchitecture and microenvironment of real organ tissues [163] in the field of tissue engineering, some studies demonstrated the possibility of printing meat and plant simulants using live cells [177,178]. The concept coincides with the idea of engineering

tissue-like encapsulation systems from simpler building blocks in a bottom-up manner. The objective of constructing tissue-like structures using 3D printing is to enable the 3D patterning of cell-based microcarriers and acquire structures with different "intra-tissue" distributions of the bioactive compounds that are encapsulated in the microcarriers, e.g., a core-shell design, a layer-by-layer design, etc. The different 3D printing patterns could be used to reflect the different distributions of bioactives in natural plant tissues, such as a higher concentration of bioactives in the peel vs. seed. These printed structures serve as models to investigate the food matrix effect on bioaccessibility of bioactive compounds at a high scale level – the tissue level, where the chemical interactions among the bioactive compounds, the intracellular components, and the extracellular matrix, as well as the mass transfer in and out of the tissue would all impact the observed release profiles during digestion.

## 4. Dissertation overview

### 4.1. Study overview and objectives

A better understanding of the bioactive compound – food matrix interaction would inspire and guide the design and development of functional foods and nutraceutical formulations for oral delivery of bioactive compounds. This research aimed to address the following gaps in this field:

(1) Current methods for studying the matrix effect of natural food on bioaccessibility of bioactive compounds often fail to decouple the effects from various contributing mechanisms, such as the chemical and structural factors.

(2) Current encapsulation systems, mostly colloidal delivery systems, have not utilized higher level matrix features to modify the release of encapsulated compounds during digestion.

This research adopted a bottom-up approach to investigate the multi-scale food matrix effect on bioaccessibility of plant-derived bioactive compounds during *in vitro* digestion. ***Figure 1. 2*** summarizes the steps taken to develop the natural-food-inspired encapsulation systems, from single-cell yeast-based microcarriers to multicellular tissue-like structures. These encapsulation systems were used to test the central hypothesis that *the encapsulation and release of bioactive compounds would be affected by the chemical and physical interactions between the bioactive compounds, the encapsulation matrices, and the digestion fluid components at different scale levels, i.e., the sub-cellular, cellular, and tissue levels.*

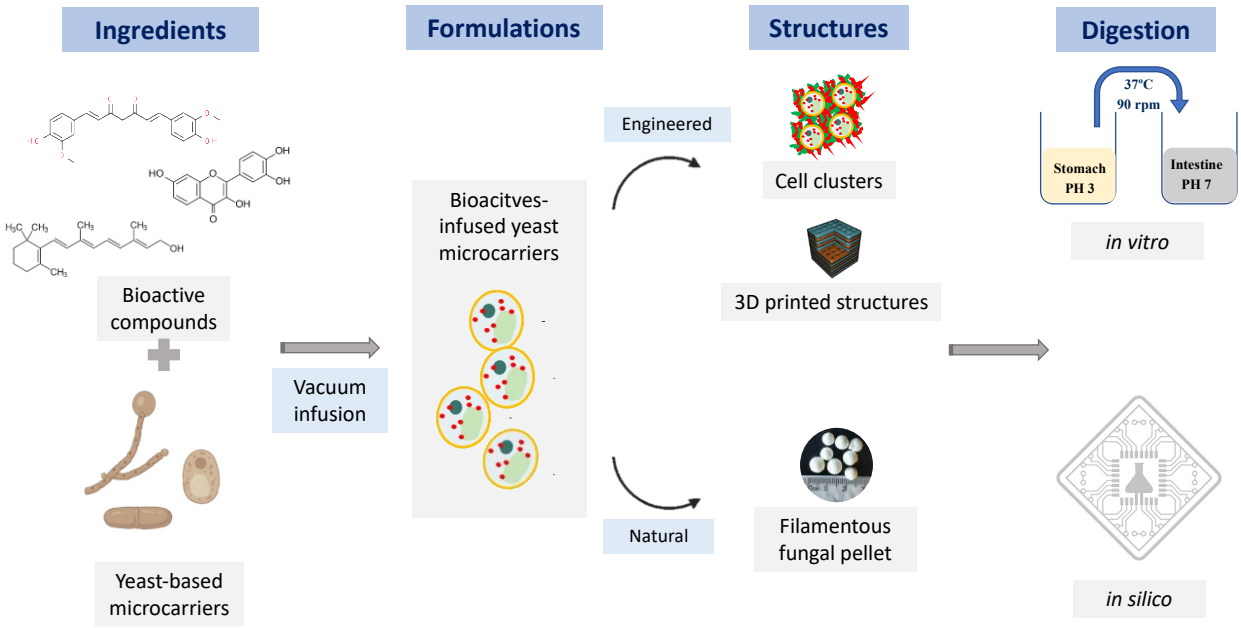


***Figure 1. 2: Overview of the different encapsulation systems constructed in this research: from yeast cell-based microcarriers to tissue-like structures.***

## 4.2. Study outline

This dissertation contains 7 chapters, with Chapter 1: introduction and Chapter 7: conclusions and future research directions. The objective and scope of the remaining 5 chapters are summarized below.

### 4.2.1. Cell-level matrix effect on encapsulation and bioaccessibility of bioactive compounds

As the first step in the bottom-up approach, Chapters 2 and 3 focus on evaluating single-cell yeast-based microcarriers for bioactive compounds in terms of the encapsulation efficiency and the release during *in vitro* digestion respectively.

Chapter 2 hypothesizes that the encapsulation efficiency of yeast-based microcarriers using vacuum-facilitated infusion can be affected by the following factors: yeast cells' protein and lipid content, bioactive compounds' hydrophobicity, and the concentration of ethanol used to solubilize the compound. To enable high-throughput screening of potential cell-based carriers for different bioactive compounds, a predictive modeling pipeline is constructed for encapsulation efficiency, including efficient data collection, proper feature selection, and a good predictive model. The pipeline is outlined in ***Figure 1. 3***.

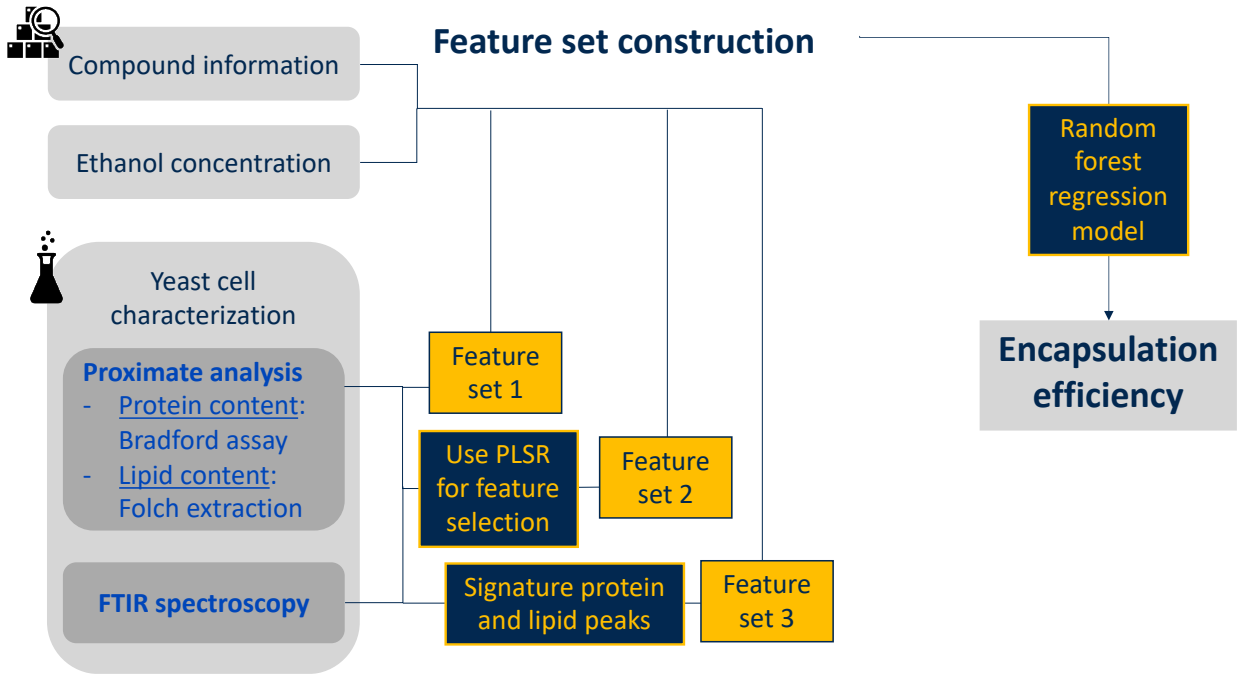


***Figure 1. 3: The predictive modeling pipeline for encapsulation efficiency of cell-based microcarriers.*** PLSR: partial least square regression.

Chapter 3 tests the hypothesis that the sub-cellular localization of bioactive compounds, as an indicator of the affinity between compounds and intracellular components, influences their release profiles during *in vitro* digestion. Cell staining and fluorescence microscopic imaging are used to examine the hypothesis. Images taken before digestion provide rich source of information to predict the release patterns of compounds from different yeast-based microcarriers using a convolutional neural network model (***Figure 1. 4***).

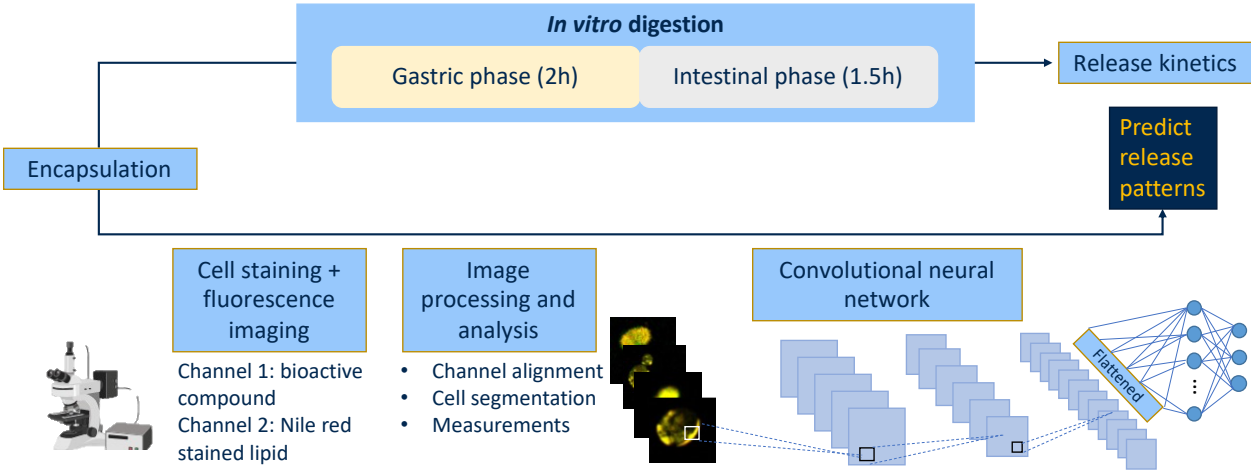


***Figure 1. 4: The pipeline of using fluorescence microscopic images of yeast-based microcarriers with encapsulated compounds to predict their release patterns during in vitro digestion.***

4.2.2. Effect of cell clustering and extracellular matrix on bioaccessibility of a model bioactive compound

Chapter 4 takes the first step from cell-based microcarriers towards the tissue-like encapsulation system. This chapter investigates the effect of microstructural features of engineered multicellular structures on the bioaccessibility of curcumin as a model compound, using a bottom-up approach (***Figure 1. 5***). In this approach, individual yeast cells with infused curcumin are coated with oppositely charged polyelectrolytes, then self-assembled into cell clusters. These cell clusters are embedded in an alginate film to form a tissue-like structure. It is hypothesized that cell clustering and extracellular matrix can both influence the release of encapsulated curcumin from the engineered cell structures during *in vitro* digestion.

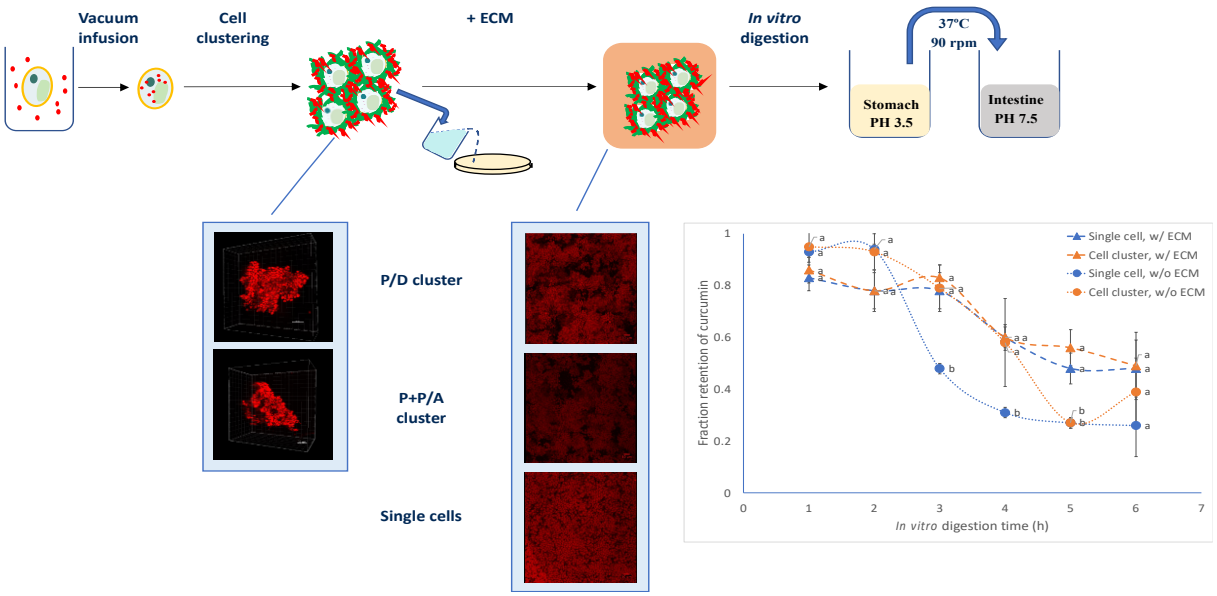


***Figure 1. 5: Graphic abstract of chapter 4: using engineered multicellular structures to investigate the effect of cell clustering and extracellular matrix on bioaccessibility of the encapsulated model compound.*** Acronyms in the figure: "ECM": extracellular matrix; "P", "D", "A" in "P/D cluster", "P+P/A cluster" stand for poly(diallyldimethylammonium chloride), dextran sulfate, and alginate respectively. These are the polyelectrolytes used to coat yeast cells. Please find more details in Chapter 4.

4.2.3. Natural multicellular matrix as an encapsulation and oral delivery system for a model bioactive compound

Chapter 5 evaluates the potential of filamentous fungal pellet (FP) as a natural multicellular matrix to encapsulate exogeneous bioactive compounds. The hypothesis is that the multicellular matrix of filamentous fungal pellet can change the release profile of curcumin as a model compound during *in vitro* digestion, compared to that from single cells (***Figure 1. 6***). Two types of multicellular curcumin encapsulation systems are constructed: (1) curcumin is directly infused into fungal cells (curcumin_in_FP); (2) curcumin is first infused into single yeast cells, then these cells are immobilized into the FP matrix (curcumin@yeast_in_FP). In the first system, the fungal cells serve as both

carriers for curcumin and a mycelia network matrix, whereas in the latter system, the single yeast cells are the carriers and the FP only functions as the matrix. Besides measuring the release kinetics of curcumin from these single-cell or multicellular systems during *in vitro* digestion, fluorescence microscopic imaging was used to visualize the distribution of curcumin in the encapsulation systems throughout the digestion process.

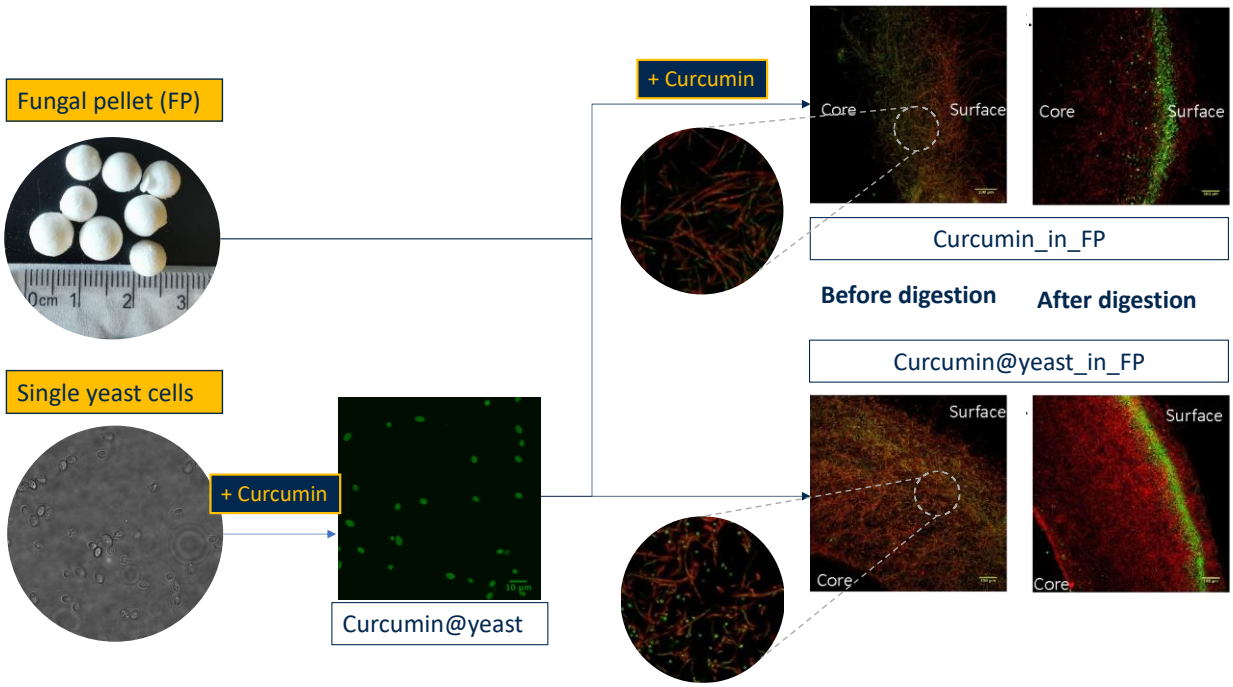


***Figure 1. 6: Graphic abstract of Chapter 5: comparison of curcumin release from single cells vs. natural multicellular encapsulation systems during in vitro digestion.***

4.2.4. Guided 3D patterning of cell-based microcarriers to modify the release profile of the encapsulated compound

There are two major objectives in Chapter 6: (1) formulate plant polysaccharide-based food inks and predict their printability from formulation parameters and rheological characterization; (2) 3D patterning of cell-based microcarriers with an

optimal ink formulation and evaluate the release profiles of the encapsulated compound during *in vitro* digestion.

As illustrated in ***Figure 1. 7***, food inks were formulated with low methoxy pectin, calcium chloride, and cellulose nanocrystalline. It is hypothesized that the rheological properties of the formulated food inks can be used to predict their printability, as assessed by two metrics through image analysis: printed filament width and roughness. Curcumin-loaded yeast cells were incorporated into an optimal ink formula to enable 3D printing of cells into tissue-like structures with different patterns: layer-by-layer and core-shell. The hypothesis is that the release profiles of curcumin from these two structures during *in vitro* digestion will be different due to the different intra-tissue distribution of bioactive compounds.

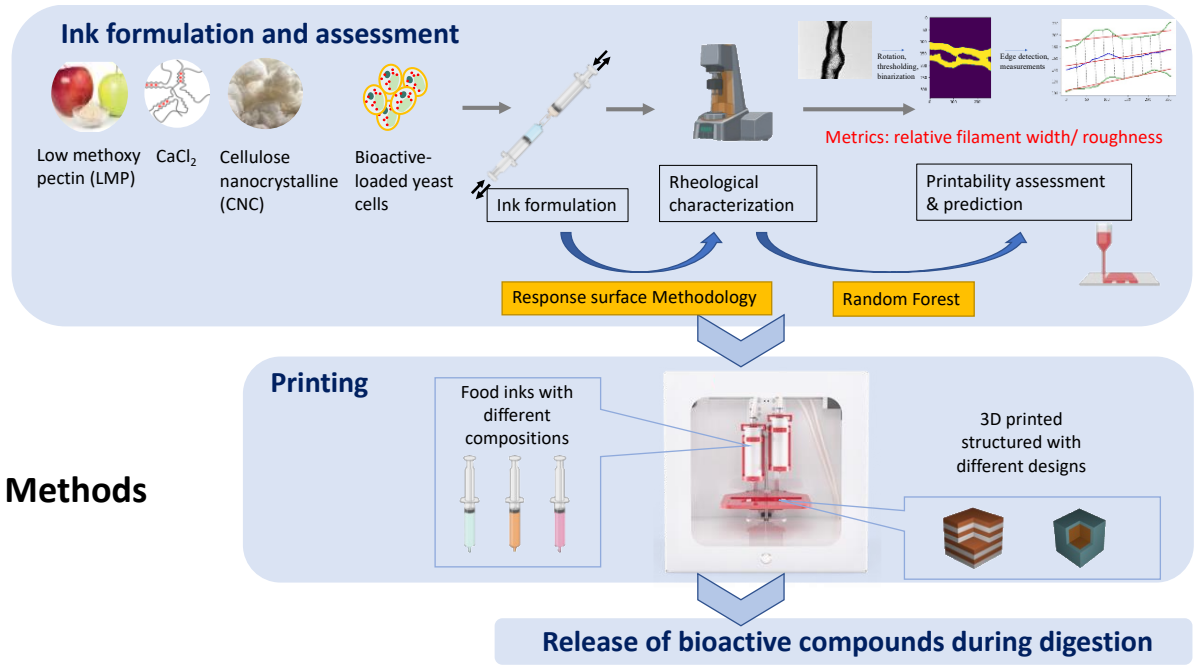


**Methods**

***Figure 1. 7: The scheme for ink development, printability assessment and prediction, 3D printing with cell-based carriers, and release profile measurement for the encapsulated compound.***

# CHAPTER 2

# Yeast-based microcarriers: biochemical profiling and predictive modeling of encapsulation efficiency for bioactive compounds

## 1. Introduction

Sustainable materials and processing technologies for the formulation of food ingredients could improve the sustainability of food systems. Many food ingredient formulations require isolation and extraction of materials from food sources and high energy processing technologies to generate structures commonly required for the functionality of these ingredient formulations. A primary example is the encapsulation process widely used in the food sector to improve the stability and controlled release of vital ingredients, including antioxidants, vitamins, bioactive peptides, flavors, and aromas etc [67–69]. Fabrication of common encapsulation systems, such as emulsions, micelles, liposomes, etc., often requires energy-intensive processes, i.e., high pressure homogenization, spray drying, to create colloidal particles with sub-micron sizes so that they can be incorporated in food formulations and achieve their functionality. Moreover, the materials used to create the encapsulation systems, including phospholipids, proteins, polysaccharides, and lipids, are commonly extracted and purified from animal, plant and microbial sources with extensive chemical processes. Furthermore, many of these encapsulation systems require addition of preservatives, including antioxidants and metal iron chelators, to maintain the stability of encapsulated compounds.

Using yeast cells as micro-carriers has emerged as a sustainable encapsulation approach. The micro-scale sized yeast cells can be utilized as natural carriers without extensive fabrication, eliminating the need for processing of food materials to extract and purify ingredients, and

reducing the energy input required to construct the colloidal delivery systems. Moreover, many previous studies have reported that the yeast cells could enhance the oxidative and thermal stability [103,110,111] of the encapsulated molecules during storage compared to colloidal carriers such as emulsions. However, unlike the fabricated colloidal carriers where the loading yield of bioactive compounds can be controlled in the fabrication process, the encapsulation yield and efficiency of compounds into yeast cells could be affected by both intrinsic factors, like the chemical nature of the compounds and the biochemical properties of the cells, as well as extrinsic factors, i.e., the pre-treatment on yeast cells before encapsulation, compound-to-cell ratio, etc. Previous studies have demonstrated the encapsulation of various types of compounds in yeast cells, including antioxidants [103], aromas [104], and many bioactive compounds [105–107]. The compounds' molecular size, shape, and the presence of hydroxyl groups [114] all could influence their permeation through the cell wall and plasma membrane. Different pre-treatment methods have been applied to yeast cells prior to encapsulation to investigate their effects on the encapsulation rate and loading yield. Examples include autolysis [118], plasmolysis [103], increasing temperature, pressure [103,107], freeze-drying [119], pulsed electric field (PEF) treatment, and osmoporation [120]. The results from these studies showed that the pre-treatments could affect the encapsulation rate and/ or the loading yield of compounds into yeast cells, by either enhancing the permeability of cells or depleting intracellular components [103,105,106,121,125]. Despite the findings from prior art, there has not been a systematic study aiming at establishing a quantitative relationship between encapsulation efficiency in yeast cells and relevant intrinsic and extrinsic factors.

In the current study, we evaluated the encapsulation efficiency of yeast cell-based encapsulation systems using vacuum-facilitated infusion, a method developed in our previous

studies to achieve rapid encapsulation of various compounds into yeast cells with higher loading yields [105,134]. The objectives were to (1) investigate the effects of the following three contributing factors to encapsulation efficiency: the encapsulated compounds' hydrophobicity, the biochemical profiles of yeast cells, as well as an extrinsic factor: the ethanol concentration used to solubilize the compounds; (2) construct an *in silico* pipeline for predicting encapsulation efficiency using the identified intrinsic and extrinsic factors. Three bioactive compounds with increasing hydrophobicity were screened: fisetin (log $k_{ow}$=1.81), curcumin (log $k_{ow}$=3.69), and retinol (log $k_{ow}$=5.68). Four yeast strains that have been reported to have different protein and lipid content [179–181] from food-related sources (**Table 2. 1**) were chosen as micro-carriers for the three bioactive compounds. Yeast cells with different chemical compositions could hypothetically lead to different encapsulation efficiency, given the different affinity of the three bioactive compounds to proteins and lipids. Although there was no direct results reported on these compounds' interactions with yeast cell proteins and lipids, several publications have described the complexation of the compounds with various proteins [49,182–189], and their different solubility in lipids [179–181]. Relevant extrinsic factors to the encapsulation efficiency using the vacuum-facilitated infusion method are vacuum pressure and ethanol concentration used to solubilize the compounds. The vacuum pressure was kept constant at a pre-determined optimal level because its effect on encapsulation efficiency has been previously evaluated and it was shown that the encapsulation yield would not further improve once a certain vacuum level was reached [105]. Ethanol concentration was evaluated as an important process parameter that can have different effects on encapsulation efficiency given different compound-cell combinations.

Construction of an *in silico* pipeline for predicting encapsulation efficiency requires efficient data collection, proper feature selection, as well as a good predictive model. This study explored

the possibility of using Fourier transformed infrared (FTIR) spectroscopy and partial least square regression (PLSR) calibration for high throughput biochemical fingerprinting of the yeast cells [190–193] and feature extraction. Random forest regression [194], an ensemble of a set of decision trees built in parallel, was selected to train the predictive model because it can capture non-linear relationships in the data, prevent overfitting, and is suitable for training on a small sample size. The results of this study would provide comprehensive understanding of the roles of extrinsic and intrinsic factors influencing encapsulation efficiency. The predictive model would enable identification of optimal biochemical profiles of yeast cells and process conditions for a certain compound to be encapsulated. Overall, these results would address a significant barrier in the application of natural cell-based carriers for encapsulation in food applications.

## 2. Materials and Methods

### 2.1. Chemicals

Curcumin derived from Curcuma longa (Turmeric) (≥ 65%, HPLC), methanol (≥99.8%), potassium phosphate monobasic and potato dextrose agar were obtained from Sigma-Aldrich (St. Louis, MO). Absolute ethanol was obtained from Koptec (King of Prussia, PA). Hydrochloric acid, magnesium chloride, yeast extract, peptone, and dextrose anhydrous were purchased from Fisher Scientific (Pittsburgh, PA). All-trans retinol (≥ 95%) and chloroform were purchased from Spectrum Chemical (New Brunswick, NJ). Fisetin (≥ 96%) was purchased from TCI Chemicals (Portland, OR). All chemicals used in yeast cell media preparation were of analytical grade. Ultrapure water (18 MΩ cm) was obtained using the in-lab Milli-Q RG water ultrapurification system from EMD Millipore (Billerica, MA).

### 2.2. Yeast strains and culture conditions

Four yeast strains from the genera *Saccharomyces*, *Yarrowia*, *Rhodotorula*, and *Cyberlindnera* were used in the current study (**Table 2. 1)**. They were food-associated species that have been reported to have various protein and lipid content levels in previous studies. The yeasts were obtained from the Phaff Yeast Culture Collection, University of California Davis, and are available for research purposes (http://phaffcollection.ucdavis.edu). The yeast strains will be referred using their Phaff collection strain ID hereafter.

**Table 2. 1: List of yeast species used as microcarriers in the current study.**

| Phaff collection strain ID | Species | Source location and habitat |
|---|---|---|
| UCDFST 70-101 | *Yarrowia lipolytica* | Slimy wiener, CA, USA |
| UCDFST 04-877[a] | *Rhodotorula babjevae* | Olive fruit fly, CA, USA |
| UCDFST 75-34 | *Cyberlindnera jadinii* | Food, ID, USA |
| UCDFST 09-448 | *Saccharomyces cerevisiae* | Fermenting olive, CA, USA |

[a] 04-877 strain was cultured for 96 h and 168 h. and the harvest cells were referred to as 04-877A and 04-877B, respectively, in the rest of the article.

For the oleaginous strains (70-101 and 04-877), media and culture conditions optimized for biomass and lipid production were used. Specifically, for 70-101, a medium with 100 g/L glycerol, 1.25 g/L $Na_2HPO_4 \cdot 2H_2O$, 2.7 g/L $KH_2PO_4$, 0.5 g/L $MgSO_4 \cdot 7\ H_2O$, and 3.8 g/L yeast extract was used (estimated molar C/N ratio = 100:1) [180]. For 04-877, Medium A [192] with 50 g/L glucose, 0.1 g/L $CaCl_2$, 0.5 g/L $NH_4Cl$, 1.5 g/L yeast extract, 7 g/L $KH_2PO_4$, 2.5 g/L $Na_2HPO_4 \cdot 2H_2O$, 1.5 g/L $MgSO_4 \cdot 7\ H_2O$, 0.08 g/L $FeCl_3 \cdot 6H_2O$, 10 mg/L $ZnSO_4 \cdot 7H_2O$, 0.07 mg/L $MnSO_4 \cdot H_2O$, 0.1 mg/L $CuSO_4$, 0.063 mg/L $Co(NO_3)_2$ was used without pH adjustment (estimated molar C/N ratio = 60.2:1) [179]. Strains 75-34 and 09-448 were cultured in YPD broth.

Culture conditions were adopted from protocols previously developed for the yeast strains [179,180].Yeast strains were revived from cryopreserved stocks, streaked on potato

dextrose agar plates, and incubated at 28 °C. Inocula were prepared from plates less than 7 days old by suspending a loopful of cells in 5 mL of deionized sterile water and transferring 0.5 mL of the cell suspension to 9.5 mL of YPD broth (for strain 70-101, 75-34, and 09-448) or Medium A (for strain 04-877) in 50 mL centrifuge tubes. The inocula were incubated at 200 rpm in a rotary shaking incubator at 24 °C for strain 04-877 or 28 °C for the rest of the strains for 24 h. 5 mL of the inocula were used to inoculate 95 mL of corresponding culture media to each strain in 500 mL Erlenmeyer flasks, resulting in 80% headspace. The following culture conditions were used: 75-34 and 09-448 cultures were incubated at 28 °C for 48 h; 70-101 culture at 28 °C for 72 h; 04-877 culture at 24 °C for 96 h and 168 h respectively before harvest. The 04-877 culture was incubated for different durations since a previous study has shown that varying the incubation time could potentially change the lipid production of the yeast strain [193]. The resulting cell cultures were referred to as 04-877A (96 h) and 04-877B (168 h) in the rest of the article. All cell cultures were incubated in a rotary shaking incubator at 200 rpm.

At the end of the incubation periods, cells were harvested by centrifuging the culture media at 2711 xg for 3 min and washed once with deionized water. The cell pellets were frozen at -80 °C overnight and lyophilized to obtain dry cell mass for the proximate analysis and FTIR spectroscopy. For bioactive encapsulation, the harvested cells were fixed in 3.7 v/v% formaldehyde at room temperature for 15 min, and then washed once with deionized water. The fixed cell pellets were stored at 4 °C before use. Three biological replicates of the cell cultures were cultivated for subsequent characterization and bioactive encapsulation.

2.3. Proximate analysis of lipid and protein content in yeast cell mass

Total lipid content of the cells was determined gravimetrically following cell lysis and lipid extraction as previously described [193] with some modifications. Briefly, triplicate aliquots (20 mg) of freeze-dried cell mass were weighed into 2.0 mL screw cap tubes. The cells were lysed with ~0.35g of 0.5 mm silica beads in 1 mL of Folch solvent [195] (2:1 of chloroform : methanol, v/v) using a Bullet Blender tissue homogenizer (Next Advance, Troy, NY, USA) at speed 10 for 3 min. After cell lysis, the content of the screw cap tube was emptied into a 15 mL centrifuge tube, to which an additional 4 mL of Folch solvent was added to extract lipid from the 20 mg of cell mass. After 20 min of extraction, 1 mL of 0.034% $MgCl_2$ solution was added, and the mixture was centrifuged at 1000 xg for 3 min to facilitate phase separation. The upper phase was removed and 1 mL of artificial upper phase (48:47:3 of methanol : water : chloroform, v/v) was added, vortexed for 10 seconds, and centrifuged at 1000 xg for 3 min to remove some proteins from the extractant. The lower organic phase was transferred to a dried, pre-weighed test tube and the chloroform was evaporated. The resulting fraction was weighed, and the total lipid content was calculated as a fraction of the dry cell mass.

Total protein content of cells was determined using the Bradford assay [196] following cell lysis and protein extraction. Triplicate aliquots (20 mg) of freeze-dried cell mass were weighed into 2.0 mL screw cap tubes. The cells were lysed with ~0.35g of 0.5 mm silica beads in 1 mL of 1 M NaOH solution with 0.15 M NaCl. After cell lysis, the tubes were heated at 60 °C for 1 h and centrifuged at 1000 xg for 3 min. The supernatant was collected for protein content measurements using the Bio-rad Bradford assay kit (Bio-rad, Hercules, CA, USA). This assay is a dye-binding assay in which the absorbance maximum for an acidic solution of Coomassie Brilliant Blue G-250 dye shifts from 465 nm to 595 nm when

bound to proteins [197]. The instruction manual provided by the manufacturer was followed to conduct the assay, using the standard procedure for microtiter plates. The absorbance measurements were conducted in 96-well plates using a SpectraMax 340 Absorbance Microplate Reader (Molecular Devises, San Jose, CA, USA). The protein concentration in the extractant was calculated against a calibration curve established using bovine serum albumin standards. The protein content of yeast cells was expressed as a fraction of the dry cell mass.

2.4. FTIR spectroscopy for yeast biochemical profiling

FTIR spectroscopy analysis of the dry cell mass was performed using a IRPrestige-21 FTIR spectrometer (Shimadzu Co., Kyoto, Japan) in absorbance mode. Direct sample measurement was enabled by using an attenuated total reflection (ATR) accessory. The spectra were recorded from 4000 - 400 $cm^{-1}$ at a resolution of 2 $cm^{-1}$. For each spectrum, 25 scans were averaged. 10 spectra were collected for each biological replicate of the cell cultures.

2.5. Feature extraction from FTIR spectra

The collected FTIR spectra were preprocessed with methods regularly used on raw IR spectra [198]. Firstly, extended multiplicative signal correction (EMSC) with up-weighted inactive spectrum region (1800 - 2500 $cm^{-1}$) was applied to remove baseline effects. Since EMSC is a model-based preprocessing method, the total of 150 spectra collected were split into training and test set with a 2:1 ratio. The EMSC model was fitted using the training set and applied to the test set. Following EMSC, the spectra were smoothed using $2^{nd}$ order polynomial fitting with a symmetric kernel over 11-point windows.

Partial least square regression (PLSR) was used to calibrate the preprocessed spectra against the corresponding lipid or protein content measured in the proximate analysis. PLSR simultaneously projects the high dimensional spectra data and the lipid or protein content to a new space defined by a group of orthogonal latent variables, called PLS components. The training set was used to fit the PLSR model and 5-fold cross validation was adopted to optimize the number of PLS components in the model so that the cross validation mean squared error was minimized. Then the performance of the fitted models in predicting lipid or protein content from FTIR spectra was evaluated using the test set. The PLS components were the new feature variables extracted from the spectra and were used in the subsequent modeling effort to predict encapsulation efficiency. The following spectral regions were examined for the lipid content prediction [199]: (1) 3100-2800 $cm^{-1}$, (2) 1800-700 $cm^{-1}$, (3) 3100-2800 $cm^{-1}$ combined with 1800-700 $cm^{-1}$. The 1700-1000 $cm^{-1}$ region was used for protein content prediction.

2.6. Encapsulation of bioactive compounds into yeast cells

Vacuum-facilitated infusion was used to encapsulate bioactive compounds into the yeast cell-based carriers as described in a previous study [105]. Briefly, the bioactive compounds were dissolved in an ethanolic solution where the formaldehyde-fixed cell pellets were dispersed to reach a certain compound-to-cell ratio. Then the cell-compound mixture was subjected to 99% vacuum treatment for 5 seconds using a vacuum sealer. After vacuum infusion, the samples were centrifuged at 2711 xg for 5 min to separate the cell pellet and supernatant.

To investigate the influential factors on encapsulation efficiency of bioactive compounds in yeast-based microcarriers, a full factorial design was used to screen three bioactive

compounds (fisetin, curcumin, retinol), five yeast cell cultures, and two different ethanol concentrations (35% vs. 50%) used during vacuum infusion, resulting in a total of 30 different combinations. For each compound-yeast-ethanol combination, samples with four different compound-to-cell ratios were prepared for the encapsulation experiments, where the compound-to-cell ratio was determined as the ratio between compound concentration (mM) and the optical density measurement of the compound-cell mixture. The optical density of cell suspensions were measured as the absorbance at 600 nm (OD600) using a microplate reader, with 200 $\mu$L of sample loaded into a well of the 96-well plate. For all samples, the target OD600 of the cell suspension was set to 2, and by varying the compound concentrations, different compound-to-cell ratios were achieved. **Table S2. 1** summarizes the factorial design and sample preparation scheme for the encapsulation experiment. The range of concentrations for each compound was determined so that it would not precipitate out due to low solubility after ethanol evaporation during the vacuum treatment.

2.7. Quantification of encapsulation yield and efficiency

The concentrations of compounds in the ethanolic solution were quantified before and after the vacuum facilitated infusion and the difference was used to calculate the encapsulation yield and efficiency according to **Equation 2. 1** and **Equation 2. 2**. Encapsulation yield was defined as the mass of encapsulated compounds per unit dry mass of the final formulation. Encapsulation efficiency was defined as the mass fraction of the bioactive compounds that was encapsulated in the cell-based carriers. Absorbance was measured at 425 nm, 362 nm, and 325 nm for curcumin, fisetin, and retinol respectively after proper dilution, and the concentrations were determined by calibrating against the

corresponding standard curve for each compound. The standard curves were established in the concentration range of 2.5 – 15 $\mu$M.

$$Encapsulation\ yield = \frac{V_i \times C_i - V_f \times C_f}{OD600_i * V_i}$$

**Equation 2. 1**

$$Encapsulation\ efficiency = \frac{Encapsulation\ yield}{C_i/OD600_i}$$

**Equation 2. 2**

$V_i, C_i$ and $V_f, C_f$ are the volume and concentration of the compound ethanolic solution before and after the vacuum infusion, and $C_i/OD600_i$ is the compound-to-cell ratio. These values were measured for each sample since deviation from the nominal values in the experimental design was expected.

2.8. Statistical analysis

Kruskal-Wallis test and *post hoc* Dunn's test were used to compare the lipid and protein content across different cell cultures. These test methods are the non-parametric version of one-way ANOVA and pairwise multiple comparisons that do not assume the samples to be from a normal distribution. False discovery rate of the multiple comparisons was controlled by the Benjamini-Hochberg procedure. Since the encapsulation efficiency did not follow a normal distribution, following the full factorial design in the encapsulation efficiency experiment, the effects of the three factors: compound, cell culture, and ethanol concentration were tested using a non-parametric, rank-based method for estimation and inference of linear models. *Post hoc* pairwise comparisons were conducted using Wilcox's rank-sum test if comparing two groups, or Dunn's test if more than two groups. Adjusted p values smaller than 0.05 were considered statistically significant. All the statistical analysis was conducted

in R (version 4.1.3) using the following *functions* from {packages}: *kruskal.test* {stats}, *dunnTest* {FSA}, *raov* {Rfit}, *wilcox.test* {stats}.

## 2.9. Predictive modeling of encapsulation efficiency

### *2.9.1. Feature sets construction*

As predictors for encapsulation efficiency, three different feature sets were constructed from the cell cultures' biochemical profiles, the compounds' chemical nature, and the ethanol concentration used in the vacuum infusion procedure. The chemical nature of the compound molecules were defined using the topological polar surface area (TPSA) and log octane-water partition coefficient (log $P_{ow}$), which were obtained from the PubChem database (https://pubchem.ncbi.nlm.nih.gov), and the free energy of binding and log permeability coefficient to several artificial or natural membrane systems were calculated using the PerMM server (https://permm.phar.umich.edu) (**Table S2. 2: Bioactive compounds' information.**). Since all these values are highly correlated with each other (**Figure S1**), only the log permeability coefficient to plasma membrane (log $P_{PM}$) was included in the feature sets. The biochemical profiles of the cell cultures were described by different variables in the three feature sets: (1) the lipid and protein content measured in the proximate analysis; (2) the PLS components extracted from the FTIR spectra using the PLSR models for lipid and protein content prediction; (3) signature peaks from the FTIR spectra for known lipid and protein functional groups. The pipeline of feature extraction and feature sets construction is summarized in a flowchart (***Figure 2. 1***).

### *2.9.2. Random forest regression*

The three feature sets were used to train random forest regression models to predict the encapsulation efficiency. 200 trees were built in a random forest for models trained with all

three feature sets. The number of samples and number of variables randomly drawn from the feature set to train each base estimator (tree) were the two hyperparameters tuned using 5-fold cross validation. All the other hyperparameters were set to default values as in the *RandomForestRegressor* function in Python's scikit-learn library.

### *2.9.3. Beta regression*

As a comparison, feature set 1 was also used to fit a beta regression model with logit link using the *betareg* function from package {betareg}. The encapsulation efficiency, as a value falling in [0,1], was assumed to follow a beta distribution. The full model is defined by **Equation 2. 3**, including the four variables in feature set 1 and their two-way interaction terms:

$$g(\mu) = \beta_0 + \sum_{i=1}^{4} \beta_i X_i + \sum_{i \neq j} \beta_{ij} X_i X_j + \epsilon,$$

**Equation 2. 3**

where $g(\cdot)$ is the logit link function, $\mu$ is the response variable encapsulation efficiency, $\beta_0 - \beta_4$ stands for the intercept, log $P_{PM}$ value of the compound, ethanol concentration, protein and lipid content of the cell culture used as microcarriers respectively. The independent variables were standardized before fitting the beta regression model. Stepwise model selection with the akaike information criterion (AIC) was used to determine which interaction terms to include in the final beta regression model. Mean squared error (MSE) and coefficient of determination ($R^2$) were used as the metrices to evaluate the performance of all the models and were calculated for both the train and test set.

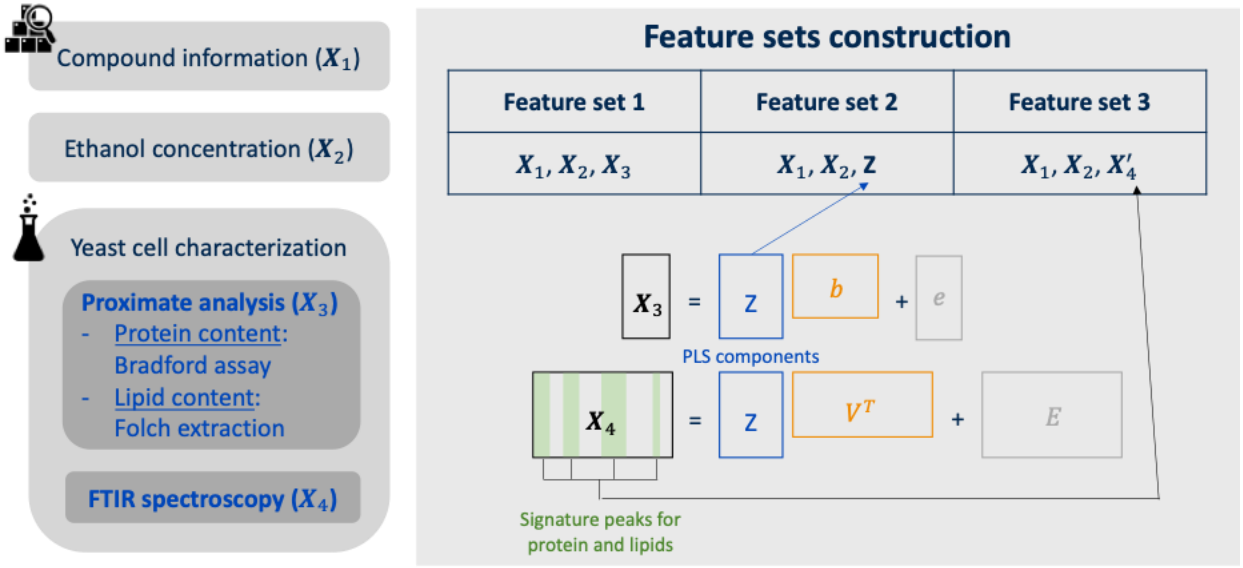


***Figure 2. 1: Feature sets construction for predictive modeling of the encapsulation efficiency.***

## 3. Results

### 3.1. Biochemical profile of the yeast cell cultures

The four yeast strains (**Table 2. 1**) were cultivated under different media and incubation conditions as described in methods section to generate five cell cultures: 75-34, 09-448, 70-101, 04-877A, and 04-877B. The proximate analysis results of cell protein and lipid content are shown in ***Figure 2. 2***. Adjusted p-values of pairwise comparisons among the five yeast strains for both lipid and protein content are summarized in **Table S2. 3**. *Rhodotorula babjevae strain* (04-877A/B) had a significantly higher lipid content and a lower protein content compared with other yeast strains. When incubated for a longer duration, strain 04-877 did achieve a higher average lipid content (41% vs. 33% on dry mass basis), but the difference was not significant. The protein content of 04-877A and 04-877B were also not significantly different from each other, both were around 8%, which, however, was lower

than other yeast strains. The rest of the yeast strains showed similar protein and lipid levels, around 12-15% lipid and 21-24% protein on the dry mass basis.

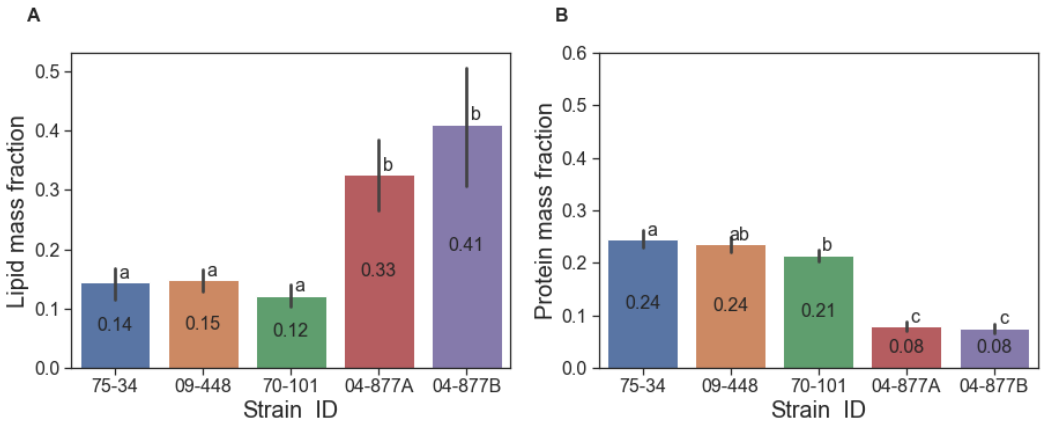


***Figure 2. 2: Lipid mass fraction (A) and protein mass fraction (B) of the five yeast cell cultures.*** The annotated values and the error bars represent the mean and standard deviation (n=9). Different lowercase letters indicate significantly different protein or lipid mass fraction across the five strains (adjusted p-value<0.05).

Besides the proximate analysis, FTIR spectroscopy was used as a high throughput method to acquire biochemical profiles of the cell cultures. ***Figure 2. 3*** shows the mean spectrum of each cell culture after pre-processing of the raw spectra, where the characteristic peaks for lipid and protein functional groups are annotated, and the peak assignments for these spectra are illustrated in **Table 2. 2**. The characteristic peaks for lipids could be found in the spectral regions of 3100-2800 $cm^{-1}$, 1800-1700 $cm^{-1}$, 1500-1300 $cm^{-1}$, and 1200-1100 $cm^{-1}$, for proteins in the region of 1700-1500 $cm^{-1}$. From visual inspection of the mean spectra, it could be observed that compared with other strains, the oleaginous strain 04-877 A/B cell cultures had higher absorbance values at peaks 2925 $cm^{-1}$, 2850 $cm^{-1}$, 1744 $cm^{-1}$, 1372 $cm^{-1}$, and 1150 $cm^{-1}$. Peaks at 2925 $cm^{-1}$, 2850 $cm^{-1}$, and 1372 $cm^{-1}$ represent the stretching or bending of $CH_3$ and $CH_2$ in acyl chains of triacylglycerols (TAGs); 1744 $cm^{-1}$ and 1150 $cm^{-1}$ represent C=O stretching and

C-O-C stretching in the ethyl esters in TAGs. Higher absorbance at these peaks indicates a higher total lipid content in the cell. Signature protein peaks at 1644 $cm^{-1}$ and 1546 $cm^{-1}$ represent amide I and amide II bands respectively. Strains 75-34 and 09-448 show the highest absorbance values at these two peaks, followed by 70-101, then by 04-877 A/B. Such a trend is consistent with the protein content quantitatively measured by the proximate analysis. It is also noted that the absorbance at peak 1744 $cm^{-1}$, indicating total lipid content, exceeds the absorbance at the protein peaks only for the oleaginous strain 04-877.

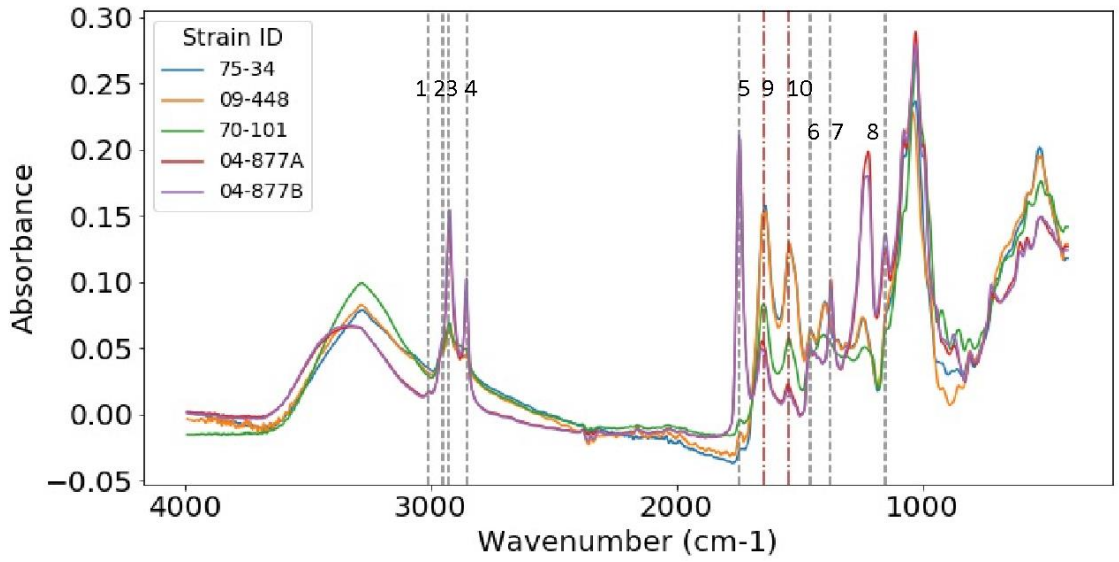


***Figure 2. 3: Pre-processed and averaged FTIR spectra of the five yeast microcarriers. Characteristic peaks of lipid and protein are labeled, and peak assignments are presented in Table 2.***

**Table 2. 2: Assignments of FTIR spectrum wavenumbers to functional groups [200].**

| Lipid Peaks | Wavenumber ($cm^{-1}$) | Functional groups |
|---|---|---|
| 1 | 3010 | =C-H stretching |
| 2 | 2952 | C–H asymmetric stretching of –CH3 |

| | | |
|---|---|---|
| 3 | 2925 | Stretching of > CH2 of acyl chains (asymmetric) |
| 4 | 2850 | Stretching of CH2 of acyl chains (symmetric) |
| 5 | 1744 | C=O stretching |
| 6 | 1456 | CH2 deformation |
| 7 | 1372 | CH3 bending |
| 8 | 1150 | C–O–C stretching |
| **Protein Peaks** | | |
| 9 | 1644 | Amide I band (C=O stretching) |
| 10 | 1546 | Amide II (CONH bending) |

3.2. Prediction of cell lipid and protein content from FTIR spectra using PLSR

The following spectral regions of the pre-processed spectra were examined for lipid content prediction using PLSR: (1) 3100-2800 $cm^{-1}$, (2) 1800-700 $cm^{-1}$, (3) 3100-2800 $cm^{-1}$ combined with 1800-700 $cm^{-1}$. The 1700-1000 $cm^{-1}$ region was used for protein content prediction. By comparing model MSE in both train and test sets, the lipid PLSR model using spectra in region (3): 3100-2800 $cm^{-1}$ combined with 1800-700 $cm^{-1}$ achieved the lowest MSE (***Figure 2. 4****A*), thus was selected to predict lipid content and extract features from the FTIR spectra. ***Figure 2. 4****C* demonstrates the prediction performance of the protein content PLSR model based on the selected spectral region. 20 and 9 PLS components were selected for the lipid and protein models respectively to achieve the minimal average MSE during cross-validation (***Figure 2. 4****B/D*). The PLSR results for the other two lipid spectral regions are presented in the supplementary materials (*Figure S2. 2*).

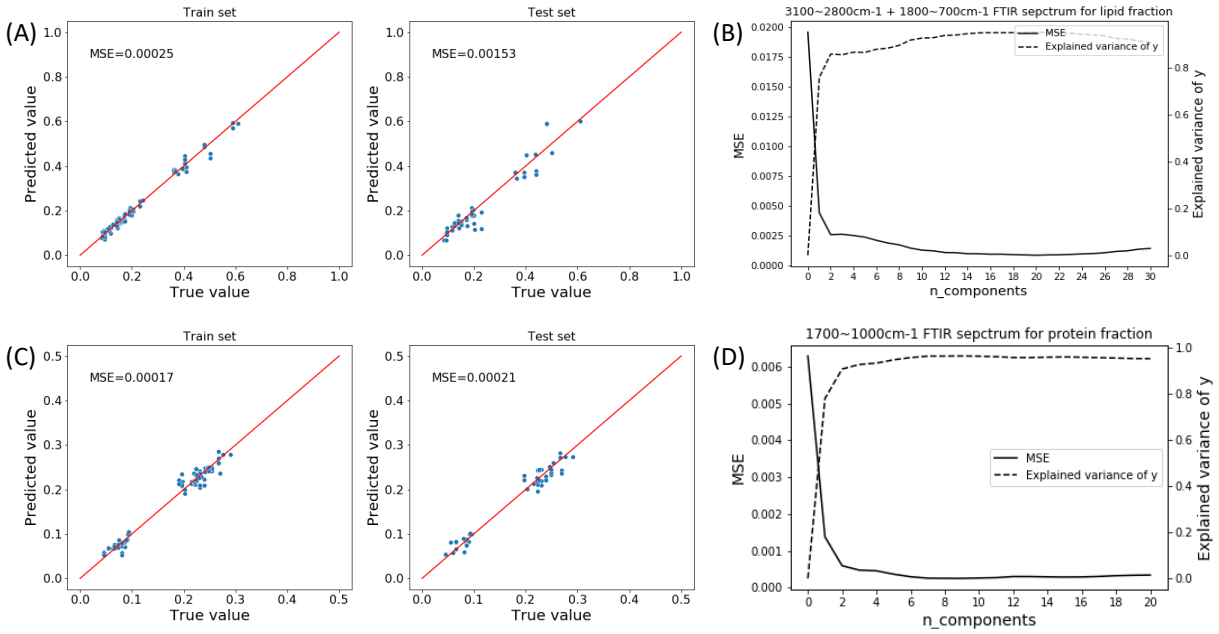


***Figure 2. 4: Prediction of lipid and protein content from FTIR spectra using PLSR.*** Predicted vs. true lipid content (A) and protein content (C) with PLSR models calibrated using the 3100-2800 $cm^{-1}$ combined with 1800-700 $cm^{-1}$ region and 1700-1000 $cm^{-1}$ region respectively. Data collected for all the biological and measurement replicates are shown as points on the graphs. The diagonal red lines indicate a complete match between predicted and true values. MSE/ explained variance of the response variable vs. number of PLS components during cross validation (B/D).

### 3.3. Encapsulation yield and efficiency of bioactive compounds in yeast cell-based microcarriers

The bioactive compounds were infused into the cell microcarriers at different compound-to-cell ratios (**Table S2. 1**). ***Figure 2. 5*** demonstrates that for all the compound-cell-ethanol concentration combinations, the encapsulation yield increased with the compound-to-cell ratio. It was expected that the cell-based microcarriers would be saturated with the encapsulated compound when the compound-to-cell ratio exceeded a certain threshold. No plateau was observed in the encapsulation yield vs. compound-to-cell ratio plots, implying that the current compound-to-cell ratio regions were below the saturation limits. Moreover, it

is noted that for all strains with retinol and most of the strains with curcumin, the relationship between encapsulation yield and compound-to-cell ratio was linear, indicated by the high $R^2$ values of the fitted linear regression (***Figure 2. 5***). Encapsulation yields for fisetin is lower than that of retinol and curcumin, and have larger variation, thus such linearity is less defined for data points in this compound group. Given these observations, it is expected that the encapsulation efficiency, calculated as $\frac{encapsulation\ yield}{compound-to-cell\ ratio}$ (**Equation 2. 2**), would be constant within the current compound-to-cell ratio region for each compound-cell-ethanol concentration combination. The encapsulation efficiency results are summarized in ***Figure 2. 6***. The rank-based ANOVA result shows that among the three factors: compound, cell-based microcarrier, ethanol concentration, and their interaction terms, only the cell-based microcarrier factor did not have a significant effect (p-value=0.15). The log $P_{PM}$ values of fisetin, curcumin, and retinol are -8.2, -4.9, 4.37 respectively, illustrating increasing hydrophobicity. Among the three compounds, fisetin had the lowest encapsulation efficiency, followed by curcumin, and retinol achieved the highest efficiency, following the same trend as the compound hydrophobicity. Fisetin encapsulation efficiency values also showed higher variance compared to the other two compounds. Overall, significantly higher encapsulation efficiency could be achieved when 35% ethanol was used as a solvent for curcumin and retinol during vacuum infusion than when 50% ethanol was used (p-value<0.001). No significant effect of ethanol concentration on encapsulation efficiency was detected for fisetin (p-value=0.80). Although the cell culture factor itself did not have a significant main effect on encapsulation efficiency, it had significant interaction effects with the other two factors, implying that the impact of cell-based microcarriers on encapsulation efficiency depended on the encapsulated compound and ethanol concentration used. For fisetin,

regardless of the ethanol concentration, no significant difference was detected across different cell cultures. For curcumin, higher efficiency was achieved with 75-34 than with other strains, especially when compared to the oleaginous 04-877 strains, the difference was significant for both ethanol concentrations. For retinol, 04-877A and 04-877B showed lower encapsulation efficiency than the other three strains when using 35% ethanol (only statistically significant for 04-877A), but significantly higher efficiency when 50% ethanol was used. Specific adjusted p-values for pairwise comparisons of encapsulation efficiency across different yeast strains within each compound-ethanol concentration combination could be found in **Table S2. 4**.

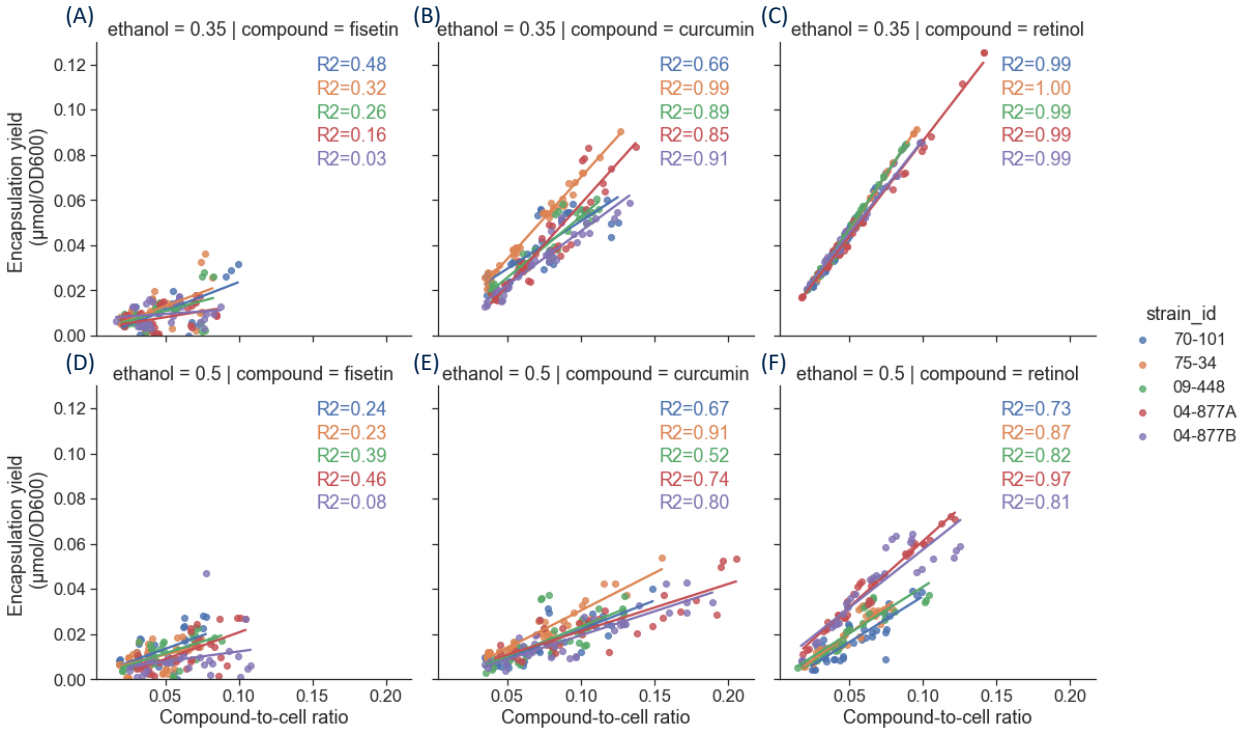


***Figure 2. 5: Encapsulation yield vs. compound-to-cell ratio for all ethanol-bioactive-yeast combinations.*** Fisetin (A/D), curcumin (B/E), and retinol (C/D) encapsulated in different yeast cell cultures as the microcarriers are color coded. (A-C) represent vacuum infusion in 35% ethanol and (D-F) in 50% ethanol. A linear regression was fitted to each compound-cell-ethanol concentration. The fitted lines and corresponding regression $R^2$ values in each subplot are color coded based on the yeast strains.

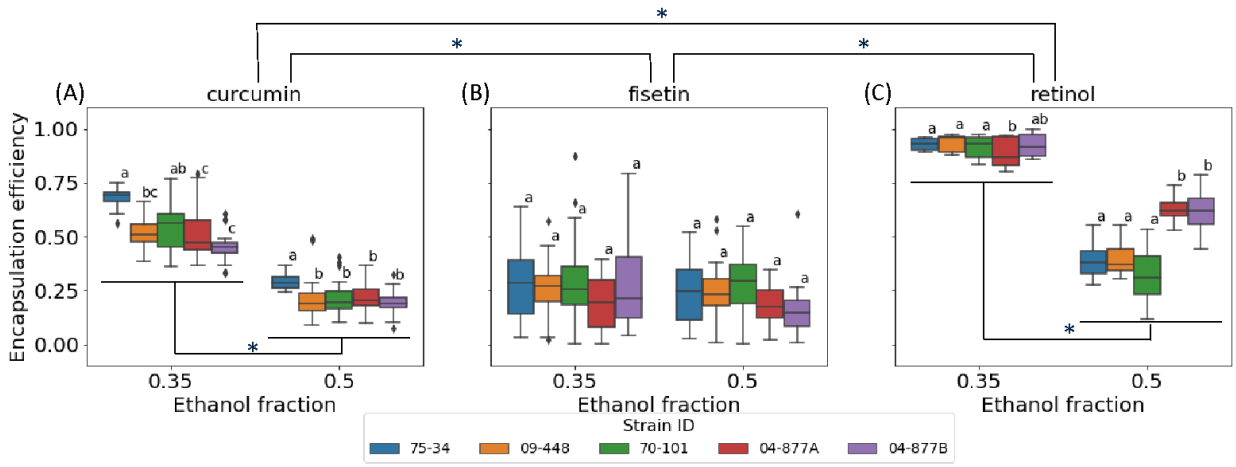


***Figure 2. 6: Encapsulation efficiency boxplots for different ethanol-compound-yeast strain combinations: (A) curcumin, (B) fisetin, (C) retinol.*** Compound level *post hoc* comparisons were conducted, and significant differences are annotated by (*) above the subplots. Within each subplot, significant difference between two ethanol concentration groups is also dictated by (*). Different lowercase letters indicate significant difference across yeast cell cultures, within each compound-ethanol combination.

3.4. Machine learning enabled prediction of encapsulation efficiency

Predictive models were constructed to link the encapsulation efficiency to the intrinsic properties of the cell-based encapsulation system: biochemical profiles of the cells, chemical nature of the encapsulated compound, as well as an external factor during the vacuum infusion process: the ethanol concentration. Random forest regression models were trained with three feature sets (*Figure 2. 1*). The key difference in these feature sets was the features selected for the biochemical profiles of the yeast cell cultures. As a comparison, a beta regression model was fitted using feature set 1 and the model coefficients and p values are described in **Table S2. 5**.

The beta regression model included all four original variables in feature set 1 and some of their interaction terms which were selected using AIC-based stepwise model selection. All

the regressors kept in the model were significant except the log $P_{PM}$ : protein fraction interaction term. Since the independent variables were standardized before fitting the beta regression model, the model coefficients could be compared and interpreted for effect size. Even with the presence of interaction terms, the effect size of log $P_{PM}$ was the largest among all variables, consistent with the observation that the encapsulation efficiency increased with increasing compound hydrophobicity (***Figure 2. 6***). The second largest effect size (absolute value) was contributed by ethanol concentration: the encapsulation efficiency would decrease with higher ethanol concentration. For lipid fraction and protein fraction, since both the main effects and interaction effects were significant and similar in effect size, it is hard to make a direct interpretation, but the beta regression results did agree with the rank-based ANOVA results in terms that the effects of cell biochemical profiles on encapsulation efficiency depended on compound and ethanol concentration. Error! Reference source not found. d emonstrates the permutation feature importance of the four variables in feature set 1. Compounds' log $P_{PM}$ values and ethanol concentration contributed dominant effect while cell's lipid and protein fraction had much smaller impact when predicting encapsulation efficiency. **Table 2. 3** and ***Figure S2. 3*** summarizes all the models' performance in terms of train and test MSE and $R^2$. The random forest models trained with the three features sets all showed better performance than the beta regression model. Random forest models trained with feature set 2 (PLS components) and 3 (characteristic peaks) showed equally good fitting in the training set, better than feature set 1, while all three feature sets had similar performance in the test set. Compared to the beta regression model, the best random forest model reduced MSE by 74% and 27% in the train and test set respectively. The results indicated that instead of the protein and lipid content of the yeast cells measured using the

time consuming and labor-intensive proximate analysis methods, the FTIR spectra, after either PLSR based feature extraction, or selection of characteristic peaks based on prior knowledge, could serve as predictors for encapsulation efficiency, resulting in as good, if not better prediction performance.

**Table 2. 3: MSE of encapsulation efficiency regression using beta regression and random forest regression models with different feature sets.**

| Feature set | Model | MSE | | $R^2$ | |
|---|---|---|---|---|---|
| | | Train | Test | Train | Test |
| 1 | Beta regression | 0.0120 | 0.0131 | 0.85 | 0.80 |
| 1 | Random forest | 0.0052 | 0.0104 | 0.93 | 0.84 |
| 2 | Random forest | 0.0032 | 0.0099 | 0.96 | 0.85 |
| 3 | Random forest | 0.0031 | 0.0095 | 0.96 | 0.86 |

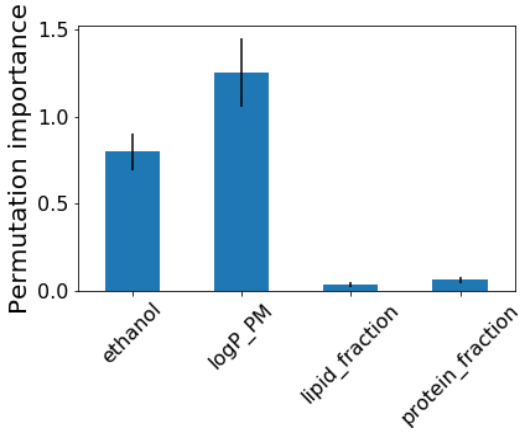


***Figure 2. 7: Permutation feature importance of the four variables in feature set 1 in the random forest regression model.***

## 4. Discussion

One of the major objectives of the encapsulation process is to deliver bioactive compounds at a higher concentration than the levels existing in natural foods. The results of the current study suggested that yeast cells are in general good encapsulation carriers for the bioactive compounds

tested in this study, which covered a wide range of hydrophobicity. ***Figure S2. 4*** showed that after encapsulation, the concentration of compounds inside the yeast cells was much higher than that in the external ethanolic solution: from around a hundred time higher for fisetin to more than four thousand time higher for retinol, which was reflected in the encapsulation efficiency as well (***Figure 2. 6***). Although no prior art has reported encapsulation of retinol in yeast cells, other encapsulation systems such as liposomes [201], silicone particles [202], etc., have been applied to retinol, with overall high efficiency: >85% in silicone particles and >98% in liposomes, which agreed with the high efficiency observed in the current study. Encapsulation of curcumin and fisetin in yeast cells have been reported in previous studies, using methods including plasmolysis [106,110] and osmoporation [203]. The encapsulation efficiency of fisetin into yeast cells was reported to vary from 4% to 30% given different processing variables [203], agreeing with the results from the current study. However, the loading yield of curcumin in yeast cells reported in Paramera et al.'s studies (~ 10 wt. %) [106,110] were much higher than that found in this study (approximately 0.8%). After carefully comparing their methods to ours, the following reasons could potentially explain for the discrepancy in the results. The compound-to-cell ratio used in these previous studies was much higher than values used in the current experimental design: 0.2~2 vs. 0.008~0.02 curcumin-to-cell mass ratio. They dispersed curcumin in either water or 50% ethanol at concentrations of 0.4 or 4 mg/mL, which was significantly higher than the compound's solubility in either solvents [105,204], implying that there must be undissolved crystals present in the curcumin-cell suspension. Based on our observations, the precipitated curcumin could not be fully washed away by water, and would be centrifuged down together with the yeast cells. Therefore, quantification of encapsulated curcumin by extracting from the cell pellet would over-estimate the loading yield. It was also observed in preliminary experiments that the loading yield

increased linearly with increasing compound-to-cell ratio (***Figure 2. 5***) up to a certain point after which the loading yield would level off (data not shown), indicating a saturation point beyond which precipitation of bioactive compounds would occur during encapsulation. Such observations agreed with results reported by Paramera et al. that lower compound-to-cell mass ratio led to a higher encapsulation efficiency [110]. Ciamponi et al. have reported similar trends for limonene, another hydrophobic compound [205]. To avoid precipitation, the compound-to-cell ratios used in the current study were kept in ranges lower than the saturation levels for all the compounds. Therefore, the highest loading yield obtained in the current study was not necessarily the highest yield possible for a compound-cell combination.

In the current study, we identified and investigated three factors that influence encapsulation efficiency in the yeast-based encapsulation system using vacuum infusion: compounds' hydrophobicity, cells' biochemical profile, and an encapsulation method related factor: ethanol concentration used to solubilize the compounds. Both the experimental (***Figure 2. 6***) and the modeling results (**Table S2. 5**, ***Figure 2. 7***) suggested that among the three factors, the compounds' hydrophobicity and ethanol concentration had dominant effects on the encapsulation efficiency, while the influence of the cells' biochemical profile, i.e., lipid and protein content, was less significant and depended on the different compound-ethanol combinations. Infusion of compounds into yeast cells could be considered as a passive diffusion process where the compounds need to permeate through the cell wall and cell membrane and partition into subcellular locations. All three bioactive compounds in the current study could diffuse freely across the cell wall given that the largest molecule curcumin has molecular weight of 368 Da, smaller than the reported maximum molecular sizes permitting through yeast cell walls (700 Da [115] ~ 60 kDa [116]). The cell membrane permeability to the bioactive compounds could be

enhanced by both ethanol [122,123,206] and vacuum treatment with high pressure reduction rate [123]. The large concentration ratio between the intracellular and extracellular environment after vacuum infusion (***Figure S2. 4***) suggested that the bioactive compounds partitioned more favorably into the cells than staying in the extracellular ethanolic solution, 35% or 50%. When subjected to vacuum, ethanol was evaporated rapidly and the solubility of all three compounds in the ethanolic solution would decrease, which could be inferred from their low water solubility and the decreased ethanol concentration. In other words, there would be an increase in the compounds' chemical potential in the extracellular environment as ethanol evaporated, motivating the compounds to partition into the more energetically favorable intracellular environment. The extent of the energetic favorability could be affected by the bioactive compounds' chemical potential in the ethanolic solution, as well as in the intracellular environment. Fisetin (log $k_{ow}$=1.81), curcumin (log $k_{ow}$=3.69), and retinol (log $k_{ow}$=5.68) have increasing hydrophobicity, and correspondingly decreasing encapsulation efficiency. Previous studies on yeast-based encapsulation also reported lower encapsulation efficiency and loading yield for fisetin than curcumin [106,203]. Such energetic favorability would be less significant when 50% ethanol was used to solubilize compounds since their solubility increase with the ethanol concentration (data not shown), translating to lower encapsulation efficiency with 50% ethanol than 35%. A similar observation was reported when retinol was encapsulated in silicone particles: with higher concentration of co-solvent (ethanol), retinol was stabilized and less likely to be embedded into the silicone particles [202].

The favorable intracellular environment for the bioactive compounds was hypothetically attributed to their binding to cellular proteins and lipids in the cell, and different compounds would have different affinity to the two components. Several publications have described the

binding of fisetin, curcumin, and retinol to cellular proteins [182–184]. Complexation of proteins with polyphenols, a group of bioactive compounds to which fisetin and curcumin belong, is well-recognized and studied [49,185,186]. The solubility of curcumin in whey and pea protein isolates was reported to be 2-3 times higher than that in canola oil [207,208], while retinol's solubility in lipids is at least 500 times more than that in proteins [209]. Such a difference in compounds' affinity to the lipid and protein was supported by the different subcellular locations of the compounds. It was shown in our previous study [105] that when dual-loaded into yeast cells, fisetin tended to concentrate more in the vacuole compared to curcumin, given its lower hydrophobicity. The subcellular localization of different bioactive compounds encapsulated in yeast cells is further investigated using cell staining and fluorescence microscopy in the following Chapter. However, the difference in compounds' affinity to proteins and lipids could not fully explain the different encapsulation efficiency observed. Other confounding factors include extraction of lipids from cells by ethanol, and different extent of ethanol evaporation when high protein or high lipid strains were dispersed. All these factors would result in different chemical potential of the compounds in the extracellular solution, thus affecting the final partition coefficient and encapsulation efficiency. Although the cell biochemical profile is not a dominant contributor to encapsulation efficiency, it could potentially affect other performance indexes of a cell-based encapsulation system, such as the release profile of the compounds during digestion, which would be further explored in future research.

Another objective of the current study was to construct an *in silico* encapsulation efficiency predictive pipeline for screening of potential cell-based microcarriers. The loading yield and encapsulation efficiency of engineered encapsulation systems, such as emulsions, liposomes, etc., can be determined during the fabrication process by modulating the ratio of mixing different

materials. However, when utilizing natural carriers such as yeast cells, there is limited control over the loading capacity without an established quantitative relationship between the encapsulation efficiency and extrinsic and intrinsic factors as investigated in the current study. The constructed *in silico* pipeline consists of biochemical profiling of yeast cells with FTIR spectroscopy, feature extraction with the calibrated PLSR model, and encapsulation efficiency prediction with a random forest model. Successful establishment of the pipeline eliminated the need for the time-consuming proximate analysis of the yeast cell cultures, accounted for the non-linear relationship between the predictors and encapsulation efficiency using the random forest model, and facilitated a better understanding of the molecular interactions between the compounds and cellular components during vacuum infusion. It also enabled high throughput screening of other cells and diverse bioactive compounds, to further enlarge and diversify the dataset so that the model can be generalized to other cell-based encapsulation systems, such as bacteria and other fungal cells, not necessarily be limited to yeast cells.

## 5. Conclusion

This study investigated the intrinsic and extrinsic factors that contribute to the encapsulation efficiency of bioactive compounds in yeast-based microcarriers using vacuum-facilitated infusion. Among the factors examined, compounds' hydrophobicity and the concentration of ethanol used to solubilize the compounds had dominant effects on the encapsulation efficiency. The effect of cell biochemical profiles on encapsulation efficiency depends on different compound-ethanol combinations and has a minor contribution to the efficiency prediction. The constructed predictive modeling pipeline for encapsulation efficiency consists of biochemical profiling of yeast cells with FTIR spectroscopy, feature extraction with the calibrated PLSR model, and encapsulation efficiency prediction with a random forest model. This pipeline

enables high throughput screening of various potential cell-based carriers for different compounds. The robustness and generalizability of the model will be further improved with more diversified dataset, i.e., cell-based carriers with greater variation in protein and lipid contents, wider range of ethanol concentrations, bioactive compounds from other chemical groups, etc.

## 6. Acknowledgement

The yeast strains used in the current study were kindly provided by the Phaff Yeast Culture Collection, University of California - Davis. This part of the research was funded by the following funding sources: AIFS center grant 2020-67021-32855 (USDA-NSF AI center research grant), USDA NIFA grant 2018-67017-27563.

## Supplements

**Table S2. 1: The 3-factor full factorial design and sample preparation scheme for the encapsulation experiment.**

| Full factorial design | | | Sample preparation scheme | |
|---|---|---|---|---|
| **Ethanol concentration** | **Cell cultures** | **Compound** | **Nominal compound concentration (mM)** | **Target compound-to-cell ratio** |
| 35% | 75-34 | Fisetin | 0.12 | 0.06 |
| | | | 0.08 | 0.04 |
| | 09-448 | | 0.04 | 0.02 |
| | | | 0.02 | 0.01 |
| | | Curcumin | 0.2 | 0.1 |
| | 70-101 | | 0.16 | 0.08 |
| | | | 0.12 | 0.06 |
| 50% | 04-877A | | 0.08 | 0.04 |
| | | Retinol | 0.2 | 0.1 |
| | | | 0.16 | 0.08 |
| | 04-877B | | 0.12 | 0.06 |
| | | | 0.08 | 0.04 |

**Table S2. 2: Bioactive compounds' information.**

| compound | TPSA | $logP_{ow}$ | Binding energy (kcal/mol) | Log $P_{BLM}$[a] | Log $P_{PM}$[b] | Log $P_{PAMPA-DS}$[c] |
|---|---|---|---|---|---|---|
| fisetin | 107 | 1.81 | -2.48 | -8.2 | -8.8 | -8.52 |
| curcumin | 93.1 | 3.29 | -2.06 | -4.9 | -5.85 | -5.75 |
| retinol | 20.2 | 5.68 | -8.94 | 4.37 | 1.66 | 2.8 |

[a] BLM: black lipid membrane

[b] PM: plasma membrane

[c] PAMPA-DS: parallel artificial membrane permeability assay using lecithin-based double sink model

**Table S2. 3: Adjusted p-values of pairwise comparisons across yeast strains for lipid fraction and protein fraction measurements.**

**Lipid fraction pairwise comparison**

| | 04-877A | 04-877B | 09-448 | 70-101 |
|---|---|---|---|---|
| **04-877B** | 5.01E-01 | | | |
| **09-448** | 8.28E-03 | 9.17E-04 | | |
| **70-101** | 6.12E-04 | 4.33E-05 | 4.31E-01 | |
| **75-34** | 5.60E-03 | 6.07E-04 | 8.58E-01 | 4.92E-01 |

**Protein fraction pairwise comparison**

| | 04-877A | 04-877B | 09-448 | 70-101 |
|---|---|---|---|---|
| **04-877B** | 7.60E-01 | | | |
| **09-448** | 5.08E-04 | 1.94E-04 | | |
| **70-101** | 1.32E-02 | 6.13E-03 | 3.62E-01 | |
| **75-34** | 2.31E-04 | 1.19E-04 | 8.00E-01 | 2.23E-01 |

**Table S2. 4: Adjusted p-values of pairwise comparisons for encapsulation efficiency across yeast strains within each compound-ethanol concentration combination.**

**Curcumin, 35% ethanol**

| | 04-877A | 04-877B | 09-448 | 70-101 |
|---|---|---|---|---|
| **04-877B** | 5.35E-01 | | | |
| **09-448** | 3.17E-01 | 1.52E-01 | | |
| **70-101** | 3.13E-02 | 7.97E-03 | 2.54E-01 | |
| **75-34** | 1.28E-03 | 1.89E-04 | 2.42E-02 | 2.69E-01 |

**Curcumin, 50% ethanol**

| | 04-877A | 04-877B | 09-448 | 70-101 |
|---|---|---|---|---|
| **04-877B** | 9.04E-01 | | | |
| **09-448** | 8.46E-01 | 9.56E-01 | | |
| **70-101** | 9.49E-01 | 9.56E-01 | 9.34E-01 | |
| **75-34** | 4.92E-02 | 3.76E-02 | 1.93E-02 | 4.40E-02 |

**Fisetin, 35% ethanol**

| | 04-877A | 04-877B | 09-448 | 70-101 |
|---|---|---|---|---|
| **04-877B** | 1.00E+00 | | | |
| **09-448** | 1.00E+00 | 1.00E+00 | | |
| **70-101** | 9.79E-01 | 1.00E+00 | 1.00E+00 | |
| **75-34** | 1.00E+00 | 1.00E+00 | 1.00E+00 | 1.00E+00 |

**Fisetin, 50% ethanol**

| | 04-877A | 04-877B | 09-448 | 70-101 |
|---|---|---|---|---|
| **04-877B** | 7.50E-01 | | | |
| **09-448** | 8.78E-01 | 7.94E-01 | | |
| **70-101** | 7.41E-01 | 6.55E-01 | 8.54E-01 | |
| **75-34** | 7.52E-01 | 7.31E-01 | 8.05E-01 | 7.77E-01 |

**Retinol, 35% ethanol**

| | 04-877A | 04-877B | 09-448 | 70-101 |
|---|---|---|---|---|
| **04-877B** | 8.12E-02 | | | |
| **09-448** | 2.78E-03 | 2.69E-01 | | |
| **70-101** | 4.92E-02 | 8.50E-01 | 3.30E-01 | |
| **75-34** | 1.93E-03 | 2.64E-01 | 9.32E-01 | 3.33E-01 |

**Retinol, 50% ethanol**

| | 04-877A | 04-877B | 09-448 | 70-101 |
|---|---|---|---|---|
| **04-877B** | 9.42E-01 | | | |
| **09-448** | 4.28E-03 | 2.68E-03 | | |
| **70-101** | 2.62E-03 | 3.85E-03 | 1.00E+00 | |
| **75-34** | 3.10E-03 | 3.11E-03 | 1.00E+00 | 8.98E-01 |

**Table S2. 5: Beta regression model coefficients' estimates and p values. The regressors included in the model were selected through AIC-based stepwise model selection.**

| | Estimate | Std. Error | z value | Pr(>\|z\|) |
|---|---|---|---|---|
| (Intercept) | -0.31 | 0.04 | -7.17 | 7.32E-13 |
| logP_PM | 1.03 | 0.05 | 21.99 | 3.45E-107 |
| ethanol | -0.65 | 0.04 | -14.92 | 2.40E-50 |
| lipid_fraction | -0.19 | 0.07 | -2.93 | 3.42E-03 |
| protein_fraction | -0.13 | 0.06 | -2.13 | 3.31E-02 |
| logP_PM:ethanol | -0.48 | 0.05 | -10.49 | 9.15E-26 |
| logP_PM:lipid_fraction | 0.14 | 0.06 | 2.13 | 3.32E-02 |
| logP_PM:protein_fraction | -0.13 | 0.07 | -1.96 | 5.03E-02 |

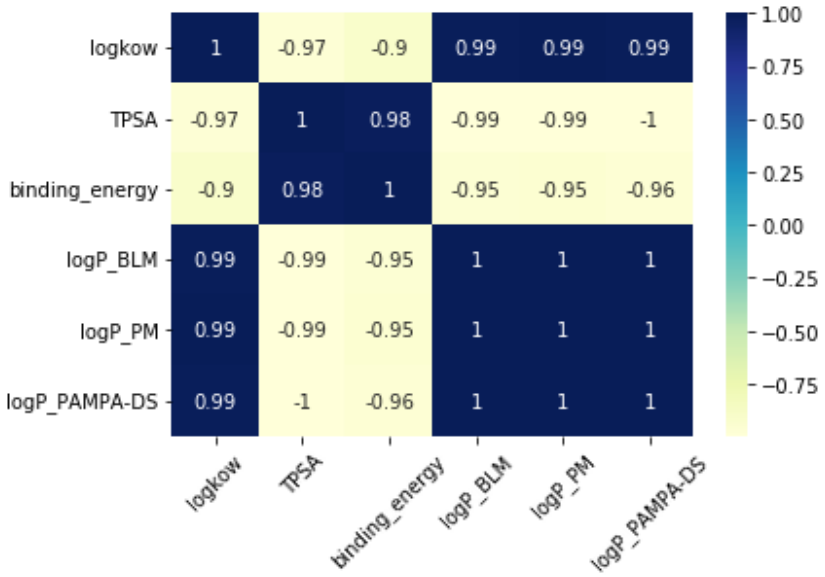


***Figure S2. 1: Correlation heatmap of the compound information variables.***

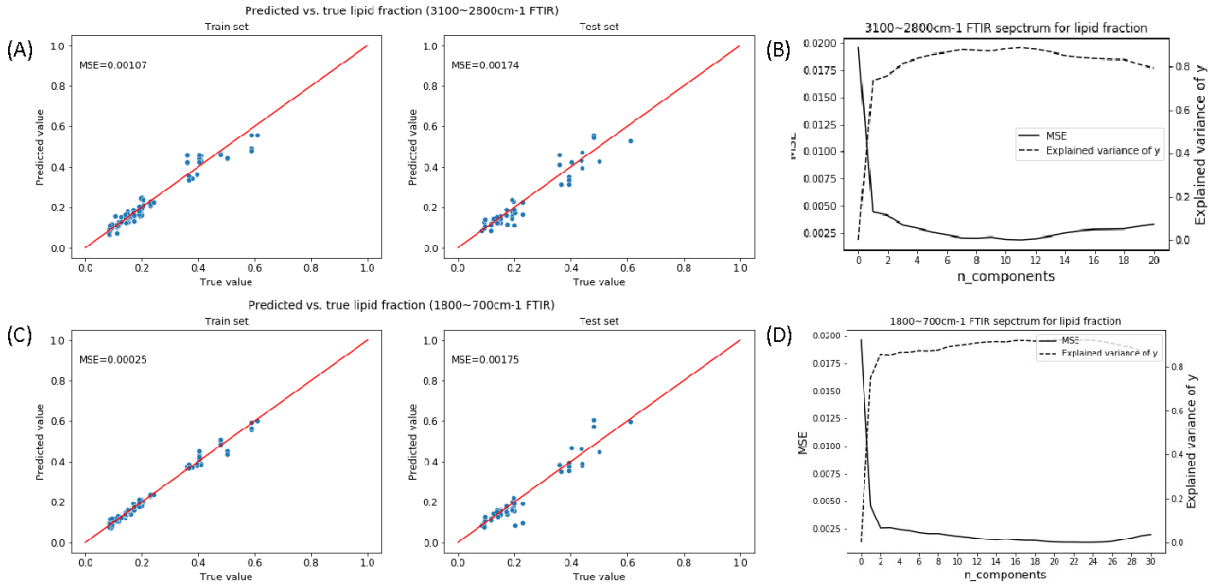


***Figure S2. 2: Prediction of lipid and protein content from FTIR spectra using PLSR.*** Predicted vs. true lipid content with PLSR models calibrated using the 3100-2800 $cm^{-1}$ region (A) and 1800-700 $cm^{-1}$ region respectively (C). MSE/ explained variance of the response variable vs. number of PLS components during cross validation (B/D).

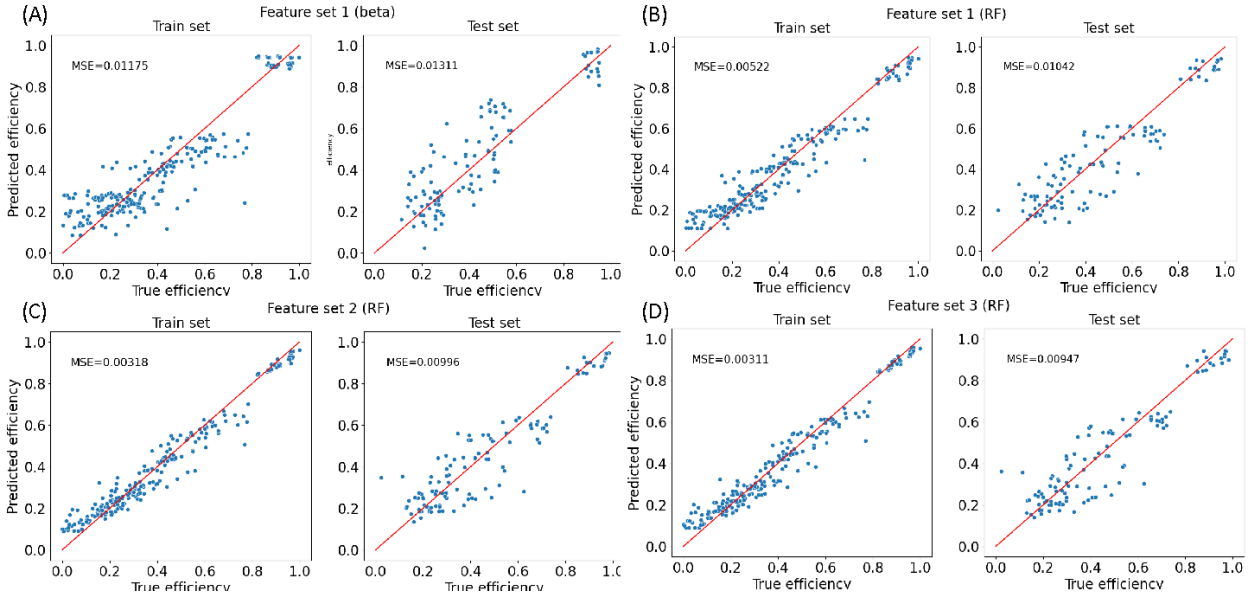


***Figure S2. 3: Predicted vs. true encapsulation efficiency in the train and test set for the beta regression model using feature set 1 (A); random forest regression models using feature set 1 (B), feature set 2 (C), and feature set 3 (D).***

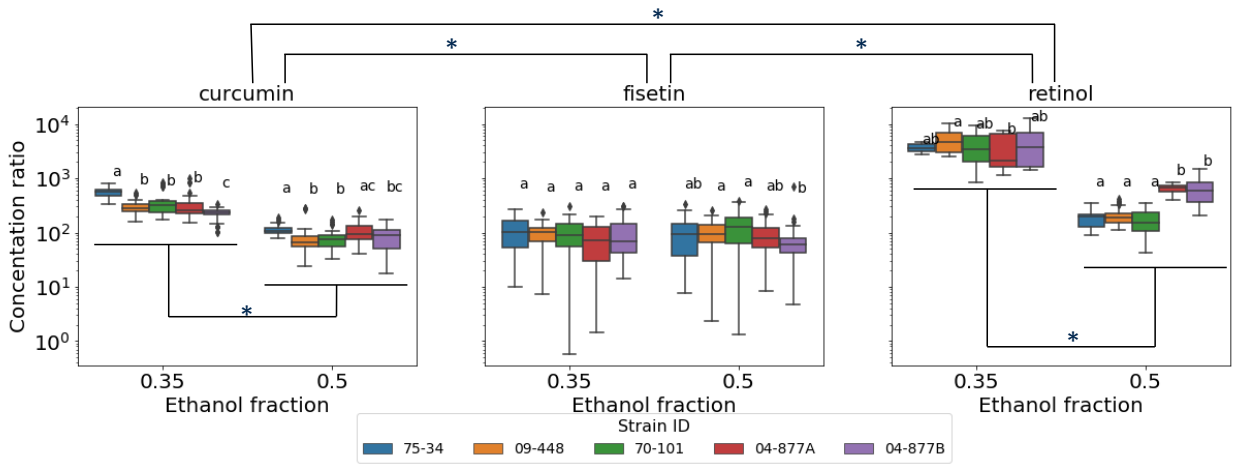


***Figure S2. 4: Concentration ratio of intracellular and extracellular compound after encapsulation for different ethanol-compound-yeast strain combinations: curcumin (left), fisetin (middle), retinol (right).*** Compound level post hoc comparisons were conducted, and significant differences are annotated by (*) above the subplots. Within each subplot, significant difference between two ethanol concentration groups is also dictated by (*). Different lowercase letters indicate significant difference across yeast cell cultures, within each compound-ethanol combination.

# CHAPTER 3

## Yeast-based microcarriers: image-based prediction of release profile patterns during *in vitro* digestion

### 1. Introduction

The release of encapsulated compounds during digestion is an important feature to evaluate for the design and function of the oral delivery systems for food applications. Ability to predict release patterns for diverse delivery systems would help select optimal carriers based on the desired stability and bioaccessibility of the encapsulated bioactive compounds. Among diverse bioactives encapsulation systems, yeast cell-based carriers and their clusters have been evaluated as model delivery systems that mimic some of the compositional and structural properties of food matrices [105,128,210]. Paramera et al. [106] have reported that curcumin in yeast microcarriers showed sustained release in simulated gastric fluid and slower degradation in simulated intestinal fluid compared to those encapsulated in modified starch and $\beta$-cyclodextrin. Young et al. [128] compared the release profile of curcumin from native yeast and yeast cell wall particles (YCWPs) in a sequential static *in vitro* gastric and intestinal digestion. The results highlighted the important role of gastric phase and the presence of bile salt in the simulated intestinal fluid on the release of curcumin. Moreover, the release rate of curcumin from YCWPs was much faster than that from native yeast cells, indicating the impact of cellular components and their interaction with the encapsulated compounds on the bioaccessibility. Although a previous study [110] attributed the different release rate of curcumin in simulated gastric fluid to the different location of the compound inside the cells, no experimental evidence was provided to support such a hypothesis. Thus, to develop a comprehensive understanding and predictive relationship

of the release profile of bioactives in cell- based carriers, there is a need to characterize intracellular distribution and association of diverse bioactives with cellular components and their impact on the release of encapsulated bioactives during digestion.

Confocal fluorescence microscopic imaging has been utilized in many studies to understand the localization and interaction of infused compounds in cell-based encapsulation systems. In these studies the autofluorescence properties of compounds, such as curcumin, fisetin [105], resveratrol [107], etc. have been used for imaging intracellular distribution of the infused bioactives. Young et al. showed that fisetin and curcumin had different subcellular distribution [105]. The compounds' localization inside the cell could be seen as a result of the differential affinity to different cellular components such as protein, polysaccharides, and lipids [211]. Polysaccharides are mostly found in the cell wall. Proteins can be solubilized in the cytosol, membrane-bounded in plasma membrane or organelles' membranes, in the cell wall as glycoproteins, or assembled in ribosomes [212]. The non-polar lipids in yeast cells are stored in the form of lipid droplets or lipid bodies, which consist of a hydrophobic core of triacylglycerols and steryl esters, surrounded by a monolayer of phospholipids [213]. To visualize the location of different cellular components, different fluorescent dyes have been used to stain different compartments of the cells, e.g., calcofluor white for cell wall, SYBR Green for nucleic acids and Nile red for lipids [214]. Thus, autofluorescence of the encapsulated compounds and combination of stains could be deployed to image the intracellular distribution of bioactives in cells and their association with major structural and chemical components of the cells such as lipid bodies. Furthermore, there is a need to develop a modeling approach for predicting the release pattern and profile as a function of the intracellular distribution of bioactives in cell-based delivery systems.

The release of bioactives during digestion from cells is a complex biochemical process involving multiple interactions among bioactives with diverse compositional and structural components of cells. Thus, the process may not be easily described by simple mechanistic models. However, the imaging data used for characterizing the intracellular distribution of bioactives could be used for training a data-based model. Among diverse data-based modeling approaches, convolutional neural networks, a type of deep learning algorithm, have been successfully applied to various image-related tasks, such as object detection, classification, segmentation etc. [215] Convolutional neural network (CNN) has gained popularity in biological domains and have been utilized to analyze and classify different types of biological images, including microscopic images of cells [216–218]. By leveraging the hierarchical feature extraction and classification capabilities of CNNs, we can extract meaningful information from the complex images without manually defining the features. To the best of our knowledge, none of the previous studies have used CNN models or other image-based modeling approaches to predict the release of bioactives from complex structures such as cells.

In the current study, compounds with different hydrophobicity (curcumin and retinol) were encapsulated into five different yeast strains with varying lipid and protein content to generate variations in intracellular distribution of the bioactives. The intracellular distribution of bioactives was characterized by counterstaining the curcumin- or retinol-loaded yeast cells with Nile red to enable assessment subcellular localization of the encapsulated compounds relative to the lipid-rich regions inside the cells. The fluorescence images of different combinations of bioactive compounds and yeast cell-based carriers were acquired and processed using an automated image analysis pipeline. The imaging data sets were used to (1) test the hypothesis that different initial subcellular localization of the encapsulated compounds would lead to

different release profiles during simulated in vitro digestion; (2) predict the release patterns using a CNN model. Successful prediction of release patterns using high-throughput microscopic images taken before digestion would significantly shorten the workflow duration for evaluating the release of bioactive compounds, facilitating the development and selection of optimal delivery systems for diverse bioactives.

## 2. Materials and Methods

### 2.1. Materials

Curcumin derived from Curcuma longa (Turmeric) (≥ 65%, HPLC), methanol (≥99.8%), potassium phosphate monobasic, ammonium sulfate, and potato dextrose agar were obtained from Sigma-Aldrich (St. Louis, MO). The bile salts (cholic acid- deoxycholic acid sodium salt mixture), and enzymes used in simulated digestion fluids preparation: pepsin from porcine gastric mucosa (activity 1064 units/mg) and pancreatin from porcine pancreas (4x USP, lipase activity >8 units/mg) were purchased from Sigma-Aldrich (St. Louis, MO). Absolute ethanol was obtained from Koptec (King of Prussia, PA). Sodium hydroxide, hydrochloric acid, potassium chloride, magnesium chloride, yeast extract, peptone, and dextrose anhydrous were procured from Fisher Scientific (Pittsburgh, PA). All-trans retinol (≥ 95%) and chloroform were purchased from Spectrum Chemical (New Brunswick, NJ). All chemicals used in yeast cell media preparation were of analytical grade. Ultrapure water (18 MΩ cm) was obtained using the in-lab Milli-Q RG water ultra purification system from EMD Millipore (Billerica, MA).

### 2.2. Yeast strains and culturing conditions

The same yeast strains and culturing conditions were used as described in Chapter 2. The resulting five yeast cultures were labeled as 75-34, 09-448, 70-101, 04-877A, and 04-877B.

2.3. Encapsulation of bioactive compounds in yeast cells

Curcumin and retinol were encapsulated in yeast cells using the same procedure as described in Chapter 2. For all compound-cell combinations, 35% ethanol, cell density of 2 OD600 units, and compound-to-cell ratio of 0.1 mM per OD600 unit were used to mix the cell and compound ethanolic solution before subjecting to vacuum treatment. The optical density of cell suspension was measured as the absorbance at 600 nm (OD600) using the microplate reader, with 200 $\mu$L of sample loaded into a well of the 96-well plate. After vacuum-facilitated infusion, the cells were harvested by centrifugation at 2711 xg for 5 min, then washed three times with water.

2.4. *In vitro* digestion

The release kinetics of curcumin or retinol encapsulated in different yeast cell cultures was measured during *in vitro* digestion following a similar procedure used by Young et al. [128] but with a different recipe of simulated digestion fluids. Simulated gastric and intestinal fluid were prepared according to the protocol developed by Minekus et al. [219] with some modifications. When preparing the electrolyte stock solutions for the digestion fluids, $NaHCO_3$ was replaced with equal molarity of NaCl and $(NH_4)_2CO_3$ was replaced with $(NH_4)_2SO_4$ to avoid a change of pH during storage. Immediately before use, 2.5 mg/mL (2660 units/mL) pepsin was added to the simulated gastric fluid (SGF) and the pH was adjusted to pH 3; 10 mg/mL (lipase activity 80 units/mL) pancreatin and 5 mg/mL bile salts were added to the simulated intestinal fluid (SIF) and the pH was adjusted to 7. Before *in vitro* digestion, SGF was pre-warmed to 37 °C. The washed cells after encapsulation were resuspended in 8 mL of pre-warmed SGF to reach OD600 of 1 and incubated in a shaking incubator at 37 °C, 100 rpm for 2 hours. The cell density in the simulated digestion fluids

was selected to ensure a sink condition for curcumin. At 0, 0.5, 1, and 2 hours, the digestion sample was briefly vortexed to ensure the cells were well suspended and 0.5 mL of cell suspension was sampled. The 0.5 mL aliquot was centrifuged at 12600 xg for 1 min to precipitate down the cells. After discarding the supernatant, 1 mL of acidified methanol or methanol was added to the cell pellet for extraction of retained curcumin or retinol respectively. 10 min of bath sonication (Branson 2510, Branson Ultrasonics) was used to facilitate the extraction of compounds. After centrifuging at 12600 xg for 10 min, the absorbance of the extractant supernatant was measured at 425 nm (curcumin) or 325 nm (retinol) using a UV-Vis spectrophotometer (GENESYS 10S Series, Thermo Scientific). The absorbance were measured in duplicates for each digesta aliquot. At the end of the 2-hour gastric digestion phase, the cells were separated from SGF by centrifugation at 2711 xg for 5 min, the supernatant was discarded and replenished with same volume of pre-warmed SIF. The same temperature and shaking conditions were used for *in vitro* small intestinal digestion, and samples were taken at 0.1, 0.5, 1, and 1.5 hours of the small intestinal phase. The 1.5-hour duration was determined based on preliminary experiment results that the % release reached an equilibrium within 1.5 hours. The same extraction and absorbance measurement procedure was conducted for these aliquots. The concentrations of compounds recovered in the extractant were calculated using corresponding calibration curves. The calibration curves were established in the concentration range of 2.5 – 15 $\mu$M. The percentage release of encapsulated compounds at time point t (hour) was calculated as:

$$\%\ Release = (1 - \frac{C_{extract}^{t}}{C_{extract}^{0}}) * 100$$

**Equation 3. 1**

$C^t_{extract}$ and $C^0_{extract}$ were the concentrations of compounds ($\mu$M) in the extractant at time t and time 0 respectively.

2.5. Hierarchical clustering of release kinetics curves

To identify different release patterns, the cumulative percentage of release at all time points were used to cluster the release kinetics curves using hierarchical clustering. Euclidean distance between each curve was calculated and the distance matrix was used to generate the hierarchical clustering.

2.6. Cell staining and fluorescence microscopic imaging

Yeast strain 09-448 and 04-877B were selected as the representative of a high protein yeast strain and a high lipid yeast strain respectively. With the two compounds, curcumin and retinol, there formed four compound-cell combinations, which were further investigated for subcellular distribution of the compounds during digestion. Nile red (NR) was used to stain the intracellular lipids of yeast cells [220] by adding Nile red stock (prepared in 50% DMSO) to the cell suspension to reach a final dye concentration of 2.5 $\mu$g/mL in 2% DMSO, and incubated at room temperature for 15 min before washing. Fluorescence microscopy was utilized to visualize the subcellular localization of the encapsulated compounds as well as the co-localization of compounds and intracellular lipids, taking advantage of the autofluorescence of curcumin and retinol, and the NR staining. A Leica TCS SP8 Multiphoton microscope (Leica Microsystem Inc.) equipped with a Mai Tai DeepSee laser was used to image the specimens. For each specimen, the images were taken at two channels: the NR channel and the compound channel. 925 nm excitation wavelength and 592 - 644 nm emission filter was to collect signals from NR. The excitation and emission wavelengths were set to 760 nm and 475 - 575 nm for curcumin; 720 nm and 426 - 506 nm for retinol.

The tile scanning function was used to automatically scan multiple fields over a specimen and collect images from both channels.

2.7. Image processing and analysis

An image processing and analysis pipeline was constructed in CellProfiler™ (version 4.1.3) [221] to facilitate automated processing of large numbers of images. *Figure 3. 1* outlines the steps in the pipeline, including alignment of the two channels (compound channel and lipid channel) to overcome the drift of samples between the laser scans at two channels, object detection from each channel, relating and filtering of objects from two channels, cell segmentation based on centroids of each object detected in the compound channel, and calculation of signal colocalization between two channels. The pipeline modules and their specifications could be found in Table S3. 1. Mander's coefficient [222] was employed to calculate the object-based colocalization index of fluorescence signals from the two channels according to Equation 3. 2:

$$Colocalization\ index = \frac{\sum_{i \in R_{coloc.}} I_i^C}{\sum_{j \in R_{compd.}} I_j^C}$$

**Equation 3. 2**

$R_{coloc.}$ is the set of pixels in the region inside a single cell that is colocalized by the compound and the lipid. $R_{compd.}$ is the set of pixels in the subcellular region occupied by the compound. $I_i^C$ and $I_j^C$ stand for the intensity of a certain pixel. The colocalization index essentially calculated the fraction of the compound's autofluorescence in areas with the Nile red (lipid) fluorescence, indicating the intensity-weighted overlap between signals from the compound channel and the lipid channel for each identified cell.

Besides the colocalization index, some other measurements were included in the pipeline, including measuring the centroid's x- and y- coordinates for each identified cell object; and area and compactness of each identified lipid droplet object (Table S3. 1). "Area" is the number of pixels in a specified region, in this case the lipid-rich region; "compactness" measures how centralized or dispersed the signals are within a region, i.e., a filled circular object would have compactness of 1, while an irregular object would have a value greater than 1. These measurements were used to characterize the images taken for cells at different time points during *in vitro* digestion.

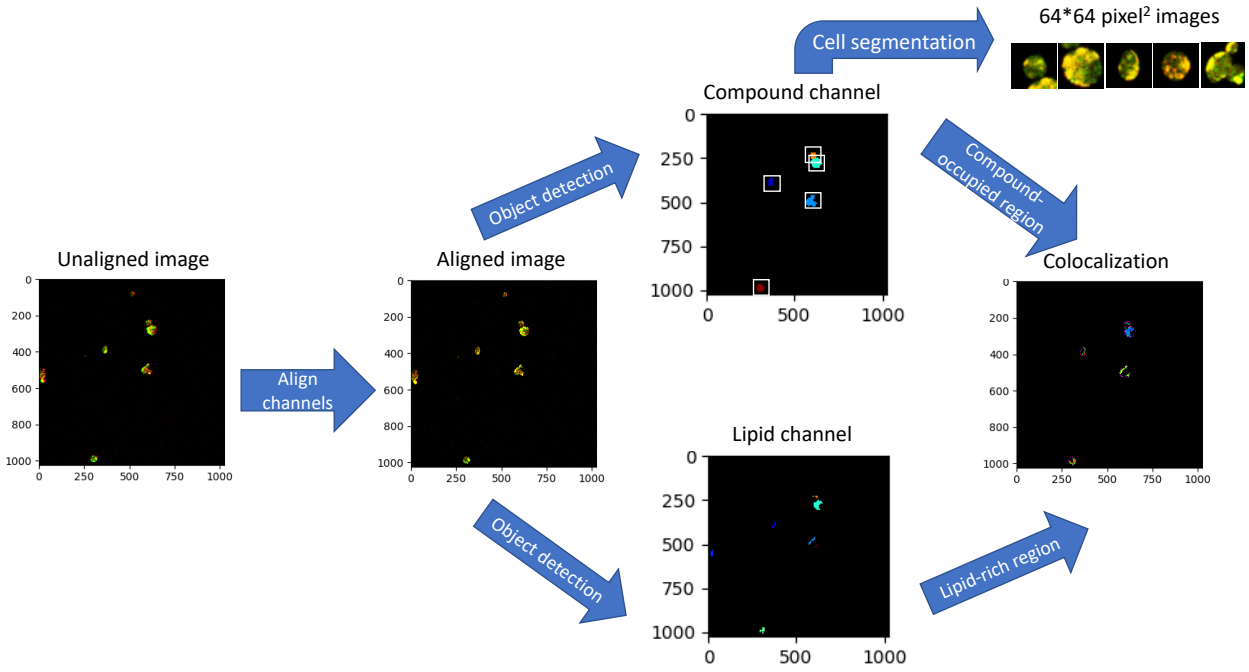


***Figure 3. 1: Automated image processing and analysis pipeline.***

2.8. Statistical analysis

Statistical inference was performed to compare the colocalization index, and area and compactness of the lipid-rich regions across different compound-cell combinations and different digestion time points. A non-parametric rank-based method for estimation and

inference of linear models was used given that these measurements were not normally distributed, and such violation of the normality assumption could not be resolved using common data transformation methods. *Post hoc* pairwise comparisons were conducted using Dunn's test. False discovery rate of the multiple comparisons was controlled by the Benjamini-Hochberg procedure. Adjusted p values smaller than 0.05 were considered statistically significant. The release kinetics curve fitting, hierarchical clustering, and statistical inferences were all conducted in R (version 4.1.3) using the following *functions* from {packages}: *nls* {stats}, *hclust* {stats}, *raov* {Rfit}, *dunnTest* {FSA}.

## 2.9. Image-based release pattern prediction with a pre-trained CNN model

### *2.9.1. Image preparation*

Fluorescence microscopic images of bioactive compound-loaded yeast cells collected before digestion (t=0 hour) were used to predict the release patterns during *in vitro* digestion. The centroids' coordinates of identified cells were used to locate the position of each cell in an image. A bounding box of 64 pixels*64 pixels was drawn around the centroid to segment the cell. Each output image was thus 64*64 in size with two channels. The cell segmentation resulted in a total of 1121 images: 299 images for the curcumin-09-448 combination, 206 for curcumin-04-877B, 370 for retinol-09-448, and 246 for retinol-04-877B.

### *2.9.2. Transfer learning*

Given the limited sample size and the large number of data needed to train a CNN model from scratch, transfer learning using a pre-trained model was selected as an appropriate approach. The pre-trained model was developed by Pärnamaa et al. [218] to classify the protein subcellular localizations in yeast cells. This model was selected

because the input for this model was based on the fluorescence microscopic images of yeast cells as well, similar to the image data in the current study. Trained on 65,000 images, the model was able to achieve a prediction accuracy of 91% for 12 different classes of protein subcellular localizations.

The original CNN model had 1 input layer, 8 convolutional layers, and 3 fully connected layers (including 1 output layer). The detailed architecture specifications could be found in the original paper [218]. When applying transfer learning, the architecture and weights of the convolutional layers were kept the same as the original model, while the fully connected layers were modified. Instead of 3 fully connected layer, only 2 were kept in the new architecture: the first fully connected layer had 128 nodes and the output layer had 3 nodes, corresponding to the number of different release patterns identified from all the release kinetics curves in the current study. The 1121 single cell images collected in the current study were randomly split into 784 for training, 168 for validation, and 169 for testing (a 7:1.5:1.5 ratio). Before using the images for modeling, the images were scaled to the range of -1 to 1. Cross-entropy loss was minimized using the AdamW optimizer, with a batch size of 64 images, and an initial learning rate of 0.001, which would be reduced by 1-fold if the validation accuracy did not improve for 5 continuous epochs. AdamW is a stochastic gradient descent method with adaptive moment estimate and weight decay, which has the advantages of fast convergence fast and better generalization of the results. The number of nodes in the first fully connected layer was tuned by searching over 32, 64, 128, and 512 nodes, with highest validation accuracy achieved with 128 nodes. After tuning the hyperparameter, data augmentation was used to enlarge the training data set and introduce more variability in the learning process. The

data augmentation was done by width and height shifts, and horizontal flip of images in the training set. Then the model was trained on the augmented data set for a maximum of 50 epochs. The CNN model was constructed and trained using the Keras API.

*2.9.3. Bootstrap confidence intervals*

To obtain confidence intervals (CI) on the prediction accuracy, precision, and recall estimates, the test set was resampled with replacement 1,000 times while keeping the number of different class labels constant. Precision and recall for each class and overall prediction accuracy were calculated in every bootstrap sample according to Equation 3. 3 and Equation 3. 4. 2.5% and 97.5% quantiles of the resulting empirical distribution were used to obtain the 95% CI.

$$Precision = \frac{True\ positive}{True\ positive + False\ positives}$$

**Equation 3. 3**

$$Recall = \frac{True\ positive}{True\ positive + False\ negatives}$$

**Equation 3. 4**

*2.9.4. t-SNE visualization*

After the test set was input into the trained model, the neuron outputs at different layers were visualized in 2D using t-SNE [223] with default parameters: the input layer, the 2nd, 4th, and 8th convolutional layers, and the two fully connected layers.

## 3. Results

### 3.1. Release patterns of encapsulated bioactive compounds from yeast cells during digestion

*Figure 3. 2* shows the release kinetics of the 10 cell-compound combinations, same as the strains and compound combinations in Chapter 2, during *in vitro* digestion of a 2-hour gastric

phase and a subsequent 1.5-hour small intestinal phase. It is clear that the release kinetics had a biphasic behavior: limited and slower release during the gastric phase and more significant and rapid release during the small intestinal phase. The release kinetics of curcumin from all the 5 yeast cell cultures showed similar patterns, featuring a rapid release at the beginning of both phases, and leveling off afterwards. 20% of encapsulated curcumin was released within the first 30 min of the gastric phase and an additional 40 - 50% was released within the first 5 min of the small intestinal phase. The release patterns of retinol were different from those of curcumin and showed variability among different yeast cell cultures. During the gastric phase, 70-101, 04-877A, and 04-877B, cultured from the two oleaginous strains *Yarrowia Lipolytica* and *Rhodotorula babjevae,* had less than 10% release; while the other two low-lipid strains, 75-34 and 09-448, showed faster release rate and released up to 40% of retinol at the end of the 2-hour gastric phase. In the following small intestinal phase, unlike curcumin, no significant burst release was observed in any of the cell cultures for retinol: less than 10% was released in the first 5 min. The final cumulative release was higher for the two low-lipid strains (80 - 95%) than the other three high-lipid cell cultures (60 - 75%).

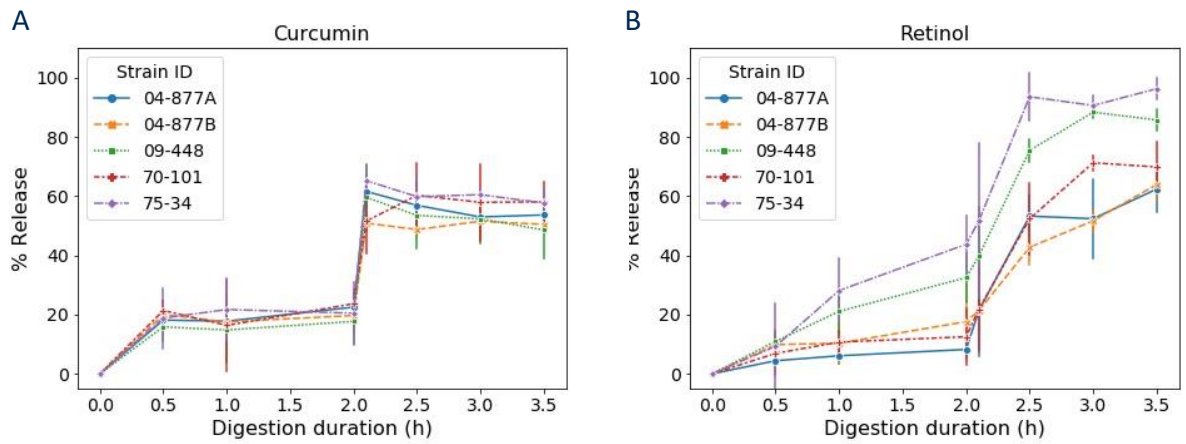


***Figure 3. 2: Release kinetics of curcumin (A) and retinol (B) from the 5 yeast cell cultures during in vitro digestion: 2 hours of gastric phase followed by 1.5 hours of small intestinal phase.*** The markers and error bars showed the mean and standard deviation (n=4) of % release measured at each sampling point for all the compound-cell combinations.

The dendrogram in *Figure 3. 3* shows the hierarchical clustering result of the release kinetics curves from all compound-cell combinations, including all replicates. The samples separated at branches closer to the root (top of the dendrogram) had larger Euclidean distances among themselves. Three distinct release patterns were identified from the dendrogram. Pattern 1 corresponded to the release profiles of curcumin from all strains of yeast cells; pattern 2 mostly corresponded to retinol release profiles from 09-448 and 75-34; while pattern 3 corresponded to retinol release profiles from 70-101, 04-877A, and 04-877B. Such clustering results confirmed the observations made from *Figure 3. 2*, that the release kinetics of curcumin was independent of the yeast cell compositions, and the retinol release profiles were different for low and high lipid strains. However, not all replicates of the release curves fit into the criteria used to describe the identified patterns. For example, two retinol-70-101 curves were found in pattern 2 instead of pattern 3, and one retinol-04-877A curve was classified into pattern 1. Such exceptions could be explained by variation in the

release data potentially due to biological variations in cell compositions and a possibility of experimental errors during a relatively large data set collection.

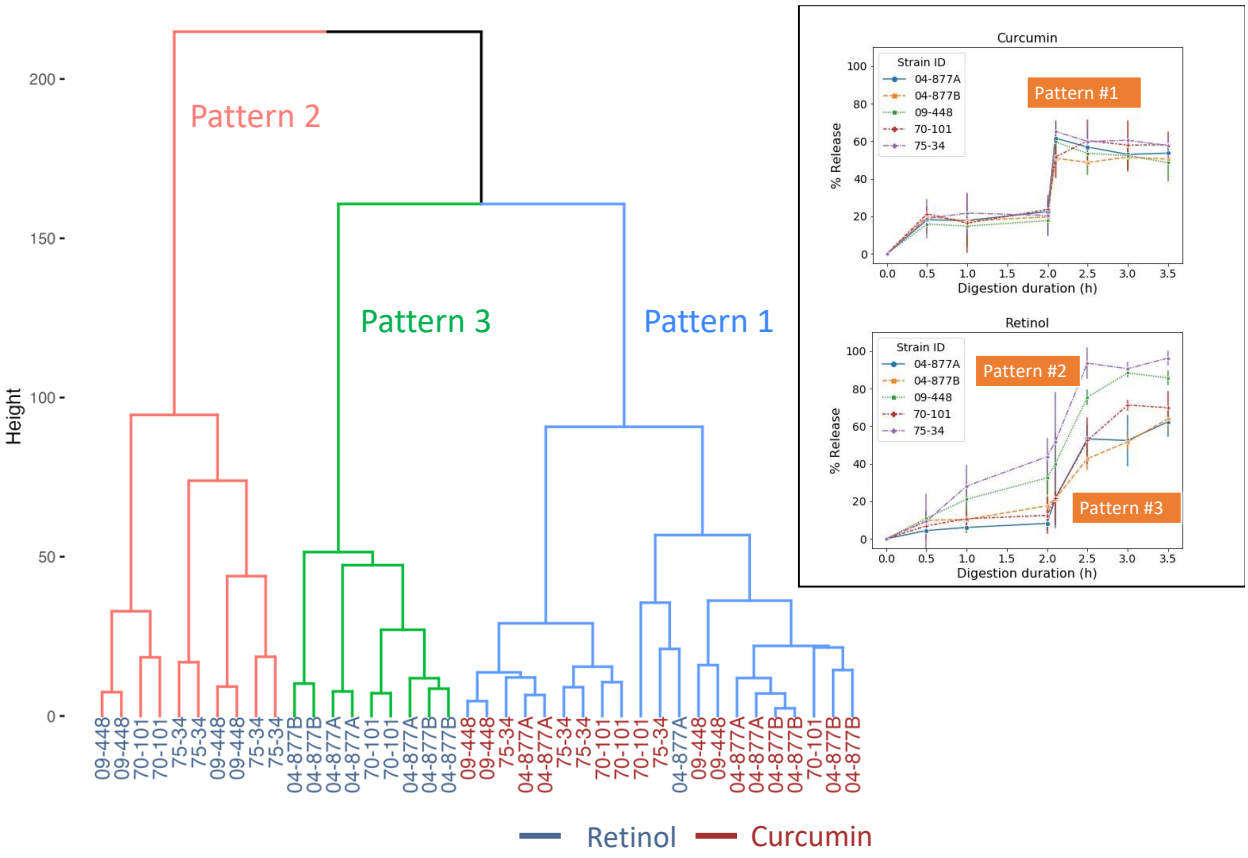


***Figure 3. 3: The dendrogram showing the hierarchical clustering of release kinetics curves.*** The samples were labeled with their corresponding cell culture IDs, and the labels were color coded according to the encapsulated compound (retinol: blue; curcumin: red). The identified release patterns were annotated on the dendrogram and the approximate release curves corresponding to each pattern were illustrated in the insert.

## 3.2. Change in cell composition and subcellular distribution of encapsulated compounds during digestion

To further investigate the role of sub-cellular distribution and cell composition in influencing the release patterns of bioactives, 04-877B and 09-448 were selected as the representative of the high-lipid and high-protein strains respectively. By encapsulating

curcumin or retinol into the two cell cultures, four compound-cell combinations were studied for the change in their subcellular structures and subcellular compound distribution during *in vitro* digestion using fluorescence imaging. Lipid bodies inside the yeast cells were stained with a fluorescent dye - Nile red and the subcellular localization of encapsulated compounds could be visualized using their autofluorescence. Figure 3. 4 demonstrates some example images taken for the four compound-cell combinations at different time points during *in vitro* digestion: time 0, 2 hours in SGF, 5min and 1h in SIF. The first observation made from the images was that the initial subcellular localization (t=0) differed for curcumin and retinol. Curcumin exhibited homogeneous distribution within the cell, while retinol was concentrated within some intracellular regions. By comparing the compound channel and lipid channel, it could be inferred that retinol preferably partitioned into the lipid bodies after encapsulation in the yeast cells due to the significant overlap of signals from the two channels. As *in vitro* digestion progressed, significant change in the morphology of lipid bodies inside the high-protein (low-lipid) 09-448 cells was observed. Before digestion and after the gastric phase, the lipid bodies in 09-448 had irregular shape and distribution in the cells. However, during the small intestinal phase, a rounded morphology of lipid bodies was observed. These changes in the shape of lipid bodies after intestinal digestion was not as significant in the high-lipid 04-877B cells. Because of the high lipid content, the Nile-red stained lipid-rich regions almost occupied the whole cytoplasmic region of the cell for 04-877B, and no identifiable changes in morphology were observed for the lipid bodies. Regarding the subcellular compound distribution during digestion, it was observed that curcumin, which was initially homogeneously distributed inside the cell, ended up colocalizing with the lipids as the digestion progressed. It could be inferred that the fraction of curcumin that was

retained inside cells after digestion resided inside the lipid-rich regions. For retinol, the autofluorescence signals almost overlapped completely with those from Nile red regardless of the digestion phases.

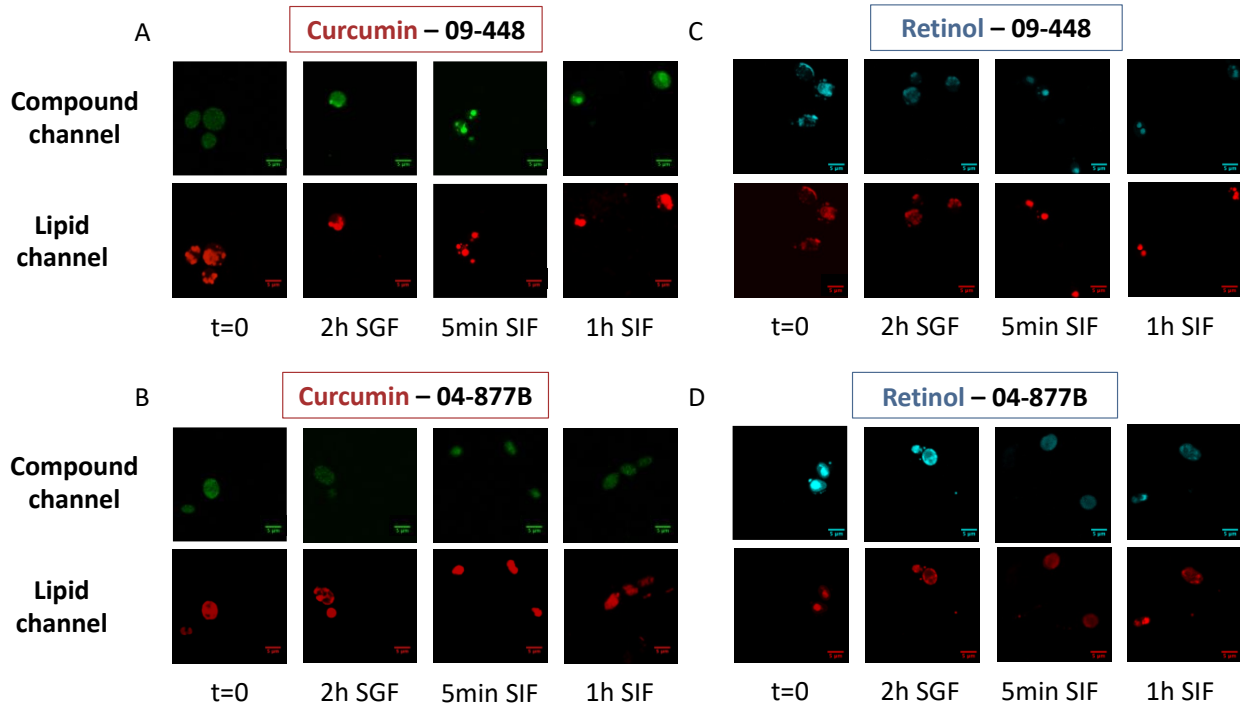


***Figure 3. 4: Fluorescence microscopic images of curcumin – 09-448 (A), curcumin – 04-877B (B), retinol – 09-448 (C), and retinol – 04-877B (D) during in vitro digestion.*** Each subplot shows the fluorescence images taken from the compound channel and the lipid channel (stained by Nile red) before digestion, 2 hours in SGF, 0.1h and 1h in SIF. The scale bars measured 5 ***μm***.

To quantify the abovementioned observations, large number of fluorescence images were acquired and an automated image processing and analysis pipeline (Figure 3. 1) was used to measure the shape (area and compactness) (Table S3. 1) of the lipid bodies and calculate the colocalization index (Equation 3. 2) of compounds and lipids for each cell identified from the images. The results are summarized in Figure 3. 5 and Figure 3. 6. Initially, 09-448 cells showed significant smaller areas of lipid-rich regions than 04-877B cells (*Figure 3. 5A*) (p-value < 0.001), consistent with the lipid content of these two strains (15% vs 41%) reported

in Chapter 2. Before digestion, the colocalization index of retinol in 09-448 cells was significantly larger than that of curcumin (p-value < 0.001), confirming the observation that encapsulated retinol mostly partitioned into lipid-rich regions. However, for 04-877B, there was no significant difference between the colocalization index of curcumin and that of retinol (p-value = 0.096), and both were larger than the corresponding values in 09-448. Since lipid occupied most of the cytosolic space in the high-lipid 04-877B cells, as evidenced by the significantly larger area of lipid bodies in 04-877B than 09-448 (Figure 3. 5A), it was expected that regardless of the compound's affinity to lipids, the colocalization index would be high. Moreover, the lipid bodies in both 09-448 and 04-877B cells became smaller in size (Figure 3. 5A), and more circular and compact in shape (Figure 3. 5B) after entering the small intestinal phase, as compared to the end of the gastric phase. Figure 3. 6B demonstrates that the colocalization index between curcumin and cellular lipids in the high-protein 09-448 cells significantly increased after the gastric and small intestinal phase, compared to that before digestion (p-value <0.001); while for retinol, the colocalization index stayed relatively constant across different time points (p-values for the difference in colocalization index from before-digestion to 2hr SGF and 5 min SIF are 0.78 and 0.68 respectively). Similar patterns were observed for 04-877B (Figure 3. 6A), except that the increase in the colocalization index between curcumin and cellular lipids after digestion was smaller compared to that in 09-448 cells.

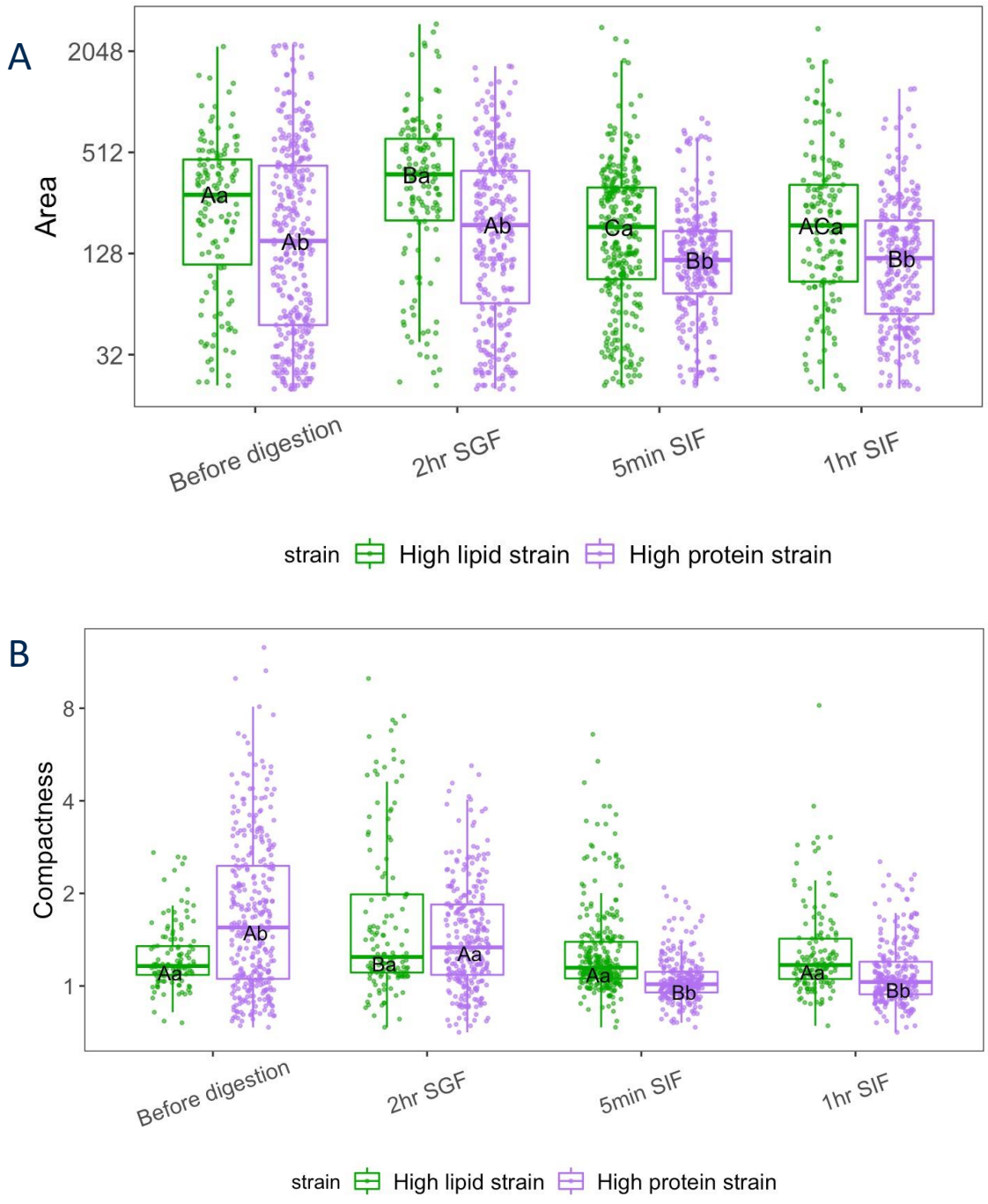


***Figure 3. 5: Boxplots of area (A) and compactness (B) of lipid droplets in the high-lipid 04-877B cells (green) and the high-protein 09-448 cells (purple) at different time points during in vitro digestion.*** The y-axis of both subplots is shown in the log2 scale. Different uppercase letters indicate significant difference across time points, while different lowercase letters indicate significant different between yeast cell strains.

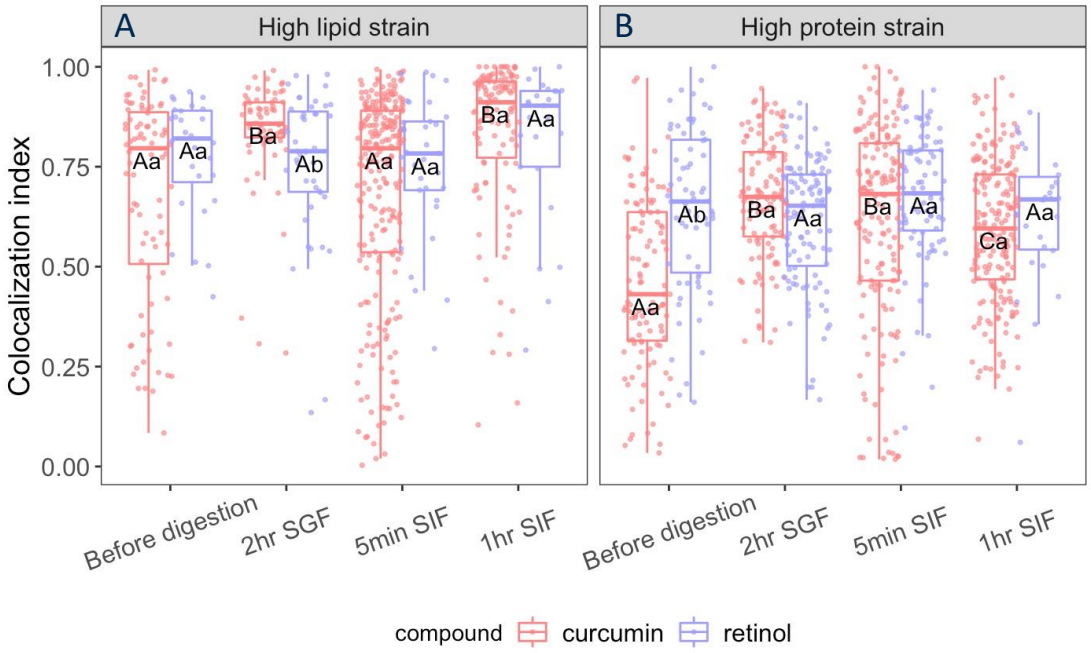


***Figure 3. 6: Boxplots of colocalization index of fluorescence signals from Nile red stained lipids and encapsulated curcumin (red), retinol (blue) at different time points during in vitro digestion. A: high-lipid 04-877B cells; B: high-protein 09-448 cells.*** Different uppercase letters indicate significant difference across time points, while different lowercase letters indicate significant different between encapsulated compounds.

### 3.3. Prediction of release patterns using fluorescence microscopic images taken before digestion

Besides the colocalization index and the area and compactness of lipid bodies, the fluorescence microscopic images could provide information about the encapsulated compounds, the cell, and their interactions, which were hypothesized to be responsible for the different release patterns observed during *in vitro* digestion. The images taken at time 0 were used to fine tune a pre-trained CNN model to predict the identified release patterns (*Figure 3. 3*). The model converged within 40 epochs during the training process and achieved a train and validation accuracy of 0.97 and 0.93 respectively at epoch # 40 (Figure S3. 1). Bootstrapped test set images were evaluated using the trained model using weights at

epoch # 40. The results illustrated that the trained model achieved a median accuracy of 0.90 (95% CI: [0.86,0.94]) on the never- seen test set images. Pattern 1 was characterized by significant initial release and rapid leveling off in both the gastric and small intestinal phase, corresponding to the release of curcumin from all cell cultures. This pattern class had the highest median recall (0.97) and lowest median precision (0.87) scores among the three release patterns. It implied that 97% of images taken for curcumin – 09-448 and curcumin – 04-877B could be classified to their correct release pattern, but 13% of images classified into pattern 1 actually belonged to other pattern classes. Release pattern 2 and 3 were represented by the release profile of retinol from 09-448 and 04-877B respectively, where pattern 2 had an overall faster release than pattern 3 (*Figure 3. 3*). Pattern 2 had the highest median precision score (0.96) among the three classes, indicating that few images would be misclassified into this pattern class. More prediction mistakes occurred for pattern 3 with the median precision and recall scores of 0.89 and 0.80. Among all the test set retinol – 04-877B images, 20% were mistakenly classified to pattern 1 or 2. From *Figure 3. 7B* we could see that 5 out of 53 retinol – 09-448 images, and 6 out of 40 retinol – 04-877B images were misclassified as pattern 1, contributing to both the lower recall of pattern 2 and 3, and the lowest precision of pattern 1. *Figure 3. 8* provides a 2D visualization of the hidden layers' outputs extracted from the CNN model after feeding in the test images set. It could be observed that the separation of the samples started to show after the 3$^{rd}$ convolutional blocks (8 convolutional layers), and became clearer after the first fully connected layer.

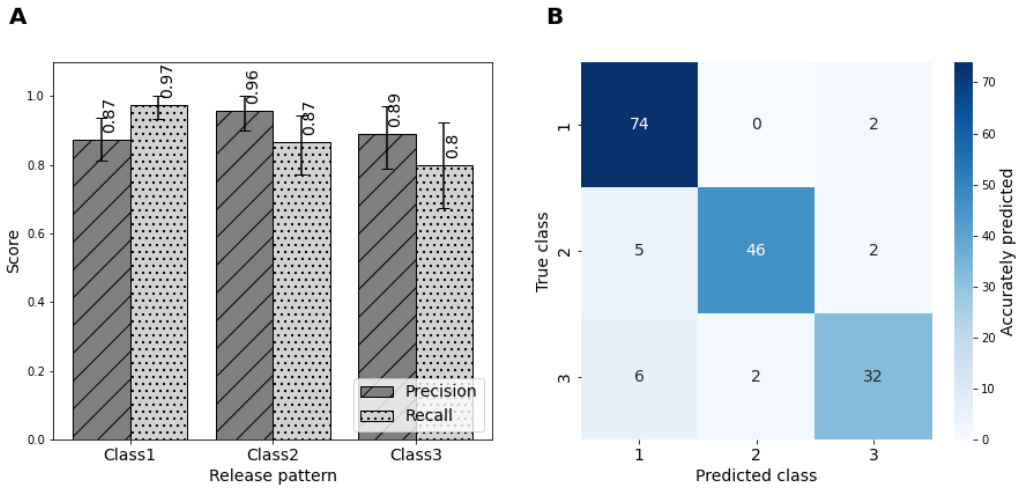


***Figure 3. 7: A: Precision and recall for the three release pattern classes predicted from bootstrap test set (the error bars indicate the 95% CIs). B: Prediction accuracy matrix for the original test set.*** The numbers in the matrix are the number of images/ samples.

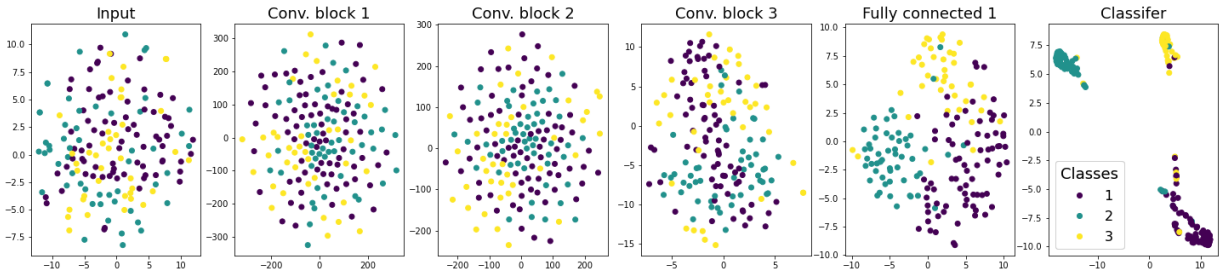


***Figure 3. 8: 2D visualization of hidden layers' outputs using the t-SNE algorithm.*** *The test images set were fed into the trained CNN model and the output was extracted from the input layer, after the 1st, 2nd, and 3rd convolutional blocks, and after each of the two fully connected layers. The dots are color coded based on their true release pattern classes.*

## 4. Discussion

*In vitro* digestion of cell-based carriers is a dynamic process in which the yeast cells undergo physical and biochemical changes, and the encapsulated compounds are released. In the current study, we observed that for compounds with different hydrophobicity and yeast cells with different biochemical profiles, their release kinetics were largely different (*Figure 3. 2*). Based

on the fluorescence images of the cell-based carriers and imaging analysis results, such different release profiles corresponded to different subcellular localization of the encapsulated compounds, which kept changing during the digestion process. The fluorescence microscopic images from both the current and previous studies [105,210] showed that after encapsulation, the compounds permeated across the cell wall and partitioned to different intracellular compartments. Both curcumin and retinol had very low water solubility, i.e., 1.63 $\mu M$ for curcumin [224] and 0.06 $\mu M$ for retinol [225]. Proteins and lipids are the major macro-compositional molecules in the intracellular compartment of yeast cells. It is reasonable to hypothesize that the encapsulated compounds, after permeating through the cell wall, either were solubilized in the lipid-rich regions or the aqueous phase, hypothetically by complexing with proteins. Since it was not feasible to introduce another dye that could globally stain all cellular proteins and be imaged with the presence of the auto-fluorescent bioactive compounds and Nile red, it was assumed that the fraction of compounds' fluorescence signals not overlapping with Nile red represented the compounds partitioning into the protein-rich aqueous phase. The homogeneous distribution of curcumin inside cells and the high degree of colocalization between retinol and lipids (*Figure 3. 6*) implied that the two compounds had different partitioning coefficients between the lipid-rich phase and protein-rich aqueous phases. Retinol is more hydrophobic than curcumin, with log $P_{ow}$ values of 5.68 and 3.29 respectively. Curcumin's solubility in whey and pea proteins (1.16 mg/g and 1.02 mg/g respectively [208]) is higher than that in various oils (0.4 to 0.8 mg/g [226]). Although the abovementioned lipids and proteins do not exist in yeast cells, it could be deduced from the differential solubility and the well-known strong affinity of curcumin to various proteins [185] that curcumin would preferably partition into the protein-rich aqueous phase once encapsulated in cells. Such a claim is also supported by the results from Chapter 2 that the high protein yeast

strains achieved higher encapsulation efficiency for curcumin. Retinol, on the other hand, is a fat-soluble compound with a much higher lipid solubility (2.5 M [209]) than curcumin. In milk, retinol is significantly more soluble in the fat phase than the proteins phase [227]. Similarly, the fluorescence microscopic images taken in the current study also showed high colocalization index between retinol and lipids, which is hypothetically attributed to the high lipid solubility of retinol.

Bioactive compounds partitioned in different subcellular compartments of the yeast cells undergo different interactions with the digestion fluids components, while the subcellular structures of the yeast cells also changed during digestion, as shown in the microscopic images. During the gastric phase, pepsin and acid in SGF could partially destroy the mannoproteins in the cell wall and plasma membrane bound proteins that are responsible for permeability [103,228], promoting the release of encapsulated compounds. In the small intestinal phase, bile salts in SIF disrupted the cellular membrane systems and the lipids coalesced into spherical droplets to minimize the interfacial area between lipids and aqueous cytosol. This statement is evidenced by the increased circularity of the lipid droplets in yeast cells after small intestinal digestion (*Figure 3. 5*). It has been shown that bile salt at high concentrations could directly dissolve cell membranes; while at lower concentrations, it could disrupt membrane integrity via more subtle effects such as modifying the membrane's permeability and fluidity [229,230]. This is the major mechanism of action for the antimicrobial effect of bile salts [231]. For curcumin, both the gastric and small intestinal phase showed a biphasic release behavior, and the release profiles were similar regardless of the yeast cells' chemical profiles. Such a biphasic behavior – initial burst release followed by limited sustained release, has been observed for curcumin in both yeast cell-based carriers [110,128] and other encapsulation systems, such as liposomes [232], modified starch, and

$\beta$-cyclodextrin [110]. In the current study, the increase in the colocalization index with lipids after digestion implied that potentially the protein-bound curcumin was released very rapidly, and the retained curcumin was either initially solubilized in lipids or re-partitioning into the lipid-rich regions. The disturbance of curcumin's partitioning equilibrium between the protein and lipid phase could be the result of acid-induced protein conformation change during the gastric phase, and the emulsification property of bile salts [233] in the small intestinal phase. It is possible that the initial burst release was so fast that no difference in release rate among different yeast cells could be captured within the short time scale. For retinol, the release rate from high-protein cells, as represented by 09-448, was faster than that from high-lipid cells, as represented by 04-877B. With higher lipid content, 04-877B cells had larger colocalization index with retinol than 09-448 cells, indicating that in 04-877B cells, a larger fraction of encapsulated retinol were compartmentalized in lipid-rich regions, and this fraction might be released at a lower rate that those bound to proteins. Bile salt is the major contributor to the release of bioactive compounds such as curcumin and retinol during from yeast-based microcarriers *in vitro* digestion [128,134]. Due to their amphiphilic nature, bile salts can self-associate to form micelles in water, or form mixed micelles with phospholipids [234]. The bile salt-phospholipid mixed micelles has been shown to be responsible for solubilizing hydrophobic drugs [234] and vitamins [235] and enhancing their uptake in the small intestine. The bile salt-aided micellization of lipid and retinol, and subsequent release into digestion fluids might be different for protein-bound or lipid-solubilized retinol, leading to different release rate. Another potential explanation is that inside 04-877B cells, there was a lower effective concentration of bile salts that were available for solubilizing retinol because the large amount of lipids present would interact with and deplete available bile salts.

Release behaviors of encapsulated compounds is an important feature to characterize for the design and development of delivery systems. However, *in vitro* digestion itself is a long process and a rate limiting step in screening potential cell-based carriers for encapsulation of diverse bioactive compounds. To enable high throughput screening, it is necessary to establish a predictive relationship between the release patterns and features of the encapsulation system that can be characterized more efficiently. The results from the current study showed that the release of encapsulated compounds from yeast-based carriers is associated with the bioactive compound's hydrophobicity, the initial amount and distribution of cellular lipids, and the partitioning of encapsulated compounds between the lipid and protein-rich aqueous phase. Furthermore, each of these features could be captured by the fluorescence microscopic images of compound-infused yeast cells taken before digestion, making these images a good data source to predict the release patterns. With the automated image acquisition and processing pipeline developed in the current study, a large number of micrographs ready for analysis could be generated in a short period of time. Problem-specific features relevant to release profiles, such as the colocalization index, area and compactness of lipid bodies, could be measured and analyzed in a standardized manner and incorporated in the automated image analysis workflow. However, defining and selecting informative features from the raw image pixels can be time-consuming and such a manual feature selection process could result in underutilization of the rich information contained in the images [236]. In the current study, instead of defining these features manually, a pre-trained CNN model with fine tuning of hyperparameters was used to classify the micrographs to their corresponding release patterns. The CNN model essentially incorporated the feature extraction step into its architecture. It processed the images by passing them through consecutive layers of neurons which learned to extract the features that could best predict the

outcome. As shown in *Figure 3. 8*, the output of the first fully connected layer in the trained model showed clear separation of samples from the three release patterns, indicating that the CNN model could be used as a feature extractor as well. Applying data augmentation to the training image set improved the model performance (data not shown) by introducing more variability to the training process, so that the model could learn a more general pattern rather than memorizing the mapping in the training set, thus preventing overfitting, and improving generalizability. Admittedly, the generalizability of the model could be further improved with additional images from other compound-cell combinations. Moreover, with an expanded data set, it could be possible to have a point-wise prediction of the release curves themselves instead of the release pattern classes. The current study demonstrated that the microscopic images could serve as fingerprints of the cell-based encapsulation system. Facilitated by automated image acquisition and processing, and a trained CNN model, the images could be used for high throughput screening of yeast cell-based carriers, as it shortened the workflow duration for release profile evaluation.

## 5. Conclusion

Curcumin and retinol encapsulated in yeast cells with different lipid and protein contents showed different subcellular localization, due to their different affinity to proteins and lipids inside the cells. All compound-cell combinations showed a biphasic release profile during *in vitro* digestion: limited release in the gastric phase and more significant release during the small intestinal phase. Three different release patterns were recognized from the release kinetics curves of different compound-cell combinations. Curcumin release curves featured rapid release at the beginning of both the gastric and small intestinal phase and levelled off quickly after exposure to the digestion fluids. For retinol, the release from the high lipid strain was less and slower

compared to from the high protein strain. The fluorescence images captured the dynamics of the cellular compositional and structural changes, as well as the changes in compound subcellular localization during *in vitro* digestion. The images taken at time 0 successfully predict the release patterns using a pre-trained CNN model after fine-tuning. Altogether, the fluorescence microscopic images linked the different release profiles of encapsulated compounds to their subcellular distributions. The CNN model shows promise as a tool for high throughput screening of yeast cell-based carriers since it shortened the workflow duration for release profile evaluation. Expanding the image dataset by including more compound-cell combinations could further improve the model performance and generalizability to a broader range of bioactive and other cell-based carriers.

## Supplements

**Table S3. 1: Modules in the automated image processing and analysis pipeline.**

| Modules | Specifications |
|---|---|
| Align | Align two channels to resolve mismatch resulting from microscopic images acquisition. |
| Gaussian Filter | Reduce signal noise from each channel. |
| Identify Primary Objects | Detect objects from both channels. Compound channel: identify compound-occupied region inside cells; lipid channel: identify lipid-rich region inside cells. |
| Relate Objects | Relate the objects detected from the two channels, i.e., relate lipid droplet objects inside one cell (identified from the lipid channel) to the corresponding cell object (identified from the compound channel). |
| Filter Objects | Filter out cell objects that have no related lipid droplet object. |
| Measure Object Size Shape | Measure the centroid coordinates for each identified cell object.<br>Measure the area and compactness of each identified lipid droplet object:<br>- Area: the number of pixels in a specified region.<br>- Compactness: The mean squared distance of the object's pixels from the centroid divided by the area. A filled circle will have a compactness of 1, with irregular objects or objects with holes having a value greater than 1. |
| Mask Objects | Identify colocalization regions between the cell object and related lipid objects (after proper thresholding). |
| Measure Object Intensity | Calculate colocalization index between the compound-occupied region and lipid-rich region for each cell object using Equation 3. 2. |
| Calculate Math | |

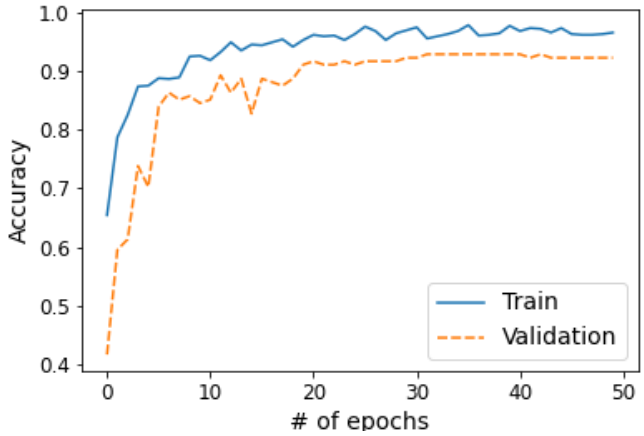


**Figure S3. 1: Prediction accuracy of the train and validation set as a function of number of epochs during model training.**

# CHAPTER 4

## Engineering cell-based microstructures to study the effect of structural complexity on *in vitro* bioaccessibility of a lipophilic bioactive compound

### 1. Introduction

Bioaccessibility of plant-derived micronutrients has been evaluated for diverse food materials with the overall motivation to understand the factors contributing to the release profiles of various micronutrients from food matrices during digestion. Plant-derived bioactive compounds, such as curcumin, can exert different effects depending on its release site in the gut [237,238], such as ameliorating gastric ulcers when targeting the stomach [239] and preventing ulcerative colitis in the colon [240]. The chemical properties of micronutrients and microstructural properties of food matrices such as plant foods are the two major factors influencing the bioaccessibility of micronutrients. Many studies have shown that differences in the chemical nature of compounds significantly contribute to the differences in their bioaccessibility and bioavailability [39,61,62]. Besides, the release profiles of bioactive compounds from plant sources are significantly influenced by the microstructure of food matrices [241], generally defined as the spatial arrangement of different food elements and their mutual interactions at scales below 100 μm. In plant-based foods, the microstructural features contributing to the bioaccessibility of bioactive compounds include chemical composition of plant cells, localization of bioactives and their interaction with various cellular components [242]. However, the current approaches of studying the food matrix effect on bioactive's bioaccessibility have limitations in decoupling the effects from chemical properties of micronutrients and microstructural properties of food matrices. For instance, one study compared the bioavailability of polyphenols from different plant origins to

investigate the effect of different molecular structures and conjugation forms of the polyphenol compounds [62]. Nevertheless, such studies often ignore the impact of structural features such as the differences in cell wall composition, localization of compounds, and the binding with food matrix elements [64].

Complementary to the influence of chemical properties of micronutrients on their bioaccessibility, some studies have evaluated the effect of food processing on the bioavailability of micronutrients. Food preparation and processing such as cutting, heating, and high-pressure treatment are known to change the microstructures of plant tissues, thus, in turn, could affect the release of micronutrients. For instance, it was reported that the release of carotenoids from plant foods occurs only after disruption of the cell walls, which may result from food processing and mastication but not during gastric digestion [243,244]. Also, cooking increased the extractability of carotenoids from food matrices by breaking down cell walls and weakening the bonding between carotenoids and pectin-like fibers in plant tissues [39]. The major limitation of using processing to study the relationship between food microstructure and nutrient bioaccessibility is that the process of modifying structural properties is not well-controlled, and more than one structural feature could be impacted simultaneously by a selected processing method. Thus, changes in the compound bioaccessibility cannot be attributed to a specific structural or compositional feature. For example, grinding could break down cells and expose polyphenols to polyphenol oxidase [245] but could also increase surface area and promote accessibility of digestive enzymes, thus increasing bioaccessibility.

The current study develops a unique approach for investigating the influence of food microstructures on the bioaccessibility of micronutrients. This approach started with the infusion of a purified model bioactive compound (curcumin), in a yeast cell-based microcarrier.

Subsequently, the microcarriers were assembled into cell clusters through polyelectrolytes-facilitated electrostatic interaction and then embedded in a continuous extracellular matrix to form a tissue-like structure. Using yeast cells as micro-carriers have emerged as a practical encapsulation approach for various compounds, including curcumin [105,106,246,247]. Yeast-based carriers, based on their micro-scale size (5 - 10 $\mu m$), eliminate the need to fabricate microparticles and can enhance the oxidative and thermal stability of encapsulated bioactives compared to colloidal carriers such as emulsions [111]. *Saccharomyces cerevisiae* is the most studied yeast strain for encapsulation applications due to its large-scale commercial production, high nutritional value, and availability as by-products of fermentation processes [108]. This study selected the vacuum-facilitated infusion process as it significantly reduces the time required for partitioning various compounds into yeast-based microcarriers [105]. The release profile of curcumin from single yeast cells during simulated digestion has been studied and reported in a previous study [128]. 3D assembly of cell-based carriers into larger cell clusters was hypothesized to decrease the surface area and increase cell-cell adhesion, thus modifying the release profile of the encapsulated model bioactive compound. Additionally, the presence of an extracellular matrix adds a barrier between the cell-encapsulated bioactive compound and the digestive environment. Previous studies have shown that encapsulating curcumin in alginate matrices retarded the compound release during simulated digestion [248,249]. To the best of our knowledge, the bottom-up assembly of cells into tissue-like structures has not been utilized to understand and modulate the release of bioactive compounds during the digestion processes.

The overall objective of the current study was to examine the effect of cell clustering and extracellular matrix on the bioaccessibility of the encapsulated model compound during simulated gastrointestinal digestion. This approach will enhance a fundamental understanding of

the role of microstructural features of cells and their assembled structures in influencing the release of bioactives. In addition, the results of this study can enable innovations in the formulation of novel food structures to control the release of bioactive compounds.

## 2. Materials and methods

### 2.1. Materials

The following reagents used in this study: poly(diallyl dimethylammonium chloride) (PDADMAC, $M_w$ 400,000 - 500,000, 20 wt.% in water), dextran sulfate sodium salt from *Leuconostoc* spp. (DSS), alginic acid sodium salt from brown algae (ALG, medium viscosity), curcumin derived from *Curcuma longa* (turmeric) [≥ 65%, HPLC], methanol, glycerol (≥99%), bile salts (cholic acid- deoxycholic acid sodium salt mixture), calcium chloride, and sodium phosphate, mono- and dibasic, were purchased from Sigma-Aldrich (St. Louis, MO). The enzymes used in simulated digestion fluids preparation were: pepsin from porcine gastric mucosa (1064 units/mg protein), lipase from porcine pancreas Type II (100-500 units/mg protein), purchased from Sigma-Aldrich (St. Louis, MO). Absolute ethanol was purchased from Koptec (King of Prussia, PA). Sodium hydroxide, hydrochloric acid, and sodium chloride were purchased from Fisher Scientific (Pittsburgh, PA). Fleischmann's Active Dry yeast, *Saccharomyces cerevisiae*, was obtained from a local grocery store. Ultrapure water (18 MΩ cm) was obtained using the in-lab Milli-Q RG water ultra-purification system from EMD Millipore (Billerica, MA).

### 2.2. Yeast cells preparation

Native yeast cells were prepared by washing 1 g of active dry yeast twice in excess of ultrapure water. The cells were pelleted down by centrifugation at 2711 xg for 5 min between each wash and once more to remove excess water.

2.3. Encapsulation of curcumin into yeast cells

Encapsulation of curcumin into yeast cells was conducted as described in a previous study[105]. Briefly, before encapsulation, 1 g of washed yeast cells were weighed into 50 mL centrifuge tubes. 3.25 mL of 100 mM phosphate buffer (pH 6.5), 1.5 mL of absolute ethanol, and 250 μL of 2.5 mg/mL curcumin in absolute ethanol were added to give a 35% ethanol concentration, and 0.0625 wt.% curcumin to yeast ratio. Samples were vortexed to facilitate dispersion of yeast cells and were subjected to 99% vacuum with a hold time of 5 seconds. After vacuum infusion, the samples were centrifuged at 2711 xg for 5 min, and the supernatant was decanted. The pelleted cells were then washed 4 times in 5 mL of ultrapure water, and centrifuged once more at the same speed and time to remove excess water.

2.4. Layer-by-layer coating of yeast cells with polyelectrolytes

The method for layer-by-layer coating was adapted from previous papers reporting the coating of yeast cells using oppositely charged polyelectrolytes layers [152,157]. Polycation PDADMAC (Mw 400 - 500 kDa) and polyanion DSS (Mw ~5 kDa) or ALG (Mw 80-120 kDa) were deposited on native yeast cells alternately. PDADMAC (20 wt.% in water) was diluted 100 times in 0.5 wt.% NaCl aqueous solution to achieve a final PDADMAC concentration of 2 mg/mL. Yeast cells with encapsulated curcumin were suspended in PDADMAC solution at a cell density of ~$10^9$ cfu/mL and shaken at 200 rpm for 20 min. Then, the cells were separated from excess PDADMAC solution by centrifugation at 2711 xg for 5 min, and the cell pellet was washed twice with ultrapure water. The resulting cells

coated with a layer of PDADMAC are referred to as PDADMAC@yeast hereafter. PDADMAC@yeast was introduced into the negatively charged polyelectrolytes: DSS or ALG (2 mg/mL in 0.5% NaCl) solution, followed by incubation at 200 rpm for 20 min, centrifugation, and washing (the separation and washing step for PDADMAC/DSS@yeast was modified as described in section 2.5). Three coating architectures were constructed using the layer-by-layer deposition step: PDADMAC@yeast, PDADMAC/DSS@yeast, and PDADMAC/ALG@yeast.

2.5. Electrostatic aggregation of yeast cells

In this study, two types of cell clusters were formed by electrostatic aggregation: PDADMAC/DSS@yeast (P/D cluster), and PDADMAC@yeast+PDADMAC/ALG@yeast (P+P/A cluster). In the previous coating step, introducing PDADMAC@yeast into DSS solution resulted in cluster formation directly. Therefore, no further aggregation step was conducted. Centrifugation of PDADMAC/DSS@yeast (P/D cluster) would lead to formation of big cell lumps that could not be easily re-dispersed by vortexing, so the cell clusters were separated from excess DSS solution by decanting supernatant after 10-minute gravitational precipitation of cell clusters. Then the P/D clusters were washed twice with water, separated by gravitational precipitation. No extensive cell flocculation was observed in the ALG coating step, therefore PDADMAC@yeast and PDADMAC/ALG@yeast were mixed at a 1 to 5 (wt. to wt.) ratio in pH 3.5, 0.5% NaCl solution for electrostatic aggregation (pH 3.5 was used to ensure stability of curcumin). After 5 min incubation at 200 rpm shaking, the P+P/A clusters were harvested and washed in the same way as P/D clusters.

2.6. Particle size and cell surface charge measurements

Surface charge of native yeast cells, polyelectrolyte-coated cells, and cell clusters was assessed based on ζ-potential, which can be determined using electrophoretic laser scattering in a Malvern Zetasizer nano-ZS (Malvern Instruments Ltd., Malvern, Worcestershire, United Kingdom). A suspension of native, coated, or clustered yeast cells was prepared in pH 3.5, 0.5 wt.% NaCl solution to reach cell density of 1 mg/mL. ζ-potential was measured in an acidic environment because the same solution was used for electrostatic clustering of cells. A 1 mL aliquot of such suspension was transferred to a cuvette and inserted into the measurement chamber of the Zetasizer. Particle size distribution of native and clustered cells before and after simulated digestion were measured using a Microtrac particle size analyzer S3500 (Microtrac Inc., Montgomeryville, PA). Approximately 600 μL of 10 mg/mL cell/cell clusters in pH 3.5, 0.5 wt.% NaCl solution was added to the sample dispersion controller filled with deionized water. Samples were mixed in the bulk water then flow through a tri-laser diffraction analyzer which measured the angular variation in intensity of light scattered as laser beams pass through a dispersed particulate sample. Particle sizes were then calculated based on Mie theory of light scattering performed using the equipment-matched software. Volume distributions of the cells or cell clusters were recorded in this study and volume mean diameters were reported. Both ζ-potential and particle size measurements were taken in triplicates for each cell/cluster type.

2.7. Cell-laden alginate film preparation

To further increase the structural complexity of the engineered cell-based microstructures, native yeast cells or the cell clusters were embedded in an alginate film. The alginate film with native cells or cell clusters was prepared as follows: 0.53 g of Alg was added to 20 mL of ultrapure water while stirring at 400 rpm to ensure complete hydration of

Alg powder. Then, the stirring speed was lowered to 300 rpm and the mixture was stirred at 100°C for 1 hour to ensure complete dissolution of ALG in water. Afterwards, the alginate solution was stirred at 100 rpm while cooled down to room temperature, after which 0.2 g of glycerol was added to the solution as plasticizer. The prepared ALG-glycerol mixture (15 mL) was added to a suspension of native cells or cell clusters in water (5 mL of 125 mg/mL) and gently mixed with a spatula. The final composition of the solution was 2 wt.% ALG, 0.75 wt.% glycerol, 3 wt.% native cells or cell clusters. The mixture was degassed under vacuum for 15 min and transferred to a casting plate with 8.5 cm diameter, left to dry on a flat surface at room temperature overnight. Dried alginate film containing native cells/ cell clusters was peeled off from the casting plate and cut into 1 cm*1 cm pieces. The alginate film was then externally crosslinked by immersing the film pieces in pH 3.5, 5% $CaCl_2$ solution for 5 min, rinsed once in water, and dried to constant weight at 37°C.

2.8. Visualizing cell clusters using confocal laser scanning microscope (CLSM)

Autofluorescence properties of curcumin enabled the fluorescent imaging of curcumin infused single cells and cell clusters. A Leica TCS SP8 STED (Leica Microsystem Inc.) with a pulsed laser tuned to 488 nm was used in confocal mode for excitation. A time-gated, hybrid detector was used to collect signal from 498 - 591 nm range, corresponding to the fluorescence of curcumin. For the two types of cell clusters without alginate film, z-stack images were taken prior to and at 40 min of simulated intestinal digestion. To prepare slides for confocal microscopic imaging, a 1.5 mm-thick spacer with 6 wells was placed on a glass slide, ~100 μL of 1 mg/mL cell clusters suspended in water was aliquot to each well, a coverslip was then placed on top of the spacer. Images of cell clusters before and during simulated digestion were taken with a 20X objective at the same laser intensity. The same

Leica TCS SP8 STED and same settings were used in confocal mode to visualize native cells and cell clusters enclosed in alginate films. One piece of alginate film was hydrated in water and placed on glass slide covered by a coverslip. A 63X objective was used instead. 3D projection of z-stack images was performed in Fiji [250]. Texture features extraction (Haralick features) was performed using the mahotas package [251] in Python 3.7.6.

2.9. *In vitro* simulated gastric and intestinal digestion

Simulated gastric fluid (SGF) was prepared according to the procedure described by Tikekar et al. [187] with some modification. Briefly, it consists of 3.2 mg/mL pepsin in 5 mg/mL NaCl solution at pH 3.5 (pH adjusted by HCl). pH of a fasted stomach is normally below 2 [252]. However, the gastric pH would rise to above 5 after food intake [253] and returned to fasted pH after secretion of hydrochloric acid. The pH of SGF chosen in the current study was around the mean value of the gastric pH within a 2-hour digestion period after food intake, and within the range of optimum pH for pepsin activity, as recommended by Minekus et al. [219] Before simulated gastric digestion, SGF was pre-warmed to 37°C. In 1.5 mL microcentrifuge tubes, aliquots of SGF (1 mL) were added to 10mg of curcumin loaded native cells or cell clusters; or to 1 piece of 1 cm*1 cm alginate film containing native cells or cell clusters. Such a sample-to-SGF ratio, same for SIF, was determined to ensure a sink condition for curcumin. The microcentrifuge tubes were incubated horizontally in a rotatory incubator at 37°C and 90 rpm for 2 hours. At 0 (before digestion), 1, and 2 hours, one sample was removed from the incubator, centrifuged, decanted, and stored in the dark for further analysis. Cell cluster samples used in subsequent intestinal digestion were removed from the incubator after 2 hours. The SGF was decanted after the cell clusters naturally precipitated down.

Simulated intestinal fluid (SIF) was prepared as described by Tikekar et al. [187] Briefly, a stock solution containing 0.025 M $KH_2PO_4$, 3.33 mg/mL $CaCl_2$ and 5 mg/mL NaCl was prepared and adjusted to pH 7.5. The stock solution was pre-warmed to 37°C. Bile salt and lipase from porcine pancreas were added to the stock right before the digestion started. The current study used two bile salt levels: 5 mg/mL for low bile salt (LBS) condition, and 25 mg/mL for high bile salt (HBS) condition. Lipase content was kept constant at 2 mg/mL for both conditions [242]. Samples from the previous gastric digestion step were re-suspended in SIF to yield a ratio of 10 mg of cells to 1mL of SIF. One sample was prepared for each time point in microcentrifuge tubes. The microcentrifuge tubes were incubated horizontally in a rotatory incubator at 37°C and 90 rpm for up to 3 hours. One tube was removed from the incubator at 0 (right after exposure to SIF), 1, 2, and 3 hours of digestion. After centrifugation and decanting, samples were saved for analysis. The time 0 samples were centrifuged right after addition of SIF to study whether there was any immediate curcumin release. All simulated digestion experiments were done in triplicate for each cell-based microstructure.

## 2.10. Swelling test of alginate films

The equilibrium swelling test was performed at 37°C in enzyme-free, and bile salt-free simulated gastric and intestinal fluids, prepared as specified in section 2.9. Before the swelling test, the alginate films were cut into 1x1 cm square pieces and dried at elevated temperature until constant weight ($w_0$). Then the dried films were immersed in either SGF or SIF. The weights of swelled films ($w_1$) were measured at predetermined time points until reaching equilibrium. The swelling ratio will be calculated as: $swelling\ ratio(\%) = \frac{w_1 - w_0}{w_0} \times 100$. The swelling kinetics experimental data were fitted to two empirical models,

namely Peleg's model [254] (Equation 4. 1), and exponential association equation model [255] (Equation 4. 2). Both models have been used to fit the swelling kinetics of polymer hydrogels [256].

$$SR(t) = \frac{t}{k_1 + k_2 t}$$

**Equation 4. 1**

where SR(t) is the swelling ratio at time t (min), $k_1$ is the kinetic constant (min*g (dry mass based)/g), and $k_2$ is the characteristic constant of the model (g (dry mass based)/g).

$$SR(t) = SR_e[1 - exp\ (-k_{R1}t)\ ]$$

**Equation 4. 2**

where $SR_e$ is the swelling ratio at equilibrium (last time point), and $k_{R1}$ is the kinetic constant ($min^{-1}$).

## 2.11. Curcumin extraction and quantification

For quantification of curcumin encapsulation yield and retention of curcumin within cell microstructures after *in vitro* digestion, curcumin was first extracted and then quantified using a UV-Vis spectrophotometer (GENESYS 10S Series, Thermo Scientific). Acidified methanol (1 mL of 1 vol.% of concentrate HCl) was used for extracting curcumin from 10 mg of native cells/ cell clusters (on a wet basis), or 1 piece of 1 cm*1 cm alginate film containing cells. Samples were then vortexed, bath sonicated for 10 min (Branson 2510, Branson Ultrasonics) and centrifuged at 12600 xg for 10 min. An aliquot of 800 µL of the supernatant was pipetted into a disposable cuvette and the absorbance at λ = 426 nm was measured. A blank was prepared from each control sample (same procedures without encapsulation of curcumin) extracted in acidified methanol. The concentration of curcumin in

extractant was calculated with reference to a regression equation (linear plot with slope of 0.1326) obtained from a calibration curve of curcumin in acidified methanol. The calibration curves were established in the concentration range of 2.5 – 15 $\mu$M. Encapsulation yield of curcumin into native yeast cells was calculated based on the following equation:

$$Encapsulation\ yield\ (\mu g/mg) = \frac{C_E}{C_Y}$$

**Equation 4. 3**

where $C_E$ is the mass (mg) of curcumin extracted from the yeast cell carriers, and $C_Y$ is the mass (mg0 of the extracted yeast cells.

The fraction of curcumin retained within the cell-based microstructures after digestion was calculated based on the following equation:

$$Fraction\ retention\ of\ curcumin = \frac{C_E(t)}{C_E(t = 0\ G)}$$

**Equation 4. 4**

where $C_E$ (t) is the mass of curcumin retained in the cell-based microstructure at a given time point during simulated digestion, and $C_E$ (t=0 G) is the mass of curcumin in the microstructure at time 0 of gastric digestion phase.

2.12. Statistical analysis

Statistical analyses were performed in R version 3.4.2. One-way ANOVA was used to evaluate the change in cell surface charge after polyelectrolyte deposition, and the change in particle size after cell clustering. A two-way ANOVA model was used to study the effect of structural complexity on the release profile of curcumin from all cell-based microstructures during *in vitro* simulated digestion. A separate set of samples was prepared for each time

point; therefore the samples across time points were considered independent. At each time point during simulated gastric and intestinal digestion, fraction retention of curcumin in the cell-based microstructures was examined as a function of cell clustering, extracellular alginate film addition, and their interaction term. In addition to the initial analysis, post hoc pairwise comparisons with Tukey's adjustment were conducted to determine any significant difference between groups. Significant values ($p<0.05$) were reported. No statistical analysis was conducted across time points.

## 3. Results

### 3.1. Layer-by-layer deposition of polyelectrolytes on yeast cells and electrostatic interaction facilitated cell clustering

Successful coating of alternating cationic and anionic polyelectrolytes on yeast cells was confirmed by ζ -potential measurements after each deposition step (measurements made at pH 3.5), as indicated in *Figure 4. 1*. Native yeast cells exhibited a slightly net negative surface charge (-2.36±0.39 mV) before coating due to the presence of amino groups, carboxyl groups, and phosphoryl groups on the cell surface [257,258]. Deposition of cationic PDADMAC onto the cell surface changed the ζ -potential to 20.2±1.11 mV. This change was attributed to the cationic ammonium group of PDADMAC. Secondary deposition of anionic DSS or ALG onto PDADMAC@yeast again reversed the surface charge to -4.01±0.91 mV and -3.88±0.21 mV, respectively, due to the sulfate groups in DSS and carboxylic acid groups in ALG. The particle size distribution of yeast cells after each coating step was evaluated based on light scattering measurements, and the volume mean diameters ($D_{4,3}$) were calculated (Table 4. 1). There was no significant increase in the volume mean diameter of yeast cells after PDADMAC coating (6.13±0.22 μm) (p-value = 0.998). This lack of

change in particle size was attributed to the steric hindrance and electrostatic repulsion among coated yeast cells, which prevented cluster formation. However, with the deposition of DSS and ALG onto PDADMAC@yeast, $D_{4,3}$ of PDADMAC/ALG@yeast and PDADMAC/DSS@yeast increased significantly to 19.62±0.44 μm and 52.67±2.96 μm respectively (p-value < 0.001), compared to ~6 μm of native and PDADMAC@yeast cells.

After layer-by-layer polyelectrolyte coating on yeast cells, one form of cell cluster architecture was formed by mixing PDADMAC@yeast and PDADMAC/ALG@yeast at a 1 to 5 (wt. to wt.) ratio in pH 3.5, 0.5% NaCl solution. This is the same physicochemical condition as in the simulated gastric fluid. This specific condition was selected for forming cell clusters to ensure that the cell clusters would not dissociate during the simulated gastric digestion due to pH change. When mixed at the selected ratio, rapid cell aggregation was observed, resulting in cell clusters (**P+P/A cluster**) with a volume mean diameter of 62.28±1.12 μm (Table 4. 1). In the case of DSS coated PDADMAC@yeast, aggregation of cells was observed upon deposition of DSS coating. Thus, these cell clusters were directly used as the second cell cluster architecture, referred to as the **P/D cluster**, for subsequent characterization. As shown in *Figure S4. 1*, native cells and cell clusters all showed unimodal distribution, while native cells had a narrower peak than both cell clusters. *Figure 4. 2* shows the 3D visualization of the two cell cluster architectures with encapsulated curcumin. The cell clusters constructed were in irregular shapes and loosely bound structures. The size of the cell clusters in the microscopic images was in the same size range as those measured using the particle size analyzer.

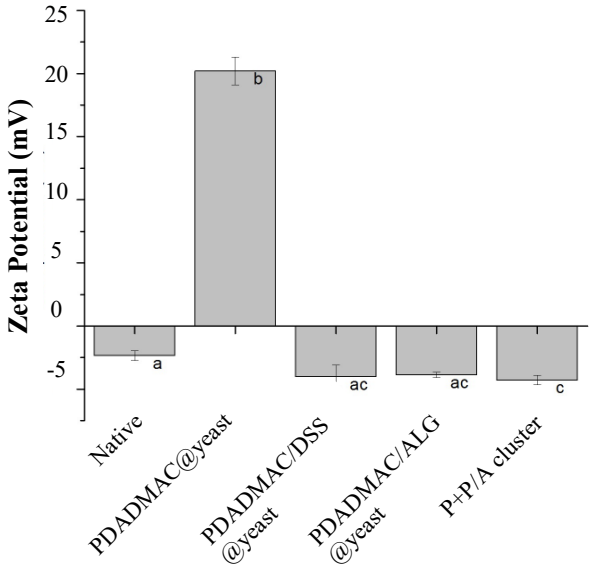


***Figure 4. 1: ζ-potential of yeast cells at different steps of layer-by-layer deposition of polyelectrolytes and cluster assembly.* 1mg/ml cells/clusters suspension in pH 3.5, 0.5% NaCl solution were used for the measurements.** The bar height and error bars represent the mean and standard deviation (n=3) of ζ-potentials. Different letters indicate significantly different values ($p<0.05$).

**Table 4. 1: Particle size of cell microstructures before and after *in vitro* digestion***

| | Particle size of different cells structures (μm) | | |
|---|---|---|---|
| | Native yeast | P/D cluster | P+P/A cluster |
| Before digestion | 5.77±0.14 $^{Aa}$ | 52.67±2.96 $^{Ba}$ | 62.28±1.12 $^{Ca}$ |
| After low bile salt digestion | 5.57±0.22 $^{Aa}$ | 51.95±0.88 $^{Ba}$ | 48.25±6.06 $^{Cb}$ |
| After high bile salt digestion | 5.50±0.35 $^{Aa}$ | 52.57±1.92 $^{Ba}$ | 45.45±1.67 $^{Cb}$ |

* Data are shown as mean±SD (n=3). Means in the same row with different superscript uppercase letters are significantly different; means in the same column with different superscript lowercase letters are significantly different.

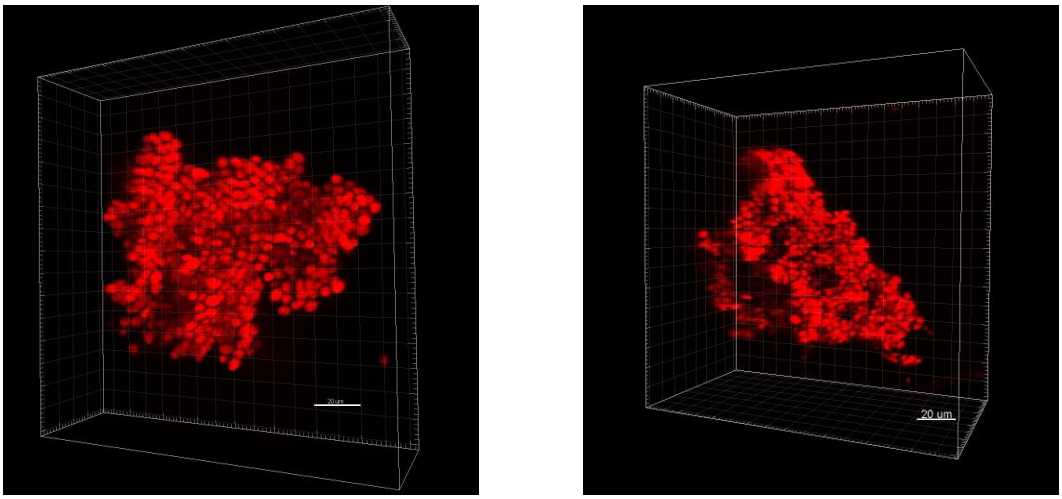


***Figure 4. 2: 3D projection of confocal microscope image of yeast cell clusters. Left: P/D cluster; right: P+P/A cluster.*** A pulsed laser tuned to 488 nm was used for excitation and emission signals were detected in the range of 498-591 nm. The images were taken using a 20X objective and the scale bar corresponds to 20 µm.

3.2. Cell clusters during *in vitro* digestion: structural stability and release of curcumin

*3.2.1. Structural stability of cell clusters*

Before investigating the release profile of encapsulated curcumin during simulated digestion, the structural stability of cell clusters in the simulated digestion fluids was evaluated. Since both the selected cell clusters, P+P/A cluster, and P/D cluster, were formed under the same set of pH and salt concentration as the SGF buffer, no significant change in the particle size of the cell clusters was observed after 2 hours of simulated SGF treatment (data not shown). During simulated small intestinal digestion, P/D clusters retained the original size of around 50 µm after the 3 hours incubation with SIF, low or high bile salt content (Table 4. 1). For the P+P/A clusters, a significant decrease in the particle size was observed after small intestinal digestion. The volume mean diameter of P+P/A clusters decreased significantly from 62.28±1.12 µm to 48.25±6.06 µm and 45.45±1.67 µm in the presence of low and high bile salt SIF respectively (p-values <

0.001 for both low and high bile salt conditions). The particle sizes of P+P/A clusters after the small intestinal phase were not significantly different between low and high bile salt conditions (p-value=0.882). The change in particle size distribution after SIF treatment is shown in *Figure S4. 1*. For the P+P/A cluster, no new peaks or significant change in the width of peaks was observed even with a reduction in the peak value after simulated digestion. In addition, the size change was observed immediately after the cell clusters were transferred to the SIF medium, while no further changes in the particle size of cell clusters were observed with extended incubation with SIF conditions.

### *3.2.2. In vitro release of encapsulated curcumin*

Retention of curcumin during the 2-hour simulated gastric digestion was expressed as the fraction of curcumin retained in cell-based microstructures at each time point during gastric digestion as compared to their original curcumin content. As shown in *Figure 4. 3*, all cell microstructures evaluated in this study retained ~80 - 95% of the initial curcumin content at the end of the 2-hour gastric phase, and no significant difference was observed between single cells and cell clusters. This result suggested that the native yeast itself as a carrier was sufficient to maintain its structural integrity and ensure the stability of curcumin under the current simulated gastric condition. Therefore, the effect of additional structural complexity on curcumin retention could not be observed during the simulated gastric digestion.

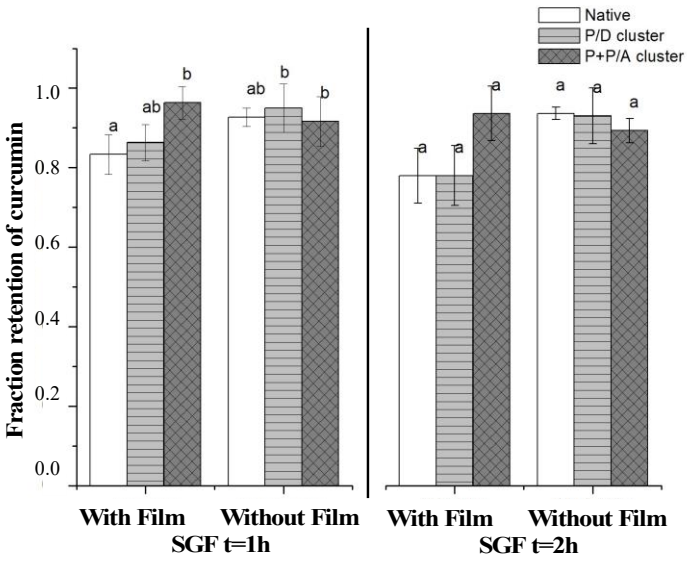


***Figure 4. 3: Effect of cluster and alginate film on the retention of curcumin after 1h and 2h simulated gastric digestion.*** *"*With/ without film" stands for the presence or absence of extracellular alginate film. Different letters in columns within the same time point indicate a significant difference in retention of curcumin among different cellular microstructures. No statistical analysis was done on measurements across time points.

All samples were then subjected to a subsequent simulated small intestinal digestion, where the release profile of curcumin in two SIF formulas with different bile salt levels was evaluated: 5 mg/mL (low bile salt) and 25 mg/mL (high bile salt). These SIF compositions with different levels of bile salt were selected based on the results of a prior study that illustrated the influence of bile salt concentration on the release rate of curcumin from yeast cells [128]. As shown in *Figure 4. 4a***,** immediately upon adding low bile salt SIF, curcumin retention decreased from ~90% after gastric digestion to 48±2% and 54±5%, respectively, for single yeast cells and P+P/A clusters without alginate film. P/D cluster was an exception in which 79±9% of curcumin was still retained. The initial release of curcumin from cell carriers and their clusters was more significant for the high bile salt SIF condition (*Figure 4. 4b*), where only 22±1%, 46±13%, and 26±5% of

curcumin was retained at time 0 in SIF, for single cells, P/D clusters, and P+P/A clusters respectively. P/D clusters had a significantly higher resistance to the initial release of curcumin than single cells and P+P/A clusters under both bile salt levels. Under low bile salt conditions, such resistance persisted for 1 hour (*Figure 4. 4a*), whereas for high bile salt conditions, the P/D clusters only showed significantly stronger resistance to curcumin release than the other two cell microstructures at t=0 (*Figure 4. 4b*). The release profile of P+P/A clusters was not significantly different from that of native yeast cells throughout the small intestinal digestion period for both bile salt conditions. It was also observed that P/D clusters were more stable than P+P/A clusters during simulated small intestinal digestion, indicated by an immediate reduction in particle size in P+P/A clusters upon addition of SIF, as shown in Table 4. 1. Such a difference might be attributed to the different ways the cells were assembled in the two types of cell clusters, which could impact the curcumin release profiles. To visualize the curcumin release process during simulated small intestinal digestion, P/D clusters and P+P/A clusters without ALG film were sampled 1 and 40 min after the addition of SIF. The samples were imaged using confocal fluorescence microscopy. *Figure 4. 5* illustrated the representative cross-section images of the two types of cell clusters during simulated small intestinal digestion. The fluorescence intensity in the microscopic images showed a trend consistent with the curcumin release data: cell clusters in high bile salt SIF retained less curcumin after 40 min, and especially under low bile salt SIF conditions, the P/D clusters retained more curcumin than P+P/A clusters up to 40 min. Moreover, the decay of curcumin fluorescence overtime did not depend on the spatial localization of cell carriers within the cluster; rather, homogeneous reduction in fluorescence intensity throughout the cluster

cross-section was observed. It implied that at least after 40 min in SIF, there was no difference in the release of curcumin from cells at different locations within the constructed cell clusters.

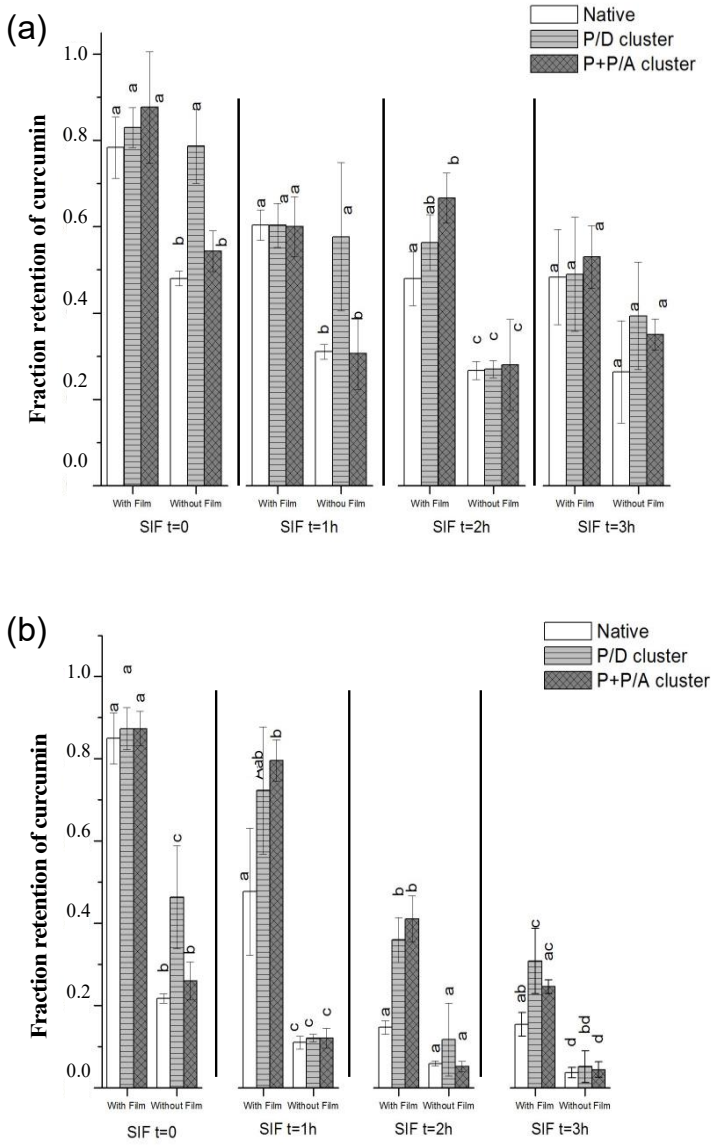


***Figure 4. 4: Effect of cluster and alginate film on the retention of curcumin during post-gastric simulated small intestinal digestion: (a) low bile salt condition; (b) high bile salt condition.*** "With/ without film" stands for the presence or absence of extracellular alginate film. Different letters in columns within the same time point indicate a significant difference in retention of curcumin among different cellular microstructures. "SIF t=0" samples were

measured after addition and immediate removal of SIF. No statistical analysis was done on measurements across time points.

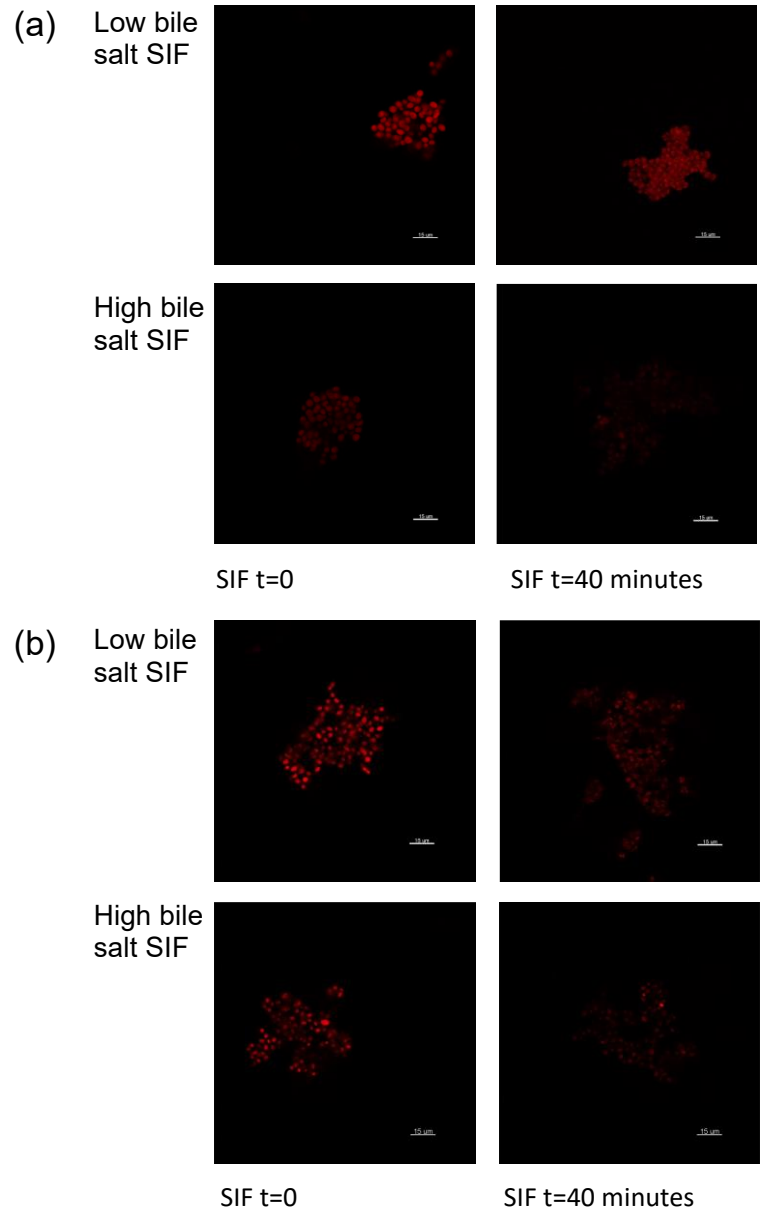


***Figure 4. 5: Cross section fluorescence microscope images of cell clusters during simulated small intestinal digestion under low and high bile salt conditions: (a) P/D cluster; (b) P+P/A cluster.*** The images were taken at t=0 and 40min. For t=0 images, SIF was added to cell clusters and immediately removed by centrifugation. The scale bar is 15μm.

3.3. Cell-laden alginate films during *in vitro* digestion: structural stability and release of curcumin

### *3.3.1. Alginate film structural stability*

To achieve a higher level of structural complexity, single cells or cell clusters containing curcumin were further encapsulated in a calcium-crosslinked alginate film. The cells or cell clusters accounted for approximately half of the dry mass of the prepared films. The loading of cells/ cell clusters in alginate film was about 2.8 mg (d.b.)/$cm^2$. The prepared alginate films containing native yeast cells and the two types of cell clusters were observed under a confocal microscope to confirm the integrity of the cell cluster structures in alginate film. The 3D projection of all three types of alginate films is shown in *Figure 4. 6*. Alginate films with cell clusters could be easily differentiated from those with native cells despite the high cell density. Native cells were uniformly distributed in the alginate film, whereas the cell clusters showed obvious aggregation and voids. Haralick features were extracted from individual slices of the z-stack image compiles (*Figure S4. 2*) to describe the image texture properties. Table S4. 1tabulates three texture features: angular second moment (ASM), contrast, and correlation. Images of alginate films with native cells, P/D clusters, and P+P/A clusters had, in this order, increasing ASM, decreasing contrast, and increasing correlation. As shown in *Figure S4. 2*, the images of cell clusters showed larger areas of background signal than that of native cells, resulting in a larger ASM value. Higher ASM values indicate a higher degree of homogeneity in the image intensity within an image. Lower contrast and higher correlation in cell cluster images translate to less local variation and a higher degree of spatial correlation of signal intensity between adjacent pixel points. All the texture features concurred with the observation from the images.

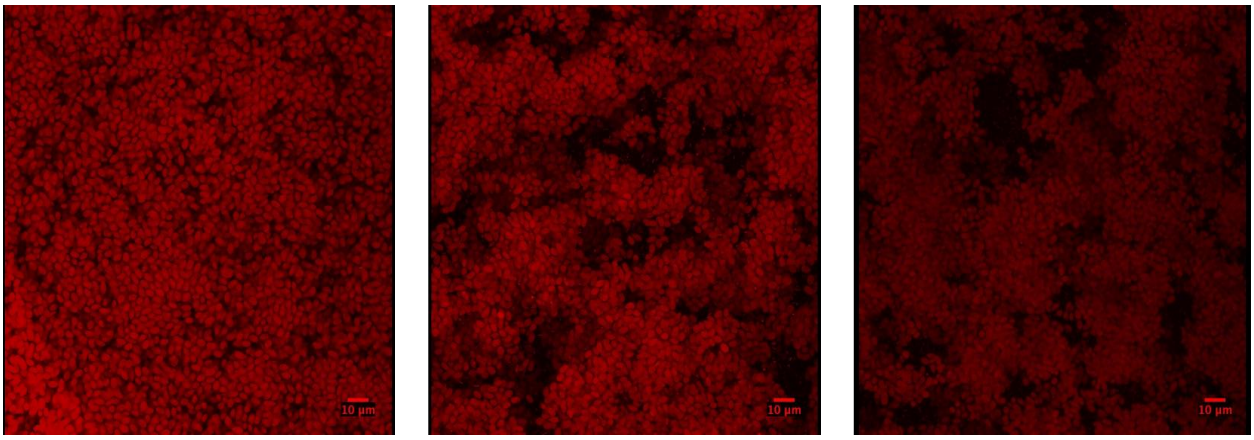


***Figure 4. 6: 3D projection of confocal microscope images of native cell (left), P/D cluster (middle), and P+P/A cluster (right) in alginate film.*** A pulsed laser tuned to 488 nm was used for excitation and emission signals were detected in the range of 498-591 nm. The images were taken using a 20X objective and the scale bar corresponds to 10 µm.

Regarding the integrity of alginate films during the simulated digestion, the film thickness was measured before and after digestion (Table 4. 2). There was no significant difference in the film thickness among alginate films containing the three different cellular structures (native vs. P/D cluster vs. P+P/A cluster). Expansion of films and a slight increase in the film thickness were observed after 5 min of initial hydration of the films in water due to swelling. After the 5-hour sequential digestion, the films remained intact, and only a slight decrease in the film thickness was recorded after small intestinal digestion.

**Table 4. 2: Change in thickness of extracellular alginate films encapsulating cells or cell clusters during *in vitro* digestion. ***

| | Native yeast | P/D cluster | P+P/A cluster |
|---|---|---|---|
| Dry crosslinked [a] | 0.07±0.01 | 0.08±0.01 | 0.09±0.01 |
| Hydrated [bc] | 0.11±0.01 | 0.11±0.02 | 0.11±0.01 |
| After gastric digestion [c] | 0.13±0.01 | 0.13±0.01 | 0.12±0.01 |
| After high bile salt intestinal digestion [ab] | 0.11±0.02 | 0.10±0.01 | 0.09±0.01 |

* Data are shown as mean±SD of triplicate experiments. Two-way mixed model ANOVA results showed that there was no significant main effect of cell structures, therefore a paired t-test was done for ALG film thickness at different stages of digestion (mean of each row), disregarding the containing cell structures. Different superscript lowercase letters indicate significant difference among row means.

To account for the effect of pH on the water absorption behavior of the films, the films were characterized for their swelling behavior in an enzyme-free SGF and an enzyme/ bile salt-free SIF. Enzymes and bile salt were excluded to eliminate the effect of potential interactions of these biochemicals with the polymeric gel and its influence on gravimetric measurements. The swelling kinetics of alginate films with individual cells and cell clusters in SGF and SIF and the model fitting results are shown in *Figure S4. 3* and Table S4. 2**.** Alginate films swelled faster and to a greater extent in enzyme-free and bile-salt-free SIF than SGF. There was no substantial difference in swelling behavior among the films embedded with different cell structures, including individual cells and cell clusters.

*3.3.2. In vitro release of curcumin from single cells and cell clusters within ALG films*

All cell microstructures, with or without the alginate film, could retain over 80% of the encapsulated curcumin in yeast during simulated gastric digestion (*Figure 4. 3*). However, upon the addition of SIF, only cell microstructures within alginate film were able to resist the initial release of encapsulated curcumin. Immediately after adding SIF, a significant amount of encapsulated curcumin was released from native cells and P+P/A clusters but not from the P/D clusters without ALG film (~ 30% released under the low bile salt condition, ~ 50% under high bile salt), (*Figure 4. 4*). The barrier effect of alginate film to curcumin release persisted throughout the 3-hour simulated small intestinal digestion under both bile salt level conditions. Under the low bile salt condition, the release profile of curcumin from single cells and P+P/A clusters were similar, where the fraction of curcumin retained in samples with alginate film was about 20-30% higher than those without alginate film for up to 2 hours. At t = 3 hours in the low bile salt condition, no significant difference was detected with and without extracellular alginate films. As shown in *Figure 4. 4a*, the release response of curcumin from the P/D cluster with and without film was not significantly different during the first hour of incubation with low bile salt SIF. The only significant difference in curcumin retention between these two groups with and without alginate films was observed after 2 hours. In *Figure 4. 4b*, under the high bile salt condition, samples with alginate film had significantly higher curcumin retention than those without alginate film at all time points for all cell microstructures. For single cells and cell clusters, the most substantial release of curcumin occurred during the first hour of small intestinal digestion. After the first hour, all three cell microstructures without alginate film retained less than 10% of curcumin. This number further decreased down to below 5% at the end of the 3-hour

small intestinal digestion period. With the barrier effect of alginate film, the final curcumin retained in single cells, P/D cluster, and P+P/A cluster was at the level of 14±3%, 28±5%, and 22±4%, respectively.

Table S4. 3 summarized the ANOVA model for curcumin retention associated with the two key variables: cell clustering and ECM (alginate film). There was a significant interaction effect between these two factors for all the time points in high bile salt SIF and the first hour for the low bile salt SIF. The interacting effect illustrates the impact of cell clustering on curcumin retention was dependent on the presence of the extracellular alginate film, as shown in *Figure 4. 4*. In high bile salt SIF (*Figure 4. 4b*), a significant effect of cell clustering on curcumin retention was only observed when the cell microstructures were encapsulated in alginate films. In low bile salt SIF, when no alginate film was present, P/D clusters showed higher curcumin retention in the first hour, but after the introduction of the film, the retention of curcumin in cells and P+P/A clusters was increased to the same level as P/D clusters (*Figure 4. 4a*).

## 4. Discussion

### 4.1. LbL deposition of polyelectrolytes on the cell surface and cell clustering

Electrostatic aggregation of colloidal particles and cells has been used to create micro-scale assemblies with unique properties [150–152,157,158]. For example, controlled electrostatic assembly of metal nanoparticles was used for generating capsules and films for material science and nanomedicine applications [151]. To the best of our knowledge, micron-scale, cell-

based bioactive delivery systems formed by electrostatic clustering have not been evaluated for their performance during simulated digestion. The current study used layer-by-layer deposition of oppositely charged polyelectrolytes to assemble yeast cells to form cell clusters. PDADMAC@yeast and native yeast cells had a similar particle size distribution, but deposition of negatively charged ALG and DSS onto PDADMAC@yeast produced cell clusters of different sizes, although they had similar net surface charge. Similar droplet aggregation was reported in previous studies where medium molecular weight chitosan (Mw 190 -310 kDa) were deposited onto the negatively charged interface of a primary emulsion [259,260]. The difference in clustering behavior of yeast cells with the addition of an anionic coating layer can be attributed to the following factors: (1) Compared with ALG, DSS has a higher charge density (charge per monomer), and thus more strongly associated with PDADMAC. According to the product specification provided by the manufacturer, DSS used in the current study had approximately 2.3 sulfate groups per glucosyl unit. In contrast, ALG has one carboxyl group per monosaccharide unit. (2) With a smaller molecular weight, DSS was added at a higher molar concentration than ALG, which may result in more clustering among PDADMAC@yeast cells. (3) The positively charged quaternary ammonium group in PDADMAC has a stronger interaction with the sulfate groups in DSS than with the carboxyl groups in ALG [261]. As a result of the different clustering behavior of DSS and ALG, two different types of cell clusters were generated. P/D clusters were harvested directly after adding DSS to PDADMAC@yeast, while P+P/A clusters were formed by mixing a positively charged PDADMAC@yeast and a negatively charged PDADMAC/ALG@yeast at a ratio of 1:5, which resulted in the largest cell clusters. Due to the different preparation steps, P/D clusters and P+P/A clusters essentially differ in their aggregation mechanisms.

P/D clusters were held together by DSS acting as crosslinkers among large PDADMAC polymers that coated yeast cells. In contrast, P+P/A clusters were formed by electrostatic attraction between oppositely charged cells. Such different clustering mechanisms translated to significantly different cluster sizes (Table 4. 1) and potentially different cellular arrangements within a cluster.

## 4.2. Structural stability of cell clusters and cell-laden alginate films during simulated digestion

A significant size reduction in cell clusters was observed during small intestinal digestion for the P+P/A cluster but not for the P/D cluster. It was hypothesized that the change in pH and salt content in the fluid caused the change in cluster size. Given that the pH of SIF (7.5) is higher than pKa of both DSS and ALG, and the quaternary ammonium cation in PADMAC is independent of pH, the surface charges of all cell types should hold during this pH transition. The high salt content in SIF, on the other hand, would have a significant impact on the effective surface charge of the oppositely charged cells. Especially the divalent calcium ions in SIF will have a more substantial charge screening effect on charged yeast cells, leading to mitigated electrostatic interactions. As discussed earlier, DSS could have a more robust interaction with PDADMAC and it was present at a higher molar concentration. Thus, the DSS facilitated crosslinking in P/D clusters could be potentially less affected by the screening effect, accounting for the higher stability of P/D clusters than P+P/A clusters.

The cell-laden alginate films were overall stable after 5 hours of simulated digestion without significant mass loss or fragmentation. In our preliminary experiments, alginate films without calcium crosslinking would dissolve after 30 min of incubation in water. Thus, the presence of calcium ions in the alginate film was critical for maintaining the film integrity

throughout the simulated digestion. A slight decrease in the film thickness was observed after 3 hours of simulated small intestinal digestion (measured using a caliper, data not reported). This decrease could be explained by the gradual release of calcium ions from crosslinked alginate film in the presence of bile salt in the intestinal fluid. Bile could bind with the calcium ions that diffused out from the alginate films and formed a white precipitate, which was observed during small intestinal digestion, especially with high bile salt levels. No bile salts were present in the gastric phase. Thus, neither white precipitate nor decrease of film thickness was observed after the gastric digestion. Losing calcium makes the alginate network less rigid, and the film could start dissolving into the water from the surface, corresponding to the decrease in film thickness. Regardless, the alginate films could still retain their shape and integrity throughout the 3-hour small intestinal digestion period.

### 4.3. *In vitro* release of curcumin from different cell-based structures during simulated digestion

Bioaccessibility of curcumin is significantly limited by its poor solubility, and various encapsulation methods have been developed to address this limitation, mostly using nanoparticles [262,263] or nano-emulsions [264]. Different factors such as droplet size, type of oil/emulsifier, etc., could all affect the stability and bioaccessibility of curcumin in such encapsulation systems, which has been reviewed elsewhere [265]. However, to the authors' best knowledge, there are no prior studies addressing the effect of food matrix microstructure on curcumin bioaccessibility, except one that reported increased curcumin accessibility during simulated digestion in the presence of excipient emulsions, which mimicked a simplified food matrix effect [266]. This previous study essentially was still addressing the solubility issue of curcumin without further considering the role of food microstructures in controlling the

release of curcumin. Among the very few studies that focus on the relationship between the structural complexity of plant tissues and the release of phytochemicals during digestion, Palmero et al. [24] evaluated the effect of natural structural barriers on carotenoids bioaccessibility in carrots. In this previous study, carrot tissues were broken down into fractions with different levels of structural complexity, from cell clusters to chromoplast, then to carotenoid enriched oil. An increase in bioaccessibility was observed with removing structural barriers in the carrot tissues [252]. Although this previous study also considered the effect of structural complexity on bioactive release, with a top-down approach, it is impossible to decouple the effects of physical cell aggregation from the extracellular matrix. To the best of our knowledge, the current study is the first one that used a bottom-up approach to investigate the relationship between structural complexity and bioactive bioaccessibility in cell-based structures.

Approximately10% of curcumin release was observed after 2 hours of *in vitro* gastric digestion (*Figure 4. 3*). This result agrees with the limited literature data about curcumin release from yeast cells [110,128]. Since no obvious rupture of cell wall and membrane or cell burst was observed after *in vitro* gastric digestion according to microscopic images [128], the release of curcumin during digestion was attributed to passive partitioning of curcumin from cells to the digestion fluid. With a log P value of 3.29, curcumin is a hydrophobic compound with very low water solubility (0.6 μg/mL) [267]. In the absence of emulsifiers or surfactants such as bile salts, limited release of curcumin in the gastric environment was observed [110]. These results also suggest that the guest-host interaction of curcumin with cellular components of yeast cells has high avidity resulting in a limited release of curcumin [238].

Cell-based carriers after gastric digestion were treated with SIF to simulate the gastrointestinal digestion process. Upon the addition of SIF, immediate release of curcumin from single yeast cells was observed. The extent of curcumin release from these cells was a function of the bile salt level in the fluid (*Figure 4. 4*). Bile salts are physiological surfactants that enhance fat digestion and the absorption of hydrophobic compounds [268]. Due to their amphiphilic nature, bile salts can self-associate to form micelles in water, and the presence of these micelles in the aqueous phase can influence the partitioning properties of curcumin between yeast microcarriers and the aqueous phase. Therefore, the SIF was likely to have a higher solubilizing capacity of curcumin then SGF. Less than 30% and 5% of curcumin were retained inside single yeast cells at the end of the 3-hour intestinal digestion under low and high bile salt conditions, respectively. This trend supports the hypothesis that bile salt micelles in the SIF can shift the partitioning equilibrium of curcumin between yeast cells and the aqueous phase. Another possible explanation for the observed release of curcumin during SIF treatment is the change in cellular composition, such as changes in cell membrane composition due to the extraction of phospholipids by bile salts. These changes may influence the binding interaction between curcumin and cellular structures.

Based on the results shown in *Figure 4. 4*, during *in vitro* digestion, the cell clustering effect on impeding the release of curcumin was limited to the early stage of small intestinal digestion. The most significant difference between single cells and cell clusters was within the first hour of SIF incubation (low bile salt) or at the stage of the initial release of curcumin immediately after adding the SIF (high bile salt). Despite the formation of cell clusters by electrostatic interaction, after this initial stage, the release of curcumin during simulated small intestinal digestion was not only limited to the outer cells in the clusters but rather a

uniform release throughout the cluster. This is supported by the homogeneous reduction in fluorescence intensity of curcumin across the cell cluster during digestion (*Figure 4. 5*). These results suggest that the electrostatic clustering of cells in the size range of 50 microns could not necessarily limit the interaction of bile salts in SIF with the cells in the cluster for an extended time. This trend contrasts with the results reported in previous studies. It was shown that for cut almond seed cubes, digestion of intracellular nutrients first happened in the surface cells with the ruptured cell walls, and gradually extended to the inner intact cells over a period of 12 hours [269]. Palmero et al. [24] also reported that the bioaccessibility of β-carotene in orange carrots was lower in large cell clusters (800 - 2000 μm) than in small cell clusters (40 - 250 μm). However, unlike the plant tissue fragments, the cell clusters constructed in the current study would not be considered as rigid matrices, based on their way of assembly, irregular shape, and porous structure. Also, they were much smaller in size than those reported by Palmero et al. [24] Moreover, the cell clusters in the previous studies were a result of physically breaking down wholesome plant tissues, thus including the combined effect of cell clustering and associated extracellular matrix. Thermal treatment has been reported solubilize the cell wall pectin that binds the cells together, leading to softening of the tissue, cell separation, and increase in the porosity of cell walls, so that the digestive enzymes may work more efficiently [26,27] and results in higher bioaccessibility of compounds such as $\beta$-carotene [26,28,29]. The cell clusters constructed in the current study had a loose and porous structure that could not impede the diffusion of digestive enzymes or bile salts into the structure.

Upon the addition of the crosslinked extracellular alginate film, the cell microstructure matrices became less porous and more rigid. The hydrated alginate film enclosing single cells

or cell clusters was a highly crosslinked hydrogel that could limit permeation of acid, enzymes, and bile salts, potentially converting the curcumin release from the "bulk erosion" mode to the "surface erosion" mode [270]. The diffusion coefficient of protons in polysaccharide hydrogels is not expected to differ from that in water [271]. However, the depletion of protons due to protonation of D-mannuronate and L-guluronate residues of alginate could still limit acid permeation into the hydrogel. Such a hypothesis is supported by the observations reported in several probiotic *in vitro* survival studies where polysaccharide gels such as alginate significantly increased the survival rate of probiotics in an acidic environment [272,273]. The same studies also showed that polysaccharide hydrogels significantly increased the survival rate of probiotics exposed to bile salt solutions. Bile salt depletion was hypothetically attributed to the binding of bile salt to alginate polymers [274] and precipitation at the presence of calcium ions [275], which were gradually released from the crosslinked alginate films during digestion. Further research is needed to investigate the contribution of these two factors to the bile salt availability throughout the digestion process. Moreover, the mutual diffusion coefficients of enzymes in polysaccharide hydrogels were around 0.2 - 0.4 of their self-diffusion coefficients in solution [33]. All these factors contributed to the barrier effect of the alginate film in slowing down the release of curcumin during simulated digestion.

## 5. Conclusion

In this work, cell-based, tissue-like microstructures were constructed using a novel bottom-up approach to study the effect of cell clustering and the role of extracellular matrix on bioaccessibility of a model bioactive compound – curcumin during *in vitro* digestion. Less than 20% of curcumin was released during the gastric phase for all cell-based microstructures and the

major difference in their release profiles were observed during the intestinal phase. P/D clusters, formed by crosslinking PDADMAC-coated yeast cells with DSS, had higher physical stability throughout the simulated gastrointestinal digestion process, and showed significant increase in curcumin retention at the onset of the small intestinal digestion phase. Such resistance to release persisted for up to one hour in SIF with low bile salt concentration but disappeared immediately under high bile salt condition. Cell clustering also did not result in any spatial difference in curcumin release, as indicated in the fluorescence microscopic images. Addition of extracellular alginate film to both single cells and cell clusters further slowed down the release of curcumin. The retention of curcumin in cell microstructures with the alginate film was significantly higher than the corresponding cell microstructures without the film for up to 2 hours under low bile salt condition and up to 3 hours under the high bile salt condition. The extracellular alginate film had a more dominating and prolonged effect on modifying the release profile of encapsulated curcumin during simulated digestion compared to cell clustering. The bottom-up approach used in this work successfully decoupled the effect of chemical composition and microstructural properties of food matrices on bioaccessibility of micronutrients. It is a versatile approach that can provide insights into the structure-bioaccessibility relationship between various micronutrients and natural or functional foods.

## 6. Acknowledgement

This work was funded by a grant from the USDA-NIFA grant no. 2018-67017-27563. The fluorescence microscopic images were taken at the UC Davis Veterinary Medicine Advanced Imaging Facility.

## Supplements

**Table S4. 1: Haralick features extracted from confocal microscopic images of single cell or cell cluster-laden alginate films: angular second moment (ASM), contrast, and correlation.**

| Cell microstructures | ASM | Contrast | Correlation |
|---|---|---|---|
| Native | 0.31±0.03[a] | 24402.92±1775.47[a] | 0.19±0.03[a] |
| P/D cluster | 0.37±0.01[a] | 17761.47±780.76[b] | 0.37±0.02[b] |
| P+P/A cluster | 0.53±0.06[b] | 11511.34±1877.12[c] | 0.47±0.03[c] |

* Data are shown as mean±SD of n=5 images. One-way ANOVA model results showed significant main effect of cell microstructures for all three features. Different superscript lowercase letters indicate significant difference among films with different cell microstructures ($p<0.05$).

**Table S4. 2: Estimated parameters of the empirical swelling kinetics models for single cell or cell cluster-laden alginate films in enzyme-free, bile salt-free SGF and SIF.**

| | | Peppa's model | | | Peleg's model | | | Exponential association equation model | |
|---|---|---|---|---|---|---|---|---|---|
| Condition | Cell microstructures | k | n | $R^2$ | $k_1$ | $k_2$ | RMSE | $k_{R1}$ | RMSE |
| Enzyme-free SGF | Native | 0.38 | 0.15 | 0.81 | 5.00 | 0.36 | 0.21 | 0.05 | 0.43 |
| | P/D cluster | 0.41 | 0.15 | 0.77 | 4.35 | 0.33 | 0.26 | 0.04 | 0.41 |
| | P+P/A cluster | 0.40 | 0.15 | 0.78 | 4.35 | 0.30 | 0.24 | 0.04 | 0.47 |
| Enzyme, bile salt-free SIF | Native | 0.22 | 0.23 | 0.91 | 6.31 | 0.20 | 0.57 | 0.02 | 1.31 |
| | P/D cluster | 0.30 | 0.19 | 0.84 | 4.40 | 0.21 | 0.44 | 0.02 | 0.97 |
| | P+P/A cluster | 0.34 | 0.17 | 0.78 | 3.80 | 0.22 | 0.45 | 0.03 | 0.82 |

**Table S4. 3: Statistical summary of the two-way ANOVA model for the fraction retention of curcumin association with cell clustering and ECM for each time point during *in vitro* gastric and small intestinal digestion. ***

| Sources of variance | p-value for curcumin retention fraction in: | | | | | | | | | |
|---|---|---|---|---|---|---|---|---|---|---|
| | SGF | | High bile salt SIF | | | | Low bile salt SIF | | | |
| | 1 hour | 2 hours | 0 hour | 1 hour | 2 hours | 3 hours | 0 hour | 1 hour | 2 hours | 3 hours |

| | | | | | | | | | | |
|---|---|---|---|---|---|---|---|---|---|---|
| Cell clustering | 1.71 e-02 | 1.88 e-01 | 1.05 e-02 | 2.30 e-02 | 6.41 e-04 | 1.04 e-02 | 5.31 e-03 | 2.95 e-02 | 5.05 e-02 | 4.60 e-01 |
| ECM | 1.21 e-02 | 8.65 e-03 | 5.59 e-10 | 2.90 e-08 | 3.96e-07 | 2.70 e-07 | 3.34 e-05 | 3.24 e-04 | 3.16 e-07 | 5.77 e-03 |
| Cell clustering*ECM | 1.29 e-01 | 2.04 e-02 | 2.29 e-02 | 3.36 e-02 | 1.64e-03 | 3.11 e-02 | 1.07 e-02 | 3.15 e-02 | 9.42 e-02 | 5.96 e-01 |

***** SGF = simulated gastric fluid, SIF = simulated intestinal fluid. The sources of variance in this model are effects from cell clustering and ECM, as well as their interaction effect. Shaded table cells are significant values ($p<0.05$).

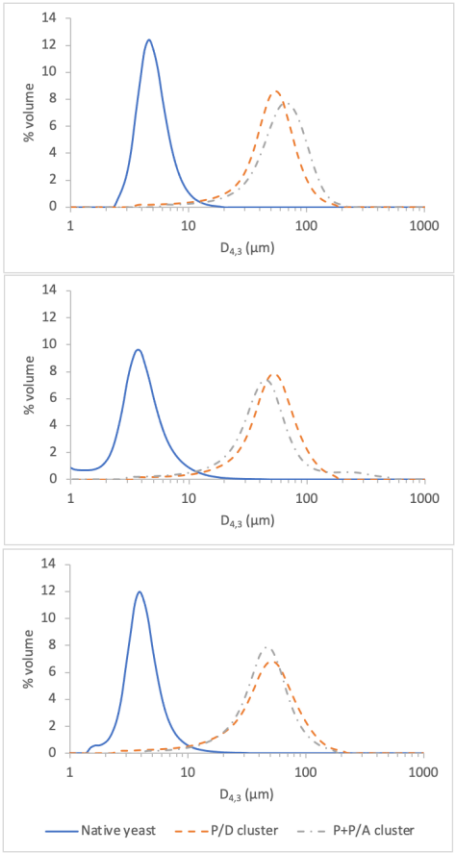


| | Native | P+P/A cluster | P/D cluster |
|---|---|---|---|
| Percentile | Before digestion | | |
| 10 | 3.32 | 28.54 | 23.04 |
| 50 | 4.64 | 60.14 | 49.40 |
| 90 | 7.13 | 102.2 | 82.37 |
| Percentile | After low bile salt digestion | | |
| 10 | 2.14 | 18.03 | 21.47 |
| 50 | 3.66 | 41.53 | 48.09 |
| 90 | 6.59 | 90.18 | 85.38 |
| Percentile | After high bile salt digestion | | |
| 10 | 19.64 | 17.73 | 17.25 |
| 50 | 43.18 | 40.47 | 46.20 |
| 90 | 77.00 | 71.26 | 88.03 |

***Figure S4. 1: Particle size distribution of native yeast, P/D cluster, and P+P/A cluster before digestion (a), after low bile salt digestion (b), and after high bile salt digestion (c)***. The 10$^{th}$, 50$^{th}$, and 90$^{th}$ percentile particle diameter for each plotted distribution is summarized in the table.

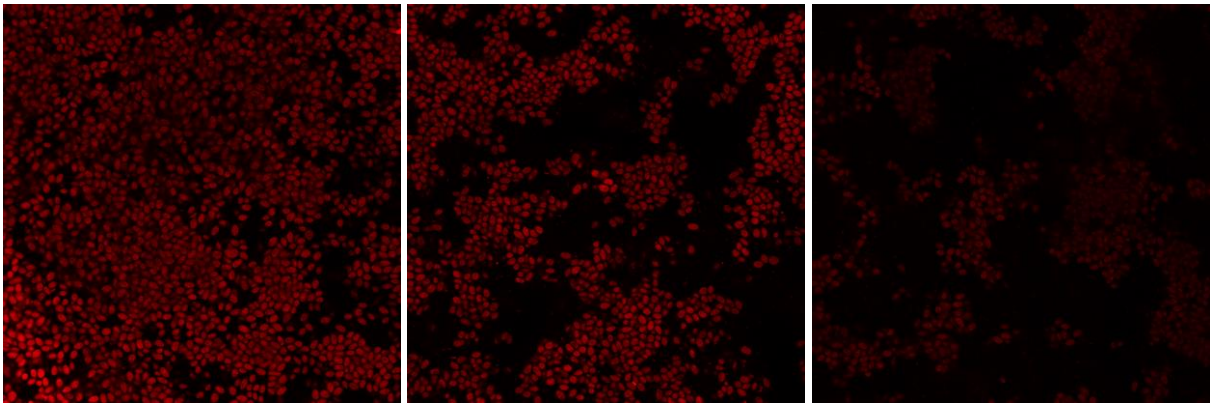

***Figure S4. 2: Individual slice in the z stack confocal microscope images of native cell (left), P/D cluster (middle), and P+P/A cluster (right) in alginate film.*** Figure 6 showed the 3D projection of the same z stack for each cell microstructure. A pulsed laser tuned to 488 nm was used for excitation and emission signals were detected in the range of 498-591 nm. The images were taken using a 20X objective.

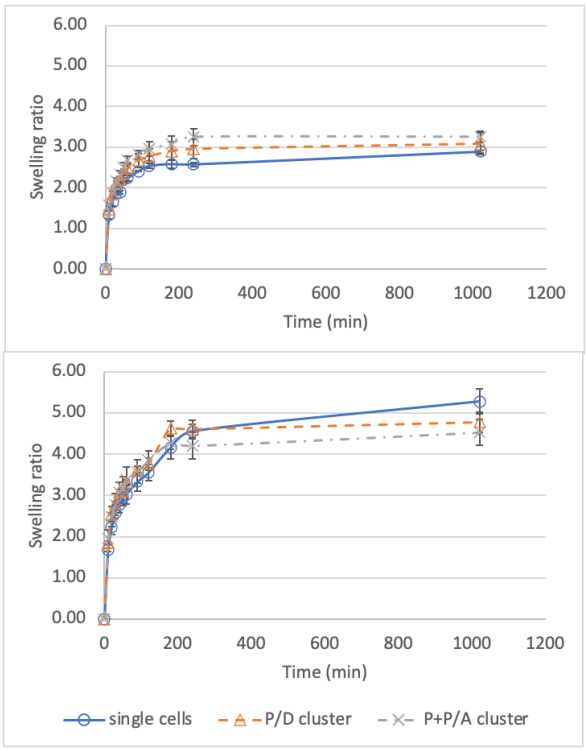


***Figure S4. 3: Swelling kinetics of single cell or cell cluster-laden alginate films in enzyme-free SGF (a) and enzyme-free, bile salt-free SIF (b).***

# CHAPTER 5

# Filamentous fungal pellet as a novel and sustainable encapsulation matrix for exogeneous bioactive compounds

## 1. Introduction

Encapsulation is a widely used process in developing food ingredient formulations to improve the stability and controlled release of vital ingredients, including antioxidants, vitamins, bioactive peptides, flavors, and aromas etc. [67–69] It often requires isolation and extraction of ingredients from food systems, as well as high energy processing technologies to generate colloidal particles with sub-micron to sub-millimeter scale sizes so that they can be incorporated in food formulations to achieve their functionality. Moreover, many of these encapsulation systems require addition of exogenous preservatives to maintain the stability of encapsulated ingredients. Cell based micro-carriers such as yeast cells has emerged as a sustainable encapsulation approach. The micro-scale sized yeast cells can be utilized as natural encapsulant without extensive fabrication, eliminating the need for extraction and purification of ingredients, and reducing the energy input required to construct the colloidal delivery systems. Furthermore, many previous studies have reported that the yeast cells could enhance the oxidative and thermal stability [103,110,111] of the encapsulated molecules during storage compared to colloidal carriers such as emulsions.

In addition to developing sustainable encapsulation systems using GRAS ingredients, there is also a need to improve the understanding of the role of chemical composition and microstructure of these ingredient formulations in influencing the release and bioaccessibility of the encapsulated bioactive compounds. Such an understanding can also contribute to our knowledge

of food matrix effect on the bioaccessibility of micronutrients [40,64,266], i.e. a chemical compound could behave differently in a free form than as a part of the food [15], due to range of chemical and physical interactions with the food matrix. The release of bioactive compounds from single yeast cells during *in vitro* digestion has been evaluated for various compounds, such as curcumin [128], resveratrol [134], etc. However, the single-cell encapsulation system lacks the complexity of natural foods, e.g., plants and vegetables, if considered as a model system to evaluate the food matrix effect on bioaccessibility of encapsulated compounds. To investigate the complex food matrix-micronutrient interactions during digestion, it is necessary to go beyond the current cell-based encapsulation systems by incorporating higher level structural features. Most of the current studies investigating the food matrix effect took the approach of applying different processing techniques on food products and evaluating their impact on bioaccessibility of the compounds of interest [62,64,65,243]. Such an approach often has limited success in decoupling the influences from chemical compositions and microstructures, since in many cases more than one chemical or structural feature of the food matrix would be modified with a single processing treatment. To evaluate the impact of microstructures on the release of bioactive compounds while controlling for chemical compositions, our previous study engineered a 3D assembly of yeast cell-based micro-carriers and compared the release profile of the bioactive compound from such assemblies to that from single cells [210] during the simulated sequential digestion, i.e., combining both the gastric and intestinal digestion phases. The results revealed that although the cell clustering was able to modify the release kinetics of the compound during digestion, its effect was limited to short term. Moreover, the approach developed in this previous study required significant modifications of yeast cells with biopolymers to enable the formation of a multicellular encapsulation system. Thus, there is a need for a scalable approach to develop sustainable

multicellular encapsulation systems without significant modifications for diverse applications in food systems.

In this study we developed a natural multicellular encapsulation system using filamentous fungal pellet to address the need for enhancing the sustainability of food ingredient technologies and to investigate the structural/matrix effect of cell-based encapsulation systems on the bioaccessibility of micronutrients. Filamentous fungus (FF) can grow on a variety of substrates [139–141], including food processing by-products and wastes, making the fungal biomass an affordable and sustainable material with low water and carbon footprints [142]. During submerged fermentation of FF, distinct fungal morphologies could be observed based on the selected fungal microorganisms and culturing conditions[135]. Fungal pellet is a dense, spherical aggregate of intertwining fungal hyphae that could be spontaneously formed by several FF species [136], such as *Aspergillus spp.*, *Penicillium spp.* etc. [137,138], under submerged, shaking culture conditions. Fungal pellets have been used as a supporting biomaterial for immobilization of other microorganisms. For example, immobilization of yeast for winemaking [276], of microalgae and bacteria for wastewater treatment [277,278] and biofuel production [279,280], etc. Recently, FF *Aspergillus oryzae* has been shown to be a good supporting material for growth of both yeast and animal cells [281]. The co-attachment of *Saccharomyces cerevisiae* and the FF *Penicillium chrysogenum* has been well-studied as a yeast biocapsule system, especially for the applications of alcoholic fermentation, such as production of wine, beer, and bioethanol [282–285]. Fungal pellet and yeast-FF biocapsule served as good multicellular model systems to study the matrix effect of these encapsulation systems on the release of encapsulated bioactives.

The two major objectives of the study were to (1) evaluate FF biomass as a natural multi-cellular encapsulation system for exogenous bioactive compounds; (2) investigate the matrix

effect endowed by the natural structure of the multicellular fungal pellet on the bioaccessibility of the encapsulated bioactive compound, and elucidate the underlying mechanisms of this matrix effect. In the current study, *Saccharomyces cerevisiae* G1 strain was chosen as the model single-cell encapsulant because of its established ability to be immobilized onto fungal pellet formed by *P. chrysogenum* H3 [286]. Two multicellular encapsulation systems: the fungal pellet itself and yeast cells immobilized in the fungal pellet were evaluated for their loading capacity of a model bioactive - curcumin during encapsulation and release during *in vitro* digestion. These results of multicellular encapsulation system were compared to the single-cell system using the *S. cerevisiae* G1 cells as the microcarriers. The FF biomass has been identified as a good source of alternative protein since it can meet the basic nutritional requirements [287]. The method used in the current study provided a cost-effective way to encapsulate exogeneous bioactive compounds into the FF biomass, which further enhance its nutritional values. Moreover, with a better understanding on the complex matrix-micronutrient interaction within this natural multicellular system, we can further potentiate FF biomass as a functional food material.

## 2. Materials and methods

### 2.1. Materials

Curcumin derived from *Curcuma longa* (turmeric) [≥ 65%, HPLC], methanol, bile salts (cholic acid- deoxycholic acid sodium salt mixture), calcium chloride, potassium phosphate monobasic, ammonium phosphate, Calcofluor white, and Nile red were purchased from Sigma-Aldrich (St. Louis, MO). Sodium hydroxide, hydrochloric acid, sodium chloride, potassium chloride, magnesium chloride, sodium phosphate monobasic, yeast extract, peptone, and dextrose anhydrous were purchased from Fisher Scientific (Pittsburgh, PA). Absolute ethanol was purchased from Koptec (King of Prussia, PA). Corn meal agar was

purchased from Neogene (Santa Clara, CA). Yeast nitrogen base without amino acids was purchased from BD (Franklin Lakes, NJ). D-Gluconic acid, 50% aqueous solution was purchased from Spectrum Chemicals (New Brunswick, NJ). The enzymes pepsin from porcine gastric mucosa (1064 units/mg protein) and pancreatin from porcine pancreas (4x USP) were purchased from Sigma-Aldrich (St. Louis, MO).

2.2. Microorganisms and growth media

*Saccharomyces cerevisiae* G1 *(MYA-2451)* and the filamentous fungus strain *Penicillium chrysogenum* H3 (UCDFST 22-448) were provided by the Department of Microbiology, University of Cordoba, Spain, and were used in this work as the single-cell and multicellular encapsulation model systems. *S. cerevisiae* G1 was grown in YPD broth (1 wt./vol.% yeast extract, 2 wt./vol.% peptone, and 2 wt./vol.% glucose) in shaking flasks at 28 °C, 175 rpm for 3 days. The G1 yeast cells were harvested by centrifuging the cell culture at 2711 xg for 5 min, then the precipitated cell pellet was washed once with Milli-Q water, lyophilized, and stored at room temperature until used. Fungal pellets were formed by growing the filamentous fungus strain *P. chrysogenum* H3 using the protocol developed by Moreno-Garacía et al.[286]. Briefly, the fungus was pre-grown in a sporulation medium containing 1.7 wt./vol.% corn meal agar, 0.1 wt./vol.% yeast extract, 0.2 wt./vol.% glucose and 2 wt./vol.% agar for 7 days at 28 °C. Yeast nitrogen base medium without amino acids, containing 0.5 wt./vol.% gluconic acid as a carbon source and buffered to pH 7 with $Na_2HPO_4$ and $KH_2HPO_4$, was used as the growth medium for fungal pellet formation. 50 mL of the medium in a 250 mL flask was inoculated with $4*10^6$ *P. chrysogenum* H3 spores and shaken at 28 °C, 175 rpm for 6 days. Under such a condition, spherical fungal pellets with diameters

of approx. 5 - 8 mm were formed. The harvested fungal pellets were washed in Milli-Q water, lyophilized, and stored at room temperature until used.

### 2.3. Vacuum-facilitated infusion of curcumin in single-cell and multicellular encapsulation systems

Three encapsulation systems were developed in the current study for curcumin, the model compound: the single-cell system using *S. cerevisiae* G1 yeast cells as the carriers (YE-c), the multicellular system using fungal pellet as the encapsulation matrices (FP-c), and the combination of these two systems (YE/FP-c). For YE-c and FP-c, curcumin was infused into the G1 yeast cells as described in CHAPTER 4. Briefly, before encapsulation, the freeze-dried, heat inactivated G1 yeast cells were rehydrated and ~ 1 g was weighed into a 50 mL centrifuge tube. 3.25 mL of milli-Q water, 1.5 mL of absolute ethanol, and 250 μL of 2.5 mg/mL curcumin in absolute ethanol were added to give a 35% ethanol concentration, and 0.0625 wt.% curcumin to yeast ratio (wet basis). For FP-c, ~20 mg of freeze-dried H3 fungal pellets were added to the same curcumin ethanolic solution. The samples were subjected to 99% vacuum with a hold time for 5 seconds. After vacuum infusion, the YE-c samples were centrifuged at 2711 xg for 5 min, and the supernatant was decanted. The pelleted cells were then washed 4 times in 5 mL of milli-Q water and centrifuged once more to remove excess water. The FP-c samples were separated from the curcumin solution and stirred in milli-Q water for 5 min, then blotted dry to remove excess water. To prepare YE/FP-c, YE-c and H3 fungal pellets were mixed at dry mass ratio of 3:1 in water, then subjected to the same vacuum treatment and washing protocol as FP-c samples. A pending patent [application number: 64/411,843] has shown that yeast cells could be efficiently immobilized in fungal biomass using this vacuum procedure. To quantify the encapsulation yield, curcumin was

extracted from the encapsulation systems using pure DMSO and measured for absorbance at 434 nm with a UV-Vis spectrophotometer (GENESYS 10S Series, Thermo Scientific) after proper dilution. The concentration of curcumin in extractant was calculated with reference to a calibration curve. Encapsulation yield was calculated as the amount of curcumin per unit dry mass of the encapsulation matrices.

## 2.4. Microscopic imaging of the multicellular encapsulation systems

### *2.4.1. Scanning electron microscopy*

To analyze the microstructure of fungal pellets, the outer and inner surface of the pellets were imaged using a Thermo Fisher Quattro S Environmental scanning electron microscope (Thermo Scientific, Rochester, NY, USA) in high vacuum mode using 5 kV accelerating voltage to capture pellets before a brief increase to 15 kV for imaging. Prior to imaging, fungal pellets with or without immobilized G1 yeast cells were freeze-dried and gold-sputter-coated. To observe the inner area of the fungal pellets, pellets were cut in half with a scalpel.

### *2.4.2. Fluorescence microscopic imaging*

Fungal pellets were sliced and stained with fluorescent dyes before imaging. To facilitate slicing, each fungal pellet was submerged in 1.5% warm agarose and cooled until solid. The piece of agarose containing the fungal pellet was cut out and mounted on the slicing platform of an oscillating tissue slicer (OTS-4500, Electron Microscopy Sciences, Hatfield, PA, USA). 250 $\mu m$ thick specimens were obtained and transferred to glass slides. Calcofluor white (CFW) and Nile red (NR) were used to stain the cell wall and intracellular lipid of the fungal hyphae cells respectively. ~ 300 $\mu L$ of CFW (10 $\mu g/mL$) and NR (5 $\mu g/mL$) solution were deposited on the fungal pellet specimen and

incubated for 15 min before rinsing with water. A Leica TCS SP8 Multiphoton microscope (Leica Microsystem Inc.) equipped with a Mai Tai DeepSee laser was used to image the specimens. A 710 nm laser excitation wavelength and 426 - 506 nm emission filter were used to collect signals from CFW; 925 nm excitation and 592 - 644 nm emission filter were used for NR.

The autofluorescence of curcumin was utilized to visualize the encapsulated curcumin in the encapsulation matrices. Due to the significant signal overlap between CFW and curcumin, Congo red (1 mg/mL) was used to stain the cell wall instead [288]. The excitation and emission wavelengths for curcumin were set to 760 nm, 475 - 575 nm; and those for Congo red were set to 910 nm, 592 - 644 nm.

## 2.5. Release of curcumin from the encapsulation systems during *in vitro* digestion

### *2.5.1. Release kinetics*

Simulated gastric and intestinal fluid were prepared according to the protocol developed by Minekus et al. [219] with some modifications. When preparing the electrolyte stock solutions for the digestion fluids, $NaHCO_3$ was replaced with equal molarity of NaCl and $(NH_4)_2CO_3$ was replaced with $(NH_4)_2SO_4$ to avoid a change of pH during storage. Immediately before use, 2.5 mg/mL (2660 units/mL) pepsin was added to the simulated gastric fluid (SGF) and the pH was adjusted to pH 3; 10 mg/mL (lipase activity 80 units/mL) pancreatin and 5 mg/mL bile salts were added to the simulated intestinal fluid (SIF) and the pH was adjusted to 7. Approximately 15 mg (dry mass) of YE-c, or 25 mg (dry mass) of FP-c or YE/FP-c (6 pellets) were weighed into 50 mL centrifuge tubes. 5 mL of SGF pre-warmed to 37 °C was added to each tube and vortexed to suspend the cells. The sample-to-digestion fluid ratios were determined to gurantee a sink condition

for curcumin, while also ensuring that the concentration of curcumin in the supernant would be above the detection limit for all samples at all time points. SGF was sampled at 60 and 120 min and centrifuged to remove any insoluble solids. The concentration of curcumin in SGF was evaluated by measuring the absorbance using the UV-VIS spectrophotometer at 424 nm. After 2 hours, the samples were harvested from SGF and transferred to the same volume of pre-warmed SIF. Then the SIF was sampled and measured for absorbance at 30, 60, 90, 120, 150, and 180 min in the same manner. The concentration of curcumin released to the supernatant was calculated according to established calibration curves. At the end of the simulated digestion, retained curcumin in the encapsulation matrices were extracted using DMSO and quantified as specified in Section 2.2. Cumulative release of curcumin at each time point was calculated from the measurements.

Cumulative release of curcumin from the three encapsulation systems in SIF were fitted to an empirical Weibull model (Equation 5. 1) proposed originally by Langenbucher [289] to describe drug release curves:

$$M = 1 - exp(-\left(\frac{t}{\gamma}\right)^{k})$$

**Equation 5. 1**

M is the cumulative fraction of released curcumin, t is the time (min) in SIF, $\gamma$ (min) and k (dimensionless) are the scale and shape parameters of the Weibull model. The goodness of curve fitting was assessed by the root mean squared error (RMSE) and the correlation coefficients between true and fitted values.

*2.5.2. Fluorescence microscopic characterization*

To visualize the migration of curcumin within the multicellular encapsulation systems during *in vitro* digestion, FP-c and YE/FP-c samples collected before digestion, after gastric phase, and after intestinal phase were sliced, stained with Congo red, and imaged with the multiphoton microscope as specified in Section 2.3.2.

### 2.6. Statistical analysis

All experiments were conducted in triplicate and each batch of samples were analyzed as described above. Pairwise t tests were conducted to compare the means among the three encapsulation systems for the loading yield. Repeated measures ANOVA was used to compare gastric phase release of curcumin across time points and encapsulation systems. P-values smaller than 0.05 were considered statistically significant.

## 3. Results and discussion

### 3.1. Microstructure of the multicellular encapsulation systems

The spherical fungal pellets formed by *P. chrysogenum* H3 showed typical features of a filamentous fungus biomass grown under submerged shaking conditions: an intertwined hyphae matrix with a sparse interior core. The H3 fungal pellets had a dense layer of hyphae near the surface, and sparser distribution of hyphae towards the core, as illustrated by the SEM images of the outer surface and the interior section of a pellet and the fluorescence microscopic image of the pellet cross section (*Figure 5. 1*). Such an observation was consistent with the previous reports of fungal pellets formed by *P. chrysogenum* H3 and other filamentous fungi [136,281,290]. Moreover, the fungal pellet's outer wall contained hyphae protruding from the surface and this "hairy" layer was less dense than the layer right beneath the surface where the hyphae formed a more structured intertwining network. With the pre-formed fungal pellets and pre-grown *S. cerevisiae* G1 yeast cells, curcumin was encapsulated

using vacuum facilitated infusion, resulting in the two encapsulation systems: FP-c and YE-c. Subsequently, YE/FP-c was created by immobilizing curcumin loaded G1 yeast cells (YE-c) in the pre-formed H3 fungal pellet through a rapid internalization facilitated by the vacuum treatment. The results based on fluorescence microscopy and SEM images (*Figure 5. 2*) demonstrate that after the vacuum treatment, yeast cells were present at both the surface and core of the fungal pellets. The SEM images showed that more yeast cells were present near the core than at the outer surface.

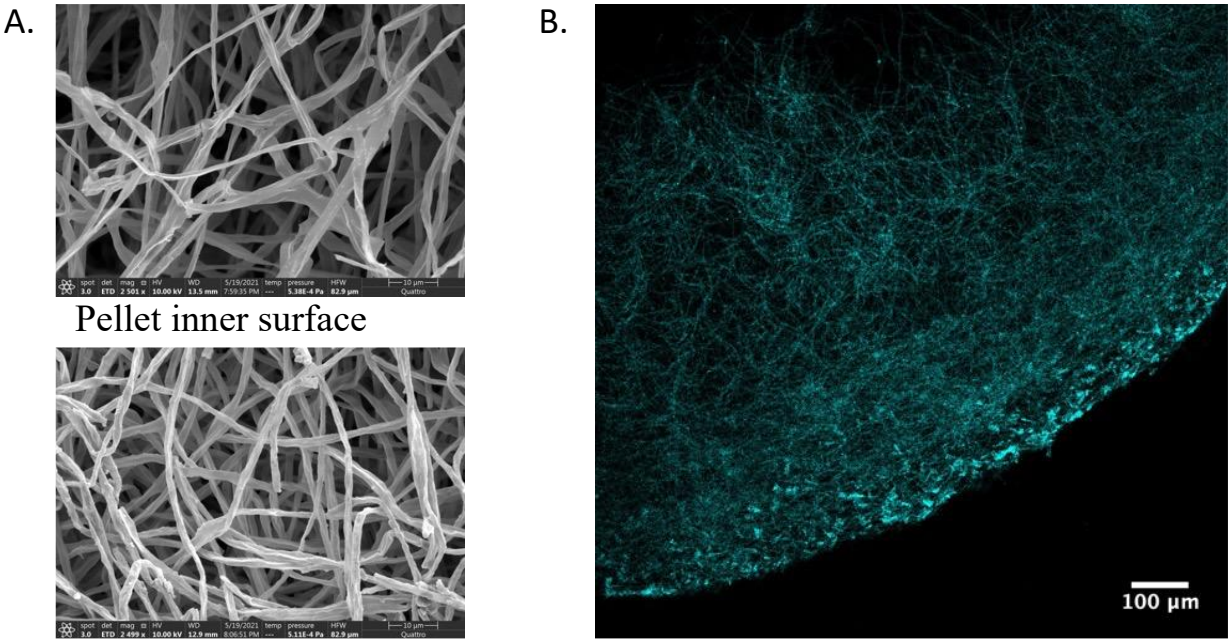


***Figure 5. 1: Characteristic images of Penicillium chrysogenum H3 fungal pellet. (A) SEM, (B) Multiphoton fluorescence microscope (stained with calcofluor white).***

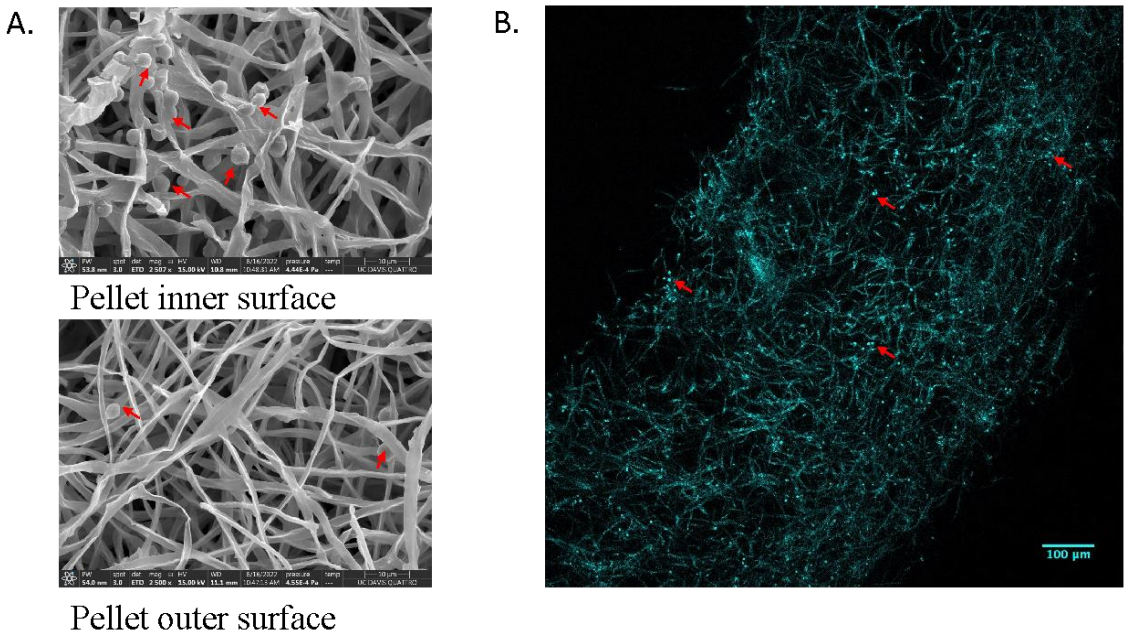


***Figure 5. 2: Characteristic images of S. cerevisiae G1 cells infused in P. chrysogenum H3 fungal pellet. (A) SEM, (B) Multiphoton fluorescence microscope (stained with calcofluor white). The red arrows point to some of the G1 yeast cells in the images.***

## 3.2. Infusion of curcumin in the encapsulation systems

The two multicellular encapsulation systems (FP-c and YE/FP-c) were prepared by directly infusing curcumin into the fungal pellet or infusing into G1 yeast cells first which were then immobilized with the fungal pellet. Figure 5. 3 shows the location of curcumin within the two encapsulation systems after vacuum infusion. Curcumin was internalized into either H3 fungal hyphae cells or G1 yeast cells. In the YE/FP-c system, the majority of curcumin was encapsulated in G1 cells, while limited amounts of curcumin could be seen inside the fungal hyphae cells as there could be some unencapsulated curcumin that partitioned into the hyphae cells during vacuum facilitated internalization of G1 cells into the fungal pellets. Table 5. 1 summarizes the encapsulation yield of curcumin in the three encapsulation systems, expressed on a dry mass basis. YE-c and FP-c had similar encapsulation yields (3.13±0.01 and 3.52±0.40 mg/g) (p-value=0.204), which was

significantly higher than that in YE/FP-c (0.87 mg/g) (p-values < 0.001). The results imply that the encapsulation efficiency of the vacuum infusion method was similar for the single cell and multicellular systems. Similar loading yield of curcumin in single yeast cells was reported by Young et al. [105], where the same vacuum infusion method was used. Higher loading capacity of curcumin in yeast cells have been reported by Paramera et al.[106,110] In their studies, a much higher compound-to-cell ratio was used, which could result in a higher encapsulation yield. Furthermore, in this study curcumin was dispersed in water or ethanolic solution at a concentration higher than the solubility of curcumin in corresponding solvents. Thus, the potential presence of un-dissolved curcumin crystals in the yeast cell suspension could influence the reported yield in the previous study as these crystals may not be removed during washing. The amount of curcumin in the YE/FP-c system was limited by the number of YE-c cells that could be immobilized in the fungal pellets, since in this system, curcumin was only loaded into G1 yeast, not directly in FP. With a similar encapsulation efficiency of curcumin in single G1 yeast cells and H3 fungal cells, we could conclude that the loading yield of curcumin in YE/FP-c to some extent reflects the mass fraction of G1 yeast cells immobilized in the multicellular FP.

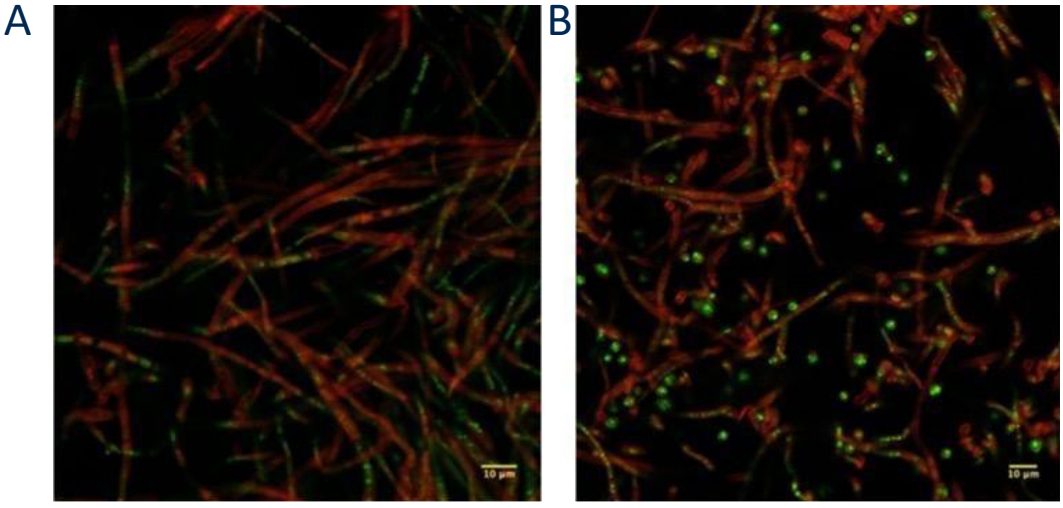


***Figure 5. 3: Multiphoton fluorescence images of FP-c (A) and YE/FP-c (B) showing the localization of curcumin (green) in fungal pellet (fungal hyphae cells stained with Congo red).***

**Table 5. 1: Loading yield of curcumin in YE-c, FP-c, and YE/FP-c.**

| Encapsulation system | Loading yield (mg/g d.b.*) (mean±sd, n=3) |
|---|---|
| YE-c | 3.13±0.01[a] |
| FP-c | 3.52±0.40[a] |
| YE/FP-c | 0.87±0.02[b] |

* d.b.: dry basis.

3.3. Release kinetics of curcumin from the encapsulation systems during *in vitro* digestion

The release profile of curcumin was evaluated for the three encapsulation systems using an *in vitro* static digestion model. The *in vitro* digestion included 2 hours of gastric phase followed by a 3-hours small intestinal phase. Consistent with results reported in previous studies about yeast-based microcarriers for curcumin [128] (as reported in **CHAPTER 2**), limited release of curcumin was observed during the gastric phase: 13±2%, 21±4%, and 30±14% for YE/FP-c, FP-c, and YE-c respectively at the end of 2 hours (*Figure 5. 4A*). Based on the repeated measures ANOVA result, the curcumin release percentage during the gastric phase is not significantly different across time points or different encapsulation systems. The three encapsulation systems showed different kinetic profiles of curcumin release during the 3-hour intestinal phase (*Figure 5. 4B*). At the end of the 3-hour small intestinal phase, the cumulative percentage of release was highest from YE-c (88%), followed by FP-c (58%), and lowest from YE/FP-c (42%). Rapid initial release was observed in both the YE-c and YE/FP-c systems. For YE-c, 50% of loaded curcumin was released within the first 30 min of the simulated intestinal phase, while less than 10% was released in the subsequent 2.5 hours. For YE/FP-c, 16% was released within 30 min and additional 13% in the following 2.5 hours. Different from these two systems, curcumin was gradually

released from FP-c without initial rapid release. The difference in release kinetics of the three encapsulation systems was captured by the fitting parameters of the Weibull model (Equation 5. 1). Many mathematical models have been proposed to describe the drug release kinetics, such as zeroth order, first order, Higuchi, Peppas, Weibull model etc. [291]. Among these models, the Weibull model has a significant flexibility in modeling diverse shape factors and release time scales using a two-parameter equation and was selected for the quantitative comparison of these release profiles. The selected model fit all three release kinetic curves well as indicated by the low RMSE and high correlation coefficients (Table 5. 2). The scale parameter ($\gamma$) defines the timescale of the curcumin release process, which is in an increasing order of YE-c < FP-c < YE/FP-c, indicating that the overall release rate was fastest in YE-c and slowest in YE/FP-c. The shape parameter (k) reflects the types of curves: k<1 indicates a parabolic curve, with large initial slope and a consistent exponential character; k=1 simplifies the model to an exponential distribution; k>1 indicates a sigmoidal curve with ascending curvature delimited by an inflection point [291]. YE-c and YE/FP-c had k<1, consistent with the observation of rapid initial release from these two systems. FP-c had the fitted k value very close to 1, demonstrating a nearly exponential release behavior.

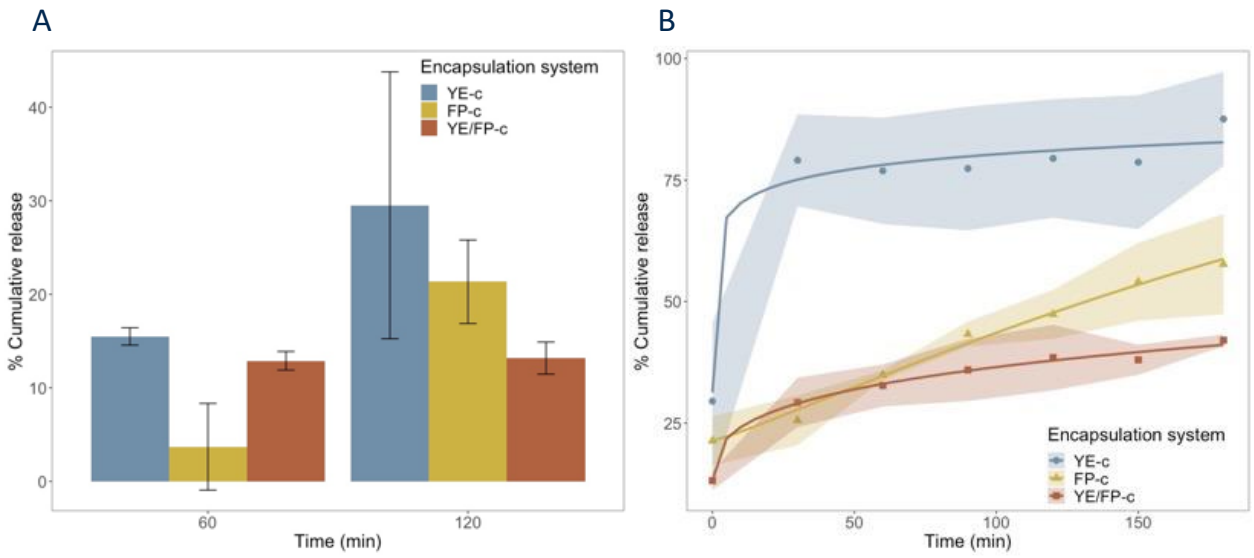


***Figure 5. 4: In vitro release of curcumin from three encapsulation systems during simulated digestion.*** **(A) 2-hour gastric phase.** The bar height and error bars indicate the mean and standard deviation (n=3) of the % cumulative release of each encapsulation system at each time point. **(B) 3-hour intestinal phase.** The markers are the mean % cumulative release (n=3).The banded areas represent the pointwise 95% confidence interval. The solid lines are the fitted Weibull model for each encapsulation system.

**Table 5. 2: Weibull model parameters fitted to the release of curcumin from the yeast-based encapsulation systems during *in vitro* small intestinal digestion, plus the model fitting RMSE and correlation coefficients.**

| ***Encapsulation system*** | ***Scale*** $(\gamma, min)$ | ***Shape (k)*** | ***RMSE*** | ***Correlation*** |
|---|---|---|---|---|
| *YE-c* | *23.78* | *0.17* | *0.043* | *0.996* |
| *FP-c* | *265.18* | *1.13* | *0.015* | *0.986* |
| *YE/FP-c* | *2426.38* | *0.36* | *0.009* | *0.996* |

Comparing the release of curcumin from YE/FP-c to that from YE-c and FP-c (*Figure 5. 4***B**), we could decouple the cell carrier effect and the matrix effect endowed by the filamentous fungus. In FP-c, the fungal cells served as both the carriers for curcumin and the 3D matrix itself, whereas for YE/FP-c, the carriers for curcumin were the G1 yeast cells and

the fungal hyphae network was only used as a 3D matrix. Our previous study showed that different matrix structures had the greatest impact on modulating the release profile from cell-based encapsulation systems during the small intestinal phase [210]. The release of curcumin from G1 yeast cells (YE-c) showed the same pattern as in other single yeast cell-based encapsulation systems [110,128]. The multicellular encapsulation systems, FP-c and YE/FP-c, modified the release profile of curcumin compared to the single-yeast system from two aspects: it eliminated the initial rapid release and reduced the overall release rate of curcumin. In our previous work [210] (as reported in CHAPTER 4), we studied the structural effect of cell clusters on the release of curcumin, where the cell clusters were formed by modifying yeast cell surface with oppositely charged polyelectrolytes coating and subsequent electrostatic aggregation. The cell clustering did mitigate the initial rapid release of curcumin compared to single cells, but such an effect diminished after 1 hour of the intestinal phase and the cumulative release at the end was similar for single cells and multi-cell clusters. Unlike the multicellular systems in the current study, the cell clusters were smaller in dimension (50 ~ 100 μm), loosely bounded and irregularly shaped. They also did not possess a well-defined surface with a densely intertwining outer wall, thus the structural or matrix effect provided by the cell clusters was very limited. Nevertheless, the matrix effect of the multicellular organization of fungal cells and their hyphae in filamentous fungal pellets was much more prominent, as indicated by the release kinetics (Table 5. 2). Similar influence of natural multicellular organization on release of micronutrients during simulated digestion has been reported for other tissues. For example, a study has illustrated the release of intracellular nutrients from the surface cells of cut almond seed cubes corresponding to the ruptured cell walls, and gradually the release was extended to the inner intact cells over a period of 12

hours [269]. Palmero et al. [24] also reported that the bioaccessibility of β-carotene in orange carrots was lower in large cell clusters (800~2000 μm) than in small cell clusters (40~250 μm).

### 3.4. Microscopic characterization of the multicellular encapsulation systems during *in vitro* digestion

Fluorescence microscopic imaging was used to visualize the spatial and temporal changes in the distribution of curcumin in fungal pellet during digestions. *Figure 5. 5* shows the distribution of curcumin in the multicellular encapsulation systems before digestion, after the gastric phase, and after the small intestinal phase. The hyphae cell wall was stained with Congo red to visualize the fungal biomass [288]. After the gastric phase, there was no significant change in the curcumin distribution in the multicellular matrices compared to the control samples before digestion. Curcumin mainly remained within either fungal hyphae cells or G1 yeast cells, in the FP-c and YE/FP-c systems respectively. After the intestinal phase, however, a band of residual curcumin-rich aggregates was observed to localize just beneath the surface of the fungal pellets in both systems, while no significant amount of curcumin was retained inside the cells where it was originally encapsulated. Such a phenomenon was observed for both FP-c and YE/FP-c. Images were taken at a higher magnification at the surface and core of YE/FP-c after the intestinal phase (*Figure S5. 1*). The G1 yeast cells inside the fungal pellet remained immobilized after the *in vitro* digestion process, while the encapsulated curcumin was released from the cells and migrated outwards from the core. Furthermore, some of the released curcumin was deposited near the surface of the fungal pellet. The close-up images show that the curcumin-rich band near the pellet surface were not G1 yeast cells

carrying curcumin, but some form of curcumin aggregates. To further elucidate the composition of these aggregates, Nile Red was used to stain the neutral lipid in native fungal pellet and the FP-c sample after the small intestinal digestion phase. The colocalization of fluorescence signals of curcumin and Nile Red in the post-digestion FP-c sample (*Figure 5.* ***6*** *A1, A2*) suggest that the curcumin aggregates observed near the surface of the fungal pellet after digestion included lipid rich deposits at the surface along with residual curcumin. *Figure 5.* ***6*** *B*, *C* demonstrate that in native fungal pellet without curcumin, such lipid aggregates also appeared near the pellet surface after small intestinal digestion, confirming the hypothesis that these lipid aggregates were likely extracted from the fungal biomass during digestion facilitated by the lipase and bile salt in SIF, and deposited beneath the outer surface of the fungal pellet with the highest hyphae density.

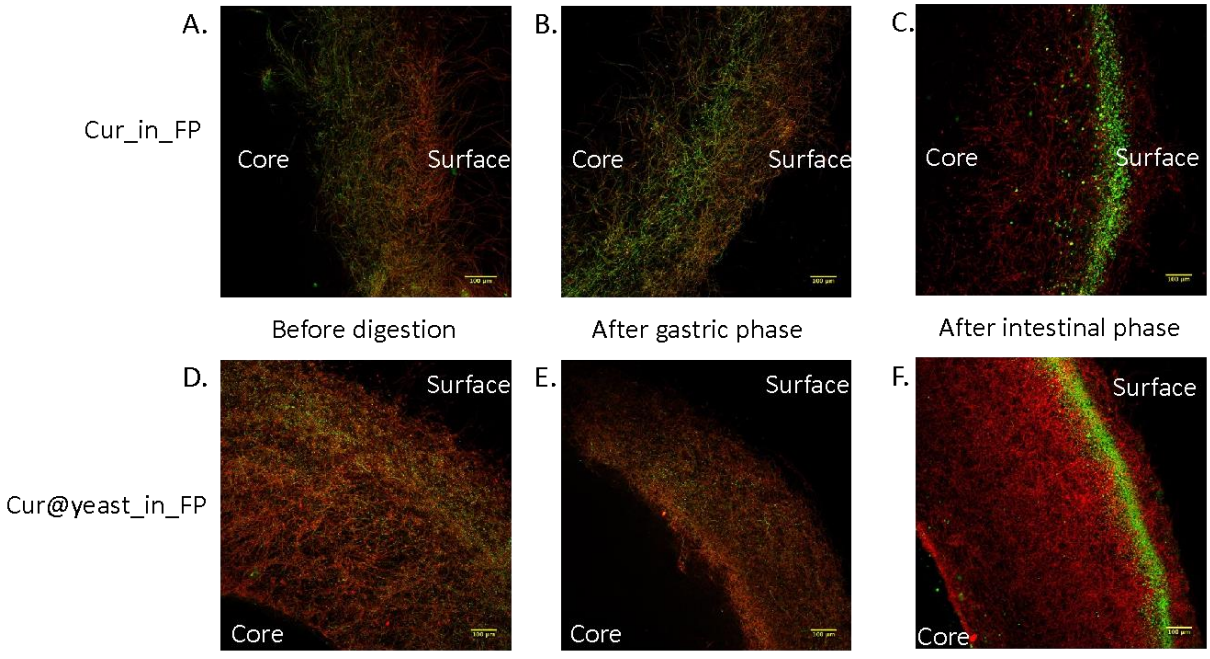


***Figure 5. 5: Multiphoton fluorescence microscopic images showing the change in curcumin (green) distribution in the multicellular encapsulation systems (fungal hyphae cell wall stained by Congo red): FP-c (A-C) and YE/FP-c (D-E) during simulated digestion.***

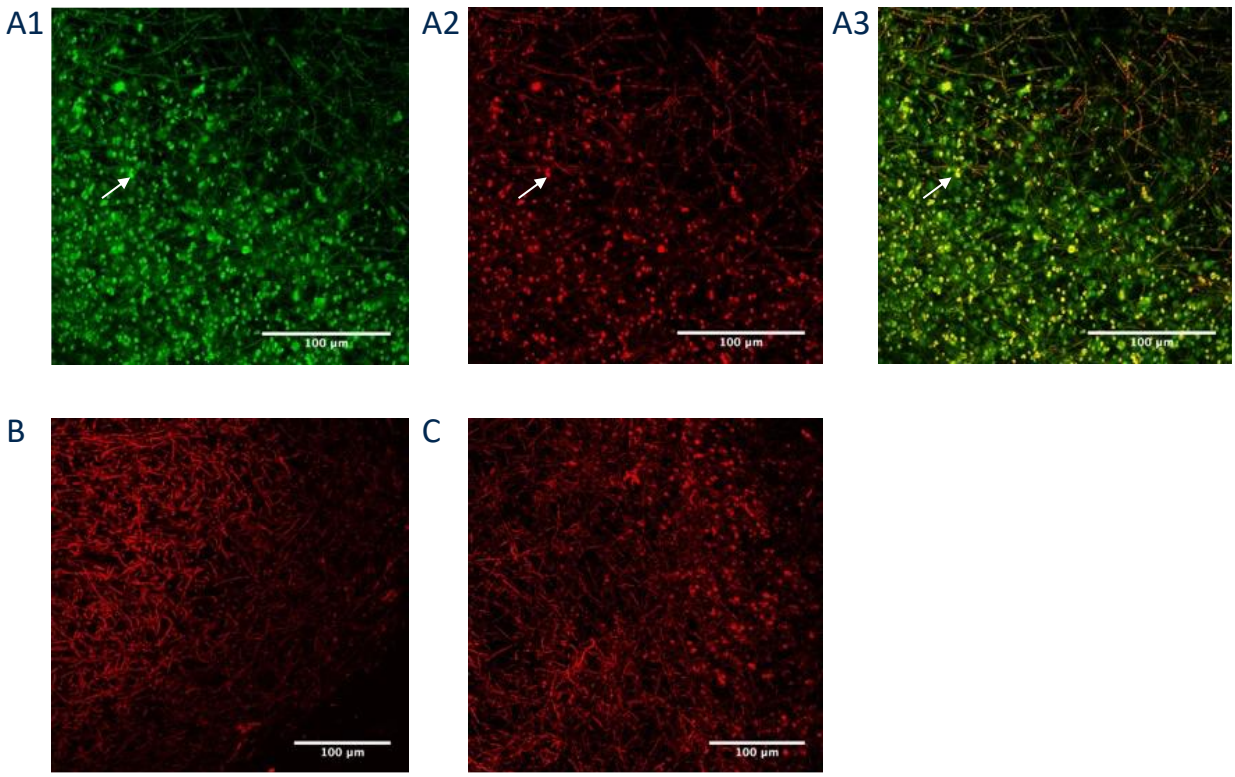


*Figure 5. 6: Multiphoton microscopic images of the post-digestion FP-c near the fungal pellet surface: curcumin channel (A1), Nile Red channel (A2); composite of the two channels (A3); Nile red-stained native fungal pellet before (B) and after digestion (C).* The white arrows point to one of the lipid-rich aggregates observed in post-digestion fungal pellet samples.

Together the imaging and release results suggest that bile salts and intestinal enzyme could diffuse freely into the fungal pellets based on their porosity [281] and could promote the release of curcumin from the multi-cellular encapsulation system, along with the intracellular lipids. However due to the dense structure of the hyphae near the surface of fungal pellet, some deposition of curcumin/lipid aggregates was also observed. The band of aggregates served as a reservoir from which curcumin was gradually released into the surrounding aqueous environment through diffusion. The hypothesized mechanism was supported by the fact that the curcumin release curves from FP-c and YE/FP-c after 30

min in the small intestinal phase were mostly linear (*Figure 5. 4B*). This segment of the kinetics curves could be fitted to both zero order and first order models with low RMSE and high correlation coefficient (Table S5. 1), with a small exponential term in the first order model. The almost linear relationship suggests a diffusion governed release behavior which is concentration independent [291]. Curcumin was highly concentrated in the aggregates beneath the pellet surface, and its release rate into the SIF was relatively slow so that the reservoir concentration stayed constant within the time scale of the experiment, leading to a zero-order behavior.

## 4. Conclusion

The current study evaluated filamentous fungal pellet as a multicellular encapsulation matrix for exogeneous bioactive compounds. Infusing bioactive compounds into fungal biomass would further enhance the nutritional values of F, and also would make it a sustainable and affordable bioactive encapsulation system. The bioactive-loaded FF also served as a model system to study the food matrix-micronutrient interaction during digestion, given its naturally-endowed 3D structure. Compared to the single-cell encapsulation system, the curcumin encapsulation efficiency was similar in the multicellular FF pellet system using vacuum facilitated infusion. The vacuum treatment not only facilitated internalization of curcumin in yeast or fungal cells, but also enabled rapid immobilization of yeast cells into the fungal pellet matrix. With the three constructed encapsulation systems (single cell, multicellular fungal pellet, and single-cell-immobilized-in-fungal pellets), we were able to decouple the role of FF as a carrier for the bioactive compound from the role of the fungal pellet as a 3D matrix, in the context of micronutrient release during digestion. Compared to the single-cell encapsulation system, the multicellular system modified the release kinetics of curcumin during *in vitro* digestion by

eliminating the initial rapid release and reducing the overall release rate of curcumin. These results provide a deeper understanding on the effect of natural edible structures on the bioaccessibility of micronutrients, and demonstrate the potential of using FF biomass as functional food materials.

## 5. Acknowledgement

The *Saccharomyces cerevisiae* G1 *(MYA-2451)* strain and the filamentous fungus strain *Penicillium chrysogenum* H3 (UCDFST 22-448) were kindly provided by the Department of Microbiology at University of Cordoba, Spain.

## Supplements

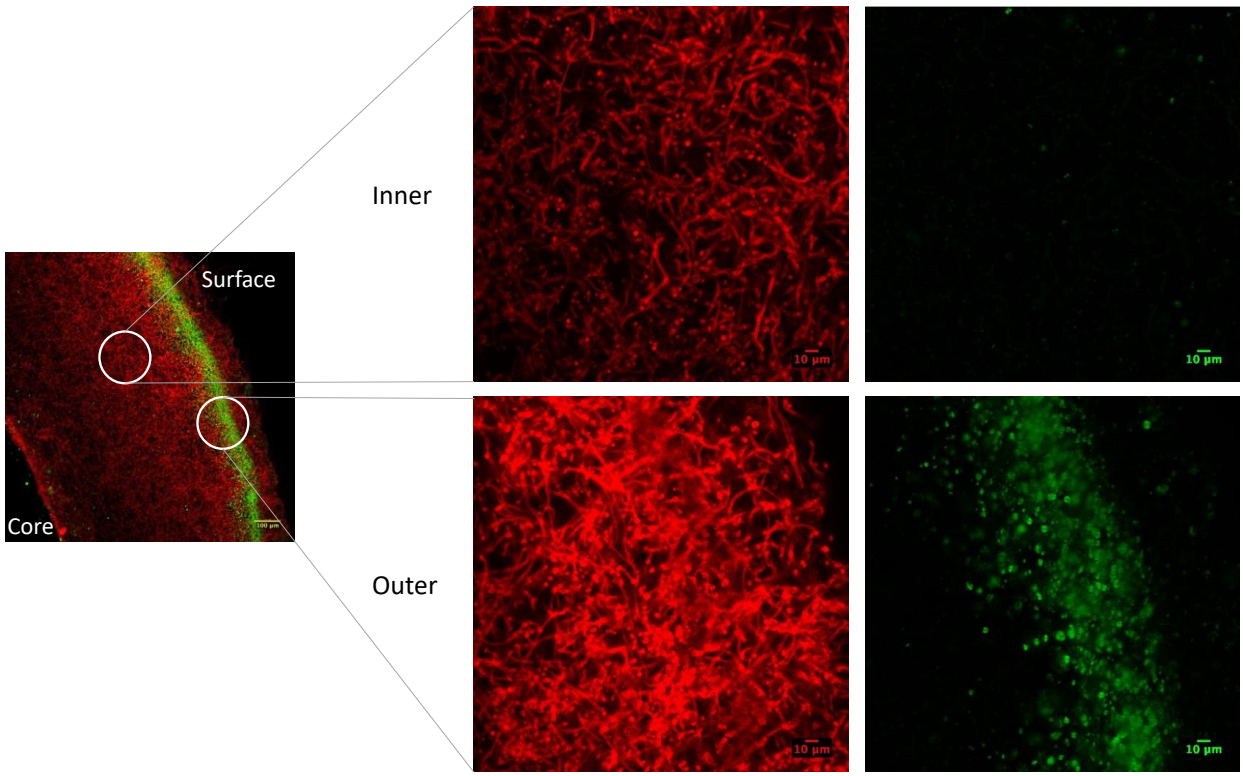


***Figure S5. 1: Distribution of curcumin (green) in YE/FP-c (fungal hyphae cell wall was stained with Congo red) after the small intestinal digestion phase (40x magnification).***

**Table S5. 1: Fitted zero order[a] and first order[b] model parameters to the release of curcumin from FP-c and YE/FP-c after 30 min into the *in vitro* intestinal phase, plus the model fitting RMSE and correlation coefficients.**

| Encapsulation system | Model | Rate (k, $10^{-3}$ $min^{-1}$) | 95% CI of k ($10^{-3}$ $min^{-1}$) | RMSE | Correlation |
|---|---|---|---|---|---|
| FP-c | Zero order | 2.11 | [1.79, 2.45] | 0.017 | 0.988 |
| | First order | 3.76 | [3.44, 4.08] | 0.0098 | 0.996 |
| YE/FP-c | Zero order | 0.784 | [0.593, 0.975] | 0.010 | 0.970 |
| | First order | 1.22 | [1.03, 1.41] | 0.0095 | 0.972 |

[a] *Zero order model:* $M_t = M_0 + kt$

[b] *First order model:* $M_t = M_0(1 - e^{-kt})$

$M_t, M_0$ *are the cumulative release at time t and time 0.*

# CHAPTER 6

# 3D printing aided patterning of cell-based microcarriers to modify release profiles of bioactive compounds during *in vitro* digestion

## 1. Introduction

A food matrix is an assembly of food molecules that interact with each other physically or chemically [16]. Both the way those food components are structurally organized at micro-, meso-, and macroscopic scales and their interactions at different length scales could influence the physical, sensorial, and nutritional properties of foods [15,16]. The term "food matrix effect" appears in the food and nutrition literature mostly to denote that a chemical compound could behave differently in a free form than as part of a food material [15]. The food matrix has a direct impact on the bioaccessibility of bioactive compounds by affecting their chemical stability, enzymatic accessibility, and release from the food structure [16]. In plant foods (i.e., fruits and vegetables) the release of bioactive compounds needs to overcome both the physical barriers imparted by the cell wall and organelle membrane, and the chemical complexation between the bioactives and the cellular matrix components[242]. Therefore, the bioaccessibility of plant-derived bioactive compounds could be influenced by various factors, such as the chemical structure of the compounds, subcellular localization of the compounds, the chemical composition of plant cells, and the spatial organization of the cells within a tissue [16,39]. One way to decouple the effects from multiple contributing factors is to use a bottom-up approach to construct model food matrices from basic building blocks and progressively adding on compositional and structural complexity. Using yeast cell-based microcarriers for bioactive compounds as the building block, **CHAPTER 2** and **CHAPTER 3** investigated the cell-level factors contributing to the

encapsulation and *in vitro* bioaccessibility of bioactives. In CHAPTER 4 and CHAPTER 5, the effect of multicellular structures on the release were evaluated by either constructing cell clusters through self-assembly of the single cells or using a natural multicellular structure as the model matrix. However, neither of these approaches has the flexibility and versatility to construct tissue-like matrices with highly controllable structural features, such as porosity and intratissue distribution of the microcarriers.

3D printing is an emerging concept for precision and modular food manufacturing to address the need for customizing food based on personal preferences and nutritional requirements [161]. It serves the purpose of creating structures with high precision guided by a digital 3D model. Among the various 3D printing techniques that have been explored for food applications, extrusion-based 3D printing is the most widely used [163,164]. This technique has the versatility to print different types of food materials, such as hot-melt extrusion of chocolate [165], room-temperature extrusion of dough, frosting, and hazelnut spread etc. [166,167], as well as extrusion of food hydrocolloids [168,169]. Food-grade hydrocolloid agents, such as various polysaccharides, can either be crosslinked to form gels via chemical modification [170] or ionic complexation [171], or added as thickening agents to modify food properties [172]. Previous studies have demonstrated the potential of developing 3D printed structures using hydrogels composed of starch [170], agar [168], alginate [173], pectin [174] or other polysaccharide-based food inks [175].

Originated from the field of tissue engineering [163], 3D printing of cell-laden bioinks into different structures has recently been applied to print meat and plant simulants [177,178]. The concept coincides with the idea of engineering tissue-like encapsulation systems in a bottom-up manner. The objective of constructing tissue-like structures using 3D printing is to enable the 3D patterning of cell-based microcarriers and acquire structures with different “intra-tissue”

distributions of the bioactive compounds that are encapsulated in the microcarriers, e.g., a core-shell design, a layer-by-layer design, etc. The different 3D printing patterns could be used to mimic the different distributions of bioactives in natural plant tissues, such as a higher concentration of bioactives in the peel vs. flesh. These printed structures could serve as models to investigate the food matrix effect on bioaccessibility of bioactive compounds at a macroscopic level – the tissue level. At this length scale, the chemical interactions among the bioactive compounds, the intracellular components, and the extracellular matrix, as well as the mass transfer in and out of the tissue would all impact the observed release profiles during digestion.

Previous studies have demonstrated the potential of developing 3D printed structures using hydrogels composed of starch [170], agar [168], alginate [173], pectin [174] or other polysaccharide-based food inks [175]. However, achieving optimal compositions for a reproducible and high-resolution printing remains a significant challenge. The challenges result from the lack of comprehensive understanding of a relationship between formulation parameters, rheological properties and printability features. As a result, previous studies have used empirical approaches to explore food ink formulations and their application to print diverse structures [292,293]. The trial-and-error procedure for formulation optimization of food inks is time consuming and often only applicable to a specific ink composition, limiting the applications of 3D printing in food systems. To qualify as a good ink, hydrogels should have two basic characteristics: extrudability and post-printing shape fidelity [176]. Rheology is commonly used to characterize hydrogel-based 3D printing inks and rheological properties have been reported in most of the ink development studies. A few studies have evaluated the relationship between formulation parameters and rheological measurements of food inks [171,294,295]. The results of these studies illustrate that the rheological properties of hydrogels largely depend on the chemical nature and concentration of the polymers,

gelling mechanisms, and the extent of crosslinking within the polymer networks. However, most studies used subjective evaluation to assess the printability of food inks through experimental observations [166,167,293,294,296]. Even for studies that did quantitative or semi-quantitative characterization of printability, most of them only focused on post-printing shape fidelity, i.e. the extent of spreading and fusion of the printed filaments, measured either manually [297] or through image analysis [176,298,299]. However, few studies have focused on assessing the smoothness of ink deposition except visual inspection during printing, which is another important printability feature reflecting the extrudability of the inks during printing. The lack of quantitative criteria for a comprehensive printability assessment prevents the development of predictive relationships between food ink properties and printability.

This study had two major aims: (1) developing plant polysaccharides-based food inks for 3D printing and evaluating the predictive relationship between inks' formulation parameters, rheological properties, and their printability; (2) producing tissue-like multicellular structures with controlled compositional and structure features using 3D printing with an optimal ink formulation and evaluating the release profiles of the encapsulated compound during *in vitro* digestion. For the first aim, low methoxy pectin (LMP) and cellulose nanocrystalline (CNC) were chosen to formulate the food inks since pectin and cellulose are the major constituents of plant cell wall [300] and the developed inks could be used to print plant-based food mimetics. Pectin is a family of heterogeneous polysaccharides rich in galacturonic acid, a proportion of which could be methyl esterified. LMP gels are generally formed through electrostatic complexation with cations such as $Ca^{2+}$. The generated polymeric network is responsible for maintaining the 3D structure of the food ink hydrogels formulated in the current study. CNC was incorporated into the gels as a minor component to modify the mechanical properties of the inks

[301,302]. Both linear regression-based response surface methodology (RSM) and machine learning models were used to evaluate the relationships between the printability, inks' composition, and rheological properties. A few studies in tissue engineering utilized RSM [296,303] or machine learning techniques [304] to model the relationship between printing parameters and printability, but were limited to a single ink composition variable and did not incorporate rheological measurements in the models. For the second aim, yeast cells loaded with a model bioactive compound (curcumin) were incorporated into an ink with optimal printability. The cell-laden ink and the cell-free ink were 3D printed into structures with two different designs: layer-by-layer design, and core-shell design. The release of curcumin from these two structures during *in vitro* digestion was measured to elucidate the effect of spatial distribution of the bioactive compound in a tissue-like encapsulation system on its bioaccessibility.

## 2. Materials and Methods

### 2.1. Materials

LMP (E440i, Unipectine™ of 100 C) was kindly provided by Cargill (Minnetonka, MN). As specified by the supplier, the product contained 86.3 wt. % of LMP (degree of esterification 7%) and 13.7 wt. % added dextrose. CNC slurry was purchased from Cellulose Lab (Fredericton, NB, Canada), which contained crystals with width 5-20 nm and length 100-250 nm. Curcumin derived from Curcuma longa (turmeric) [≥ 65%, HPLC grade], calcium chloride, sodium tetraborate decahydrate, bile salts (cholic acid- deoxycholic acid sodium salt mixture), potassium phosphate monobasic, and ammonium phosphate were purchased from Sigma-Aldrich (St. Louis, MO). The enzymes used in simulated digestion fluids preparation: pepsin from porcine gastric mucosa (1064 units/mg protein), pancreatin from porcine pancreas (4x USP), were also purchased from Sigma-Aldrich (St. Louis, MO).

Sulfamic acid was purchased from EMD Millipore Corporation (Billerica, MA). Absolute ethanol was purchased from Koptec (King of Prussia, PA). Sodium hydroxide, hydrochloric acid, sodium chloride, sulfuric acid, magnesium chloride, and potassium chloride were purchased from Fisher Scientific (Pittsburg, PA). 3-phenylphenol (m-hydroxydiphenyl) was purchased from Spectrum Chemical Mfg. Corp. (New Brunswick, NJ). Fleischmann's Active Dry yeast, *Saccharomyces cerevisiae*, was obtained from a local grocery store. Ultrapure water (18 MΩ cm) was obtained using a Milli-Q RG water ultra-purification system (EMD Millipore, Billerica, MA).

## 2.2. Food ink preparation

### *2.2.1. Cell-free ink formulations*

The food inks were formulated as hydrogels composed of different concentrations of LMP and CNC, and varying amount of $CaCl_2$ was used to induce LMP gelation. Total polysaccharide (LMP + CNC) concentration, LMP-to-CNC mass ratio (expressed as pectin fraction in regression models (Equation 6. 1)), and calcium crosslinking density (referred to as R hereafter) were the three formulation parameters used in the experimental design, as summarized in Table 6. 1. The crosslink density was defined as the stoichiometric ratio between the molarity of $Ca^{2+}$ and that of $COO^-$ (Equation 6. 2). The molarity of $COO^-$ was calculated from the total uronic acid content of LMP and its degree of methoxylation, as shown in Equation 6. 3. LMP used in the current study contained 1.92 mmol galacturonic acid equivalence per gram, measured using a colorimetric assay, as described in previous studies [305,306]. For each ink formula, $CaCl_2$ solution with different concentrations was prepared based on the specified LMP concentration and crosslinking density (R).

$$pectin\ fraction = \frac{LMP\ (g)}{LMP\ (g) + CNC\ (g)}$$

**Equation 6. 1**

$$Crosslinking\ density\ (R) = \frac{2 * [Ca^{2+}]}{[COO^{-}]}$$

**Equation 6. 2**

$$[COO^{-}] = [galacturonic\ acid\ equivalance] * (1 - degree\ of\ methoxylation)$$

**Equation 6. 3**

Solution containing 4.29, 6.43, or 8.57 wt.% of LMP was prepared by dissolving the pectin powder in 80 °C water and maintained at the same temperature for 10 min, then continuous stirring for 2 hours at room temperature to ensure fully hydration while cooling. The CNC slurry was adjusted to 3, 4.5, or 6 wt.%. The prepared pectin solution and $CaCl_2$ solution were separately loaded into two syringes, connected with a Luer-lock connector, and mixed at a volumetric ratio of 7:3. The resulting partially crosslinked pectin solution would have LMP concentration of 3, 4.5, or 6 wt.%, same as the CNC slurry, and different crosslinking density as determined by the $CaCl_2$ solution concentration. Then, the partially crosslinked pectin solution was mixed thoroughly with CNC slurry with the same concentration at different ratios depending on the target LMP-to-CNC ratio. A schematic diagram summarizing the ink preparation steps is provided in *Figure 6. 1*. Bubble generation was avoided at best during mixing by expelling air from the syringes while mixing. The final food inks were stored at 4ºC and used for 3D printing and rheological measurements between 12-48 hours after preparation.

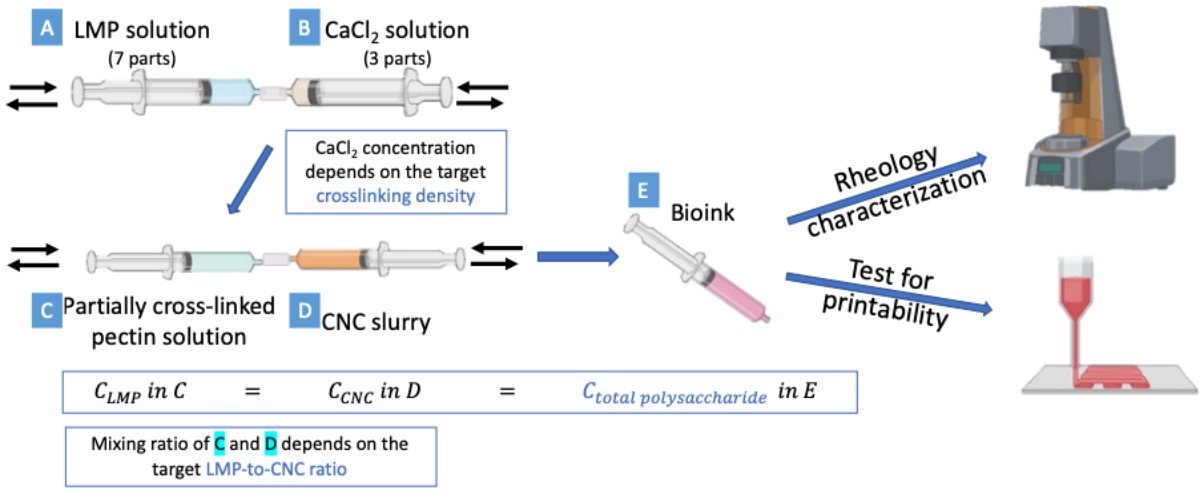


***Figure 6. 1: A schematic diagram of the ink preparation steps and subsequent characterizations.***

*2.2.2. Curcumin encapsulation in yeast cells and cell-laden ink*

Vacuum-facilitated infusion was used to encapsulate curcumin into yeast cells using an established protocol [105]. First, yeast cells were suspended in water and heat inactivated at 90 °C for 30 min. After cooling and washing, the cells were resuspended in ethanolic solution of curcumin to reach a final cell density of OD600 = 2.4, compound-to-cell ratio = 0.25 $\mu mol$/OD600 unit, and ethanol concentration of 35%. Then the cell-compound mixtures were then subjected to 99% vacuum treatment for 5 seconds. After vacuum infusion, the samples were centrifuged at 2711 xg for 5 min to pellet down the cells The cell pellet was washed once with 10% ethanol and 3 more times with purified water to remove unencapsulated curcumin.

The ink formulation with 4.5% LMP, and a crosslinking density R=0.35 (without CNC) was selected to prepare the cell-laden ink. Varying amounts of curcumin-loaded yeast cells was weighed and added to the $CaCl_2$ solution first, and then the cell-$CaCl_2$ mixture was mixed with the LMP solution in the same way as described in section 2.2.1.

Cell pellets with different masses were incorporated in the ink to reach final cell density in the ink of 0, 2.25, 4.5, 6.75 w/v%, on a wet mass basis.

## 2.3. Rheological measurements

To investigate the effect of the three formulation parameters on the food ink's rheological properties, the following three tests were performed: *(1) steady-state flow test; (2) dynamic viscoelastic properties test; and (3) recovery test.* The rheological measurements were conducted using an MCR 302 stress-controlled rheometer (Anton-Paar, Graz, Austria) equipped with a 25 mm parallel plate geometry and using a 0.55 mm measurement gap, at 25 ± 0.1°C.

### *2.3.1.* Steady-state flow

The shear thinning behavior of the food inks was evaluated using a steady-state flow test [307]. Shear stress was recorded while changing the shear rate in the range of 0.1 $s^{-1}$ to 100 $s^{-1}$. The results were then fitted using the Herschel-Bulkley equation:

$$\tau = \tau_0 + k\dot{\gamma}^n$$

**Equation 6. 4**

where $\tau$ is the shear stress (Pa), $\dot{\gamma}$ the shear rate ($s^{-1}$), k the consistency index, and n the flow index.

### *2.3.2. Dynamic viscoelastic behavior*

The evolution of the storage modulus (G') and loss modulus (G") with increasing strain ($\gamma_0$) and angular frequency ($\omega$) was measured for all food inks. Amplitude sweeps were performed in the range of 0.01 to 100% strain at $\omega$=1 rads/s (0.16 Hz) to determine the limit of linearity where the hydrogel collapsed and a sudden drop in G' occurred. The

limit of linearity was found where the storage modulus dropped to 95% of the plateau value at low strain amplitudes. The shear stress at the limit of linearity was the yield stress ($\tau_y$). The shear stress at the crossover between G' and G" curves was defined as the flow stress ($\tau_f$). The region between $\tau_y$ and $\tau_f$ could be considered as the transition region where the flow behavior transitions from being dominated by the elastic component to the viscous component. A flow transition index ($\frac{\tau_f}{\tau_y}$) was defined to indicate the relative decrease in stress between the limit of linearity and crossover. Frequency sweeps were performed from 0.06 to 100 rad/s at 1% strain (within the linear strain range for all food inks) to determine the frequency dependency of G' and G", and the phase angle δ. The loss factor tan(δ) = G"/G' was calculated at 0.1 rad/s as an indicator of the gelation state of the hydrogels.

*2.3.3. Shear recovery*

The recoverability of hydrogels after applying high shear rate was monitored under conditions simulating the 3D printing process [307]. The viscosity of hydrogels was measured as the shear rate underwent a three-step change: 0.1 $s^{-1}$ for 60 s (step 1), 600 $s^{-1}$ for 10 s (step 2), and again 0.1 $s^{-1}$ for 60 s (step 3). The three steps simulated the low-high-low shear rate that the food ink would experience before, during, and after 3D printing. A recovery index was calculated as the ratio between the mean viscosity during step 3 to that during step 1.

2.4. 3D printing and printability assessment

In this study, the food inks were printed using an Allevi 2 bioprinter (Allevi, Inc., Philadelphia, PA). 25-gauge nozzles (i.d. 0.26 mm) were used for printing. Extrusion

pressure, layer height, nozzle velocity, and printing patterns were manipulated using the Allevi online software. The printer settings were tuned for each food ink. The optimal pressure was the minimum pressure needed to extrude a continuous filament with relatively uniform diameter. The layer height and translational nozzle velocity were adjusted to ensure that the printed filament could be continuously deposited on a glass slide.

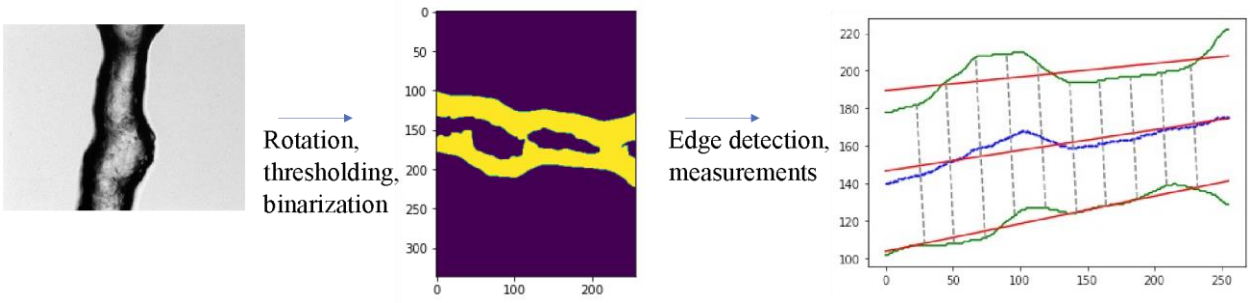


**Figure 6. 2*: Schematic diagram of measuring the printed filament width and roughness through image analysis.***

To assess the printability of the food inks, the printed filaments were imaged using an optical microscope (Olympus IX71) with a 4x magnification objective lens. From the acquired micrographs, filament width and roughness were evaluated. Figure 6. 2 showed a schematic diagram of how these two measurements were extracted from the bright field images of printed filaments. The images were first rotated so that all the filaments in the images aligned along the X direction (horizontally), then thresholded and binarized to facilitate identification of the filament edges. The centerline of a filament was generated by connecting the midpoints of the vertical segments connecting the upper and lower edges. Then linear trendlines were fitted to each of the upper edge, the center line, and the lower edge. At 10 equally spaced points along the center trendline, perpendicular segments were drawn until they intersected with the upper and lower edges. Filament width was calculated as the average length of these 10 segments. A relative width index was calculated as:

$$Relative\ width = \frac{measured\ width - target\ width}{target\ width}$$

**Equation 6. 5**

where the target width was the inner diameter of the nozzle: 260 $\mu$m. Filament roughness was defined as the mean squared error between the y coordinates of detected edges and those of their corresponding fitted trendlines, then averaged for upper and lower edges:

$$Roughness = \frac{1}{2}\sum_{l=1}^{2}\frac{1}{n}\sum_{i=1}^{n}(y_i^{edge_l} - y_i^{trendline_l})^2$$

**Equation 6. 6**

$(x_i^{edge_l}, y_i^{edge_l})$ are coordinates of points on the upper edge of the filament when l=1 and the lower edge when l=2; $(x_i^{trendline_l}, y_i^{trendline_l})$ are coordinates on trend lines defined in the same way; n is the total number of pixels along the x direction. Both filament width and roughness were averaged over 5 images, taken at different locations on one printed filament, and both filament width and roughness measurements were averaged over the 5 images. The image analysis was conducted in Python. Based on the relative width index and roughness measurements, binary labels were generated for each of these two metrics with pre-specified thresholds. Moreover, as a final printability assessment combining both metrics, a binary ink quality label was generated: a good ink should be printed with high resolution (low relative width index) and smoothness (less roughness). The criteria for classification of the ink formulations and their corresponding labels for the three printability assessment metrics are provided in Table S6. 1.

Grid cubes (5*5*5 $mm^3$) and 8 mm * 8 mm 3-layer grids, both with 1 mm line spacing were printed using different food inks for visual inspection of printing quality. The optimized

printing setting for each ink was used (Table S6. 2). The printed structures were inspected for defects such as line fusion, interrupted extrusion, shape deformation, etc. After printing, the printed objects were submerged in 90 mM $CaCl_2$ solution for 10 min for post-printing crosslinking.

2.5. Experimental design and model construction

A Box-Behnken experimental design was adopted using the 3 formulation parameters given in Table 6. 1. This resulted in 15 inks with 13 different compositions (Table S6. 3). Triplicates of the food inks were prepared independently for the rheological measurements, printability assessment, and 3D printing inspection.

**Table 6. 1: Food ink formulation parameters used in the Box-Behnken design.**

| Formulation parameters | Low | Medium | High |
|---|---|---|---|
| Total polysaccharide | 3% | 4.5% | 6% |
| LMP : CNC | 6:4 | 8:2 | 10:0 |
| $R = 2*[Ca^{2+}]/[COO^-]$ | 0.35 | 0.45 | 0.55 |

Pairwise Pearson's correlation and principal component analysis (PCA) was conducted on all the rheological measurements: the flow index (n) from the fitted Herschel-Bulkley equation, storage and loss modulus (G', G"), loss factor (tan(δ)), yield stress ($\tau_Y$), flow transition index, and recovery index. Four response variables (Y): the first two principal components of the rheology PCA model, together with the printability assessment measurements: filament width and roughness, were separately regressed on to the three formulation parameters (total polysaccharide: X1, pectin fraction: X2, crosslinking density: X3) and their two-way interaction terms:

$$Y = \beta_0 + \beta_1 X1 + \beta_2 X2 + \beta_3 X3 + [\beta_4 X1X2 + \beta_5 X1X3 + \beta_6 X2X3] + \epsilon$$

**Equation 6. 7**

Given the normality assumption behind the p-value calculation of the regression coefficients, filament width and roughness were log transformed before fitting the regression models. Ordinary least square regression with Akaike information criterion (AIC)-based stepwise model selection was used to determine which interaction terms to include in the regression model. AIC estimates the relative quality of statistical models for a given data set. An interaction term would be included in the model only if the addition of this term reduced the AIC of the updated model. Significance level was chosen to be 0.05 whenever a p-value was reported.

To better predict the ink printability and explore the possibility of generalizing the model beyond current formulation parameters, random forest classification models were built to predict the width label and roughness label using the food inks' rheological properties and/ or the formulation parameters. Given the small sample size, stratified repeated 5-fold cross validation was used to train and test the models. Stratification based on the response labels guaranteed that the ratio between label classes was the same in the train and test set for every train-test split during cross validation. The cross-validation classification accuracy for each feature set and response variable were reported. To predict the binary ink quality label, both a direct and an indirect approach were taken. For a direct prediction, the binary quality label was predicted as the response variable in the same way using cross validation. The indirect approach combined the prediction results from the previously trained models on width label and roughness label to obtain a predicted binary quality label in the same way as the true binary quality label was generated. The regression analysis was conducted in R (version

4.1.3) and the random forest models were constructed using the scikit-learn library in Python (version 3.7.10).

2.6. 3D patterning of curcumin-loaded yeast cells using 3D printing

Two syringes containing the cell-free ink and cell-laden ink were used to print 5 mm*5 mm*5 mm solid cubes with two types of designs: layer-by-layer design and core-shell design (*Figure 6. 3*). In the layer-by-layer design, the cell-free ink and cell-laden ink were print alternately in layers. Each layer was designed to be 0.625 mm high, and 4 layers of each ink were printed to make up the 5 mm tall cube. In the core-shell design, the core was a 4 mm*4 mm*4 mm cube in the center printed using the cell-laden ink, which was surrounded by a 0.5 mm thick shell of the cell-free ink. The same post-printing crosslinking treatment was done on these cubes.

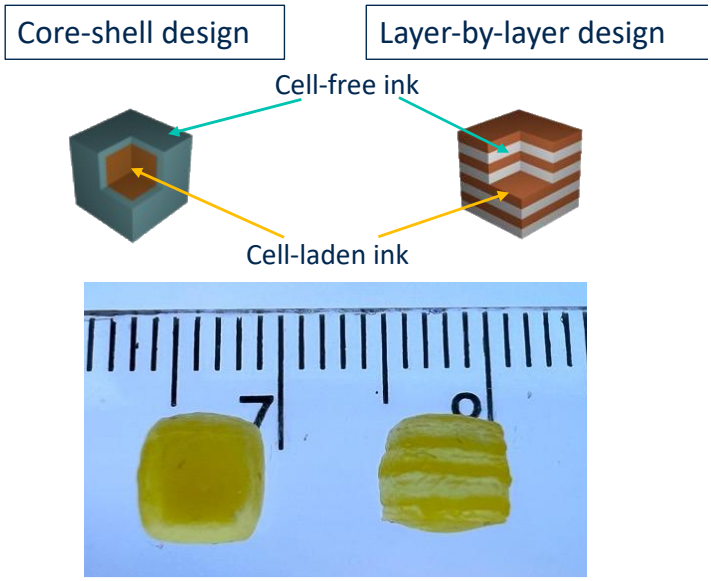


***Figure 6. 3: Core-shell and layer-by-layer patterning of curcumin loaded yeast cells in 3D printed structures.***

2.7. Release of curcumin from the tissue-like encapsulation systems during *in vitro* digestion

*2.7.1. Release kinetics*

Simulated gastric and intestinal fluid were prepared according to the protocol developed by Minekus et al. [219] with some modifications. When preparing the electrolyte stock solutions for the digestion fluids, $NaHCO_3$ was replaced with equal molarity of NaCl and $(NH_4)_2CO_3$ was replaced with $(NH_4)_2SO_4$ to avoid a change of pH during storage. Immediately before use, 2.5 mg/mL (2660 units/mL) pepsin was added to the simulated gastric fluid (SGF) and the pH was adjusted to pH 3; 10 mg/mL (lipase activity 80 units/mL) pancreatin and 5 mg/mL bile salts were added to the simulated intestinal fluid (SIF) and the pH was adjusted to 7. The original bile salt concentration in SIF was 5 mg/mL. A concentration much higher than the physiologically relevant value was used in this study to accelerate the release so that detectable amount of curcumin released could be measured within a reasonable duration.

The tissue-like encapsulation systems were subject to a sequential *in vitro* digestion. 3 printed cubes (~0.125g/cube) were transferred into a 50 mL centrifuge tube. 4 mL of SGF pre-warmed to 37 °C was added to each tube and incubated in a shaking incubator at 37 °C and 100 rpm for 2 hours. At the end of the gastric phase, the SGF was discarded, and 4 mL of SIF pre-warmed to 37 °C was added. At 1, 2, 3, 5, 7, 10 hours of the intestinal phase, 0.5 mL of the SIF was aliquoted and centrifuged at 7235 xg for 1 min to remove the precipitate in SIF. The small intestinal phase was extended to 10 hours because limited amount of curcumin was released with a physiologically relevant duration (3 hours). Fresh SIF was added to replenish the aliquoted volume. The absorbance of the supernatant was measured at 422 nm in a 96-well plate using a SpectraMax340 microplate reader (Molecular Devices, San Jose, CA, USA). The

concentration of curcumin in the supernatant was calculated according to an established calibration curve. Curcumin released during the gastric phase was very minimal and below the detection limit of the current method, thus was not reported. At the end of the simulated digestion, retained curcumin in the cubes were extracted using DMSO and quantified using the microplate reader after proper dilution. Cumulative release of curcumin at each time point was calculated from the measurements, accounting for the fresh SIF replenishment at each sampling time point. The whole set of experiments was repeated three times.

*2.7.2. Fluorescence microscopic characterization*

To visualize the migration of curcumin within the tissue-like encapsulation systems during *in vitro* digestion, the printed cubes collected 0, 1, 3, and 5 hours into the intestinal phase were sliced using an oscillating tissue slicer (OTS-4500, Electron Microscopy Sciences, Hatfield, PA, USA). 200 $\mu m$ thick specimens were sectioned, transferred to glass slides and imaged with a Leica TCS SP8 Multiphoton microscope (Leica Microsystem Inc.) equipped with a Mai Tai DeepSee laser. The excitation and emission wavelengths for curcumin were set to 760 nm, 475 - 575 nm.

## 3. Results

### 3.1. Rheological properties of food inks

Using a Box-Behnken design, 13 different food ink formulations with three components: LMP, CNC, and $CaCl_2$ were developed (Table S6. 3). The ranges of total polysaccharide concentration and crosslinking density were chosen based on alginate or pectin-based bioink formulations reported in previous studies, as well as preliminary experiments [303,307]. These

formulations were evaluated for rheological characteristics, including the shear-thinning, viscoelastic, and thixotropic properties.

### *3.1.1. Shear-thinning properties*

In the steady-state flow test, the viscosity of all the food inks decreased with the increasing shear rate in the range from 0.1 $s^{-1}$ to 100 $s^{-1}$, indicating a shear thinning behavior. *Figure 6. 4* demonstrates the characteristic shear thinning behavior of three representative formulations. All formulations had a flow index (n) (Equation 6. 4) lower than one (Table S6. 4), confirming their pseudoplastic nature.

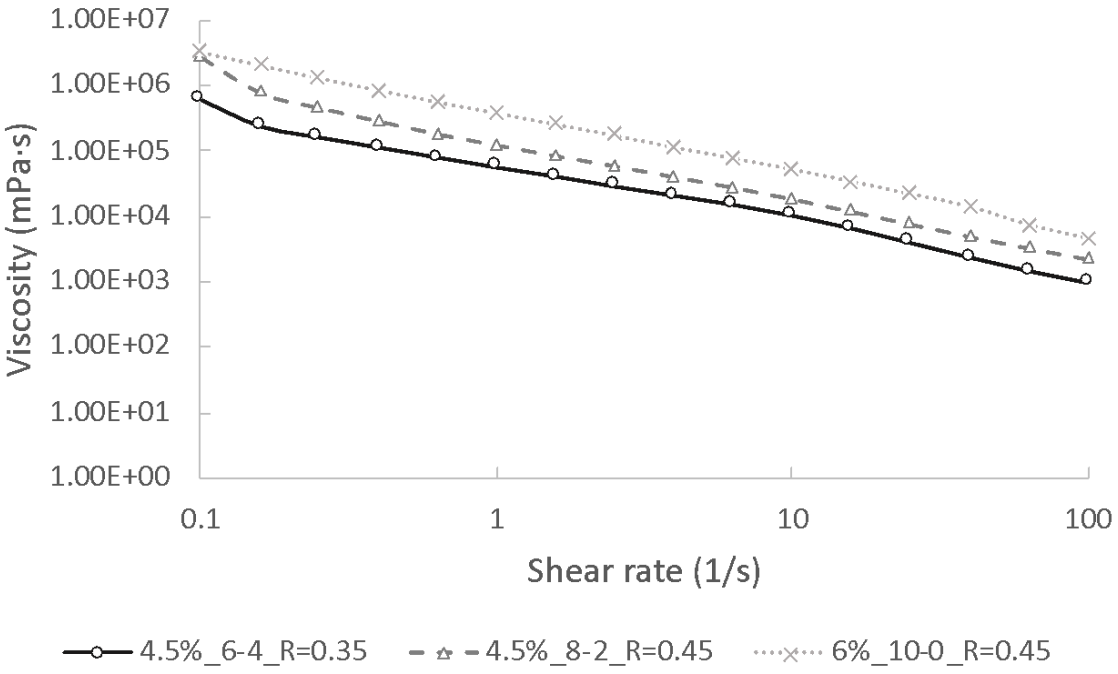


***Figure 6. 4: Shear thinning property of three representative bioinks: 3% total polysaccharide/6-4 pectin-to-CNC ratio/R=0.45 crosslinking density (4.5%/6-4/R=0.35); 4.5%/8-2/R=0.45; 6%/10-0/R=0.45.***

### *3.1.2. Viscoelastic properties of food inks.*

The evolution of G'and G" of food inks during the strain amplitude sweep is shown in *Figure 6. 5*. G' and G" indicate the elastic and viscous properties of a material

respectively. The linear viscoelastic region (LVR) of the food ink compositions was found between 1% and 10% strain amplitude, above which the gels fluidized and large reduction in G' was observed. Above the limit of linearity, G' decreased monotonically, while G" increased first before it started to decrease. This phenomenon is described as the weak strain overshoot beyond the LVR [308]. Such a phenomenon was observed for all food inks except 3%_8-2_R=0.35, which contained 3% total polysaccharide, 8-2 LMP-to-CNC ratio, and crosslinking density of 0.35. Table S6. 4 summarizes the yield stress and flow transition index of the food inks developed in this study. Yield stress would give an indication of the relative ability of the gels to flow during extrusion. The flow transition index reflects the brittleness of the hydrogels: the closer the index is to 1, the higher is the tendency of the hydrogel to undergo brittle fracture [309]. Higher total polysaccharide content, higher pectin fraction, and higher crosslinking density all led to a larger yield stress and a narrower flow transition region. *Figure 6. 5* shows the frequency-dependence of G' and G" for the same set of food inks, in the range of 0.06 - 100 rad/s. In this range, G' was greater than G" and was relatively frequency-independent for almost all the food inks, indicating that the gels behaved like an elastic solid, which is common for a covalently crosslinked interwoven polymer network [310]. As shown in Table S6. 4, all the inks with crosslinking density R=0.55 had loss factor smaller than 0.1, and all the ones with R=0.35 had loss factor greater than 0.1, with a few being above 0.2. Loss factor reflects the gelation state of hydrogels and small loss factor indicates dominance of the elastic nature of the material, correlating to a stronger and a more crosslinked gel [311].

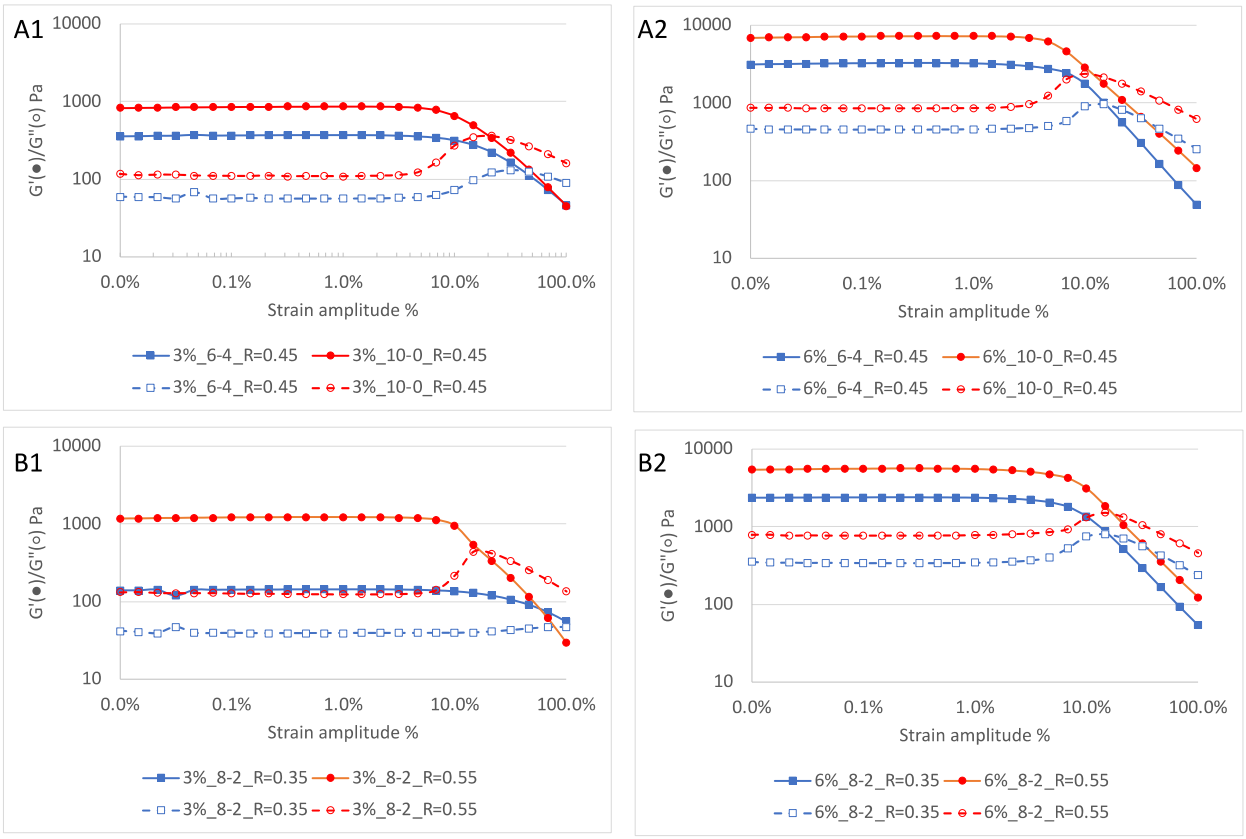


***Figure 6. 5: Storage modulus G' (solid line) and loss modulus G" (dashed line) vs. strain amplitude at ω = 1 rad/s for food inks composed of 3% (A1, B1) and 6% (A2, B2) total polysaccharide.*** Subplots A1 and A2 showed the effect of different pectin-to-CNC ratio; subplots B1 and B2 showed the effect of different crosslinking density.

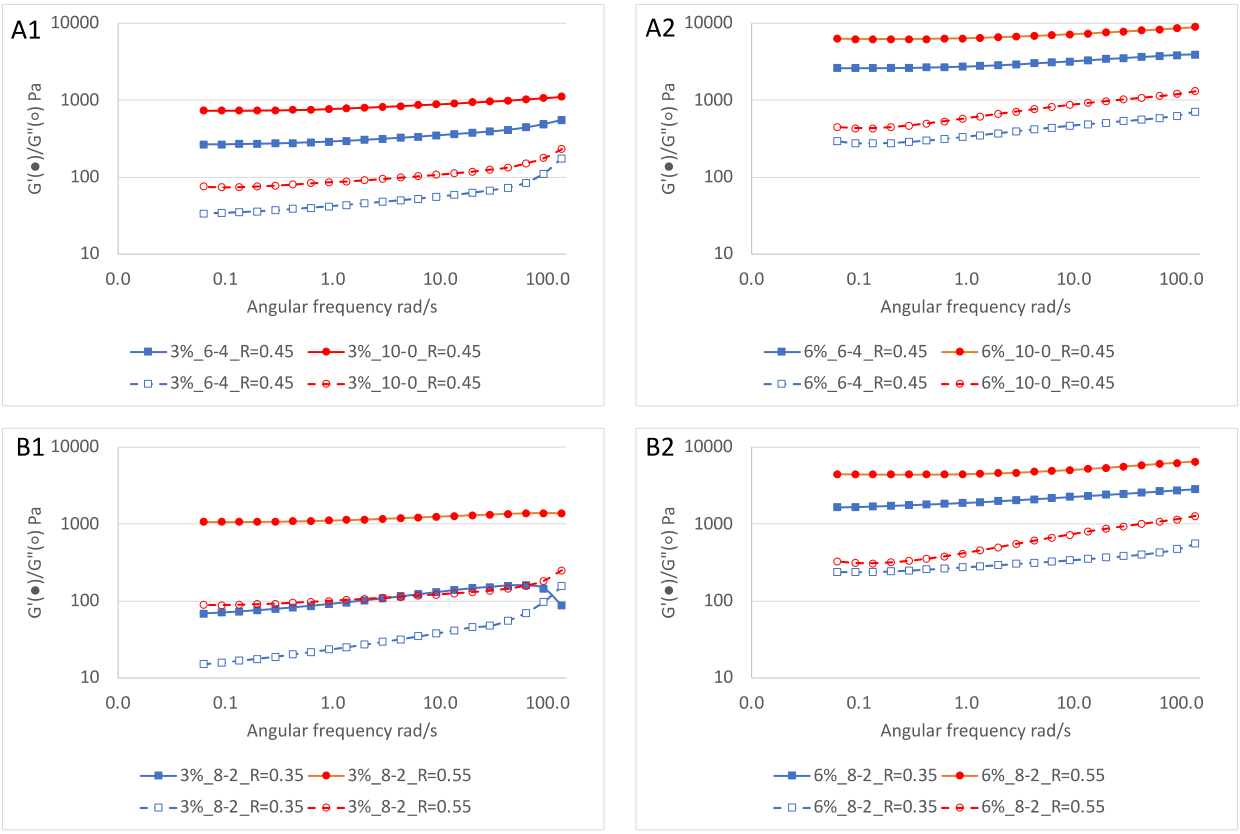


***Figure 6. 6: Storage modulus G' (solid line) and loss modulus G" (dashed line) vs. angular frequency at 1% strain amplitude for food inks composed of 3% (A1, B1) and 6% (A2, B2) total polysaccharide.*** Subplots A1 and A2 showed the effect of different pectin-to-CNC ratio; subplots B1 and B2 showed the effect of different crosslinking density.

### *3.1.3. Thixotropic properties of food inks.*

Thixotropic properties of the food inks was tested in a three-step recovery test. When subjected to a high shear rate, all food inks showed a rapid decrease in viscosity as expected given their shear thinning nature. The ability of the viscosity to recover after reducing the shear rate indicated how likely the printed filaments would spread after printing, thus was regarded as an indicator of shape fidelity of the printed objects. *Figure 6. 7* shows the viscosity change of the three representative food inks during the three-step recovery test: 4.5%_6-4_ R=0.35, 4.5%_8-2_0.45, and 6%_10-0_0.45. It could be observed that ink 4.5%_6-4_0.35 required a longer time to recover to an equilibrium

viscosity, compared with the other two inks. Also, as shown in Table S6. 4, among the three inks, 6%_10-0_0.45 had the highest recovery index, defined as the ratio between the mean viscosity during step 3 to that during step 1, followed by 4.5%_8-2_0.45, while 4.5%_6-4_0.35 was the lowest. Inks with low recovery indices and longer recovery times were more susceptible to spreading post printing, resulting in poor shape fidelity.

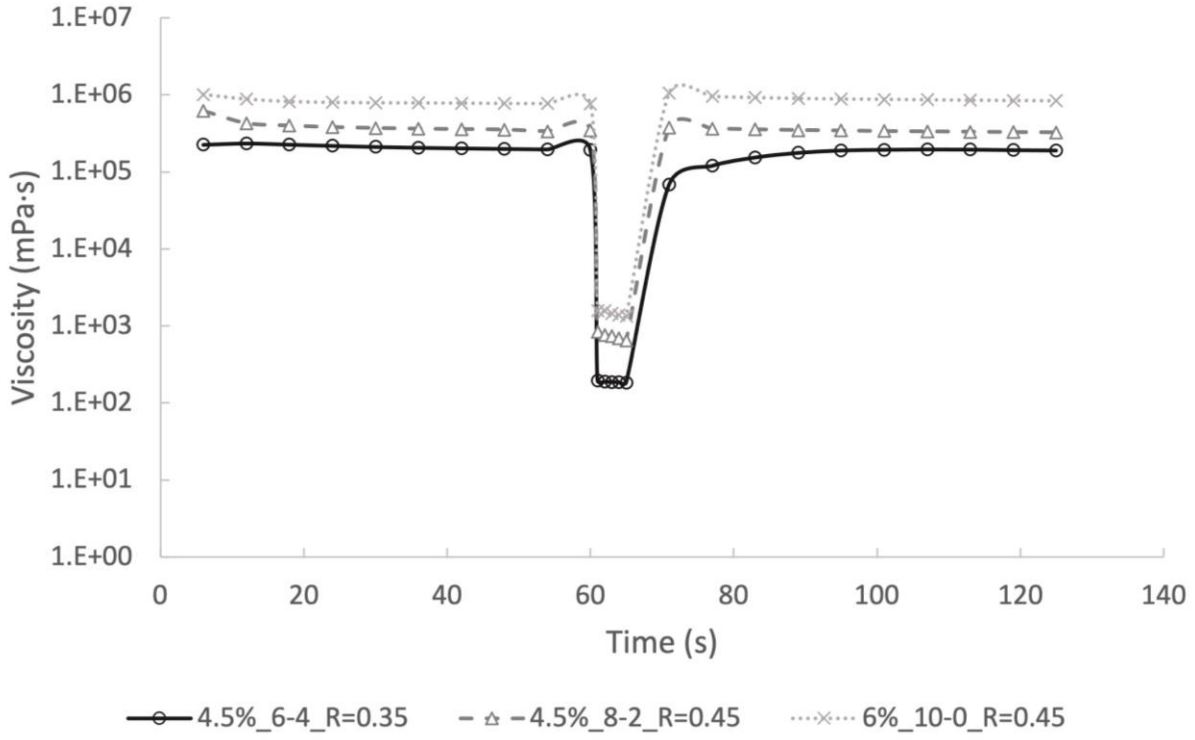


***Figure 6. 7: Viscosity recovery of selected bioinks: 3% total polysaccharide_6-4 pectin-to-CNC ratio_R=0.45 crosslinking density (4.5%_6-4_R=0.35); 4.5%_8-2_R=0.45; 6%_10_R=0.45.***

3.2. 3D printing and printability characterization

The 13 food ink formulations were printed into filaments using the printing parameters optimized for each ink, as specified in Table S6. 2. All the inks were printed with the same nozzle moving speed (6 mm/s) but with different extrusion pressure and layer height (the distance in z direction that the nozzle moved up after printing each layer). The extrusion

pressure was optimized to address variations in the rheological characteristics of the inks and the layer height was adjusted to account for the different degrees of expansion of the printed filaments upon extrusion. During printing, it was observed that most of the inks were deposited with some lag time after the pressure was applied, due to their viscoelastic nature. Three ink formulations appeared to be very thin and experienced extensive spreading after deposition: 3%_6-4_R=0.45, 3%_8-2_0.35, and 4.5%_6-4_0.35. The ink formulations with the following compositions 4.5%_10-0_0.55, 6%_10-0_0.45, 6%_8-2_0.55 formed strong gels that required very high pressure to overcome the initial yield stress to flow. The deposition of these inks was unsmooth and inconsistent, often resulting in broken filaments. Two of the inks with 3% total polysaccharide ( 3%_10-0_0.45, 3%_8-2_0.55) did not require high extrusion pressure but exhibited un-smoothness during printing. The rest of the inks could be successfully printed with a continuous deposition and good shape fidelity based on visual observation. The printing parameters used for these inks generally fell into the range of 15 - 25 psi of pressure and 0.31 - 0.35 mm layer height (Table S6. 2). Besides the visual inspection, the printed filaments were imaged under optical microscope and measured for filament width and roughness, as summarized in Table S6. 4. *Figure 6. 8* shows a scatterplot of filament roughness vs. relative width index together with the thresholds selected to binarize these two metrics. The threshold levels were determined based on preliminary experiments (Table S6. 1). Samples falling into each of the four width-roughness label combinations were color-coded and kernel density estimation plots were used to visualize the distribution of inks in each group based on the selected ink printability metrics.

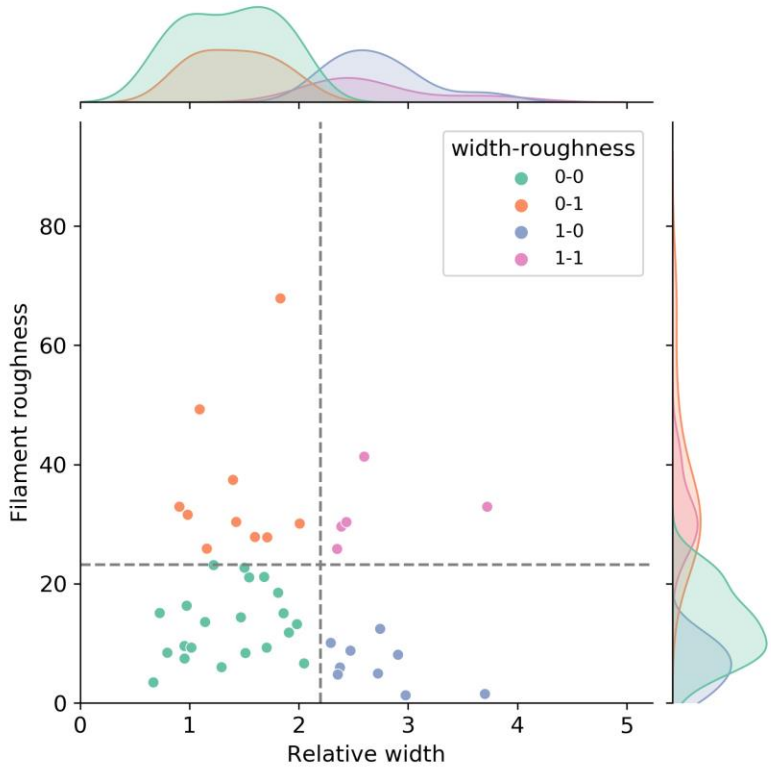


***Figure 6. 8: Scatterplot of filament roughness vs. relative width index, color-coded by the width-roughness combination label.*** The dashed lines indicated the thresholds used to binarize the two metrics. The kernel density estimation plots were used to visualize the distribution of inks in each group regarding the two metrics. Samples in the left bottom quadrant (green dots) are inks classified as good inks (label 0 for the binary quality label).

To demonstrate the ability of the developed inks for high-resolution printing, three ink formulations with width-roughness label of 1-0, 0-0, and 0-1 respectively were selected for test printing of a 3D structure, corresponding to formulations 4.5% _6-4_R=0.35, 4.5%_8-2_0.45, and 6%_10-0_0.45. With each ink, a 5*5*5 $mm^3$ 3D grid structure with 1 mm line space (*Figure 6. 9 A-C*) and an 8 mm* 8mm 3-layer grid with 1 mm spacing (*Figure 6. 9 D-F*) was printed. Both the 3D grid cubes and the 3-layer grid structures were submerged in 90 mM $CaCl_2$ solution after printing. The dimensions of the objects shown in *Figure 6. 9* were smaller than the designed values due to crosslinking. Although the deposition of ink 4.5%_6-

4_0.35 was smooth and uniform, the 3D grid cube printed with this ink showed round edges and as more layers were deposited, the base of the cube partially collapsed under the influence of gravity, indicating low shape fidelity. *Figure 6. 9 D-F* provides a better visualization of whether the filaments within a grid fused together when printed at a 1mm line spacing. Based on the observations, we concluded that formulation 4.5%_6-4_0.35 was too thin to be suitable 3D printing inks. On the contrary, formulation 6%/10-0/0.45 could not be deposited smoothly and intermittent breaking of filaments were observed during printing. As a result, the printed objects (*Figure 6. 9 C, F*) showed apparent defects. Formulation 4.5%_8-2_0.45 could be deposited regularly and uniformly, and the printed structures showed clean and sharp edges, the 1 mm line spacing was well-maintained as designed as well (*Figure 6. 9* B,E). Smooth deposition and high shape fidelity made this formulation a good candidate for 3D printing.

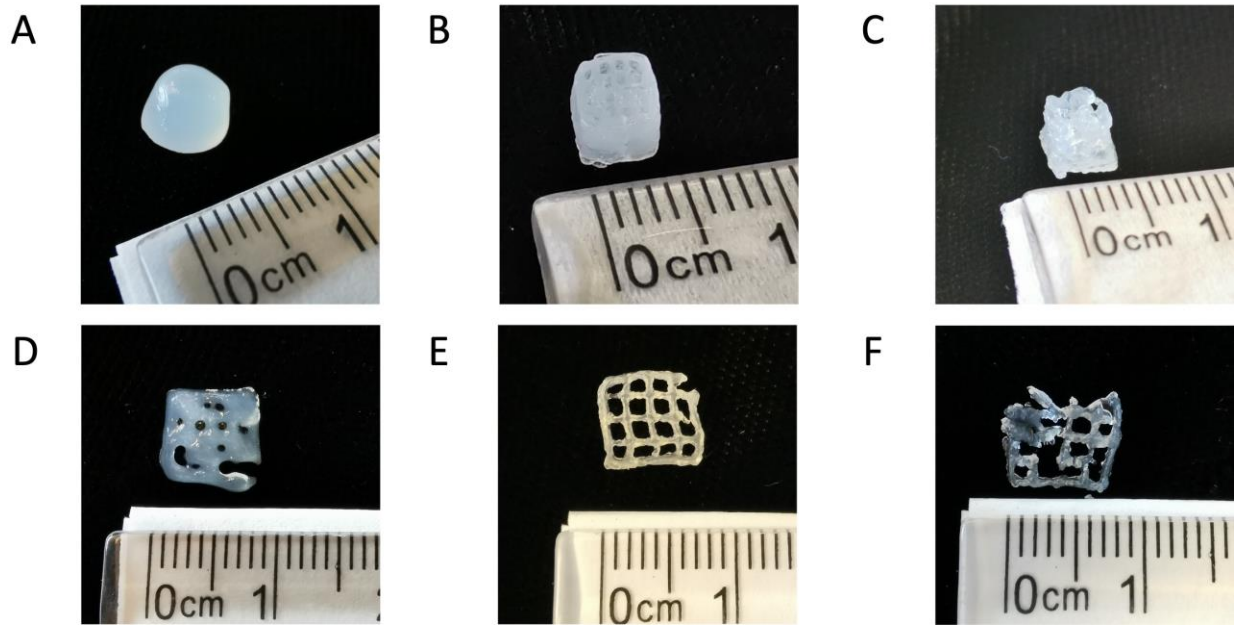


***Figure 6. 9: Representative samples of printed grid cubes (5*5*5 $mm^3$ with 1mm gap) (A, B, C) and 3-layer grids (8*8 $mm^2$ with 1mm gap) (D, E, F) using three food ink formulas: (A, D). 4.5% total polysaccharide/6-4 pectin-to-CNC ratio/R=0.35 crosslinking density (width-***

***roughness label 1-0); (B, E) 4.5%/8-2/R=0.45 (width-roughness label 0-0); (C, F) 6%/10-0/R=0.45 (width-roughness label 0-1).***

3.3. Regression models of rheological properties and printability measurements on ink formulation parameters

As shown in *Figure 6. 10A*, many of the rheological characterizations were significantly correlated. For example, the strong positive correlation among storage modulus, loss modulus, yield stress, and recovery index confirmed that these measurements were all positively associated with stronger gels. Additionally, the loss factor and flow transition index showed significantly negative correlation with the abovementioned measurements since stronger gels would have lower loss factor and shorter flow transition region. Flow index did not have significant correlation with any of the other rheological characterizations. Due to the high collinearity, PCA was implemented to reduce dimension of the variable space and determine the principal components of rheological measurements. The PCA biplot (*Figure 6. 10B*) showed that most of the rheological measurements had high loadings in the space of the first principal component (PC), except the fitted flow index (n), which was more associated with the second PC. This was consistent with the insignificant correlation between flow index and other variables. The first two PCs accounted for 57.9% and 16.6% of the total variance and the first four PCs accounted for more than 90% of the total variance (*Figure 6. 10C*).

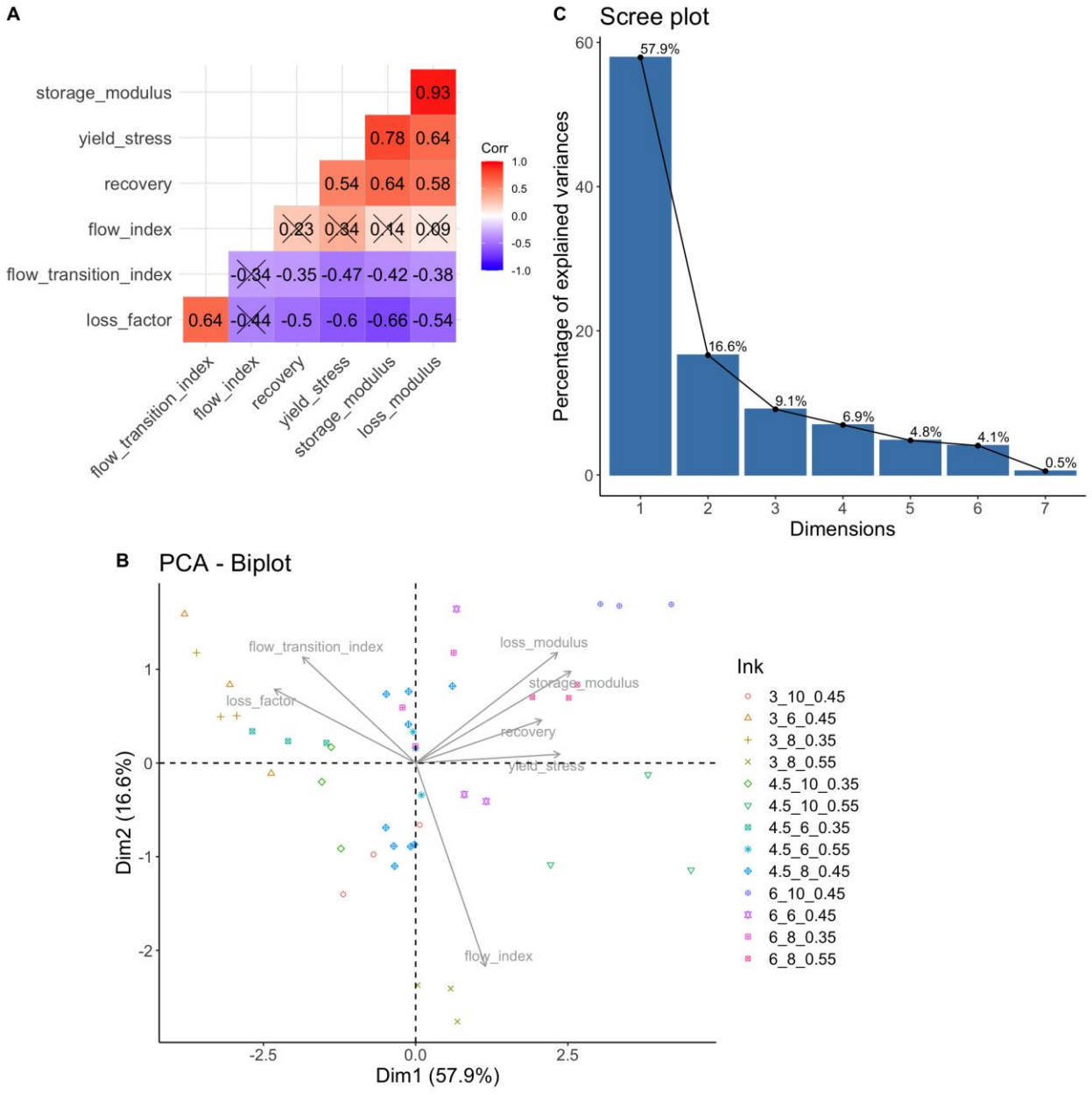


***Figure 6. 10: Correlation matrix (A), PCA biplot (B), and PCA scree plot (C) of the rheological characterizations of food inks.*** The correlation indices were crossed out if the correlation was not significant ($p>0.05$) for the pair of variables. The nomenclature for the ink formulation is **"**% total polysaccharide_pectin fraction_crosslinking density**".**

RSM was used to investigate the effect of the formulation parameters on the rheological and printability measurements. The response surfaces for log(filament width), log(filament roughness), and the first 2 PCs from the PCA of rheological measurements were constructed

based on the least square regression models as specified in Equation 6. 7. The regression coefficients ($\beta_1 - \beta_6$ in *Equation 4*), their p-values and $R^2$ of the models are summarized in Table 6. 2. *Figure 6. 11* displays the response surface plots of the four response variables as a function of the total polysaccharide and the crosslinking density at different pectin fraction levels. It could be observed from the response surfaces for log(filament width) (*Figure 6. 11A*) that it decreased with increasing total polysaccharide, pectin fraction, and crosslinking density, and the response surfaces had some curvature: a steeper reduction in filament width was observed with increasing total polysaccharide at lower crosslinking density; the effect of increasing crosslinking density on reducing filament width was more obvious at lower total polysaccharide concentration and lower pectin fraction. The observations were consistent with the regression coefficients from the least square regression model in Table 6. 2**.** The main effects of the three formulation parameters on filament width were all significant. Two interaction terms: total polysaccharide - crosslinking density, pectin fraction - crosslinking density included in the final model, although not significant, did improve the overall model quality. The response surface plot for log(filament roughness) (*Figure 6. 11B*) shows that it was positively associated with increasing pectin fraction and crosslinking density but not significantly influenced by the total polysaccharide, and the surfaces were flat and parallel, indicating little interaction effects. The 1$^{st}$ principal component of rheological measurements, PCA (rheo_PC1) was positively associated with total polysaccharide, pectin fraction, and crosslinking density (*Figure 6. 11C*)**.** Also, since pectin was the only element which could be crosslinked by calcium, not CNC, the higher was the mass fraction of pectin in the gel, the more dominant was the crosslinking density effect on the rheological properties. Table 6. 2 shows that the regression coefficient for total polysaccharide is positive and significant,

consistent with the response surface plots. However, the regression coefficients of crosslinking density and pectin fraction on rheo_PC1 were both negative, opposite to what was observed in *Figure 6. 11C*. This could be attributed to the significant interaction term between crosslinking density and pectin fraction, which had a large effect. As a result, after accounting for the interaction terms (X2*X3 in *Equation 4*), the effect size of each individual variable (X2, X3) diminished or even have a reversed sign. Therefore, no standalone interpretation should be made for regression coefficients of individual variables when their interaction terms were included in the model. Rheo_PC2 response surfaces (*Figure 6. 11D*) show strong interactions among formulation parameters and one relatively clear trend was that at the lowest total polysaccharide level, rheo_PC2 decreased with increasing crosslinking density and increasing pectin fraction. Among the four response variables, rheo_PC1 was the most well-explained by the linear regression model, with the highest adjusted $R^2$ score of 0.93. All the other response variables were not very well-explained since their adjusted $R^2$ was only around 0.5. The unexplained variance could be attributed to nonlinear relationships between the formulation parameters and the response variables and high-order terms that were not included in the current model (*Equation 4*).

**Table 6. 2: Regression coefficients, *p-values* and adjusted $R^2$ of the ordinary least-square regression models of filament width, roughness, rheo_pc1, and rheo_pc2 as response variables, and formula parameters as covariates.**

| Term | Filament width [a] | | Filament roughness [a] | | Rheo_PC1 | | Rheo_PC2 | |
|---|---|---|---|---|---|---|---|---|
| | Estimate | P-value | Estimate | P-value | Estimate | P-value | Estimate | P-value |
| Intercept | 10.7 | 3.13e-10* | -1.62 | 0.0574 | -5.14 | 0.0689 | 15.3 | 8.48e-3* |
| Total polysaccharide | -0.347 | 0.0463* | -0.151 | 0.0719 | 1.29 | <2e-16* | -4.20 | 1.87e-5* |
| Pectin fraction | -3.01 | 0.0221* | 3.11 | 8.49e-6* | -9.14 | 9.63e-3* | -2.78 | 0.634 |
| Crosslinking density R | -6.43 | 0.0273* | 5.45 | 6.32e-5* | -9.30 | 0.129 | -17.7 | 0.108 |
| TotalPS:PC_frac[b] | / | / | / | / | / | / | 2.26 | 2.83e-3* |
| TotalPS:R[b] | 0.5378 | 0.154 | / | / | / | / | 5.96 | 1.50e-4* |
| PC_frac:R[b] | 4.60 | 0.105 | / | / | 30.0 | 2.16e-4* | -17.9 | 0.0999 |
| **Adjusted $R^2$** | 0.47 | | 0.51 | | 0.93 | | 0.51 | |

[a] log transformation was performed on filament width and roughness before regression.

[b] Coefficients of interaction terms excluded from the final model after the AIC guided model selection process were not shown.

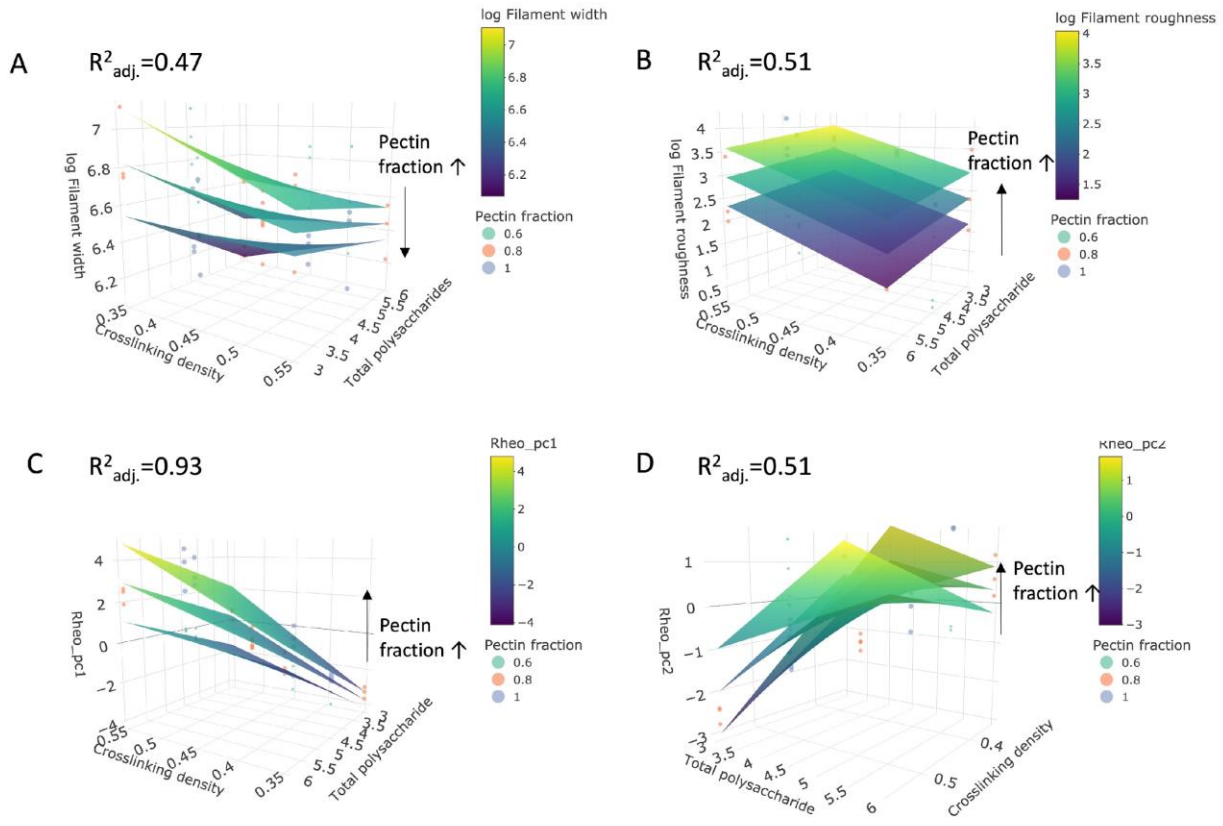


***Figure 6. 11: Response surface plots of (A) printed filament width, (B) filament roughness, (C) rheo_PC1, and (D) rheo_PC2 as a function of formula parameters.*** The orientation of the axis of the 3D plots was adjusted to better visualize the response surfaces.

3.4. Machine learning enabled prediction of food inks' printability

The RSM results reflected that the formulation parameters had a linear relationship with Rheo_PC1 (adj. $R^2 = 0.93$), but not with the printability metrics, indicating the need for nonlinear models. Therefore, we constructed random forest classification models to predict the ink's width and roughness labels, as well as the binary quality label, classified using criteria described in Table S6. 1. Three feature sets were used to predict the labels: formulation parameters alone, rheological measurements alone, or rheological measurements + formulation parameters.Error! Reference source not found. Table 6. 3 summarizes the

cross-validation prediction accuracy for the random forest classifiers on each label using the three feature sets. The prediction accuracy did not show a sizable difference between classifiers trained with the rheological measurements alone or with formulation + rheology. However, training with formulation parameters alone resulted in 5 - 10% lower accuracy compared to the other two feature sets. This comparison implicated that the rheological measurements formed a better feature set than the formulation parameters for ink printability prediction and adding formulation parameters to the model did not further improve the prediction accuracy. Such results were expected since the linear regression model showed that the formulation parameters were highly associated with the Rheo_PC1. Using the rheology only feature set, 0.97 and 0.82 mean accuracy was achieved for the prediction of the width label in the train and test sets respectively, and 0.88 and 0.82 for the roughness label. After a closer inspection on the misclassified samples, it was found that the most frequently misclassified samples were those predicted to print thinner and smoother filaments based on their rheological profile, but the actual prints had filaments width and roughness larger than the cutoff thresholds. There was some degree of overfitting in the models for both labels. It is common for the training set to have a higher prediction accuracy than the test set. Given the small size of the test set (n=15) in this study, even one noisy sample could reduce the accuracy of the prediction (1/15≈7%). Such variability in the test set prediction accuracy is reflected by the higher standard deviation in the repeated 5-fold cross-validation accuracy score compared to the training set (Table 6. 3). Table S6. 2 summarized the rheological measurements of inks in each label class and Figure S6. 1 visualized their distributions stratified by the labels. Inspecting these results provided insight into the feature importance of each rheological measurement in classifying the ink samples with different width and

roughness labels. Inks that printed thinner filaments (width label 0) had significantly lower flow transition index, loss factor, and larger G', G", yield stress, all of which correspond to stronger gels with higher brittleness and more resistance to flow. On the other hand, smoother filaments (roughness label 0) often resulted from inks with significantly larger flow transition index, loss factor, and lower yield stress.

**Table 6. 3: Cross validation classification accuracy (mean ± sd) for the width and roughness label, and the binary quality label with indirect and direct prediction approaches using rheological measurements and/or formulation parameters.**

| Ink quality metrics | Feature set | Data split | Accuracy |
|---|---|---|---|
| **Relative filament width** | **Formula + rheology** | **Train** | 0.97±0.03 |
| | | **Test** | 0.81±0.10 |
| | **Formula only** | **Train** | 0.89±0.02 |
| | | **Test** | 0.74±0.12 |
| | **Rheology only** | **Train** | 0.97±0.03 |
| | | **Test** | 0.82±0.10 |
| **Filament roughness** | **Formula + rheology** | **Train** | 0.90±0.03 |
| | | **Test** | 0.78±0.12 |
| | **Formula only** | **Train** | 0.84±0.03 |
| | | **Test** | 0.76±0.12 |
| | **Rheology only** | **Train** | 0.88±0.03 |
| | | **Test** | 0.82±0.10 |
| **Binary ink quality** (Indirect prediction) | **Formula + rheology** | **Train** | 0.88±0.03 |
| | | **Test** | 0.86±0.11 |
| | **Formula only** | **Train** | 0.79±0.04 |
| | | **Test** | 0.78±0.13 |
| | **Rheology only** | **Train** | 0.88±0.04 |
| | | **Test** | 0.87±0.08 |
| **Binary ink quality** (Direct prediction) | **Formula + rheology** | **Train** | 0.92±0.02 |
| | | **Test** | 0.74±0.13 |
| | **Formula only** | **Train** | 0.82±0.03 |
| | | **Test** | 0.70±0.15 |
| | **Rheology only** | **Train** | 0.92±0.02 |
| | | **Test** | 0.75±0.14 |

**Table 6. 4: Summary of rheological measurements for cell-free inks (mean ± SD) stratified by width labels, roughness labels, and the width-roughness combinations.**

| Labels | Class | Flow index | Flow transition index | Storage modulus (Pa) | Loss modulus (Pa) | Loss factor | Recovery | Yield stress (Pa) |
|---|---|---|---|---|---|---|---|---|
| Width | 0 | 0.47 ± 0.1 | 2.22 ± 0.83 | 2475.46 ± 1857.57 | 230.97 ± 129.03 | 0.11 ± 0.03 | 0.79 ± 0.15 | 115.17 ± 101.29 |
| | 1 | 0.44 ± 0.12 | 2.87 ± 1.05 | 885.7 ± 1065.13 | 104.09 ± 142.82 | 0.15 ± 0.06 | 0.7 ± 0.16 | 44.39 ± 27.99 |
| | P value[a] | 0.411 | 0.03* | 0.005* | 0.005* | 0.003* | 0.063 | 0.014* |
| Roughness | 0 | 0.44 ± 0.08 | 2.66 ± 0.92 | 1671.67 ± 1495.92 | 180.7 ± 132.56 | 0.13 ± 0.04 | 0.75 ± 0.14 | 67.56 ± 45.38 |
| | 1 | 0.49 ± 0.15 | 1.93 ± 0.8 | 2599.26 ± 2222.3 | 213.08 ± 168.99 | 0.1 ± 0.04 | 0.8 ± 0.19 | 144.33 ± 133.0 |
| | P value[a] | 0.116 | 0.011* | 0.104 | 0.485 | 0.015* | 0.366 | 0.006* |
| Combined | 0 | 0.45 ± 0.07 | 2.43 ± 0.89 | 1954.52 ± 1515.7 | 203.87 ± 106.25 | 0.12 ± 0.03 | 0.76 ± 0.12 | 79.35 ± 47.1 |
| | 1 | 0.46 ± 0.13 | 2.41 ± 1.0 | 2003.92 ± 2050.1 | 180.67 ± 172.96 | 0.12 ± 0.05 | 0.77 ± 0.19 | 105.23 ± 116.93 |
| | P value[a] | 0.707 | 0.926 | 0.928 | 0.597 | 0.836 | 0.901 | 0.348 |

[a] The p values indicated the statistical significance of t test between class 0 and 1 for each rheological measurement. Significant difference ($p<0.05$) between classes were annotated by *.

Formulations classified as good inks (class 0 in the binary quality label) were the ones that achieved a balance between the two desirable but conflicting printing properties: thin filament width and low roughness, which made differentiating them from other formulations a challenging task. As described in Section 2.4, a direct and an indirect approach was taken to predict the binary quality label. In direct prediction, the binary quality label was directly predicted as the response using the three feature sets with cross-validation. The indirect approach combined the prediction results from the previously trained models on the width label and roughness label to obtain a predicted binary quality label in the same way as the true binary quality label was generated. As shown in Table S6. 4, when using the rheological

measurements as the feature set, the direct prediction approach achieved higher mean accuracy during training (0.92) compared to the indirect approach (0.88). However, it also had a higher degree of overfitting, reflected by a lower mean accuracy during testing (0.75) than the indirect approach (0.87). On the other hand, the indirect method had the same level of accuracy during training and testing, indicating limited overfitting. It could also be noticed that the mean accuracy of predicting the binary quality label with the indirect approach was higher than both the width and roughness models. The binary quality label combined the width and roughness criteria, but it sufficed to only differentiate samples with the 0-0 width-roughness combination from all other combinations. Such a scheme allowed it to absorb some prediction errors in the separate models based on width and roughness measurements and improve the prediction accuracy of the binary quality label.

### 3.5. Rheological characterization of cell-laden inks

After printability assessment, the ink formula with 4.5% LMP and crosslinking density R=0.35 was selected to prepare the cell-laden ink. To evaluate whether incorporating yeast cells would change the rheological properties of the inks, ink formulations containing 0, 2.25, 4.5, and 6.75 w/v% yeast cells (wet mass basis) were prepared and subject to the same rheological tests as the cell-free inks. The results are summarized in Table 6. 5. Among all the measurements, the only significant difference was observed in storage modulus and loss factor between the 0% and 6.75% cell density inks, indicating that the 6.75% cell ink was more elastic than the cell-free ink with the same LMP concentration and crosslinking density. At lower cell densities, adding cells into the formulate ink did not change its rheological properties significantly.

**Table 6. 5: Summary of rheological measurements for cell-laden inks formulated with 4.5% pectin and crosslinking density R=0.35.**

| Cell density (%) | G'(kPa) | G"(kPa) | Loss factor | Yield stress (kPa) | Flow stress (kPa) | Flow transition index |
|---|---|---|---|---|---|---|
| 0 | 16.6±3.734 | 2.02±0.380 | 0.123±0.005 | 0.782±0.171 | 0.741±0.059 | 0.971±0.171 |
| 2.25 | 20.2±3.74 | 2.27±0.288 | 0.113±0.008 | 1.23±0.175 | 0.981±0.085 | 0.807±0.092 |
| 4.5 | 29.6±11.5 | 2.84±0.698 | 0.099±0.016 | 1.58±0.546 | 1.36±0.608 | 0.844±0.119 |
| 6.75 | 37.8±8.31 | 3.41±0.673 | 0.090±0.005 | 1.26±0.393 | 1.31±0.639 | 1.02±0.203 |

### 3.6. 3D patterning of curcumin-loaded yeast cells in tissue-like structures and curcumin release during *in vitro* digestion

The ink with 4.5% cells was used to 3D print the tissue-like structures. The curcumin concentration in the printed structures, normalized against the wet mass, were132.47$\pm$8.28 $\mu g/g$ for the core-shell structure and 161.58$\pm$28.75 $\mu g/g$ for the layer-by-layer structure. By design, the two types of printed structures should have the same volume of cell-laden ink, thus the same curcumin concentration. The small discrepancy originated from the deviation of real-life printing from the design, and the variation in printing across different cubes.

After the 2-hour gastric phase, no detectable amount of curcumin was released. Subsequently, an accelerated dissolution test in SIF with elevated bile salt concentration was conducted. The release kinetics of curcumin in the modified SIF were monitored up to 10 hours for the two tissue-like structures. As shown in *Figure 6. 12*, the release process did not reach an equilibrium for either structure after 10 hours. At the end of 10 hours, 31.81 $\pm$0.49% and 56.01$\pm$1.40% of curcumin was released from the layer-by-layer and core-shell structures respectively. The layer-by-layer structure had a shorter lag phase than the core-shell design before released curcumin could be detected in the solution. Also, the layer-by-layer structure had a faster release rate of curcumin than the core-shell structure.

*Figure 6. 13* visualizes the change in curcumin localization within the printed structures throughout the intestinal digestion process. Before digestion, the curcumin resided inside yeast cells. Since the cell-free ink would not be fluorescent, only the cell-laden ink could be visualized, showing a stripped pattern for the layer-by-layer structure, and a solid square (core) for the core-shell structure. For both types of structures, a curcumin-dense ring was formed at the surface of the structure as early as 1 hour in the SIF. For the core-shell structure, the ring was homogeneous in terms of fluorescence intensity, while in the layer-by-layer structure, higher signal intensity was observed at the edge of cell-laden bands, especially at early hours during the digestion.

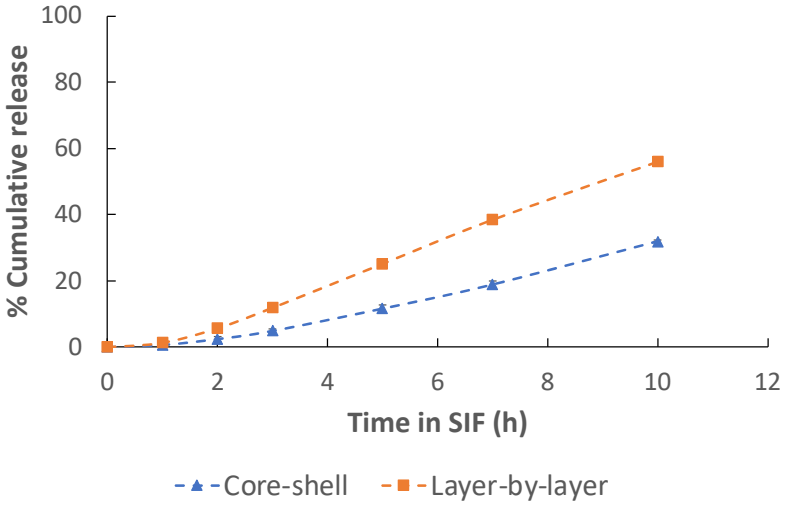


***Figure 6. 12: % Cumulative release of curcumin from the core-shell and layer-by-layer tissue-like structures during in vitro intestinal digestion.*** The markers and error bars indicate the mean and standard deviation (n=3) of the % cumulative release at each time point for the two structures.

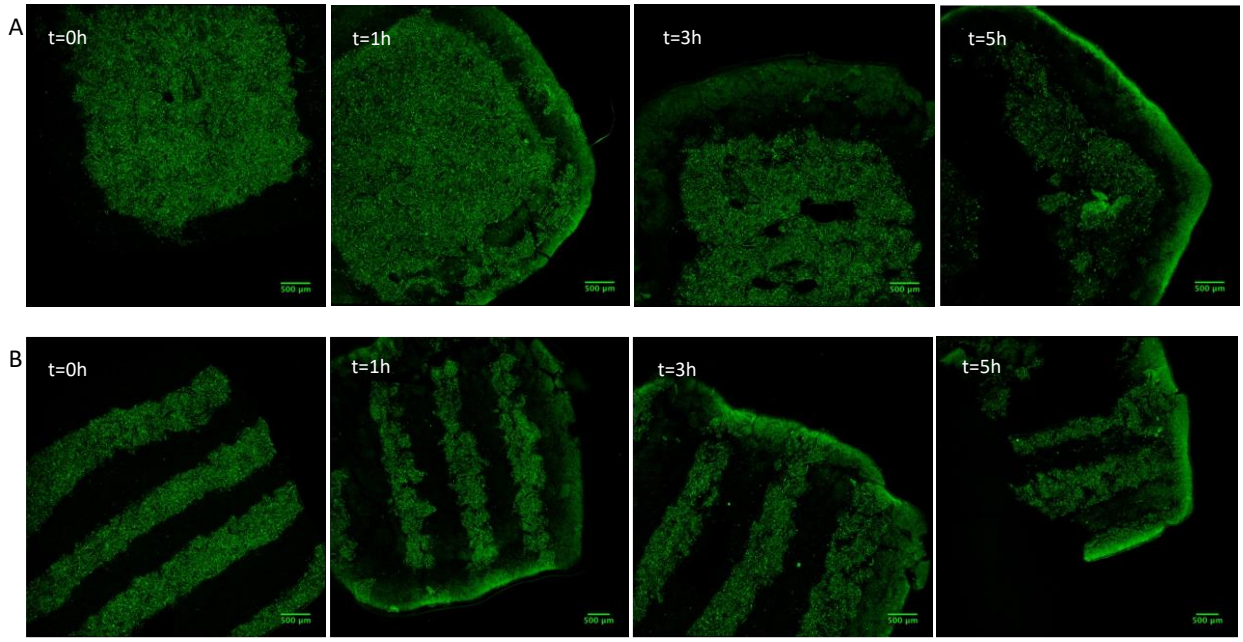


***Figure 6. 13: Fluorescence images of curcumin distribution within the printed structures at 0, 1, 3, and 5 hours in the small intestinal digestion phase.*** A. Core-shell structure; B. Layer-by-layer structure. The scale bars represent 100 ***μm***.

## 4. Discussion

### 4.1. Food inks' rheological properties are affected by LMP and CNC concentrations, and $Ca^{2+}$ crosslinking density

All the food inks in the current study were formulated using different combinations of LMP, $CaCl_2$, and CNC. Rheological characterization of the food inks generated a fingerprint for each formulation. Linking the fingerprints to the formulation parameters helped unveil the structure-function relationship of the polysaccharides and ionic crosslinking in the hydrogels. The results show that the gel strength is positively associated with LMP concentration and crosslinking density. While keeping the LMP-to-CNC ratio constant, increasing total polysaccharide concentration from 3% to 6% resulted in a more than 10-fold increase in G' and G" at an angular frequency of 0.1 rad/s. Even with a lower crosslinking density, the 6% total polysaccharide gels were stronger than the 3% gels (*Figure 6. 6* and

Table S6. 4). This result is in agreement with results reported in previous studies about LMP gelation behavior [312,313]. The gelation mechanism of LMP has been described using a modified "egg-box" model. Three types of LMP- $Ca^{2+}$ complexation contribute to the gelation of LMP: rod-like junction zones between two antiparallel polyuronates chains, monocomplexes within a single polyuronates chain, and point-like crosslinking [314,315]. In the low crosslinking density regime (R<1) where all the inks formulated in the current study belong, the formation of rod-like bundles prevails and dominates over monocomplexes or point-like crosslinks [314], showing the characteristics of semiflexible polymer networks [316]. A slight increase in R in this regime allows for more extensive bundle formation among the polymer chains, resulting in a more interconnected polymer network [312,314,317,318]. Moreover, our results show that the increase in G' with R was more significant in gels with lower LMP concentrations: increasing R from 0.35 to 0.55 in 3% gels led to a 10-fold increase in G', while in 6% gels, a 3-fold increase was observed (*Figure 6. 6*). This overall trend is attributed to the suppression of bundle formation at higher pectin concentrations [319] in the case of LMP- $Ca^{2+}$ gels with R<1. Besides the linear viscoelastic characteristics, the fluid behavior beyond the LVR has also been used to classify complex fluids [308]. The food ink formulations in the current study all exhibited the following behavior: at large strain amplitude, G' decreases monotonically and G" increases first then decreases (*Figure 6. 5*). The overshoot of G" arises as a result of the balance between the formation and destruction of the polymer junction zones under deformation [320,321]. In the LMP-Ca system, the structural cause of the G" overshoot is believed to be the unzipping and reformation of the egg-box bundles [319]. Eventually, at sufficiently high strain amplitude, the microstructural alignments

become dominant, and both G' and G" decrease but G' decreases faster, resulting of a crossover between G' and G", indicating that the gel has collapsed and started to flow [321].

Another polysaccharide component in ink formulations was CNC. Although previous studies have illustrated that due to its high aspect ratio, CNC can have outstanding mechanical properties akin to the function of cellulose in plant cell walls [302], the results of this study suggested that increasing CNC mass fraction reduced the gel strength. This effect could be attributed to a reduction of LMP mass fraction as the total polysaccharide content was maintained constant. *Figure S6. 2* illustrates the influence of adding CNC to the gel while keeping the LMP concentration constant (i.e., increasing the total polysaccharide content). These results validate that increasing CNC concentration significantly increases G' and G" of the gels, confirming the reinforcing effect of CNC. However, the mass fraction of CNC in our ink formulations was relatively low (at most 2.4%) and increasing CNC concentration was always coupled with the dilution of LMP, which overshadowed the reinforcing effect of CNC. In conclusion, the rheological characteristics of the bioinks were dominated by the LMP-calcium network, with minor contributions from the addition of CNC.

4.2. Prediction of food inks' printability from rheological characterizations

One of the key challenges in constructing a predictive model for inks' printability is to develop a comprehensive set of metrics for assessing printing performance. The two measures of printability in the current study were smoothness of deposition and shape fidelity after printability. Many of the previous studies have focused on shape fidelity measurements using different methods, including measuring the width and height of the filaments [293,304], size and circularity [176,296] of the holes in a printed grid pattern, 'sharpness' of the angle at a

corner of a printed structure [299], etc., while limited efforts have been made for quantitative characterization of smoothness of ink deposition. In this study, a quantitative assessment of both metrics was achieved by measuring the width and roughness of the printed filament with image analysis. In addition, 3-layer grids and 5*5*5 $mm^3$ grid cubes were printed with three representative ink formulations to demonstrate the stackability of the inks (*Figure 6. 9*). Besides establishing the quantitative metrics to assess printability, this study also constructed predictive relationships between the rheological measurements and the printability of the inks. To the best of our knowledge, among the few studies trying to relate food inks' rheological properties to printing behaviors, only simple correlations or linear regressions have been established [166,293]. However, both the current study and the previous investigations [166,297] have demonstrated that linear regressions are not sufficient to fully explain the relationship between different rheological measurements and printability metrics. Therefore, in the current study, random forest models were trained on the rheological characteristics and formulation parameters of the inks to predict the filament width and roughness labels and, ultimately, the binary ink quality label, which combined the two metrics. A one-step prediction of the binary quality label from the feature sets seemed to be the most direct approach; however, none of the rheological measurements were significantly different between the two binary quality classes (Table 6. 4). This was expected since the "non-optimal" inks group (class 1 in the binary quality label) included the ones that were either too weak or too strong to be printed, resulting in a wide range of rheological properties within this group. Therefore, direct prediction of ink quality could be challenging. An alternative indirect approach trained two separate models on the width and roughness labels and combined the classification results from both models to generate the predicted binary quality

label. Comparing the prediction results using the direct and indirect approaches, it could be concluded that the indirect method achieved higher mean accuracy and less overfitting. Given the relatively small sample size, especially with a nonlinear relationship, the direct prediction models were more susceptible to outliers and overfitting. With an increase in the sample size, the model performance was expected to improve further. Another advantage of using the indirect prediction approach was that the width and roughness model provided guidance on downstream improvement of the ink based on the predicted limitation of the printability metrics.

Different feature sets were also compared for their prediction capacity: formulation parameters, rheological measurements, and a combination of these two. Models trained with rheological measurements alone showed the best prediction accuracy among the three feature sets, implicating that it is possible to generalize the model beyond the current formulation parameters to other polysaccharide-based compositions. The evidence from this and other studies [294,295,303] supported that rheological fingerprints of hydrogel-based inks are often well correlated with the formulation parameters, but their relationship with printability is complicated and nonlinear. Rheological characterization is versatile for hydrogels formulated with different compositions. For development of future food ink encompassing a broader range of ingredients, models trained using formulation parameters would not be applicable, but those trained with rheological measurements could still be valid.

### 4.3. Effect of 3D patterning of cell-based microcarriers on the release profile of curcumin

Using the optimized ink formulation, tissue-like structures were printed with different patterns using the cell-free and cell-laden inks. These tissue-like structures served as models to investigate the effect of curcumin's intratissue localization on its release profile during *in*

*vitro* digestion. Since previous studies have shown that the bile salts play an important role in the release of curcumin during the intestinal phase [128,210], a bile salt concentration much higher than the physiologically relevant value was used to accelerate the curcumin release process. However, even with this approach, the release rate of curcumin from either of the printed structures was very slow (*Figure 6. 12*): 32% and 58% of the initial loaded curcumin were released from the core-shell and layer-by-layer structure respectively even after 10 hours in the modified SIF. As a comparison, under the same bile salt concentration, around 80% of curcumin was immediately released from free, individual yeast cells within first 10 min in SIF [210]. Our previous study showed that polyelectrolytes-mediated clustering of yeast cells and embedment of cells in thin alginate films could modify the release profile of encapsulated curcumin to different extent (CHAPTER 4) [210]. With a collective effect from both cell clustering and the extracellular alginate matrix, 70% of curcumin was released after 3 hours in high bile salt SIF. In this case, only 11% and 19% were released from the core-shell and layer-by-layer structure respectively at 3 hours. The process of curcumin release from the printed structures was regulated by both chemical reactions and mass transfer. With a log P value of 3.29, curcumin is a hydrophobic compound with very low water solubility (0.6 μg/mL)[267]. A limited amount of curcumin was released during the gastric phase because curcumin could not be solubilized in SGF. Bile salts are physiological surfactants that enhance fat digestion and the absorption of hydrophobic compounds[268]. Due to their amphiphilic nature, bile salts can self-associate to form micelles and aid in solubilizing curcumin. For curcumin to be released from the yeast cells, the bile salt molecules need to penetrate the cell wall and plasma membrane and extract curcumin from the intracellular components it originally bound to. Based on previous results that burst release of curcumin

took place in SIF, such a dissociation-reassociation reaction should have a high reaction rate. When yeast cells were embedded in a matrix, as was the case in this study, the mass transfer became the dominant factor governing the release process. The bile salts in SIF first need to diffuse into the printed cube. Once they come into contact with the cells, the bile salts are able to extract curcumin and formed curcumin-bile complexes. These complexes again needed to diffuse out into the SIF solution to be captured as the released fraction. In this process, bile salts could be depleted in various ways. They can form precipitates with calcium [322] that is abundant in the crosslinked pectin network. Moreover, pectin can also interact and bind with bile salts [323]. Lastly, besides curcumin, bile salt can also interact with yeast cell components, such as cell membranes and cellular lipids [324]. The curcumin-dense ring which formed at the surface of the cubes (*Figure 6. 13*) could be the result of the diffusion and accumulation of bile salts and curcumin-bile complexes at the cube surfaces. The release rate of curcumin from the core-shell structure was slower than that from the layer-by-layer structure. Such a result was expected since in the layer-by-layer structure, the cell-laden layers were directly exposed to SIF at time 0, while in the core-shell structure, the bile salts needed to penetrate the cell-free shell first and the curcumin-bile complexes needed to subsequently diffuse out to be released into the solution. Future research such as mechanistic modeling of the curcumin release process is needed to verify this hypothesis. Admittedly, the long digestion time and high bile salt conditions used in the current study in order to perform an accelerated test were not physiologically relevant. However, as a proof-of-concept study, the results demonstrated that it is possible to modulate the release profile of bioactive compounds encapsulated in cell-based carriers by changing localization of the cells. With this understanding and guidance from a potential mechanistic model, it is possible to

modify the structural features of the tissue-like structure, e.g., increasing porosity, so that a desirable release profile can be achieved under physiologically relevant conditions.

## 5. Conclusion

This investigation is a proof-of-concept study to demonstrate that 3D printing with cell-laden inks could be a versatile platform to create tissue-like matrices with different compositional and structural features. Hydrogel-based food inks formulated with low methoxyl pectin, cellulose nanocrystals and calcium chloride were developed, characterized, and successfully 3D printed. Calcium-crosslinked LMP hydrogel maintained the 3D network of the food inks, and CNC exhibited a micro-scale enforcing effect akin to their functionality in plant cell walls. The rheological properties of the hydrogels were found to be linearly associated with the formulation parameters. Printability of the food inks was assessed and quantified with two metrics: printed filaments' width and roughness. The ink printability could be predicted with high accuracy with random forest classifiers trained on the rheological measurements without specifying formulation parameters, demonstrating the possibility to generalize the model to other polysaccharide-based inks with different compositions. With the optimal ink formulation, guided 3D patterning of cell-based microcarriers was realized using 3D printing. The created structures could be used to investigate various food matrix effects on the bioaccessibility of encapsulated bioactive compounds, such as the spatial distribution of compounds that was evaluated in the current study. In the future, other structural features could be incorporated into the tissue-like encapsulation systems through 3D printing, such as porosity, to fine tune the release profiles of the encapsulated compounds.

## 6. Acknowledgement

This research has been supported by the following funding sources and grants: USDA-NIFA Grant 12447449, AIFS Center Grant 2020-67021-32855 (USDA-NSF AI Center research grant), and USDA NIFA grant 2018-67017-27563. The rheological characterizations of the food inks were conducted in Dr. Gail Bornhorst's lab at UC Davis, assisted by Dr. Clay Swackhamer.

## Supplements

**Table S6. 1: Ink formulations classification criteria based on printability measurements.**

| Metrics | Classification thresholds |
|---|---|
| Relative width index | $Width\ label = \{0\ if\ relative\ width \leq 2.2\ 1\ if\ relative\ width > 2.2$ |
| Roughness | $Roughness\ label = \{0\ if\ roughness \leq 23.2\ 1\ if\ roughness > 23.2$ |
| Binary quality label | $Binary\ quality\ label = \{0\ if\ width\ label = 0\ and\ roughness\ label = 0\ 1\ otherwise$ |

**Table S6. 2: Optimized printer settings for each food ink formulation.**

| Food Inks | Printer settings | |
|---|---|---|
| | Pressure (psi) | layer height (mm) |
| 3%/10-0/0.45 | 13 | 0.35 |
| 3%/6-4/0.45 | 6 | 0.31 |
| 3%/8-2/0.35 | 4 | 0.38 |
| 3%/8-2/0.55 | 13 | 0.31 |
| 4.5%/10-0/0.35 | 14 | 0.31 |
| 4.5%/10-0/0.55 | 24 | 0.31 |
| 4.5%/6-4/0.35 | 10 | 0.38 |
| 4.5%/6-4/0.55 | 18 | 0.31 |
| 4.5%/8-2/0.45 | 15 | 0.31 |
| 6%/10-0/0.45 | 24 | 0.31 |
| 6%/6-4/0.45 | 16 | 0.33 |
| 6%/8-2/0.35 | 14 | 0.33 |
| 6%/8-2/0.55 | 40 | 0.28 |

**Table S6. 3: The 13 food ink formulations from the Box-Behnken design.**

| Rep | Total polysaccharide (%) | Pectin fraction | $R = 2[Ca^{2+}]/[COO^{-}]$ |
|---|---|---|---|
| 1 | 3 | 0.6 | 0.45 |
| 1 | 6 | 0.6 | 0.45 |
| 1 | 3 | 1 | 0.45 |
| 1 | 6 | 1 | 0.45 |
| 1 | 3 | 0.8 | 0.35 |
| 1 | 6 | 0.8 | 0.35 |
| 1 | 3 | 0.8 | 0.55 |
| 1 | 6 | 0.8 | 0.55 |
| 1 | 4.5 | 0.6 | 0.35 |
| 1 | 4.5 | 1 | 0.35 |
| 1 | 4.5 | 0.6 | 0.55 |
| 1 | 4.5 | 1 | 0.55 |
| 3 | 4.5 | 0.8 | 0.45 |

**Table S6. 4: Summary of rheological and printability measurements of the 13 food ink formulations.**

| Ink* | Total polysaccharide% | Pectin fraction | Crosslinking density R | Flow index | Loss factor | Yield stress (Pa) | Flow transition index | Recovery | Filament width (um) | Filament roughness |
|---|---|---|---|---|---|---|---|---|---|---|
| 3%/10-0/0.45 | 3 | 1 | 0.45 | 0.46±0.03 | 0.1±0.01 | 60.25±6.08 | 1.87±0.09 | 0.67±0.18 | 704.71±163.92 | 23.66±8.79 |
| 3%/6-4/0.45 | 3 | 0.6 | 0.45 | 0.34±0.03 | 0.16±0.03 | 17.59±5.92 | 4.47±1.23 | 0.54±0.05 | 879.09±90.72 | 14.95±9.85 |
| 3%/8-2/0.35 | 3 | 0.8 | 0.35 | 0.31±0.01 | 0.23±0.01 | 18.39±1.4 | 2.85±0.71 | 0.56±0.06 | 985.65±210.17 | 15.91±14.96 |
| 3%/8-2/0.55 | 3 | 0.8 | 0.55 | 0.67±0.05 | 0.09±0 | 78.84±1.33 | 1.37±0.13 | 0.74±0.1 | 817.52±169.3 | 36.35±5.56 |
| 4.5%/10-0/0.35 | 4.5 | 1 | 0.35 | 0.47±0.06 | 0.14±0.01 | 45.04±4.04 | 2.84±0.35 | 0.6±0.02 | 596.37±138.9 | 10.21±1.38 |
| 4.5%/10-0/0.55 | 4.5 | 1 | 0.55 | 0.63±0.04 | 0.07±0 | 311.53±191.75 | 1.58±0.2 | 0.98±0.16 | 645.81±130.59 | 42.85±21.81 |
| 4.5%/6-4/0.35 | 4.5 | 0.6 | 0.35 | 0.46±0.03 | 0.18±0.01 | 25.85±3.05 | 3.99±0.31 | 0.73±0.06 | 1044.92±172.64 | 2.9±2.63 |
| 4.5%/6-4/0.55 | 4.5 | 0.6 | 0.55 | 0.39±0.05 | 0.09±0.01 | 74.59±7.75 | 2.13±0.6 | 0.76±0.02 | 796.01±210.59 | 9.09±3.71 |
| 4.5%/8-2/0.45 | 4.5 | 0.8 | 0.45 | 0.44±0.11 | 0.12±0.01 | 70.26±18.49 | 2.01±0.37 | 0.76±0.07 | 646.44±85.29 | 21.45±4.8 |
| 6%/10-0/0.45 | 6 | 1 | 0.45 | 0.37±0.01 | 0.08±0.01 | 225.54±60.28 | 1.49±0.11 | 1.01±0.12 | 503.12±48.78 | 31.96±17.09 |
| 6%/6-4/0.45 | 6 | 0.6 | 0.45 | 0.52±0.07 | 0.12±0.04 | 83.63±14.76 | 2.6±0.32 | 0.82±0.14 | 841.48±166.31 | 7.35±2.1 |
| 6%/8-2/0.35 | 6 | 0.8 | 0.35 | 0.43±0.05 | 0.14±0.01 | 71±8.85 | 2.59±0.22 | 0.89±0.01 | 548.43±169.98 | 8.96±5.82 |
| 6%/8-2/0.55 | 6 | 0.8 | 0.55 | 0.48±0.06 | 0.07±0 | 174.26±18.58 | 2.45±0.3 | 0.79±0.03 | 614.32±98.75 | 15.69±12.74 |

*The ink names were written as total polysaccharide%/pectin-to-CNC ratio/crosslinking density R.

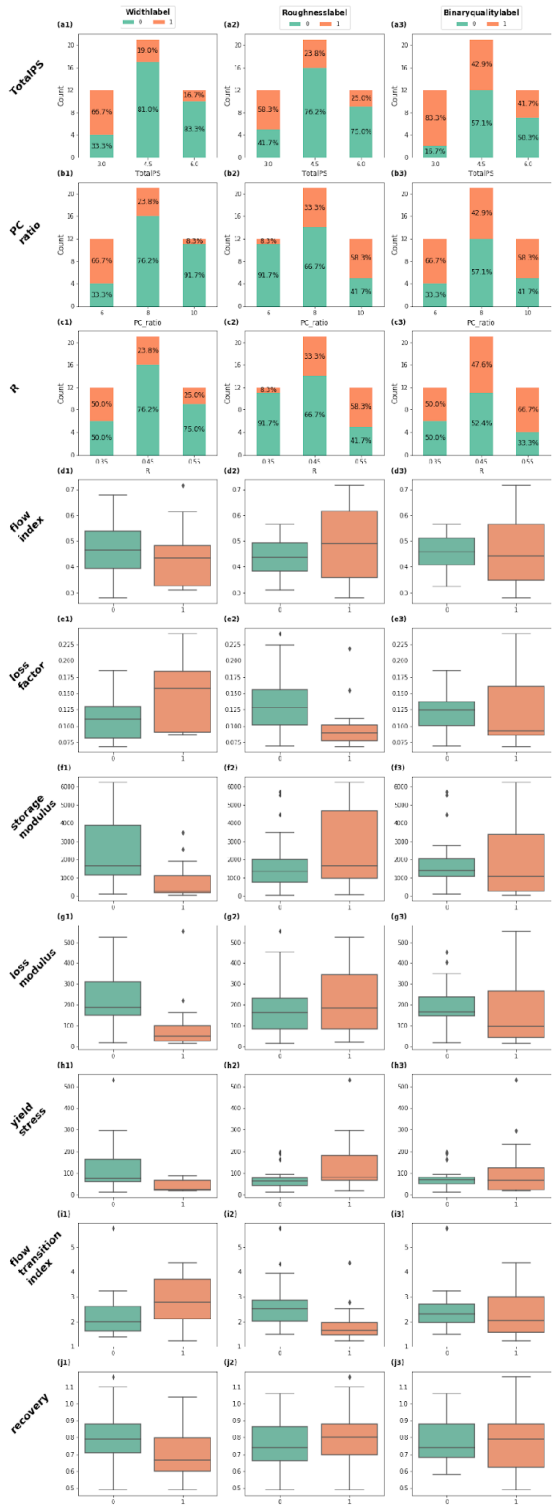


**Figure S6. 1***: Distribution of formulation parameters (a1-c3) and rheological measurements (d1-j3) for inks stratified by width labels, roughness labels, and binary quality labels. Bar plots and boxplots were used for formulation parameters and rheological measurements respectively.*

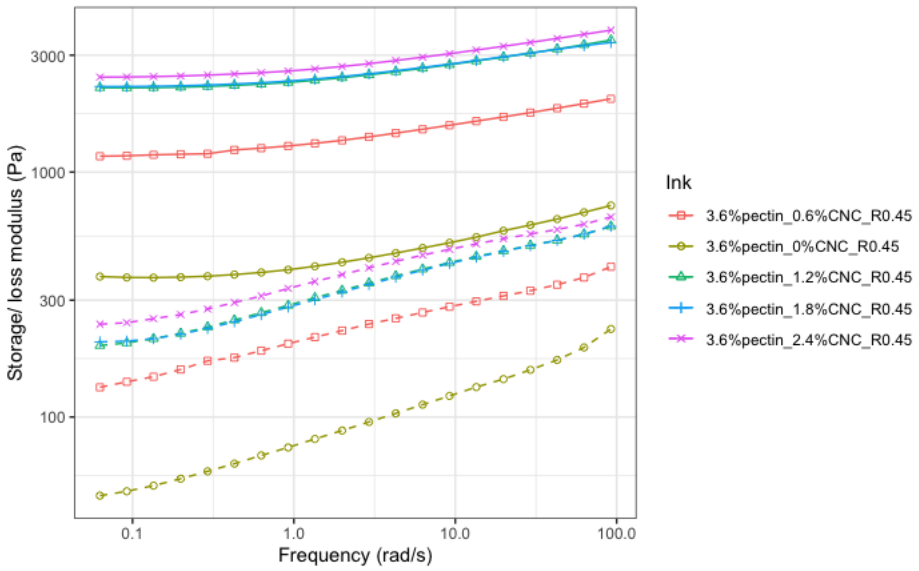


***Figure S6. 2: Storage modulus G' (solid line) and loss modulus G" (dashed line) vs. angular frequency at 1% strain amplitude for bioinks composed of 3.6% pectin, R=0.45, and different levels of CNC.***

# CHAPTER 7

# Conclusions

This research adopted a bottom-up approach to investigate the multi-scale food matrix effect on bioaccessibility of plant-derived bioactive compounds during in vitro digestion. Using yeast cell-based microcarriers as building blocks, natural food-inspired tissue-like encapsulation systems were constructed. A combined experimental and modeling approach was taken to investigate bioactive compound – food matrix interactions in the encapsulation systems with different levels of compositional and structural complexities. CHAPTER 2 and CHAPTER 3 evaluated the contributing factors to the encapsulation and release of bioactive compounds in single yeast cells. CHAPTER 2 identified bioactive compounds' hydrophobicity and the concentration of ethanol used to solubilize the compounds as the major contributor to the encapsulation efficiency. CHAPTER 3 revealed that the affinity of bioactive compounds for different cellular components (i.e., proteins and lipids) resulted in different localization of the encapsulated molecules inside yeast cells. The difference in cells' biochemical profile and compounds' subcellular localization were associated with the different release profiles observed during *in vitro* digestion. CHAPTER 4 took the first step towards constructing a tissue-like encapsulation system by assembling single yeast cells into cell clusters through electrostatic aggregation and introducing an extracellular matrix as a second structural level. The results confirmed the dominant effect from the extracellular matrix on modifying a model compound's (curcumin) release profiles and a prolonged cell clustering effect with the presence of the extracellular matrix. CHAPTER 5 explored the possibility of using filamentous fungal pellets as a natural multicellular matrix to encapsulate the model compound (curcumin). It was found that compared to single yeast cells, the multicellular fungal pellet eliminated the burst release of

curcumin and reduced the overall release rate during *in vitro* digestion. Finally, CHAPTER 6 developed plant polysaccharides-based food inks for 3D printing and used 3D printing to assemble the curcumin -loaded yeast cells to achieve different intratissue localization of the compounds. Different release profiles were observed for structures printed with different matrix architectures. However, further research is needed to design and construct structures that can realize controlled release under physiologically relevant conditions.

From the perspective of investigating the food matrix effect on the bioaccessibility of bioactive compounds, this research found that different mechanisms contributed to the release of compounds at different scale levels. At a cellular level, it was mainly the interactions among the bioactive compounds, the cellular components, and the digestion fluids that controlled the release kinetics. Such interactions include complex formation and dissociation between bioactives and proteins, partition among the extracellular environment and intracellular lipid-rich phase and protein-rich aqueous phase, as well as the changes in cellular composition and intracellular structures due to the acid gastric environment, the actions of bile salts in the small intestinal phase, and enzymes in the digestion fluids. At a tissue level, besides the abovementioned interactions, physical barriers to compounds' release become more significant, such as diffusion impediment and physical entrapment of both digestion fluids components into and bioactives out of the tissue-like structures, due to the presence of extracellular matrix or the assembly of single cells.

From an application perspective, with the findings of the current research, together with the versatile 3D printing platform, it is possible to design and develop nutraceutical products where the spatiotemporal release of bioactive compounds could be modulated at different levels, i.e., subcellular, cellular, and tissue levels. To facilitate more efficient formulation development and

optimization, this research incorporated the element of *in-silico* evaluation by constructing predictive models for various formulation-related assessment indices, including the encapsulation efficiency and release patterns of compounds in cell-based carriers, and printability of food inks. Through the efforts to construct the *in silico* evaluation pipelines, we exploited multimodal data to characterize the encapsulation systems, such as biochemical assays, IT spectra, and microscopic images; and utilized statistical tools and machine learning/ deep learning algorithms for proper feature selection and model training. Admittedly, the predictive models constructed in this research are still fragmented and future work is needed to connect the dots so that a complete *in silico* pipeline can be used to evaluate and optimize the performance of a more complex nutraceutical or functional food products. The following research directions could potentially be pursued:

- Broadening the range of bioactive compounds and incorporating different types of cell-based carriers in the investigation of the encapsulation and release processes. Enlarging and diversifying the data set can help improve the generalizability of the predictive models.
- Mechanistic modeling of the release processes of bioactive compounds from single yeast cells and 3D printed structures. With validated mechanisms and parameters, these models can potentially be generalized to other model food systems.
- Exploring physics-informed machine learning to integrate potentially noisy and sparse experimental data with partially known mechanisms and physical laws to model the release of bioactive compounds from food systems with more complex compositions and structures.

# Bibliography


1. H.-K. Biesalski, L. O. Dragsted, I. Elmadfa, R. Grossklaus, M. Müller, D. Schrenk, P. Walter and P. Weber, Bioactive compounds: definition and assessment of activity., *Nutrition*, 2009, **25**, 1202–1205.

2. B. S. Patil, G. K. Jayaprakasha, K. N. Chidambara Murthy and A. Vikram, Bioactive compounds: historical perspectives, opportunities, and challenges., *J. Agric. Food Chem.*, 2009, **57**, 8142–8160.

3. E. S. Teoh, in *Medicinal orchids of asia*, Springer International Publishing, Cham, 2016, pp. 59–73.

4. C. M. Weaver, Bioactive foods and ingredients for health., *Adv. Nutr.*, 2014, **5**, 306S–11S.

5. A. Rietveld and S. Wiseman, Antioxidant effects of tea: evidence from human clinical trials., *J. Nutr.*, 2003, **133**, 3285S-3292S.

6. C. I. R. Gill, S. Haldar, L. A. Boyd, R. Bennett, J. Whiteford, M. Butler, J. R. Pearson, I. Bradbury and I. R. Rowland, Watercress supplementation in diet reduces lymphocyte DNA damage and alters blood antioxidant status in healthy adults., *Am. J. Clin. Nutr.*, 2007, **85**, 504–510.

7. S. D. Deodhar, R. Sethi and R. C. Srimal, Preliminary study on antirheumatic activity of curcumin (diferuloyl methane)., *Indian J. Med. Res.*, 1980, **71**, 632–634.

8. O. Kucuk, F. H. Sarkar, W. Sakr, Z. Djuric, M. N. Pollak, F. Khachik, Y. W. Li, M. Banerjee, D. Grignon, J. S. Bertram, J. D. Crissman, E. J. Pontes and D. P. Wood, Phase II randomized clinical trial of lycopene supplementation before radical prostatectomy., *Cancer Epidemiol. Biomarkers Prev.*, 2001, **10**, 861–868.

9. H. Mukhtar and N. Ahmad, Tea polyphenols: prevention of cancer and optimizing health., *Am. J. Clin. Nutr.*, 2000, **71**, 1698S–702S; discussion 1703S.

10. M. D'Archivio, C. Filesi, R. Varì, B. Scazzocchio and R. Masella, Bioavailability of the polyphenols: status and controversies., *Int. J. Mol. Sci.*, 2010, **11**, 1321–1342.

11. J. M. Carbonell-Capella, M. Buniowska, F. J. Barba, M. J. Esteve and A. Frígola, Analytical Methods for Determining Bioavailability and Bioaccessibility of Bioactive Compounds from Fruits and Vegetables: A Review., *Comp. Rev. Food Sci. Food Safety*, 2014, **13**, 155–171.

12. G. Lietz, in *Carotenoids and human health*, ed. S. A. Tanumihardjo, Humana Press, Totowa, NJ, 2013, pp. 129–140.

13. M. van Lieshout, C. E. West and R. B. van Breemen, Isotopic tracer techniques for studying the bioavailability and bioefficacy of dietary carotenoids, particularly beta-carotene, in humans: a review., *Am. J. Clin. Nutr.*, 2003, **77**, 12–28.

14. E. Fernández-García, I. Carvajal-Lérida and A. Pérez-Gálvez, In vitro bioaccessibility assessment as a prediction tool of nutritional efficiency., *Nutr. Res.*, 2009, **29**, 751–760.

15. E. Capuano, T. Oliviero and M. A. J. S. van Boekel, Modeling food matrix effects on chemical reactivity: Challenges and perspectives., *Crit. Rev. Food Sci. Nutr.*, 2018, **58**, 2814–2828.

16. J. M. Aguilera, The food matrix: implications in processing, nutrition and health., *Crit. Rev. Food Sci. Nutr.*, 2019, **59**, 3612–3629.

17. A. D. T. Phan, B. M. Flanagan, B. R. D'Arcy and M. J. Gidley, Binding selectivity of dietary polyphenols to different plant cell wall components: Quantification and mechanism., *Food Chem.*, 2017, **233**, 216–227.

18. Z. A. Popper ed., *The plant cell wall*, Humana Press, Totowa, NJ, 2011.

19. P. R. Ellis, C. W. C. Kendall, Y. Ren, C. Parker, J. F. Pacy, K. W. Waldron and D. J. A. Jenkins, Role of cell walls in the bioaccessibility of lipids in almond seeds., *Am. J. Clin. Nutr.*, 2004, **80**, 604–613.

20. M. M. L. Grundy, F. Carrière, A. R. Mackie, D. A. Gray, P. J. Butterworth and P. R. Ellis, The role of plant cell wall encapsulation and porosity in regulating lipolysis during the digestion of almond seeds., *Food Funct.*, 2016, **7**, 69–78.

21. L. Lemmens, I. Colle, S. Van Buggenhout, P. Palmero, A. Van Loey and M. Hendrickx, Carotenoid bioaccessibility in fruit- and vegetable-based food products as affected by product (micro)structural characteristics and the presence of lipids: A review, *Trends Food Sci. Technol.*, 2014, **38**, 125–135.

22. M. M. L. Grundy, P. J. Wilde, P. J. Butterworth, R. Gray and P. R. Ellis, Impact of cell wall encapsulation of almonds on in vitro duodenal lipolysis., *Food Chem.*, 2015, **185**, 405–412.

23. K. R. N. Moelants, L. Lemmens, M. Vandebroeck, S. Van Buggenhout, A. M. Van Loey and M. E. Hendrickx, Relation between particle size and carotenoid bioaccessibility in carrot- and tomato-derived suspensions., *J. Agric. Food Chem.*, 2012, **60**, 11995–12003.

24. P. Palmero, L. Lemmens, A. Ribas-Agustí, C. Sosa, K. Met, J. de Dieu Umutoni, M. Hendrickx and A. Van Loey, Novel targeted approach to better understand how natural structural barriers govern carotenoid in vitro bioaccessibility in vegetable-based systems., *Food Chem.*, 2013, **141**, 2036–2043.

25. J. F. V. Vincent, in *Food Materials Science*, eds. J. M. Aguilera and P. J. Lillford, Springer New York, New York, NY, 2008, pp. 11–20.

26. V. Dewanto, X. Wu, K. K. Adom and R. H. Liu, Thermal processing enhances the nutritional value of tomatoes by increasing total antioxidant activity., *J. Agric. Food Chem.*, 2002, **50**, 3010–3014.

27. L. Lemmens, S. Van Buggenhout, A. M. Van Loey and M. E. Hendrickx, Particle size reduction leading to cell wall rupture is more important for the β-carotene bioaccessibility of raw compared to thermally processed carrots., *J. Agric. Food Chem.*, 2010, **58**, 12769–12776.

28. R. Yimnirun and Y. Laosiritaworn, Towards a better understanding of the relationship between the β-carotene in vitro bio-accessibility and pectin structural changes: A case study on carrots, *Food Research International*, 2009.

29. E. Hedrén, V. Diaz and U. Svanberg, Estimation of carotenoid accessibility from carrots determined by an in vitro digestion method., *Eur. J. Clin. Nutr.*, 2002, **56**, 425–430.

30. S. Van Buggenhout, M. Lille, I. Messagie, A. V. Loey, K. Autio and M. Hendrickx, Impact of pretreatment and freezing conditions on the microstructure of frozen carrots: Quantification and relation to texture loss, *Eur. Food Res. Technol.*, 2006, **222**, 543–553.

31. S. Kamiloglu, Effect of different freezing methods on the bioaccessibility of strawberry polyphenols, *Int. J. Food Sci. Technol.*, 2019, **54**, 2652–2660.

32. A. Voilley and I. Souchon, in *Flavour in Food*, Elsevier, 2006, pp. 117–132.

33. J. Thévenot, C. Cauty, D. Legland, D. Dupont and J. Floury, Pepsin diffusion in dairy gels depends on casein concentration and microstructure., *Food Chem.*, 2017, **223**, 54–61.

34. S. Banerjee and S. Bhattacharya, Food gels: gelling process and new applications., *Crit. Rev. Food Sci. Nutr.*, 2012, **52**, 334–346.

35. M. Arab, M. Yousefi, E. Khanniri, M. Azari, V. Ghasemzadeh-Mohammadi and N. Mollakhalili-Meybodi, A comprehensive review on yogurt syneresis: effect of processing conditions and added additives, *J. Food Sci. Technol.*, 2022.

36. P. Duboc and B. Mollet, Applications of exopolysaccharides in the dairy industry, *International Dairy Journal*, 2001, **11**, 759–768.

37. G. T. Rich, A. Fillery-Travis and M. L. Parker, Low pH enhances the transfer of carotene from carrot juice to olive oil., *Lipids*, 1998, **33**, 985–992.

38. W. Stahl, H. van den Berg, J. Arthur, A. Bast, J. Dainty, R. M. Faulks, C. Gärtner, G. Haenen, P. Hollman, B. Holst, F. J. Kelly, M. C. Polidori, C. Rice-Evans, S. Southon, T.

van Vliet, J. Viña-Ribes, G. Williamson and S. B. Astley, Bioavailability and metabolism., *Mol. Aspects Med.*, 2002, **23**, 39–100.

39. J. R. Zhou, E. T. Gugger and J. W. Erdman, The crystalline form of carotenes and the food matrix in carrot root decrease the relative bioavailability of beta- and alpha-carotene in the ferret model., *J. Am. Coll. Nutr.*, 1996, **15**, 84–91.

40. M. J. Rodríguez-Roque, B. de Ancos, R. Sánchez-Vega, C. Sánchez-Moreno, M. P. Cano, P. Elez-Martínez and O. Martín-Belloso, Food matrix and processing influence on carotenoid bioaccessibility and lipophilic antioxidant activity of fruit juice-based beverages., *Food Funct.*, 2016, **7**, 380–389.

41. D. Y. Low, B. D'Arcy and M. J. Gidley, Mastication effects on carotenoid bioaccessibility from mango fruit tissue, *Food Res. Int*, 2015, **67**, 238–246.

42. L. Yonekura and A. Nagao, Intestinal absorption of dietary carotenoids., *Mol. Nutr. Food Res.*, 2007, **51**, 107–115.

43. T. A. J. Verrijssen, S. H. E. Verkempinck, S. Christiaens, A. M. Van Loey and M. E. Hendrickx, The effect of pectin on in vitro β-carotene bioaccessibility and lipid digestion in low fat emulsions, *Food Hydrocoll.*, 2015, **49**, 73–81.

44. Y. Ke, L. Deng, T. Dai, M. Xiao, M. Chen, R. Liang, W. Liu, C. Liu and J. Chen, Effects of cell wall polysaccharides on the bioaccessibility of carotenoids, polyphenols, and minerals: an overview., *Crit. Rev. Food Sci. Nutr.*, 2022, 1–14.

45. H. Palafox-Carlos, J. F. Ayala-Zavala and G. A. González-Aguilar, The role of dietary fiber in the bioaccessibility and bioavailability of fruit and vegetable antioxidants., *J. Food Sci.*, 2011, **76**, R6–R15.

46. A. Al-Yafeai and V. Böhm, In vitro bioaccessibility of carotenoids and vitamin E in rosehip products and tomato paste as affected by pectin contents and food processing., *J. Agric. Food Chem.*, 2018, **66**, 3801–3809.

47. J. De Jesus Ornelas-Paz, M. L. Failla, E. M. Yahia and A. Gardea-Bejar, Impact of the stage of ripening and dietary fat on in vitro bioaccessibility of beta-carotene in "Ataulfo" mango., *J. Agric. Food Chem.*, 2008, **56**, 1511–1516.

48. X. Liu, J. Liu, J. Bi, J. Yi, J. Peng, C. Ning, C. K. D. Wellala and B. Zhang, Effects of high pressure homogenization on pectin structural characteristics and carotenoid bioaccessibility of carrot juice., *Carbohydr. Polym.*, 2019, **203**, 176–184.

49. C. Le Bourvellec and C. M. G. C. Renard, Interactions between polyphenols and macromolecules: quantification methods and mechanisms., *Crit. Rev. Food Sci. Nutr.*, 2012, **52**, 213–248.

50. M. Viuda-Martos, R. Lucas-Gonzalez, C. Ballester-Costa, J. A. Pérez-Álvarez, L. A. Muñoz and J. Fernández-López, Evaluation of protective effect of different dietary fibers on polyphenolic profile stability of maqui berry (Aristotelia chilensis (Molina) Stuntz) during in vitro gastrointestinal digestion., *Food Funct.*, 2018, **9**, 573–584.

51. G. R. Velderrain-Rodríguez, L. Salvia-Trujillo and O. Martín-Belloso, Lipid Digestibility and Polyphenols Bioaccessibility of Oil-in-Water Emulsions Containing Avocado Peel and Seed Extracts as Affected by the Presence of Low Methoxyl Pectin, *Foods*, 2021, **10**, 2193.

52. F. J. Blancas-Benitez, G. Mercado-Mercado, A. E. Quirós-Sauceda, E. Montalvo-González, G. A. González-Aguilar and S. G. Sáyago-Ayerdi, Bioaccessibility of polyphenols associated with dietary fiber and in vitro kinetics release of polyphenols in Mexican "Ataulfo" mango (Mangifera indica L.) by-products., *Food Funct.*, 2015, **6**, 859–868.

53. A. Padayachee, G. Netzel, M. Netzel, L. Day, D. Mikkelsen and M. J. Gidley, Lack of release of bound anthocyanins and phenolic acids from carrot plant cell walls and model composites during simulated gastric and small intestinal digestion., *Food Funct.*, 2013, **4**, 906–916.

54. M. Tamura, T. Iwami, K. Hirayama and K. Itoh, High Fiber Diet Supplemented with Rice Bran Hemicellulose May Reduce Daidzein Absorption in Mice, *Food Sci. Technol. Res.*, 2009, **15**, 141–146.

55. J. Koh, Z. Xu and L. Wicker, Blueberry pectin and increased anthocyanins stability under in vitro digestion., *Food Chem.*, 2020, **302**, 125343.

56. A. D. T. Phan, G. Netzel, D. Wang, B. M. Flanagan, B. R. D'Arcy and M. J. Gidley, Binding of dietary polyphenols to cellulose: structural and nutritional aspects., *Food Chem.*, 2015, **171**, 388–396.

57. T. Ozdal, D. A. Sela, J. Xiao, D. Boyacioglu, F. Chen and E. Capanoglu, The Reciprocal Interactions between Polyphenols and Gut Microbiota and Effects on Bioaccessibility., *Nutrients*, 2016, **8**, 78.

58. Z. Yin, Y. Wu, Y. Chen, X. Qie, M. Zeng, Z. Wang, F. Qin, J. Chen and Z. He, Analysis of the interaction between cyanidin-3-O-glucoside and casein hydrolysates and its effect on the antioxidant ability of the complexes., *Food Chem.*, 2021, **340**, 127915.

59. X. Qie, Y. Cheng, Y. Chen, M. Zeng, Z. Wang, F. Qin, J. Chen, W. Li and Z. He, In vitro phenolic bioaccessibility of coffee beverages with milk and soy subjected to thermal treatment and protein-phenolic interactions., *Food Chem.*, 2022, **375**, 131644.

60. Z. He, Y. Tao, M. Zeng, S. Zhang, G. Tao, F. Qin and J. Chen, High pressure homogenization processing, thermal treatment and milk matrix affect in vitro

bioaccessibility of phenolics in apple, grape and orange juice to different extents., *Food Chem.*, 2016, **200**, 107–116.

61. K. H. van het Hof, I. A. Brouwer, C. E. West, E. Haddeman, R. P. Steegers-Theunissen, M. van Dusseldorp, J. A. Weststrate, T. K. Eskes and J. G. Hautvast, Bioavailability of lutein from vegetables is 5 times higher than that of beta-carotene., *Am. J. Clin. Nutr.*, 1999, **70**, 261–268.

62. A. Scalbert and G. Williamson, Dietary intake and bioavailability of polyphenols., *J. Nutr.*, 2000, **130**, 2073S–85S.

63. N. Thakur, P. Raigond, Y. Singh, T. Mishra, B. Singh, M. K. Lal and S. Dutt, Recent updates on bioaccessibility of phytonutrients, *Trends Food Sci. Technol.*, 2020, **97**, 366–380.

64. P. C. Hollman, J. M. van Trijp, M. N. Buysman, M. S. van der Gaag, M. J. Mengelers, J. H. de Vries and M. B. Katan, Relative bioavailability of the antioxidant flavonoid quercetin from various foods in man., *FEBS Lett.*, 1997, **418**, 152–156.

65. C. Manach, A. Scalbert, C. Morand, C. Rémésy and L. Jiménez, Polyphenols: food sources and bioavailability., *Am. J. Clin. Nutr.*, 2004, **79**, 727–747.

66. L. O'Sullivan, M. A. Jiwan, T. Daly, N. M. O'Brien and S. A. Aherne, Bioaccessibility, uptake, and transport of carotenoids from peppers (Capsicum spp.) using the coupled in vitro digestion and human intestinal Caco-2 cell model., *J. Agric. Food Chem.*, 2010, **58**, 5374–5379.

67. J. E. Aguilar-Toalá, D. Quintanar-Guerrero, A. M. Liceaga and M. L. Zambrano-Zaragoza, Encapsulation of bioactive peptides: a strategy to improve the stability, protect the nutraceutical bioactivity and support their food applications., *RSC Adv.*, 2022, **12**, 6449–6458.

68. J. Luana Carvalho de Queiroz, I. Medeiros, A. Costa Trajano, G. Piuvezam, A. Clara de França Nunes, T. Souza Passos and A. Heloneida de Araújo Morais, Encapsulation techniques perfect the antioxidant action of carotenoids: A systematic review of how this effect is promoted., *Food Chem.*, 2022, **385**, 132593.

69. J. Ubbink and J. Krüger, Physical approaches for the delivery of active ingredients in foods, *Trends Food Sci. Technol.*, 2006, **17**, 244–254.

70. D. J. McClements, Encapsulation, protection, and delivery of bioactive proteins and peptides using nanoparticle and microparticle systems: A review., *Adv. Colloid Interface Sci.*, 2018, **253**, 1–22.

71. D. J. McClements, E. A. Decker, Y. Park and J. Weiss, Structural design principles for delivery of bioactive components in nutraceuticals and functional foods., *Crit. Rev. Food Sci. Nutr.*, 2009, **49**, 577–606.

72. S. Friberg, K. Larsson and J. Sjoblom eds., *Food Emulsions*, CRC Press, 4th, revised edn, 2003.

73. D. J. McClements, *Food emulsions: principles, practices, and techniques, third edition*, CRC Press, 2015.

74. J. Flanagan and H. Singh, Conjugation of sodium caseinate and gum arabic catalyzed by transglutaminase., *J. Agric. Food Chem.*, 2006, **54**, 7305–7310.

75. T. Subramani and H. Ganapathyswamy, An overview of liposomal nano-encapsulation techniques and its applications in food and nutraceutical., *J. Food Sci. Technol.*, 2020, **57**, 3545–3555.

76. P. Kaur, T. Garg, G. Rath, R. S. R. Murthy and A. K. Goyal, Surfactant-based drug delivery systems for treating drug-resistant lung cancer., *Drug Deliv.*, 2016, **23**, 727–738.

77. M. J. Rosen, *Surfactants and interfacial phenomena*, John Wiley & Sons, Inc., Hoboken, NJ, USA, 2004.

78. L. Chen, G. E. Remondetto and M. Subirade, Food protein-based materials as nutraceutical delivery systems, *Trends Food Sci. Technol.*, 2006, **17**, 272–283.

79. S. W. Cui ed., *Food carbohydrates: chemistry, physical properties, and applications*, CRC Press, 2005.

80. J. Xu, L. Yang, Y. Nie, M. Yang, W. Wu, Z. Wang, X. Wang and J. Zhong, Effect of transglutaminase crosslinking on the structural, physicochemical, functional, and emulsion stabilization properties of three types of gelatins, *LWT*, 2022, **163**, 113543.

81. I. T. Norton and W. J. Frith, Microstructure design in mixed biopolymer composites, *Food Hydrocoll.*, 2001, **15**, 543–553.

82. D. J. McClements, Non-covalent interactions between proteins and polysaccharides., *Biotechnol. Adv.*, 2006, **24**, 621–625.

83. A. Acevedo-Fani, A. Dave and H. Singh, Nature-Assembled Structures for Delivery of Bioactive Compounds and Their Potential in Functional Foods., *Front. Chem.*, 2020, **8**, 564021.

84. J. T. C. Tzen, Yz. Cao, P. Laurent, C. Ratnayake and A. H. C. Huang, Lipids, Proteins, and Structure of Seed Oil Bodies from Diverse Species., *Plant Physiol.*, 1993, **101**, 267–276.

85. F. Acevedo, M. Rubilar, I. Jofré, M. Villarroel, P. Navarrete, M. Esparza, F. Romero, E. A. Vilches, V. Acevedo and C. Shene, Oil bodies as a potential microencapsulation carrier for astaxanthin stabilisation and safe delivery., *J. Microencapsul.*, 2014, **31**, 488–500.

86. I. D. Fisk, R. S. T. Linforth, A. J. Taylor and D. A. Gray, Aroma encapsulation and aroma delivery by oil body suspensions derived from sunflower seeds (Helianthus annus), *Eur. Food Res. Technol.*, 2011, **232**, 905–910.

87. H. W. Heid and T. W. Keenan, Intracellular origin and secretion of milk fat globules., *Eur. J. Cell Biol.*, 2005, **84**, 245–258.

88. A. Masedunskas, Y. Chen, R. Stussman, R. Weigert and I. H. Mather, Kinetics of milk lipid droplet transport, growth, and secretion revealed by intravital imaging: lipid droplet release is intermittently stimulated by oxytocin., *Mol. Biol. Cell*, 2017, **28**, 935–946.

89. M. Alshehab, M. G. Reis, L. Day and N. Nitin, Milk fat globules, a novel carrier for delivery of exogenous cholecalciferol., *Food Res. Int.*, 2019, **126**, 108579.

90. M. Alshehab and N. Nitin, Encapsulation and release of curcumin using an intact milk fat globule delivery system., *Food Funct.*, 2019, **10**, 7121–7130.

91. C. Holt, J. A. Carver, H. Ecroyd and D. C. Thorn, Invited review: Caseins and the casein micelle: their biological functions, structures, and behavior in foods., *J. Dairy Sci.*, 2013, **96**, 6127–6146.

92. A. Sahu, N. Kasoju and U. Bora, Fluorescence study of the curcumin-casein micelle complexation and its application as a drug nanocarrier to cancer cells., *Biomacromolecules*, 2008, **9**, 2905–2912.

93. M. S. Mohan, J. L. Jurat-Fuentes and F. Harte, Binding of vitamin A by casein micelles in commercial skim milk., *J. Dairy Sci.*, 2013, **96**, 790–798.

94. M. Cheema, M. S. Mohan, S. R. Campagna, J. L. Jurat-Fuentes and F. M. Harte, The association of low-molecular-weight hydrophobic compounds with native casein micelles in bovine milk., *J. Dairy Sci.*, 2015, **98**, 5155–5163.

95. V. A. Mittal, A. Ellis, A. Ye, S. Das and H. Singh, Influence of calcium depletion on iron-binding properties of milk., *J. Dairy Sci.*, 2015, **98**, 2103–2113.

96. V. A. Mittal, A. Ellis, A. Ye, P. J. B. Edwards, S. Das and H. Singh, Iron binding to caseins in the presence of orthophosphate, *Food Chem.*, 2016, **190**, 128–134.

97. A. Roach, J. Dunlap and F. Harte, Association of triclosan to casein proteins through solvent-mediated high-pressure homogenization., *J. Food Sci.*, 2009, **74**, N23-9.

98. E. Semo, E. Kesselman, D. Danino and Y. Livney, Casein micelle as a natural nano-capsular vehicle for nutraceuticals, *Food Hydrocoll.*, 2007, **21**, 936–942.

99. A. K. Thompson, A. Couchoud and H. Singh, Comparison of hydrophobic and hydrophilic encapsulation using liposomes prepared from milk fat globule-derived phospholipids and soya phospholipids, *Dairy Sci. Technol.*, 2009, **89**, 99–113.

100. S. He and A. Ye, Formation and gastrointestinal digestion of β-carotene emulsion stabilized by milk fat globule membrane, *J. Food Process Eng.*, 2019, **42**.

101. M.-T. Chang, T.-R. Tsai, C.-Y. Lee, Y.-S. Wei, Y.-J. Chen, C.-R. Chen and J. T. C. Tzen, Elevating bioavailability of curcumin via encapsulation with a novel formulation of artificial oil bodies., *J. Agric. Food Chem.*, 2013, **61**, 9666–9671.

102. E. Dadkhodazade, E. Khanniri, N. Khorshidian, S. M. Hosseini, A. M. Mortazavian and E. Moghaddas Kia, Yeast cells for encapsulation of bioactive compounds in food products: A review., *Biotechnol. Prog.*, 2021, **37**, e3138.

103. G. Shi, L. Rao, H. Yu, H. Xiang, G. Pen, S. Long and C. Yang, Yeast-cell-based microencapsulation of chlorogenic acid as a water-soluble antioxidant, *J. Food Eng.*, 2007, **80**, 1060–1067.

104. N. J. Zuidam and E. Heinrich, in *Encapsulation technologies for active food ingredients and food processing*, eds. N. J. Zuidam and V. Nedovic, Springer New York, New York, NY, 2010, pp. 127–160.

105. S. Young, S. Dea and N. Nitin, Vacuum facilitated infusion of bioactives into yeast microcarriers: Evaluation of a novel encapsulation approach., *Food Res. Int.*, 2017, **100**, 100–112.

106. E. I. Paramera, S. J. Konteles and V. T. Karathanos, Microencapsulation of curcumin in cells of Saccharomyces cerevisiae, *Food Chem.*, 2011, **125**, 892–902.

107. G. Shi, L. Rao, H. Yu, H. Xiang, H. Yang and R. Ji, Stabilization and encapsulation of photosensitive resveratrol within yeast cell., *Int. J. Pharm.*, 2008, **349**, 83–93.

108. V. Đorđević, B. Balanč, A. Belščak-Cvitanović, S. Lević, K. Trifković, A. Kalušević, I. Kostić, D. Komes, B. Bugarski and V. Nedović, Trends in encapsulation technologies for delivery of food bioactive compounds, *Food Eng. Rev.*, 2015, **7**, 452–490.

109. US Pat. US4001480A, 1976.

110. E. I. Paramera, S. J. Konteles and V. T. Karathanos, Stability and release properties of curcumin encapsulated in Saccharomyces cerevisiae, β-cyclodextrin and modified starch, *Food Chem.*, 2011, **125**, 913–922.

111. S. Young and N. Nitin, Thermal and oxidative stability of curcumin encapsulated in yeast microcarriers., *Food Chem.*, 2019, **275**, 1–7.

112. C.-K. Chow and S. P. Palecek, Enzyme encapsulation in permeabilized Saccharomyces cerevisiae cells., *Biotechnol. Prog.*, 2004, **20**, 449–456.

113. G. Kogan, M. Pajtinka, M. Babincova, E. Miadokova, P. Rauko, D. Slamenova and T. A. Korolenko, Yeast cell wall polysaccharides as antioxidants and antimutagens: can they fight cancer?, *Neoplasma*, 2008, **55**, 387–393.

114. J. R. Bishop, G. Nelson and J. Lamb, Microencapsulation in yeast cells., *J. Microencapsul.*, 1998, **15**, 761–773.

115. R. Scherrer, L. Louden and P. Gerhardt, Porosity of the yeast cell wall and membrane., *J. Bacteriol.*, 1974, **118**, 534–540.

116. R. A. Smith, M. J. Duncan and D. T. Moir, Heterologous protein secretion from yeast., *Science*, 1985, **229**, 1219–1224.

117. B. N. Pham-Hoang, C. Romero-Guido, H. Phan-Thi and Y. Waché, Encapsulation in a natural, preformed, multi-component and complex capsule: yeast cells., *Appl. Microbiol. Biotechnol.*, 2013, **97**, 6635–6645.

118. H. Tanguler and H. Erten, Utilisation of spent brewer's yeast for yeast extract production by autolysis: The effect of temperature, *Food and Bioproducts Processing*, 2008, **86**, 317–321.

119. A. B. Yarlagadda, M. G. Wilkinson, S. P. Ryan, I. A. Doolan, M. G. O'sullivan and K. N. Kilcawley, Utilisation of a cell-free extract of lactic acid bacteria entrapped in yeast to enhance flavour development in Cheddar cheese, *Int. J. Dairy Technol.*, 2014, **67**, 21–30.

120. M. R. da Silva Pedrini, S. Dupont, A. de Anchieta Câmara, L. Beney and P. Gervais, Osmoporation: a simple way to internalize hydrophilic molecules into yeast., *Appl. Microbiol. Biotechnol.*, 2014, **98**, 1271–1280.

121. G. Dimopoulos, A. Katsimichas, D. Tsimogiannis, V. Oreopoulou and P. Taoukis, Cell permeabilization processes for improved encapsulation of oregano essential oil in yeast cells, *J. Food Eng.*, 2021, **294**, 110408.

122. D. M. Fenton, Solvent treatment for β-d-galactosidase release from yeast cells, *Enzyme Microb. Technol.*, 1982, **4**, 229–232.

123. X. Song and Y. Li, CELL MEMBRANE DAMAGE BY VACUUM TREATMENT AT DIFFERENT PRESSURE REDUCTION RATES, *J. Food Process Eng.*, 2012, **35**, 915–922.

124. X. Quan Shi and P. Fito Maupoey, Vacuum osmotic dehydration of fruits, *Drying Technology*, 1993, **11**, 1429–1442.

125. A. Czerniak, P. Kubiak, W. Białas and T. Jankowski, Improvement of oxidative stability of menhaden fish oil by microencapsulation within biocapsules formed of yeast cells, *J. Food Eng.*, 2015, **167**, 2–11.

126. C. D. Melia and S. S. Davis, Review article: mechanisms of drug release from tablets and capsules. I: Disintegration., *Aliment. Pharmacol. Ther.*, 1989, **3**, 223–232.

127. C. D. Melia and S. S. Davis, Review article: mechanisms of drug release from tablets and capsules. 2. Dissolution., *Aliment. Pharmacol. Ther.*, 1989, **3**, 513–525.

128. S. Young, R. Rai and N. Nitin, Bioaccessibility of curcumin encapsulated in yeast cells and yeast cell wall particles., *Food Chem.*, 2020, **309**, 125700.

129. L. D. Muiznieks and F. W. Keeley, Molecular assembly and mechanical properties of the extracellular matrix: A fibrous protein perspective., *Biochim. Biophys. Acta*, 2013, **1832**, 866–875.

130. Scientific concepts of functional foods in Europe. Consensus document., *Br. J. Nutr.*, 1999, **81 Suppl 1**, S1-27.

131. S. M. Alzamora, D. Salvatori, M. S. Tapia, A. López-Malo, J. Welti-Chanes and P. Fito, Novel functional foods from vegetable matrices impregnated with biologically active compounds, *J. Food Eng.*, 2005, **67**, 205–214.

132. A. Rózek, J. V. García-Pérez, F. López, C. Güell and M. Ferrando, Infusion of grape phenolics into fruits and vegetables by osmotic treatment: Phenolic stability during air drying, *J. Food Eng.*, 2010, **99**, 142–150.

133. H. Mújica-Paz, A. Valdez-Fragoso, A. López-Malo, E. Palou and J. Welti-Chanes, Impregnation and osmotic dehydration of some fruits: effect of the vacuum pressure and syrup concentration, *J. Food Eng.*, 2003, **57**, 305–314.

134. R. Rai, C. Merrell, W. Yokoyama and N. Nitin, Infusion of trans-resveratrol in micron-scale grape skin powder for enhanced stability and bioaccessibility., *Food Chem.*, 2021, **340**, 127894.

135. P. A. Gibbs, R. J. Seviour and F. Schmid, Growth of filamentous fungi in submerged culture: problems and possible solutions., *Crit. Rev. Biotechnol.*, 2000, **20**, 17–48.

136. J. Zhang and J. Zhang, The filamentous fungal pellet and forces driving its formation., *Crit. Rev. Biotechnol.*, 2016, **36**, 1066–1077.

137. A. Amanullah, P. Jüsten, A. Davies, G. C. Paul, A. W. Nienow and C. R. Thomas, Agitation induced mycelial fragmentation of Aspergillus oryzae and Penicillium chrysogenum., *Biochem. Eng. J.*, 2000, **5**, 109–114.

138. H. Y. Makagiansar, P. Ayazi Shamlou, C. R. Thomas and M. D. Lilly, The influence of mechanical forces on the morphology and penicillin production of Penicillium chrysogenum, *Bioprocess Engineering*, 1993, **9**, 83–90.

139. J. P. Blakeman, A. R. McCracken and D. A. Seaby, Changes brought about in solid substrates after fermentations of mixtures of cereals and pulses withRhizopus oryzae, *J. Sci. Food Agric.*, 1988, **45**, 109–118.

140. R. Gmoser, R. Fristedt, K. Larsson, I. Undeland, M. J. Taherzadeh and P. R. Lennartsson, From stale bread and brewers spent grain to a new food source using edible filamentous fungi., *Bioengineered*, 2020, **11**, 582–598.

141. Seyedeh Fatemeh Seyed Reihani and K. Khosravi-Darani, Mycoprotein Production from Date Waste Using Fusarium venenatum in a Submerged Culture, *Applied Food Biotechnology*, 2018.

142. P. F. Souza Filho, D. Andersson, J. A. Ferreira and M. J. Taherzadeh, Mycoprotein: environmental impact and health aspects., *World J. Microbiol. Biotechnol.*, 2019, **35**, 147.

143. V. L. Tsang and S. N. Bhatia, Three-dimensional tissue fabrication., *Adv. Drug Deliv. Rev.*, 2004, **56**, 1635–1647.

144. D. Dutta, A. Pulsipher, W. Luo and M. N. Yousaf, Synthetic chemoselective rewiring of cell surfaces: generation of three-dimensional tissue structures., *J. Am. Chem. Soc.*, 2011, **133**, 8704–8713.

145. Z. J. Gartner and C. R. Bertozzi, Programmed assembly of 3-dimensional microtissues with defined cellular connectivity., *Proc Natl Acad Sci USA*, 2009, **106**, 4606–4610.

146. M. Hamon, T. Ozawa, K. Montagne, N. Kojima, R. Ishii, S. Yamaguchi, T. Nagamune, T. Ushida and Y. Sakai, Avidin-biotin-based approach to forming heterotypic cell clusters and cell sheets on a gas-permeable membrane., *Biofabrication*, 2011, **3**, 034111.

147. P. A. De Bank, Q. Hou, R. M. Warner, I. V. Wood, B. E. Ali, S. Macneil, D. A. Kendall, B. Kellam, K. M. Shakesheff and L. D. K. Buttery, Accelerated formation of multicellular 3-D structures by cell-to-cell cross-linking., *Biotechnol. Bioeng.*, 2007, **97**, 1617–1625.

148. X.-Q. Dou, J. Zhang and C. Feng, Biotin-Avidin Based Universal Cell-Matrix Interaction for Promoting Three-Dimensional Cell Adhesion., *ACS Appl. Mater. Interfaces*, 2015, **7**, 20786–20792.

149. N. S. Selden, M. E. Todhunter, N. Y. Jee, J. S. Liu, K. E. Broaders and Z. J. Gartner, Chemically programmed cell adhesion with membrane-anchored oligonucleotides., *J. Am. Chem. Soc.*, 2012, **134**, 765–768.

150. S. Chien and K. M. Jan, Red cell aggregation by macromolecules: roles of surface adsorption and electrostatic repulsion., *J. Supramol. Struct.*, 1973, **1**, 385–409.

151. J. P. Chapel and J. F. Berret, Versatile electrostatic assembly of nanoparticles and polyelectrolytes: Coating, clustering and layer-by-layer processes, *Curr. Opin. Colloid Interface Sci*, 2012, **17**, 97–105.

152. A. I. Zamaleeva, I. R. Sharipova, A. V. Porfireva, G. A. Evtugyn and R. F. Fakhrullin, Polyelectrolyte-mediated assembly of multiwalled carbon nanotubes on living yeast cells., *Langmuir*, 2010, **26**, 2671–2679.

153. Y. Teramura and H. Iwata, Cell surface modification with polymers for biomedical studies, *Soft Matter*, 2010, **6**, 1081.

154. L. K. Mahal, K. J. Yarema and C. R. Bertozzi, Engineering chemical reactivity on cell surfaces through oligosaccharide biosynthesis., *Science*, 1997, **276**, 1125–1128.

155. S. C. Hsiao, B. J. Shum, H. Onoe, E. S. Douglas, Z. J. Gartner, R. A. Mathies, C. R. Bertozzi and M. B. Francis, Direct cell surface modification with DNA for the capture of primary cells and the investigation of myotube formation on defined patterns., *Langmuir*, 2009, **25**, 6985–6991.

156. P. M. Claesson, E. Poptoshev, E. Blomberg and A. Dedinaite, Polyelectrolyte-mediated surface interactions., *Adv. Colloid Interface Sci.*, 2005, **114–115**, 173–187.

157. A. Diaspro, D. Silvano, S. Krol, O. Cavalleri and A. Gliozzi, Single Living Cell Encapsulation in Nano-organized Polyelectrolyte Shells, *Langmuir*, 2002, **18**, 5047–5050.

158. A. N. Shipway, M. Lahav, R. Gabai and I. Willner, Investigations into the Electrostatically Induced Aggregation of Au Nanoparticles†, *Langmuir*, 2000, **16**, 8789–8795.

159. H. Paris, H. Mokhtarian, E. Coatanéa, M. Museau and I. F. Ituarte, Comparative environmental impacts of additive and subtractive manufacturing technologies, *CIRP Annals*, 2016, **65**, 29–32.

160. B. Berman, 3-D printing: The new industrial revolution, *Bus. Horiz.*, 2012, **55**, 155–162.

161. A. Derossi, R. Caporizzi, D. Azzollini and C. Severini, Application of 3D printing for customized food. A case on the development of a fruit-based snack for children, *J. Food Eng.*, 2018, **220**, 65–75.

162. Z. Liu, M. Zhang, B. Bhandari and Y. Wang, 3D printing: Printing precision and application in food sector, *Trends Food Sci. Technol.*, 2017, **69**, 83–94.

163. M. Askari, M. Afzali Naniz, M. Kouhi, A. Saberi, A. Zolfagharian and M. Bodaghi, Recent progress in extrusion 3D bioprinting of hydrogel biomaterials for tissue regeneration: a comprehensive review with focus on advanced fabrication techniques., *Biomater. Sci.*, 2021, **9**, 535–573.

164. J. Sun, W. Zhou, L. Yan, D. Huang and L. Lin, Extrusion-based food printing for digitalized food design and nutrition control, *J. Food Eng.*, 2017, **220**, 1–11.

165. L. Hao, S. Mellor, O. Seaman, J. Henderson, N. Sewell and M. Sloan, Material characterisation and process development for chocolate additive layer manufacturing, *Virtual Phys. Prototyp.*, 2010, **5**, 57–64.

166. S. Zhu, M. A. Stieger, A. J. van der Goot and M. A. I. Schutyser, Extrusion-based 3D printing of food pastes: Correlating rheological properties with printing behaviour, *Innovative Food Science & Emerging Technologies*, 2019, **58**, 102214.

167. C. Severini, A. Derossi and D. Azzollini, Variables affecting the printability of foods: Preliminary tests on cereal-based products, *Innovative Food Science & Emerging Technologies*, 2016, **38**, 281–291.

168. R. Serizawa, M. Shitara, J. Gong, M. Makino, M. H. Kabir and H. Furukawa, presented in part at the SPIE Smart Structures and Materials + Nondestructive Evaluation and Health Monitoring, 9 March 2014.

169. D. L. Cohen, J. I. Lipton, M. Cutler, D. Coulter, A. Vesco and H. Lipson, Hydrocolloid Printing: A Novel Platform for Customized Food Production, *University of Texas at Austin*, 2009.

170. H. Ismail, M. Irani and Z. Ahmad, Starch-Based Hydrogels: Present Status and Applications, *International Journal of Polymeric Materials and Polymeric Biomaterials*, 2013, **62**, 411–420.

171. T. Agarwal, M. Costantini and T. K. Maiti, Extrusion 3D printing with Pectin-based ink formulations: Recent trends in tissue engineering and food manufacturing, *Biomedical Engineering Advances*, 2021, **2**, 100018.

172. R. S. M. Azam, M. Zhang, B. Bhandari and C. Yang, Effect of Different Gums on Features of 3D Printed Object Based on Vitamin-D Enriched Orange Concentrate, *Food Biophys.*, 2018, **13**, 250–262.

173. K. Markstedt, A. Mantas, I. Tournier, H. Martínez Ávila, D. Hägg and P. Gatenholm, 3D Bioprinting Human Chondrocytes with Nanocellulose-Alginate Bioink for Cartilage Tissue Engineering Applications., *Biomacromolecules*, 2015, **16**, 1489–1496.

174. V. Vancauwenberghe, P. Verboven, J. Lammertyn and B. Nicolaï, Development of a coaxial extrusion deposition for 3D printing of customizable pectin-based food simulant, *J. Food Eng.*, 2018, **225**, 42–52.

175. Ö. Yildirim and A. Arslan-Yildiz, Development of a hydrocolloid bio-ink for 3D bioprinting., *Biomater. Sci.*, 2022, **10**, 6707–6717.

176. S. Kyle, Z. M. Jessop, A. Al-Sabah and I. S. Whitaker, "Printability" of Candidate Biomaterials for Extrusion Based 3D Printing: State-of-the-Art., *Adv. Healthc. Mater.*, 2017, **6**.

177. V. Vancauwenberghe, P. Verboven, V. B. M. Mbong, E. Vanstreels, J. Lammertyn and B. Nicolai, 3D printing of plant tissue for innovative food manufacturing: Encapsulation of alive plant cells into pectin based bio-ink, *Journal of Food Engineering*, 2017.

178. F. C. Godoi, S. Prakash and B. R. Bhandari, 3d printing technologies applied for food design: Status and prospects, *J. Food Eng.*, 2016, **179**, 44–54.

179. L. A. Garay, I. R. Sitepu, T. Cajka, I. Chandra, S. Shi, T. Lin, J. B. German, O. Fiehn and K. L. Boundy-Mills, Eighteen new oleaginous yeast species., *J. Ind. Microbiol. Biotechnol.*, 2016, **43**, 887–900.

180. M. Kuttiraja, A. Douha, J. R. Valéro and R. D. Tyagi, Elucidating the Effect of Glycerol Concentration and C/N Ratio on Lipid Production Using Yarrowia lipolytica SKY7., *Appl. Biochem. Biotechnol.*, 2016, **180**, 1586–1600.

181. M. Sousa-Silva, D. Vieira, P. Soares, M. Casal and I. Soares-Silva, Expanding the Knowledge on the Skillful Yeast Cyberlindnera jadinii., *J Fungi (Basel)*, 2021, **7**.

182. Y.-R. Zhang, Y.-Q. Zhao and J.-F. Huang, Retinoid-binding proteins: similar protein architectures bind similar ligands via completely different ways., *PLoS ONE*, 2012, **7**, e36772.

183. B. Sengupta, A. Banerjee and P. K. Sengupta, Interactions of the plant flavonoid fisetin with macromolecular targets: insights from fluorescence spectroscopic studies., *J Photochem Photobiol B, Biol*, 2005, **80**, 79–86.

184. R. Chakrabarti, P. S. Rawat, B. M. Cooke, R. L. Coppel and S. Patankar, Cellular effects of curcumin on Plasmodium falciparum include disruption of microtubules., *PLoS ONE*, 2013, **8**, e57302.

185. S. C. Gupta, S. Prasad, J. H. Kim, S. Patchva, L. J. Webb, I. K. Priyadarsini and B. B. Aggarwal, Multitargeting by curcumin as revealed by molecular interaction studies., *Nat. Prod. Rep.*, 2011, **28**, 1937–1955.

186. B. Wang, J. Wang and X.-H. Zhao, Bioactivity of Two Polyphenols Quercetin and Fisetin against Human Gastric Adenocarcinoma AGS Cells as Affected by Two Coexisting Proteins., *Molecules*, 2022, **27**.

187. R. V. Tikekar, Y. Pan and N. Nitin, Fate of curcumin encapsulated in silica nanoparticle stabilized Pickering emulsion during storage and simulated digestion, *Food Res. Int*, 2013, **51**, 370–377.

188. N. Mignet, J. Seguin and G. G. Chabot, Bioavailability of polyphenol liposomes: a challenge ahead., *Pharmaceutics*, 2013, **5**, 457–471.

189. E. I. Taha, S. Al-Saidan, A. M. Samy and M. A. Khan, Preparation and in vitro characterization of self-nanoemulsified drug delivery system (SNEDDS) of all-trans-retinol acetate., *Int. J. Pharm.*, 2004, **285**, 109–119.

190. V. Shapaval, N. K. Afseth, G. Vogt and A. Kohler, Fourier transform infrared spectroscopy for the prediction of fatty acid profiles in Mucor fungi grown in media with different carbon sources., *Microb. Cell Fact.*, 2014, **13**, 86.

191. G. Kosa, V. Shapaval, A. Kohler and B. Zimmermann, FTIR spectroscopy as a unified method for simultaneous analysis of intra- and extracellular metabolites in high-throughput screening of microbial bioprocesses., *Microb. Cell Fact.*, 2017, **16**, 195.

192. M. Suutari, P. Priha and S. Laakso, Temperature shifts in regulation of lipids accumulated byLipomyces starkeyi, *J. Am. Oil Chem. Soc.*, 1993, **70**, 891–894.

193. I. R. Sitepu, R. Sestric, L. Ignatia, D. Levin, J. B. German, L. A. Gillies, L. A. G. Almada and K. L. Boundy-Mills, Manipulation of culture conditions alters lipid content and fatty acid profiles of a wide variety of known and new oleaginous yeast species., *Bioresour. Technol.*, 2013, **144**, 360–369.

194. Tin Kam Ho, presented in part at the 3rd International Conference on Document Analysis and Recognition, 1995.

195. J. Folch, M. Lees and G. H. Sloane Stanley, A simple method for the isolation and purification of total lipides from animal tissues., *J. Biol. Chem.*, 1957, **226**, 497–509.

196. M. M. Bradford, A rapid and sensitive method for the quantitation of microgram quantities of protein utilizing the principle of protein-dye binding., *Anal. Biochem.*, 1976, **72**, 248–254.

197. A. H. Reisner, P. Nemes and C. Bucholtz, The use of Coomassie Brilliant Blue G250 perchloric acid solution for staining in electrophoresis and isoelectric focusing on polyacrylamide gels, *Anal. Biochem.*, 1975, **64**, 509–516.

198. B. Zimmermann and A. Kohler, Optimizing Savitzky-Golay parameters for improving spectral resolution and quantification in infrared spectroscopy., *Appl. Spectrosc.*, 2013, **67**, 892–902.

199. V. Shapaval, J. Brandenburg, J. Blomqvist, V. Tafintseva, V. Passoth, M. Sandgren and A. Kohler, Biochemical profiling, prediction of total lipid content and fatty acid profile in oleaginous yeasts by FTIR spectroscopy., *Biotechnol. Biofuels*, 2019, **12**, 140.

200. G. Kosa, A. Kohler, V. Tafintseva, B. Zimmermann, K. Forfang, N. K. Afseth, D. Tzimorotas, K. S. Vuoristo, S. J. Horn, J. Mounier and V. Shapaval, Microtiter plate cultivation of oleaginous fungi and monitoring of lipogenesis by high-throughput FTIR spectroscopy., *Microb. Cell Fact.*, 2017, **16**, 101.

201. Y. G. Chmykh and J. L. Nadeau, Characterization of Retinol Stabilized in Phosphatidylcholine Vesicles with and without Antioxidants., *ACS Omega*, 2020, **5**, 18367–18375.

202. C. W. Shields, J. P. White, E. G. Osta, J. Patel, S. Rajkumar, N. Kirby, J.-P. Therrien and S. Zauscher, Encapsulation and controlled release of retinol from silicone particles for topical delivery., *J. Control. Release*, 2018, **278**, 37–48.

203. A. A. de Câmara, S. Dupont, L. Beney, P. Gervais, A. Rosenthal, R. T. P. Correia and M. R. da S. Pedrini, Fisetin yeast-based bio-capsules via osmoporation: effects of process variables on the encapsulation efficiency and internalized fisetin content., *Appl. Microbiol. Biotechnol.*, 2016, **100**, 5547–5558.

204. B. T. Kurien and R. H. Scofield, Increasing aqueous solubility of curcumin for improving bioavailability., *Trends Pharmacol. Sci.*, 2009, **30**, 334–5; author reply 335.

205. F. Ciamponi, C. Duckham and N. Tirelli, Yeast cells as microcapsules. Analytical tools and process variables in the encapsulation of hydrophobes in S. cerevisiae., *Appl. Microbiol. Biotechnol.*, 2012, **95**, 1445–1456.

206. Y. Liu, H. Hama, Y. Fujita, A. Kondo, Y. Inoue, A. Kimura and H. Fukuda, Production of S-lactoylglutathione by high activity whole cell biocatalysts prepared by permeabilization of recombinant saccharomyces cerevisiae with alcohols., *Biotechnol. Bioeng.*, 1999, **64**, 54–60.

207. Y. Pan, R. V. Tikekar and N. Nitin, Effect of antioxidant properties of lecithin emulsifier on oxidative stability of encapsulated bioactive compounds., *Int. J. Pharm.*, 2013, **450**, 129–137.

208. U. Kannamangalam Vijayan, N. N. Shah, A. B. Muley and R. S. Singhal, Complexation of curcumin using proteins to enhance aqueous solubility and bioaccessibility: Pea protein vis-à-vis whey protein, *J. Food Eng.*, 2021, **292**, 110258.

209. Scientific Committee of Consumer Safety - SCCS. Electronic address: SANTE-C2-SCCS@ec.europa.eu and C. Rousselle, Opinion of the Scientific Committee on Consumer Safety (SCCS) - Final version of the Opinion on Vitamin A (retinol, retinyl acetate and retinyl palmitate) in cosmetic products., *Regul. Toxicol. Pharmacol.*, 2017, **84**, 102–104.

210. Y. Lu, R. Rai and N. Nitin, Engineering cell-based microstructures to study the effect of structural complexity on in vitro bioaccessibility of a lipophilic bioactive compound., *Food Funct.*, 2022, **13**, 6560–6573.

211. A. P. Bertolo, A. P. Biz, A. P. Kempka, E. Rigo and D. Cavalheiro, Yeast (Saccharomyces cerevisiae): evaluation of cellular disruption processes, chemical composition, functional properties and digestibility., *J. Food Sci. Technol.*, 2019, **56**, 3697–3706.

212. V. Ganeva, B. Angelova, B. Galutzov, V. Goltsev and M. Zhiponova, Extraction of proteins and other intracellular bioactive compounds from baker's yeasts by pulsed electric field treatment., *Front. Bioeng. Biotechnol.*, 2020, **8**, 552335.

213. K. Grillitsch, M. Connerth, H. Köfeler, T. N. Arrey, B. Rietschel, B. Wagner, M. Karas and G. Daum, Lipid particles/droplets of the yeast Saccharomyces cerevisiae revisited: lipidome meets proteome., *Biochim. Biophys. Acta*, 2011, **1811**, 1165–1176.

214. P. Greenspan, E. P. Mayer and S. D. Fowler, Nile red: a selective fluorescent stain for intracellular lipid droplets., *J. Cell Biol.*, 1985, **100**, 965–973.

215. Z. Li, F. Liu, W. Yang, S. Peng and J. Zhou, A survey of convolutional neural networks: analysis, applications, and prospects., *IEEE Trans. Neural Netw. Learn. Syst.*, 2022, **33**, 6999–7019.

216. J. Qin, W. Pan, X. Xiang, Y. Tan and G. Hou, A biological image classification method based on improved CNN, *Ecol. Inform.*, 2020, **58**, 101093.

217. D. Ciresan, A. Giusti, L. Gambardella and J. Schmidhuber, Deep Neural Networks Segment Neuronal Membranes in Electron Microscopy Images, *Advances in Neural Information Processing Systems*, 2012.

218. T. Pärnamaa and L. Parts, Accurate Classification of Protein Subcellular Localization from High-Throughput Microscopy Images Using Deep Learning., *G3 (Bethesda)*, 2017, **7**, 1385–1392.

219. M. Minekus, M. Alminger, P. Alvito, S. Ballance, T. Bohn, C. Bourlieu, F. Carrière, R. Boutrou, M. Corredig, D. Dupont, C. Dufour, L. Egger, M. Golding, S. Karakaya, B. Kirkhus, S. Le Feunteun, U. Lesmes, A. Macierzanka, A. Mackie, S. Marze, D. J. McClements, O. Ménard, I. Recio, C. N. Santos, R. P. Singh, G. E. Vegarud, M. S. J.

Wickham, W. Weitschies and A. Brodkorb, A standardised static in vitro digestion method suitable for food - an international consensus., *Food Funct.*, 2014, **5**, 1113–1124.

220. K. A. Rostron and C. L. Lawrence, Nile red staining of neutral lipids in yeast., *Methods Mol. Biol.*, 2017, **1560**, 219–229.

221. D. R. Stirling, M. J. Swain-Bowden, A. M. Lucas, A. E. Carpenter, B. A. Cimini and A. Goodman, CellProfiler 4: improvements in speed, utility and usability., *BMC Bioinformatics*, 2021, **22**, 433.

222. E. M. M. Manders, F. J. Verbeek and J. A. Aten, Measurement of co-localization of objects in dual-colour confocal images., *J. Microsc.*, 1993, **169**, 375–382.

223. L. van der Maaten and G. Hinton, Visualizing Data using t-SNE, *Journal of Machine Learning Research*, 2008.

224. J. Górnicka, M. Mika, O. Wróblewska, P. Siudem and K. Paradowska, Methods to Improve the Solubility of Curcumin from Turmeric., *Life (Basel)*, 2023, **13**.

225. E. Z. Szuts and F. I. Harosi, Solubility of retinoids in water., *Arch. Biochem. Biophys.*, 1991, **287**, 297–304.

226. G., Development of curcumin based ophthalmic formulation, *Am. J. Infect. Dis.*, 2012, **8**, 41–49.

227. G. Kontopidis, C. Holt and L. Sawyer, Invited review: beta-lactoglobulin: binding properties, structure, and function., *J. Dairy Sci.*, 2004, **87**, 785–796.

228. H. Zlotnik, M. P. Fernandez, B. Bowers and E. Cabib, Saccharomyces cerevisiae mannoproteins form an external cell wall layer that determines wall porosity., *J. Bacteriol.*, 1984, **159**, 1018–1026.

229. R. Coleman, P. J. Lowe and D. Billington, Membrane lipid composition and susceptibility to bile salt damage, *Biochimica et Biophysica Acta (BBA) - Biomembranes*, 1980, **599**, 294–300.

230. D. M. Heuman, R. S. Bajaj and Q. Lin, Adsorption of mixtures of bile salt taurine conjugates to lecithin-cholesterol membranes: implications for bile salt toxicity and cytoprotection., *J. Lipid Res.*, 1996, **37**, 562–573.

231. M. Begley, C. G. M. Gahan and C. Hill, The interaction between bacteria and bile., *FEMS Microbiol. Rev.*, 2005, **29**, 625–651.

232. M. Hasan, K. Elkhoury, C. J. F. Kahn, E. Arab-Tehrany and M. Linder, Preparation, Characterization, and Release Kinetics of Chitosan-Coated Nanoliposomes Encapsulating Curcumin in Simulated Environments., *Molecules*, 2019, **24**.

233. N. M. Sagar, M. McFarlane, C. Nwokolo, K. D. Bardhan and R. P. Arasaradnam, Mechanisms of triglyceride metabolism in patients with bile acid diarrhea., *World J. Gastroenterol.*, 2016, **22**, 6757–6763.

234. A. J. Clulow, B. Barber, M. Salim, T. Ryan and B. J. Boyd, Synergistic and antagonistic effects of non-ionic surfactants with bile salt + phospholipid mixed micelles on the solubility of poorly water-soluble drugs., *Int. J. Pharm.*, 2020, **588**, 119762.

235. P. Borel, Factors affecting intestinal absorption of highly lipophilic food microconstituents (fat-soluble vitamins, carotenoids and phytosterols)., *Clin. Chem. Lab. Med.*, 2003, **41**, 979–994.

236. M. V. Boland, M. K. Markey and R. F. Murphy, Automated recognition of patterns characteristic of subcellular structures in fluorescence microscopy images., *Cytometry*, 1998, **33**, 366–375.

237. A. Shehzad, F. Wahid and Y. S. Lee, Curcumin in cancer chemoprevention: molecular targets, pharmacokinetics, bioavailability, and clinical trials., *Arch Pharm (Weinheim)*, 2010, **343**, 489–499.

238. M. S. Mathew, K. Vinod, P. S. Jayaram, R. S. Jayasree and K. Joseph, Improved Bioavailability of Curcumin in Gliadin-Protected Gold Quantum Cluster for Targeted Delivery., *ACS Omega*, 2019, **4**, 14169–14178.

239. S. Prasad, A. K. Tyagi and B. B. Aggarwal, Recent developments in delivery, bioavailability, absorption and metabolism of curcumin: the golden pigment from golden spice., *Cancer Res. Treat.*, 2014, **46**, 2–18.

240. M. S. Baliga, N. Joseph, M. V. Venkataranganna, A. Saxena, V. Ponemone and R. Fayad, Curcumin, an active component of turmeric in the prevention and treatment of ulcerative colitis: preclinical and clinical observations., *Food Funct.*, 2012, **3**, 1109–1117.

241. J. Boyer and R. H. Liu, Apple phytochemicals and their health benefits., *Nutr. J.*, 2004, **3**, 5.

242. A. Wright, C. Pietrangelo and A. Macnaughton, Influence of simulated upper intestinal parameters on the efficiency of beta carotene micellarisation using an in vitro model of digestion, *Food Chem.*, 2007.

243. K. H. van het Hof, B. C. de Boer, L. B. Tijburg, B. R. Lucius, I. Zijp, C. E. West, J. G. Hautvast and J. A. Weststrate, Carotenoid bioavailability in humans from tomatoes processed in different ways determined from the carotenoid response in the triglyceride-rich lipoprotein fraction of plasma after a single consumption and in plasma after four days of consumption., *J. Nutr.*, 2000, **130**, 1189–1196.

244. A. J. Edwards, C. H. Nguyen, C.-S. You, J. E. Swanson, C. Emenhiser and R. S. Parker, Alpha- and beta-carotene from a commercial puree are more bioavailable to humans than from boiled-mashed carrots, as determined using an extrinsic stable isotope reference method., *J. Nutr.*, 2002, **132**, 159–167.

245. M. Abid, S. Jabbar, T. Wu, M. M. Hashim, B. Hu, S. Lei and X. Zeng, Sonication enhances polyphenolic compounds, sugars, carotenoids and mineral elements of apple juice., *Ultrason. Sonochem.*, 2014, **21**, 93–97.

246. G. Nelson, S. C. Duckham and M. E. D. Crothers, in *Polymeric drug delivery I: particulate drug carriers*, ed. S. Svenson, American Chemical Society, Washington, DC, 2006, vol. 923, pp. 268–281.

247. R. Salari, O. Rajabi, Z. Khashyarmanesh, M. Fathi Najafi and B. S. Fazly Bazzaz, Characterization of Encapsulated Berberine in Yeast Cells of Saccharomyces cerevisiae., *Iran. J. Pharm. Res.*, 2015, **14**, 1247–1256.

248. Z. Zhang, R. Zhang, L. Zou, L. Chen, Y. Ahmed, W. Al Bishri, K. Balamash and D. J. McClements, Encapsulation of curcumin in polysaccharide-based hydrogel beads: Impact of bead type on lipid digestion and curcumin bioaccessibility, *Food Hydrocoll.*, 2016, **58**, 160–170.

249. B. Zeeb, A. H. Saberi, J. Weiss and D. J. McClements, Formation and characterization of filled hydrogel beads based on calcium alginate: Factors influencing nanoemulsion retention and release, *Food Hydrocoll.*, 2015, **50**, 27–36.

250. I. I. Moraru, J. C. Schaff, B. M. Slepchenko, M. L. Blinov, F. Morgan, A. Lakshminarayana, F. Gao, Y. Li and L. M. Loew, Virtual Cell modelling and simulation software environment., *IET Syst. Biol.*, 2008, **2**, 352–362.

251. L. P. Coelho, Mahotas: Open source software for scriptable computer vision, *J. Open Res. Softw.*, 2013, **1**, e3.

252. J. R. Malagelada, G. F. Longstreth, W. H. Summerskill and V. L. Go, Measurement of gastric functions during digestion of ordinary solid meals in man., *Gastroenterology*, 1976, **70**, 203–210.

253. L. Kalantzi, K. Goumas, V. Kalioras, B. Abrahamsson, J. B. Dressman and C. Reppas, Characterization of the human upper gastrointestinal contents under conditions simulating bioavailability/bioequivalence studies., *Pharm. Res.*, 2006, **23**, 165–176.

254. M. Peleg, An empirical model for the description of moisture sorption curves, *J. Food Sci.*, 1988, **53**, 1216–1217.

255. K. G. Kaptso, Y. N. Njintang, A. E. Komnek, J. Hounhouigan, J. Scher and C. M. F. Mbofung, Physical properties and rehydration kinetics of two varieties of cowpea (Vigna

unguiculata) and bambara groundnuts (Voandzeia subterranea) seeds, *J. Food Eng.*, 2008, **86**, 91–99.

256. A. S. Kipcak, O. Ismail, I. Doymaz and S. Piskin, Modeling and Investigation of the Swelling Kinetics of Acrylamide-Sodium Acrylate Hydrogel, *J. Chem.*, 2014, **2014**, 1–8.

257. M. Liu, F. Dong, W. Zhang, X. Nie, H. Wei, S. Sun, X. Zhong, Y. Liu and D. Wang, Contribution of surface functional groups and interface interaction to biosorption of strontium ions by Saccharomyces cerevisiae under culture conditions, *RSC Adv.*, 2017, **7**, 50880–50888.

258. S. M. Tazhibaeva, K. B. Musabekov, A. B. Orazymbetova and A. A. Zhubanova, Surface properties of yeast cells, *Colloid Journal*, 2003, **65**, 122–124.

259. S. Ogawa, E. A. Decker and D. J. McClements, Production and characterization of O/W emulsions containing cationic droplets stabilized by lecithin-chitosan membranes., *J. Agric. Food Chem.*, 2003, **51**, 2806–2812.

260. T. Aoki, E. A. Decker and D. J. McClements, Influence of environmental stresses on stability of O/W emulsions containing droplets stabilized by multilayered membranes produced by a layer-by-layer electrostatic deposition technique, *Food Hydrocoll.*, 2005, **19**, 209–220.

261. E. Dickinson, Hydrocolloids at interfaces and the influence on the properties of dispersed systems, *Food Hydrocoll.*, 2003, **17**, 25–39.

262. L. Zou, B. Zheng, R. Zhang, Z. Zhang, W. Liu, C. Liu, H. Xiao and D. J. McClements, Enhancing the bioaccessibility of hydrophobic bioactive agents using mixed colloidal dispersions: Curcumin-loaded zein nanoparticles plus digestible lipid nanoparticles, *Food Res. Int*, 2016, **81**, 74–82.

263. A. E. Krausz, B. L. Adler, V. Cabral, M. Navati, J. Doerner, R. A. Charafeddine, D. Chandra, H. Liang, L. Gunther, A. Clendaniel, S. Harper, J. M. Friedman, J. D. Nosanchuk and A. J. Friedman, Curcumin-encapsulated nanoparticles as innovative antimicrobial and wound healing agent., *Nanomedicine*, 2015, **11**, 195–206.

264. B. Zheng, S. Peng, X. Zhang and D. J. McClements, Impact of Delivery System Type on Curcumin Bioaccessibility: Comparison of Curcumin-Loaded Nanoemulsions with Commercial Curcumin Supplements., *J. Agric. Food Chem.*, 2018, **66**, 10816–10826.

265. A. Araiza-Calahorra, M. Akhtar and A. Sarkar, Recent advances in emulsion-based delivery approaches for curcumin: From encapsulation to bioaccessibility, *Trends Food Sci. Technol.*, 2018, **71**, 155–169.

266. L. Zou, W. Liu, C. Liu, H. Xiao and D. J. McClements, Utilizing food matrix effects to enhance nutraceutical bioavailability: increase of curcumin bioaccessibility using excipient emulsions., *J. Agric. Food Chem.*, 2015, **63**, 2052–2062.

267. B. T. Kurien, A. Singh, H. Matsumoto and R. H. Scofield, Improving the solubility and pharmacological efficacy of curcumin by heat treatment., *Assay Drug Dev. Technol.*, 2007, **5**, 567–576.

268. N. Pavlović, S. Goločorbin-Kon, M. Đanić, B. Stanimirov, H. Al-Salami, K. Stankov and M. Mikov, Bile acids and their derivatives as potential modifiers of drug release and pharmacokinetic profiles., *Front. Pharmacol.*, 2018, **9**, 1283.

269. G. Mandalari, R. M. Faulks, G. T. Rich, V. Lo Turco, D. R. Picout, R. B. Lo Curto, G. Bisignano, P. Dugo, G. Dugo, K. W. Waldron, P. R. Ellis and M. S. J. Wickham, Release of protein, lipid, and vitamin E from almond seeds during digestion., *J. Agric. Food Chem.*, 2008, **56**, 3409–3416.

270. F. von Burkersroda, L. Schedl and A. Göpferich, Why degradable polymers undergo surface erosion or bulk erosion., *Biomaterials*, 2002, **23**, 4221–4231.

271. N. Amdursky, R. Orbach, E. Gazit and D. Huppert, Probing the inner cavities of hydrogels by proton diffusion, *J. Phys. Chem. C*, 2009, **113**, 19500–19505.

272. X. Y. Li, X. G. Chen, Z. W. Sun, H. J. Park and D.-S. Cha, Preparation of alginate/chitosan/carboxymethyl chitosan complex microcapsules and application in Lactobacillus casei ATCC 393, *Carbohydr. Polym.*, 2011, **83**, 1479–1485.

273. A. Dafe, H. Etemadi, A. Dilmaghani and G. R. Mahdavinia, Investigation of pectin/starch hydrogel as a carrier for oral delivery of probiotic bacteria., *Int. J. Biol. Macromol.*, 2017, **97**, 536–543.

274. W. Wang, M. Onnagawa, Y. Yoshie and T. Suzuki, Binding of bile salts to soluble and insoluble dietary fibers of seaweeds, *Fisheries Sci.*, 2001, **67**, 1169–1173.

275. J. J. Gu, A. F. Hofmann, H. T. Ton-Nu, C. D. Schteingart and K. J. Mysels, Solubility of calcium salts of unconjugated and conjugated natural bile acids., *J. Lipid Res.*, 1992, **33**, 635–646.

276. M. Ogawa, L. F. Bisson, T. García-Martínez, J. C. Mauricio and J. Moreno-García, New insights on yeast and filamentous fungus adhesion in a natural co-immobilization system: proposed advances and applications in wine industry., *Appl. Microbiol. Biotechnol.*, 2019, **103**, 4723–4731.

277. N. Mohd Nasir, F. H. Mohd Yunos, H. H. Wan Jusoh, A. Mohammad, S. S. Lam and A. Jusoh, Subtopic: Advances in water and wastewater treatment harvesting of Chlorella sp.

microalgae using Aspergillus niger as bio-flocculant for aquaculture wastewater treatment., *J. Environ. Manage.*, 2019, **249**, 109373.

278. W. Zhou, Y. Cheng, Y. Li, Y. Wan, Y. Liu, X. Lin and R. Ruan, Novel fungal pelletization-assisted technology for algae harvesting and wastewater treatment., *Appl. Biochem. Biotechnol.*, 2012, **167**, 214–228.

279. A. F. Miranda, M. Taha, D. Wrede, P. Morrison, A. S. Ball, T. Stevenson and A. Mouradov, Lipid production in association of filamentous fungi with genetically modified cyanobacterial cells., *Biotechnol. Biofuels*, 2015, **8**, 179.

280. A. Bhattacharya, M. Mathur, P. Kumar and A. Malik, Potential role of N-acetyl glucosamine in Aspergillus fumigatus-assisted Chlorella pyrenoidosa harvesting., *Biotechnol. Biofuels*, 2019, **12**, 178.

281. M. Ogawa, J. Moreno García, N. Nitin, K. Baar and D. E. Block, Assessing edible filamentous fungal carriers as cell supports for growth of yeast and cultivated meat, *Foods*, 2022, **11**, 3142.

282. T. García-Martínez, A. Puig-Pujol, R. A. Peinado, J. Moreno and J. C. Mauricio, Potential use of wine yeasts immobilized on Penicillium chrysogenum for ethanol production, *J. Chem. Technol. Biotechnol.*, 2012, **87**, 351–359.

283. R. A. Peinado, J. J. Moreno, J. M. Villalba, J. A. González-Reyes, J. M. Ortega and J. C. Mauricio, Yeast biocapsules: A new immobilization method and their applications, *Enzyme Microb. Technol.*, 2006, **40**, 79–84.

284. M. Ogawa, P. Carmona-Jiménez, T. García-Martínez, J. V. Jorrín-Novo, J. Moreno, M. D. Rey and J. Moreno-García, Use of yeast biocapsules as a fungal-based immobilized cell technology for Indian Pale Ale-type beer brewing., *Appl. Microbiol. Biotechnol.*, 2022, **106**, 7615–7625.

285. J. R. López-Menchero, M. Ogawa, J. C. Mauricio, J. Moreno and J. M. García, Effect of calcium alginate coating on the cell retention and fermentation of a fungus-yeast immobilization system, *LWT*, 2021, 111250.

286. J. Moreno-García, T. García-Martinez, J. Moreno, J. C. Mauricio, M. Ogawa, P. Luong and L. F. Bisson, Impact of Yeast Flocculation and Biofilm Formation on Yeast-Fungus Coadhesion in a Novel Immobilization System, *Am. J. Enol. Vitic.*, 2018, **69**, 278–288.

287. P. J. Strong, R. Self, K. Allikian, E. Szewczyk, R. Speight, I. O'Hara and M. D. Harrison, Filamentous fungi for future functional food and feed., *Curr. Opin. Biotechnol.*, 2022, **76**, 102729.

288. M. Slifkin and R. Cumbie, Congo red as a fluorochrome for the rapid detection of fungi., *J. Clin. Microbiol.*, 1988, **26**, 827–830.

289. F. Langenbucher, Linearization of dissolution rate curves by the Weibull distribution., *J. Pharm. Pharmacol.*, 1972, **24**, 979–981.

290. T. García-Martínez, R. A. Peinado, J. Moreno, I. García-García and J. C. Mauricio, Co-culture of Penicillium chrysogenum and Saccharomyces cerevisiae leading to the immobilization of yeast, *J. Chem. Technol. Biotechnol.*, 2011, **86**, 812–817.

291. Bruschi, in *Strategies to Modify the Drug Release from Pharmaceutical Systems*, Elsevier, 2015, pp. 63–86.

292. F. Yang, M. Zhang, B. Bhandari and Y. Liu, Investigation on lemon juice gel as food material for 3D printing and optimization of printing parameters, *LWT - Food Science and Technology*, 2018, **87**, 67–76.

293. X. Zeng, T. Li, J. Zhu, L. Chen and B. Zheng, Printability improvement of rice starch gel via catechin and procyanidin in hot extrusion 3D printing, *Food Hydrocoll.*, 2021, **121**, 106997.

294. Z. Liu, H. Chen, B. Zheng, F. Xie and L. Chen, Understanding the structure and rheological properties of potato starch induced by hot-extrusion 3D printing, *Food Hydrocoll.*, 2020, **105**, 105812.

295. X. Zeng, H. Chen, L. Chen and B. Zheng, Insights into the relationship between structure and rheological properties of starch gels in hot-extrusion 3D printing., *Food Chem.*, 2021, **342**, 128362.

296. L. Ouyang, R. Yao, Y. Zhao and W. Sun, Effect of bioink properties on printability and cell viability for 3D bioplotting of embryonic stem cells., *Biofabrication*, 2016, **8**, 035020.

297. Z. Liu, B. Bhandari, S. Prakash, S. Mantihal and M. Zhang, Linking rheology and printability of a multicomponent gel system of carrageenan-xanthan-starch in extrusion based additive manufacturing, *Food Hydrocoll.*, 2019, **87**, 413–424.

298. Y. Ma, M. A. I. Schutyser, R. M. Boom and L. Zhang, Predicting the extrudability of complex food materials during 3D printing based on image analysis and gray-box data-driven modelling, *Innovative Food Science & Emerging Technologies*, 2021, **73**, 102764.

299. Y. He, F. Yang, H. Zhao, Q. Gao, B. Xia and J. Fu, Research on the printability of hydrogels in 3D bioprinting., *Sci. Rep.*, 2016, **6**, 29977.

300. P. Lopez-Sanchez, M. Martinez-Sanz, M. R. Bonilla, D. Wang, E. P. Gilbert, J. R. Stokes and M. J. Gidley, Cellulose-pectin composite hydrogels: Intermolecular interactions and material properties depend on order of assembly., *Carbohydr. Polym.*, 2017, **162**, 71–81.

301. M. K. Hausmann, P. A. Rühs, G. Siqueira, J. Läuger, R. Libanori, T. Zimmermann and A. R. Studart, Dynamics of Cellulose Nanocrystal Alignment during 3D Printing., *ACS Nano*, 2018, **12**, 6926–6937.

302. G. Siqueira, D. Kokkinis, R. Libanori, M. K. Hausmann, A. S. Gladman, A. Neels, P. Tingaut, T. Zimmermann, J. A. Lewis and A. R. Studart, Cellulose nanocrystal inks for 3D printing of textured cellular architectures, *Adv. Funct. Mater*, 2017, **27**, 1604619.

303. V. Vancauwenberghe, L. Katalagarianakis, Z. Wang, M. Meerts, M. Hertog, P. Verboven, P. Moldenaers, M. E. Hendrickx, J. Lammertyn and B. Nicolaï, Pectin based food-ink formulations for 3-D printing of customizable porous food simulants, *Innovative Food Science & Emerging Technologies*, 2017, **42**, 138–150.

304. A. Conev, E. E. Litsa, M. R. Perez, M. Diba, A. G. Mikos and L. E. Kavraki, Machine Learning-Guided Three-Dimensional Printing of Tissue Engineering Scaffolds., *Tissue Eng. Part A*, 2020, **26**, 1359–1368.

305. J. Müller-Maatsch, M. Bencivenni, A. Caligiani, T. Tedeschi, G. Bruggeman, M. Bosch, J. Petrusan, B. Van Droogenbroeck, K. Elst and S. Sforza, Pectin content and composition from different food waste streams., *Food Chem.*, 2016, **201**, 37–45.

306. C.-C. Hung and P. H. Santschi, Spectrophotometric determination of total uronic acids in seawater using cation-exchange separation and pre-concentration by lyophilization, *Anal. Chim. Acta*, 2001, **427**, 111–117.

307. H. Li, Y. J. Tan, K. F. Leong and L. Li, 3D Bioprinting of Highly Thixotropic Alginate/Methylcellulose Hydrogel with Strong Interface Bonding., *ACS Appl. Mater. Interfaces*, 2017, **9**, 20086–20097.

308. K. Hyun, S. H. Kim, K. H. Ahn and S. J. Lee, Large amplitude oscillatory shear as a way to classify the complex fluids, *J Nonnewton Fluid Mech*, 2002, **107**, 51–65.

309. Amplitude sweeps :: Anton Paar Wiki, https://wiki.anton-paar.com/en/amplitude-sweeps/, .

310. G. Stojkov, Z. Niyazov, F. Picchioni and R. K. Bose, Relationship between Structure and Rheology of Hydrogels for Various Applications., *Gels*, 2021, **7**.

311. M. A. Rao, in *Rheology of fluid, semisolid, and solid foods*, Springer US, Boston, MA, 2014, pp. 63–159.

312. I. Fraeye, E. Doungla, T. Duvetter, P. Moldenaers, A. Van Loey and M. Hendrickx, Influence of intrinsic and extrinsic factors on rheology of pectin–calcium gels, *Food Hydrocoll.*, 2009, **23**, 2069–2077.

313. S. M. Cardoso, M. A. Coimbra and J. A. Lopes da Silva, Calcium-mediated gelation of an olive pomace pectic extract, *Carbohydr. Polym.*, 2003, **52**, 125–133.

314. I. Ventura, J. Jammal and H. Bianco-Peled, Insights into the nanostructure of low-methoxyl pectin-calcium gels., *Carbohydr. Polym.*, 2013, **97**, 650–658.

315. L. Cao, W. Lu, A. Mata, K. Nishinari and Y. Fang, Egg-box model-based gelation of alginate and pectin: A review., *Carbohydr. Polym.*, 2020, **242**, 116389.

316. R. R. Vincent and M. A. K. Williams, Microrheological investigations give insights into the microstructure and functionality of pectin gels., *Carbohydr. Res.*, 2009, **344**, 1863–1871.

317. D. Lootens, F. Capel, D. Durand, T. Nicolai, P. Boulenguer and V. Langendorff, Influence of pH, Ca concentration, temperature and amidation on the gelation of low methoxyl pectin, *Food Hydrocoll.*, 2003, **17**, 237–244.

318. A. Cárdenas, F. M. Goycoolea and M. Rinaudo, On the gelling behaviour of 'nopal' (Opuntia ficus indica) low methoxyl pectin, *Carbohydr. Polym.*, 2008, **73**, 212–222.

319. J. John, D. Ray, V. K. Aswal, A. P. Deshpande and S. Varughese, Dissipation and strain-stiffening behavior of pectin-Ca gels under LAOS., *Soft Matter*, 2019, **15**, 6852–6866.

320. H. G. Sim, K. H. Ahn and S. J. Lee, Large amplitude oscillatory shear behavior of complex fluids investigated by a network model: a guideline for classification, *J Nonnewton Fluid Mech*, 2003, **112**, 237–250.

321. K. Hyun, M. Wilhelm, C. O. Klein, K. S. Cho, J. G. Nam, K. H. Ahn, S. J. Lee, R. H. Ewoldt and G. H. McKinley, A review of nonlinear oscillatory shear tests: Analysis and application of large amplitude oscillatory shear (LAOS), *Prog. Polym. Sci.*, 2011, **36**, 1697–1753.

322. A. F. Hofmann and K. J. Mysels, Bile acid solubility and precipitation in vitro and in vivo: the role of conjugation, pH, and Ca2+ ions., *J. Lipid Res.*, 1992, **33**, 617–626.

323. M. Espinal-Ruiz, F. Parada-Alfonso, L.-P. Restrepo-Sánchez, C.-E. Narváez-Cuenca and D. J. McClements, Interaction of a dietary fiber (pectin) with gastrointestinal components (bile salts, calcium, and lipase): a calorimetry, electrophoresis, and turbidity study., *J. Agric. Food Chem.*, 2014, **62**, 12620–12630.

324. M. C. Neves, H. A. L. Filipe, R. L. Reis, J. P. Prates Ramalho, F. Coreta-Gomes, M. J. Moreno and L. M. S. Loura, Interaction of bile salts with lipid bilayers: an atomistic molecular dynamics study., *Front. Physiol.*, 2019, **10**, 393.